Faculty of Sciences

Department of Analytical Chemistry

Research group: Electrochemistry and Surface Analysis

Synthesis and Characterization of Self-healing Cerium-Doped Silane Hybrid Coatings on Steel Surfaces

Thesis submitted in fulfillment of the requirements for the degree of

Doctor of Science: Chemistry

By

Roohangiz Zandi Zand

Supervisor: Prof Dr *Annemie Adriaens*

Co-supervisor: Prof Dr *Kim Verbeken*

Acknowledgements

One of the joys of completion is to look over the past journey and remember all the friends and family who have helped and supported along this long but fulfilling road.

Firstly, I would like to express my heartfelt gratitude to Prof. Dr. Annemie Adriaens for her so precious guidance, kindness and patience during these past five years. I appreciate all her contributions of time, ideas, and funding to make my Ph.D. experience productive and stimulating.

I am also thankful to Prof. Dr. Kim Verbeken for his precious technical advice and help, especially for providing the metallic materials from Arcelor Mittal Gent and for providing the condition and equipment for doing all necessary instrumental tests in his group in the material engineering department of Ghent University.

I gratefully acknowledge the members of my Ph.D. committee for their time and valuable feedback on a preliminary version of this thesis. It is no easy task, reviewing a thesis, and I am grateful for their thoughtful and detailed comments. Thank you for helping to shape and guide the direction of the work with your careful and constructive comments.

This thesis was partly funded by Ghent University and therefore I would also like to thank UGent for its generous support. I am also very grateful to Arcelor Mittal Gent for providing the metallic materials.

As a member of Ghent University, I have been surrounded by wonderful colleagues, who have provided a rich and fertile environment to study and explore new ideas. I would like to thank my friends in the ESA group: Rosie, Pieter-Jan, Elbeshary, Peter, Alice, Farzin and especially, Victoria and Michel who have been so helpful in providing advice many times during the writing and revision of my last papers. The group has been a source of friendships as well as good advice and collaboration. I am grateful for the chance to visit and be a part of this group. Thank you for welcoming me as a friend and helping to develop the ideas in this thesis.

I would also like to thank the technical staff of the department, especially Pieter Van Hoe, Paul Scheerlinck, Davy De Pauw, Philip Brondeel, Chantal Hufkens and Tine Veevaete who helped me every time. I also wish to acknowledge Peter Mast, Michel Moors, Christa

Sonck, Veerle Boterberg, Sandra Van Vlierberghe, Babs Lemmens, Pieter Cools and Vitaliy Bliznuk for their technical assistance.

I am deeply thankful to my family for their love, support, and sacrifices. Without them, this thesis would never have been written.

This last word of acknowledgment I have saved for my dear husband, Alireza, who has been with me all these years and has made them the best years of my life.

I dedicate this thesis to my little angle, Amirali, who was born on 23th September 2014. I love you all dearly.

Roohangiz ZandiZand

Ghent, Belgium

September 2015

Summary

This work explores the synthesis via a sol–gel method and self-healing properties of cerium-doped silane hybrid coatings employing 3-glycidoxypropyltrimethoxysilane (GPTMS) and bisphenol A (BPA), as a cross-linking agent. The aim for these coatings is to protect steel structures from corrosion in marine environments. The analysis covers seven main areas. In the first and second section, the effects of the coating drying method and the addition of cerium ions, as a dopant, and bisphenol A, as a cross-linking agent, are examined on the microstructure and corrosion resistance of the hybrid silane coatings. The self-healing properties of the coatings doped with cerium nitrate and ceria nanoparticles are then evaluated by comparing intact and artificially scratched films. The fourth and fifth section of this work examine how the cerium nitrate concentration and the activation of ceria nanoparticles with cerium nitrate affect the ability of cerium-doped silane hybrid coatings to protect against corrosion. Finally the effect of the ceria nanoparticles concentration and its combination with zirconia nanoparticles is studied on the self-healing properties of cerium ions inhibited silane coatings. The microscopic features, morphology as well as microstructural features of the coated substrates were evaluated using Fourier transform infrared spectroscopy (FTIR), atomic force microscopy (AFM) and scanning electron microscopy (SEM). The corrosion behavior of the sol–gel coatings was investigated using natural salt spray tests, electrochemical impedance spectroscopy (EIS) and potentiodynamic polarization tests.

Samenvatting

Dit werk bestudeert de sol-gelsynthese en de zelfhelende eigenschappen van cerium gedopeerde silaanhybridedeklagen. Hierbij wordt gebruik gemaakt van 3-glycidoxypropyltrimethoxysilaan (GPTMS) en bisphenol A (BPA) als een crosslinker. De doelstelling van deze deklagen is de corrosiebescherming van stalen structuren in een mariene omgeving.

Het werk bevat zeven onderdelen. In een eerste en tweede deel worden de invloeden van de droogmethode van de deklaag en de toevoeging van ceriumionen, als dopeermiddel, en bisphenol A, als crosslinker, bestudeerd met betrekking tot de microstructuur en corrosie-inhibitie van de deklagen. Vervolgens worden de zelfhelende eigenschappen van de deklagen gedopeerd met ceriumnitraat en cerianopartikels geëvalueerd door een vergelijking te maken tussen intacte en artificieel beschadigde films. Het vierde en vijfde deel van dit werk evalueert hoe de ceriumnitraat concentratie en de activatie van cerianopartikels met ceriumnitraat de corrosie-inhibitie van de deklagen beïnvloedt. Tot slot wordt de invloed van de cerianopartikelconcentratie en de combinatie met zirconiapartikels nagegaan op de zelfhelende karakteristieken van de deklagen.

De microscopische kenmerken, alsook de morfologie en de microstructurele kenmerken van de deklagen werden in dit werk bestudeerd met Fourier transformatie-infraroodspectroscopie (FTIR), atomaire krachtmicroscopie (AFM) en rasterelektronenmicroscopie (SEM). Het corrosiegedrag van de sol-gel deklagen werd bestudeerd met zoutnevelexperimenten, elektrochemische impedantiespectroscopie (EIS) en polarisatietesten.

TABLE OF CONTENT

Chapter 2

Chapter 3

Chapter 10

INTRODUCTION

1.1. Corrosion

Corrosion is the gradual degradation of a material due to chemical or electrochemical interactions with its environment. It damages the appearance and useful properties of a material such as its strength, ductility and permeability to corrosive liquids and gases. All materials—metals, polymers, ceramics, composites are susceptible to corrosion. A metal can corrode by electrochemical oxidation through its reaction with an oxidant (e.g., oxygen) to form metallic oxide(s) or salts(s). The rusting of iron to form iron oxide is a well-known example of electrochemical corrosion [1, 2].

Metals corrode because of their high free energy content. In their natural state most metals are chemically combined with other elements in metallic ores. Refining a metal consists of transforming an energetically stable ore into a less-energetically-favorable metallic phase and therefore often comprises of processes which consume high amounts of energy. Metals thus processed will always tend to return to their stable oxide phase, and its chemical re-combination to form ore-like compounds is a natural process. These thermodynamic principles ensure that metal will always react with its environment, making corrosion inevitable [3].

1.1.1. Consequences of corrosion

Corrosion largely affects our society, and has a substantial economic impact. The U.S. National Association of Corrosion Engineers estimated the total annual cost of corrosion in the United States to be $1 trillion in March 2013 or 3.1% of the nation's gross domestic product, thus demonstrating the broad and expensive challenge that impeding the corrosion of equipment and materials presents [4, 5].

The economic impact of corrosion also has a significant effect on technological developments and industry. The development of new technologies often has to consider the problem of corrosion, which can limit their economic or technical feasibility. For example, oil drilling, both offshore and on land, encounters corrosion such as sulfide stress corrosion and microbiological corrosion. These problems compound the difficulties faced in the highly corrosive marine environment [6]. Another example, which can cause serious problems to industry and consumers, is the closure of industrial plants (e.g., nuclear, process, power) because of corrosion problems [7-9].

Corrosion can also affect safety and health. The failure or breakdown of metal structures (e.g., bridges, cars, and aircraft) [10, 11] or even metal prosthetic devices in the

body through corrosion and broken connections can have serious impacts on safety and health and can cause severe injuries [12-14].

Another impact of corrosion is the loss of liquids through leaking containers, storage tanks, or transportation lines, which can cause severe accidents and hazards [15, 16]. Corrosion can also accelerate the deterioration of precious artistic or cultural artifacts, for example the deterioration of bronze statues in highly polluted environments [17].

1.1.2. The corrosion process

Corrosion is a natural process. When a piece of bare iron is exposed to moisture, its surface will be covered with rust in a few hours. The formation of rust will be accelerated by the presence of salt in the moisture. Corrosion can occur through reduction–oxidation (redox) reactions on the metal's surface. In the case of an iron substrate, at an anodic site the iron dissolves as ferrous ions with an associated release of electrons. This dissolution of the iron will continue if the released electrons can pass to a cathodic site on the metal's surface where they can react with some reducible component of the electrolyte to remove them from the metal. This redox process occurs through the following two separate-but-simultaneous half-reaction systems [1, 5, 18]:

the anodic reaction (corrosion)

$$Fe \rightarrow Fe^{2+} + 2e^{-} \qquad \text{(Eq. 1.1)}$$

and the cathodic reactions (simplified)

$$2H^{+} + 2e^{-} \rightarrow H_2 \qquad \text{(Eq. 1.2 a)}$$

or $$H_2O + \tfrac{1}{2} O_2 + 2e \rightarrow 2OH^{-}. \qquad \text{(Eq. 1.2 b)}$$

Reaction 1.2a is the more common cathodic reaction in acids and in the pH range 6.5–8.5. The more important cathodic reaction is the oxygen reduction reaction (1.2b). Combining the oxidation and reduction half-reactions gives a balanced chemical equation for the overall reaction of iron, oxygen, and water:

$$Fe + ½\ O_2 + H_2O \rightarrow Fe^{2+} + 2OH^- \quad \text{(Eq. 1.3)}$$

The Fe^{2+} and OH^- product ions may combine to form solid iron(II) hydroxide as a corrosion residue:

$$Fe^{2+} + 2OH^- \rightarrow Fe(OH)_2, \text{ iron (II) hydroxide.} \quad \text{(Eq. 1.4)}$$

This reaction is almost never observed, because the iron(II) hydroxide reacts further with oxygen and water to form hydrated iron(III) oxide (reaction 1.5) and flaky red–brown solid rust ($Fe_2O_3.nH_2O$) (reaction 1.6):

$$4Fe(OH)_2 + 2H_2O + O_2 \rightarrow 4Fe(OH)_3, \text{ hydrated iron (III) oxide} \quad \text{(Eq. 1.5)}$$

$$4Fe(OH)_2 + O_2(g) + xH_2O \rightarrow 2Fe_2O_3.(x+4)H_2O, \text{ rust} \quad \text{(Eq. 1.6)}$$

1.1.3. Types of corrosion

Corrosion occurs in various forms and can be classified based on its formation mechanism, which could involve either electrochemical or direct chemical reactions. Eight common types of corrosion are listed below [19].

1.1.3.1. Uniform Corrosion: This type of corrosion, also known as **general** attack corrosion, results from chemical or electrochemical reactions degrading the metal's entire exposed surface, or a large fraction of it. This type of corrosion is predictable, controllable, and often preventable [20, 21].

1.1.3.2. Localized Corrosion: This type of corrosion involves intense attacks at localized sites of the metal structure while the rest of the surface corrodes much more slowly. Localized corrosion can be classified into three types, as follows [20, 22, 23]:

- Pitting corrosion: Pits are small holes or cavities that develop in a metal due to limited, localized de-passivation; this area then becomes anodic. An unknown but potentially broad area simultaneously becomes cathodic, producing a localized galvanic reaction. The corrosion can penetrate the metal and lead to its failure. This form of corrosion, which can originate at microscopic defects on a metallic surface, is far more dangerous than uniform corrosion damage. It is often covered by an accumulation of corrosion products, which makes it difficult to detect, model, and prevent [20, 24-26].
- Crevice corrosion: This form of corrosion, also called contact corrosion, occurs at the regions of contact either between different metals or between metals and nonmetals. Crevice corrosion can be initiated either in acidic conditions or by an extremely low availability of oxygen in a crevice. It may occur at washers, clamps, sand grains, and under gaskets; it can also occur at applied protective films [20, 24, 26].
- Filiform corrosion: This affects painted or plated surfaces through the permeation of moisture through small defects in the coating. It results in the formation of long branching filaments of corrosion product, which develop from the original corrosion pit and degrade the protective coating [20, 27, 28].

1.1.3.3. Galvanic Corrosion: Galvanic corrosion can occur owing to an electric potential difference between two dissimilar metals in the presence of an electrolyte and an electron-conductive path. The potential difference causes electrons to flow between the two metals. The metal with the lower equilibrium potential thus acts as the anode of an electrochemical cell, and therefore corrodes and deteriorates more quickly than it would alone, while at the cathode no corrosion processes take place than it would otherwise. In this form of corrosion,

the intense corrosion of the anode is called galvanic corrosion and at the cathode no corrosion processes take place that known as cathodic protection [20, 29, 30].

1.1.3.4. Environmental cracking: Environmental cracking is the formation and growth of cracks in a corrosive environment, which causes the failure of metals. Chemical, heat, and tensile stress can result in the following types of environmental corrosion [20, 31]:

- Stress corrosion cracking
- Corrosion fatigue
- Hydrogen-induced cracking
- Liquid metal embrittlement

1.1.3.5. Flow-assisted corrosion: Flow-assisted corrosion, also called flow-accelerated corrosion, occurs when a normally protective film oxide present on a metal surface is dissolved or removed by wind or a fast-flowing liquid such as water. The underlying metal is exposed to further corrosion and deterioration, which then re-creates the oxide film [20, 32, 33].

1.1.3.6. Intergranular corrosion: This form of corrosion, also known as intergranular attack, is a chemical or electrochemical attack on the boundaries of metal crystallites, which are more susceptible to corrosion than their interiors. It often occurs owing to impurities in the metal, which can accumulate at higher concentrations near the grain boundaries [20, 34, 35].

1.1.3.7. De–alloying: De-alloying, or selective leaching, is a rare and unusual form of corrosion that occurs in certain metal alloys such as brass and gray cast iron. The alloy loses its active element and retains the relatively stable corrosion-resistant component in a porous state on the metal surface [20, 36].

1.1.3.8. Fretting corrosion: Fretting corrosion is a rapid corrosion damage that occurs as a result of repeated wearing, weight, and/or vibration at the asperities of contact surfaces. It is characterized by the formation of pits, grooves, and oxide debris on the surfaces. This type of

corrosion is often found in rotation and impact machinery, bolted assemblies, ball or roller bearings, and surfaces exposed to vibration during transportation [20, 37, 38].

1.1.4. Corrosion prevention

Corrosion cannot be avoided, but it can be retarded or delayed in certain cases by using proper techniques. Depending on the metal to be protected, there are several corrosion-prevention methods, which are generally classified into six groups:

- Conditioning the corrosive environment
- Conditioning the metal and surface
- Cathodic protection
- Corrosion inhibitors
- Plating
- Coating the metal

1.1.4.1. Environmental modification (conditioning the corrosive environment): Corrosion can occur through the chemical interaction of metals and alloys with impurities or gases that are naturally present in the unregulated surrounding environment. Therefore, deterioration could be impeded by purifying or altering the corrosive environment. The most important corrosive agents are water vapor, acid fumes, salts, hydrogen sulfide, and chloride. Water plays a major role in provoking the attack by other agents (except hydrogen sulfide); therefore, drying the atmosphere can be useful to prevent corrosion. Reducing or controlling other pollutants, when satisfactory drying is not possible, can also be important in reducing the corrosion rate. For example, treatments to adjust the hardness, alkalinity, and oxygen content of the feed water for boilers can be useful to reduce corrosion within the unit [39, 40].

1.1.4.2. Conditioning the metal and the surface: Monitoring and understanding the environmental conditions that cause corrosion and changing the type of metal being used can lead to significant reductions in corrosion. The alloying of metals to obtain materials that are resistant to corrosion in specific environments is constantly under investigation. Stainless steel, an iron-based alloy with chromium and possibly nickel additions, is an example of an alloy designed for corrosion prevention. Its protection is given by an invisibly thin, naturally formed film of chromium sesquioxide Cr_2O_3[41].

The monitoring of surface texture and morphology is also important for corrosion protection of metals. Cracks or crevices produced on a surface as a result of wear, tear, or manufacturing flaws can result in a greater rate of corrosion. Therefore, appropriate monitoring and elimination of unnecessary surface conditions, as well as ensuring that a system is designed to avoid reactive metal combinations with corrosive agents, can be effective in corrosion reduction [42].

1.1.4.3. Cathodic protection: The corrosion of a metal surface can be controlled by converting unwanted anodic sites on the surface to cathodic sites by the application of an opposing current, which supplies free electrons and forces the polarization of local anodes to local cathodes. This method can take two forms, as follows [43, 44]:

- A sacrificial system can be employed to introduce galvanic anodes. The protected metal is connected to a relatively easily corroded sacrificial metal that acts as the anode, which corrodes instead of the protected metal.
- Impressed current protection introduces an alternative source of direct electrical current to the electrolyte. The negative terminal of the current source is connected to the metal, and the positive terminal is connected to an auxiliary un-sacrificed anode to complete the electrical circuit.

Cathodic protection systems can be used to protect a wide range of metallic structures in various environments such as the steel in water or fuel pipelines, storage tanks, pier piles, and the hulls of ships and boats. It can also be employed in offshore oil platforms, onshore oil well casings, and metal reinforcement bars in concrete buildings and structures.

1.1.4.4. Corrosion inhibitors: Corrosion inhibitors are chemical additives that, when added to a corrosive aqueous or gaseous environment, decrease the corrosion rate of a metal or alloy. Inhibitors are generally distributed from a solution or dispersion, and are often adsorbed onto metallic surfaces. The result is the formation of a protective film or passivation layer that prevents the access of corrosive ions or gases to the metal surface and slows the corrosion rate [41]. Inhibitors retard corrosion via three mechanisms, as follows [45-47]:

- a change in the anodic or cathodic polarization behavior,
- a reduction in the diffusion or movement of ions to the metallic surface, and
- an increase in the electrical resistance of the metallic surface.

1.1.4.5. Plating: A metallic coating or plating is a surface covering of one metal deposited on the conductive surface of another. Plating can be decorative as well as protective. Plating can improve paint adhesion, IR reflectivity, or durability, or can be used to reduce friction or to harden the metal [41, 48]. There are various ways to plate metals. Four common types are described as follows [48]:

- Electroplating: A thin layer of ionic metal (e.g., copper, nickel, tin, or chromium) is deposited on a substrate (generally steel, carbon, platinum, titanium, or lead) in a chemical solution (i.e., an electrolytic bath) containing salts of the metal to be deposited [20, 41].

- Mechanical plating: Fine metallic particles of such as zinc, cadmium, tin, or copper can be imparted on a substrate by cold welding, which involves tumbling the substrate with the metal powder and glass beads in a treated aqueous solution [20].
- Electroless plating: The coating metal (e.g., cobalt, nickel, gold, silver, or copper) is deposited on the substrate metal via several simultaneous chemical reactions in an aqueous solution without the use of electrical power [41, 49].
- Plating by hot dipping: Iron, steel, or aluminum can be coated with a zinc layer by their immersion in a molten zinc bath at 460°C [50].

1.1.4.6. Coating the metal: A coating can be applied to a metal as a passive method of corrosion protection. The interposition of a corrosion-resistant physical barrier can separate a metal from aggressive media such as moisture, salts, and acids. Coatings can be of various materials, as follows.

- Solvent-based protective agents: The evaporation of the solvent from a solution containing a protective agent applied to a surface will leave a protective film on the substrate. The drying time is dependent on the nature of the solvent and the thickness of the protective film. These corrosion protection agents are often highly flammable, and may only be used in closed systems for reasons of occupational safety. Varnishes, enamels, and lacquers can be classified in this group [51, 52].
- Water-based protective agents: These anti-corrosion agents include emulsions and dispersions. The use of water gives an advantage in that other solvents are not generally needed, but it makes these agents highly temperature dependent; they are at risk of freezing or increasing in viscosity. The elevated water content also introduces a further drawback of increased relative humidity in the packaging area [53, 54].

- Corrosion-protective oils without solvent: These solutions produce poor-quality coatings that can be modified by the use of corrosion inhibitors. Lubricant oils used for corrosion protection in closed systems can be classified in this group [55, 56].
- The object to be packaged is immersed in hot wax at 100°C. No solid bonds form between the film and the metallic surface, meaning the film can be easily removed [57, 58].
- Hybrid silane sol-gel materials: These materials, also known as organic–inorganic hybrid materials, are differentiated from traditional polymer composites through the use of nano-sized organic and inorganic moieties in a single homogenous phase. Hybrid materials are organically modified metallic alkoxides that are synthesized via well-known sol-gel procedures. The chemical structure of the organic precursor and the ratio of organic to inorganic moieties can be manipulated to adjust these hybrid materials from being very soft and flexible to being hard and brittle. These materials combine the advantages of organic materials (e.g., flexibility, low dielectric constant, and ductility) and those of inorganic materials (e.g., heat resistance, retention of mechanical properties at high temperature, and low thermal expansion), which gives them unique mechanical, electrical, and optical properties and thus wide applicability.

  Of these various protection methods, thin sol-gel films from hybrid silicon alkoxide precursors have received growing interest in recent decades as efficient pre-treatments to promote adhesion between organic coatings and metal surfaces. In particular, the recent development of water-based silicon alkoxide sol-gel pre-treatments has promoted interest in these conversion layers as a “green” technology [41, 59]. In this context, this thesis considers hybrid silicon alkoxides molecules for the development of effective and environmentally friendly protection systems against corrosion.

1.2. Hybrid silane sol-gel coatings

The need to replace carcinogenic chromate-based anti-corrosion surface treatments has promoted the development of new environmentally friendly pre-treatments [60, 61]. Among the possible replacements, hybrid organic–inorganic sol-gel coatings have attracted considerable interest owing to their hydrophobicity, adhesion strength, and anti-corrosion properties [62] [63]. These coatings have been used to protect steel, zinc, aluminum, and magnesium substrates. Hybrid coatings can be prepared via a sol-gel procedure using organic polymers and metallic alkoxides of zirconium, titanium, cerium, tin, aluminum, and silane as the main precursors [64].

A silane sol-gel film can allow an organic coating to adhere strongly to a metal substrate. It also provides a thin barrier that effectively prevents oxygen from diffusing to the metal [65]. The good barrier properties of such films arise through the formation of a dense –Si–O–Si– network, which hinders the penetration of corrosive species to the substrate. Consequently, the effectiveness of silane coating pre-treatments strongly depends on the barrier properties of the film [66-68]. These barrier properties can be enhanced through the addition of small amounts of chemicals with specific properties, such as self-healing [69]. Self-healing can be defined as the partial recovery of the protective properties of a damaged coated system [67].

Recent investigations of sol-gel processes have aimed to develop silane sol-gel coatings doped with environmentally compatible inhibitors, such as cerium compounds [69-72]. These systems can combine the barrier properties of silane sol-gel coatings with the ability of the cerium ions to inhibit corrosion [72, 73]. Cerium ions inhibit corrosion by migrating through the coating to the location of attack (e.g., a defect in the coating), and then reacting to passivate the site. Therefore, they act as cathodic inhibitors at active sites through

the precipitation of insoluble cerium hydroxide at local regions of high pH [72, 74]. Cerium nitrate can improve the protection of galvanized steel substrates from corrosion when used either as a conversion film [75-77] or as a corrosion inhibitor through its addition to a silane formulation [73, 78-80].

The protective properties of silane coatings can also be improved by the addition of oxide nanoparticles, which can be synthesized in the films, as demonstrated for sol-gel coatings [67, 81], or they can be added to the pre-treatment solutions [81]. Mg alloys pre-treated with sol-gel coatings containing ZrO_2 and CeO_2 nanoparticles have been reported to show enhanced corrosion protection (due to the CeO_2) and improved wear resistance (due to the ZrO_2) [81]. Montemor et al. [67, 81] reported a new approach that involves the modification of bis- (triethoxysilylpropyl) tetra sulfide silane (BTESPT) with nanoparticles such as CeO_2, SiO_2, or CeO_2–ZrO_2. Improved corrosion resistance could also be achieved by initially activating the nanoparticles with cerium nitrate. Ceria nanoparticles were shown to be very effective fillers, improving both the barrier properties of the silane coatings and the overall corrosion resistance.

The protective behavior of the silane based sol-gel coatings depends on the various effective parameters such as concentration of cerium ions and nanoparticles, coating curing condition, effect of additives such as alcohols or diols and nanoparticles and pH of electrolyte solution (see above). Against the vast work on the study of the protective performance of cerium doped silane sol-gel coatings, very little has been focused on optimizing these parameters. Montemor *et al.* [82] studied the protection performance of cerium doped silane coating in 0.05 M NaCl solutions with different pH. Phanasgaonkar *et al.* [83] investigated the effect of curing temperature, silica nanoparticles- and cerium on surface morphology and corrosion behaviour of hybrid silane coatings on mild steel.

In comparison with other metal–organic-based precursors, the chemistry of silicon–organic-based sol-gel films and the mechanism of their interaction with a metallic substrate and an organic coating have been widely examined [84, 85]. Deposition of hybrid silane sol-gel coatings generally occurs in four stages, as follows [86-89]:

1. the hydrolysis of the silicon alkoxides molecules;

2. the condensation reaction and polymerization of monomers to form chains and particles;

3. the growth of the particles (or chains) and

4. the agglomeration of the polymer structures and the formation of a network.

Both the hydrolysis and condensation reactions generally occur simultaneously once the hydrolysis reaction has been initiated. In the presence of water, Si–OR groups (where R is an organic group) hydrolyze to Si–OH (silanol) groups following approximately the steps in Figure 1.1.

As shown in the figure, both the hydrolysis and condensation steps generate low-molecular-weight byproducts such as alcohol and water, which must be removed from the system. Their removal during drying causes further condensation and shrinkage of the tetrahedral SiO_2 network [87, 88].

Silane solutions can be applied to a metal substrate through various techniques (e.g., spraying, electro-deposition, and dip- and spin-coating), of which dip- and spin-coating are the two most-commonly used methods [86, 87].

Hydrolysis

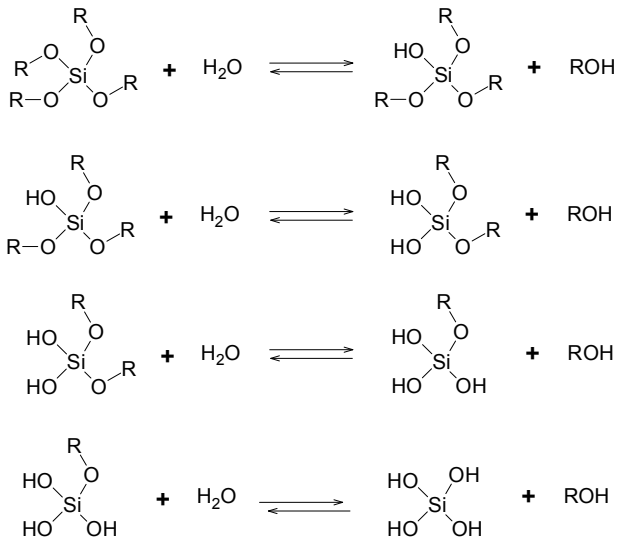

Alcohol Condensation (Alcoxolation)

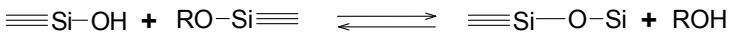

Water Condensation (Oxolation)

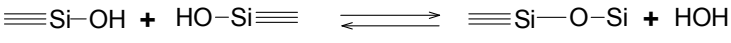

Overall reaction

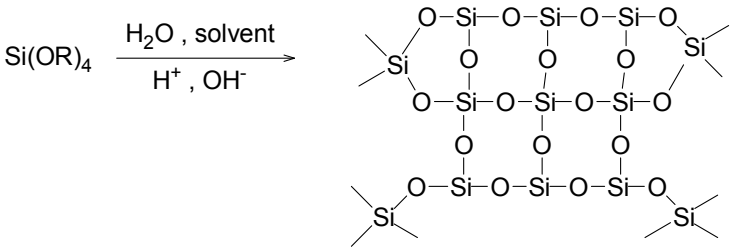

Figure 1.1. Hydrolysis and condensation reaction involved in making sol-gel derived silica materials (Reprinted with permission from J. Wen and G. Wilkes, Chem. Mater. 8 (1996) 1667 [90]. Copyright American Chemical Society).

As illustrated in Figure 1.2, when a hybrid coating is applied to a metallic surface, silanol groups can interact with hydroxyl groups in equilibrium with the oxide film on the

metal surface. This silanol–hydroxyl interaction can lead to the formation of strong covalent bonds that cause appropriate adhesion of silane hybrid coatings on metallic surface [90].

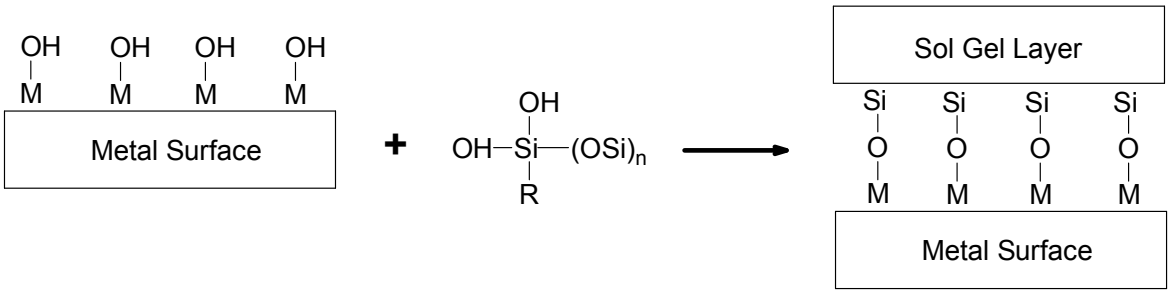

Figure 1.2. Evolution of a covalently bound sol-gel derived thin film on a metal surface (Reprinted with permission from T.L. Metrok et.al., Progress in Organic Coatings 41 (2001) 233 [90]. Copyright Elsevier).

As far as organofunctional silanes are concerned, the mechanism of film formation is very similar. Organofunctional silanes are hybrid molecules containing one or more non-hydrolysable substituents linked to the silicon atom [91]. The structure of this kind of molecules is shown in Figure 1.3:

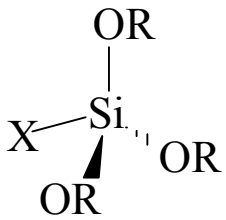

Figure 1.3. Structure of organofunctional silanes (Reprinted with permission from F. Beari et al., Journal of Organometallic Chemistry 625 (2001) 208 [91]. Copyright Elsevier).

Where RO is a hydrolysable group, such as methoxy, ethoxy, or acetoxy, and X is an organofunctional group, such as amino, methacryloxy, epoxy, etc. The organofunctional alkoxysilanes are classified according to their organic functions:

- Aminosilanes: the organic function is a primary or secondary amine
- Glycioxysilanes: the organic function is an epoxide and
- Mercaptosilanes: the organic function is a thiol.

These molecules, because they have two different reactive groups on their structure, can react and couple with very different materials. This allows them to be used in a wide range of applications, for example as adhesion promoters, crosslinking agents, and mechanical reinforcements of ceramic surfaces. Alkoxide groups in the presence of water can be hydrolyzed to generate a sol-gel network, which can be connected to an inorganic metal substrate by chemical bonds. Conversely, the organic functionality embedded in the silane film can be polymerized and chemically interact with an organic coating. In this simple model, a permanent bond between the inorganic substrate and the organic matrix is produced by means of stable chemical bonds [91].

1.3. Scope and objectives of this work

The aim of this work is the evaluation of the self-healing properties of cerium-doped silane hybrid coatings, which can be used as environmentally compatible protective coatings for steel surfaces that are subjected to corrosion in specific environments. In this work, the effects of various parameters upon the microstructure, morphology, and protective properties of the coatings, such as the coating curing condition, the cerium ion concentration, and the presence of additives including bisphenol A (BPA), cerium nitrate, CeO_2 nanoparticles, and

ZrO_2 nanoparticles were investigated. Four different types of steels were considered: austenitic 316L and 304L stainless steels (SS), hot-dip galvanized steel (HDG), and electro-galvanized steel (ELG). Based on literature data [93, 94], their corrosion resistance in a NaCl solution is ranked as: 316L SS > 304L SS > HDG > ELG. This use of this set of substrates allows us to obtain a better view of the corrosion inhibition performance of cerium doped silane hybrid coatings and in some cases results in a decrease of the experimental time. An example of this is the duration of the salt spray test of the silane hybrid coating modified with cerium nitrate and CeO_2 nanoparticles on 304L SS and HDG substrates that was reduced from 2000 h to 144 h respectively (Chapters 5 and 7).

The influence of cerium and BPA, as well as the drying conditions, on the microstructures of the coatings were examined using Fourier transform infrared (FTIR) spectroscopy. The morphological and microscopic features of the coated substrates were evaluated using atomic force microscopy (AFM) and scanning electron microscopy (SEM) before and after corrosion testing. Corrosion of the sol-gel coatings was assessed via neutral salt spray tests, electrochemical impedance spectroscopy (EIS), and potentiodynamic polarization tests.

The research work of the thesis is divided into seven parts. After an explanation of the methodology used in this work (Chapter 2), the first research part (Chapter 3) focuses on evaluating the structure and corrosion protection performance of silane hybrid coating (SHC) as a pre-treatment on austenitic 316L SS. The SHC were prepared from the hydrolysis and condensation of 3-glycidoxypropyl-trimethoxysilane (GPTMS) precursor and BPA cross-linking agent in acid-catalyzed conditions. The resulting colloidal sol was applied to cleaned substrates by dip coating. To study the effects of the drying method on the microscopic features and morphology of the hybrid coatings, a series of the silane-treated substrates was

dried at ambient temperature (25°C) for 2 weeks. Another series was dried at ambient temperature for 24 h and placed in a furnace to cure at temperatures ranging from ambient to 130°C for 90 min to allow extensive cross-linking in the silane films.

The second part (Chapter 4) consists of a detailed study of Ce–doped SHC on 304L SS specimens with $Ce(NO_3)_3\ 6H_2O$ as a corrosion inhibitor. Furthermore, the effects of BPA as a cross-linking agent on the microscopic features, morphology, and corrosion performance of the Ce-doped SHC were assessed. In comparison with 316L SS, 304L SS has a lower corrosion resistance in NaCl solution, which allows it to better demonstrate the corrosion inhibition performance of the Ce-doped SHC. The Ce-doped sol-gel coatings can also provide self-healing properties, which can automatically repair corroded areas, thereby providing long-term corrosion protection.

The most suitable way to evaluate the self-healing ability of a coating is via the application of an artificial defect on its surface and the monitoring of its behavior using, for example, electrochemical impedance spectroscopy [82]. Therefore, the third part (Chapter 5) consists of an investigation of the self-healing ability of cerium-modified sol-gel coatings on 304L SS substrates by monitoring their electrochemical behavior before and after the application of a defect. Cerium nitrate and cerium oxide nanoparticles were used as Ce sources, and the electrochemical behavior of the sol-gel coatings doped with cerium nitrate was compared with that of sol-gel coatings containing cerium oxide nanoparticles. The coated samples were immersed in the electrolyte for one week, before a defect was created on the surface.

Other works [69, 94] have shown that the protective behavior of pre-treatments based on Ce-doped silane solutions depends on the dopant concentration. Their results also suggest that there is an optimum concentration of dopant, because higher or lower concentrations

impair the coating barrier properties. Therefore, in the fourth part (Chapter 6), the effects of Ce concentration on the morphology and the protective performance of Ce-doped silane hybrid coatings applied to HDG were investigated. The low corrosion resistance of the HDG substrates in comparison with that shown by 316L or 304L SS, allow a better estimation of the effect of Ce concentration on the protective performance of the silane coatings.

A new approach is proposed in the fifth part (Chapter 7) to study Ce-doped silane coatings: CeO_2 nanoparticles were activated with Ce ions and then used as fillers in the silane films. The nanoparticles were added to improve the barrier properties of the silane film, and the presence of cerium ions aimed to introduce corrosion inhibition properties to the bulk of the silane film. The nanoparticles with Ce ions were activated to reduce the agglomeration of nanoparticles by stabilizing their surface charge, as demonstrated elsewhere [67].

Literature data suggest that the protective behavior of silane coatings modified with cerium-salt-activated CeO_2 nanoparticles depends on the concentration of the nanoparticles [81]. Therefore, part six (Chapter 8) focuses on the effects of the concentration of CeO_2 nanoparticles on the barrier properties and the self-healing performance of silane coatings filled with cerium-activated nanoparticles on electro-galvanized steel substrates. ELG steel has a smooth surface and is coated with a thinner layer of zinc in comparison with HDG steel. Thin layers of zinc coating provide lower protection, and thus allowed a better estimation of the barrier properties of the nanoparticles. The practical aspect of the work involved the synthesis of cerium-doped silane coatings with different $CeNO_3/CeO_2$ molar ratios.

Corrosion inhibitors directly introduced into the silane formulation have difficulty providing long-term protection to metals. To heal corrosion spots, a slow release of the inhibitor would be desirable [95, 96]. This shortcoming calls for the development of nano-reservoirs to isolate inhibitors and prevent their direct interaction with the sol-gel matrix.

Cerium-salt-activated nanoparticles fix cerium ions on their surface, distributing the inhibitor molecules homogeneously in the bulk of the film, and slowly releasing them when required [63, 97]. Literature data suggest that zirconium oxides possess attractive properties such as improved resistance to wear and corrosion, biocompatibility, and heat resistance, as well as good adhesion to metallic surfaces [62]. These particles could act as a reservoir for corrosion inhibitors, and thus might facilitate an important enhancement of their barrier properties. Compared with CeO_2 nanoparticles, ZrO_2 nanoparticles are inert and can no longer offer adequate protection if the coating is damaged owing to their lack of self-healing capabilities [62]. The combination of CeO_2 and ZrO_2 nanoparticles can play an active role in corrosion protection performance when they are added as fillers to hybrid silane coatings. In this context, the last part (Chapter 9) focuses on the protective behavior of silane coatings modified with cerium-salt-activated CeO_2–ZrO_2 nanoparticles on electro-galvanized steel substrate.

Finally, the major outcomes of the research are summarized in the concluding chapter.

References

1. H. Kaesche, Metalic Corrosion: Principles of Physical Chemistry and Current Problems, National Association of Corrosion Engineers, Houston, TX, USA, 1985.
2. L. Selwyn, Metals and Corrosion, a Handbook for the Conversation Professional, Canadian Conservation Institute, Ottawa, Canada, 2004.
3. D.E.J. Talbot, J.D.R. Talbot, Corrosion Science and Technology, CRC Press, Taylor and Francis Group, Abington, UK, 1997.
4. S. Sharma, P. Nagar, I. Singh Sodhi, Governometrics and Technological Innovation for Public Policy Design and Precision, IGI global, Hershey, PA, USA, 2014.

5. D. Landolt, Corrosion and Surface Chemistry of Metals, CRC Press, Taylor and Francis Group, Abington, UK, 1993.
6. S. Papavinasam, Corrosion Control in the Oil and Gas Industry, Elsevier, Amsterdam, 2013.
7. M. Le Calvar, I. De Curières, Corrosion issues in pressurized water reactor (PWR) systems, in: D. Féron (Ed.) Nuclear Corrosion Science and Engineering, Woodhead Publishing, Cambridge, 2012, pp. 473-547.
8. N. Mundhenk, P. Huttenloch, B. Sanjuan, T. Kohl, H. Steger, R. Zorn, Corrosion and scaling as interrelated phenomena in an operating geothermal power plant, Corrosion Science 70 (2013) 17-28.
9. P. Fauvet, Corrosion issues in nuclear fuel reprocessing plants, in: D. Féron (Ed.) Nuclear Corrosion Science and Engineering, Woodhead Publishing, Cambridge, 2012, pp. 679-728.
10. E.-S.M. Sherif, The role of corrosion inhibitors in protecting metallic structures against corrosion in harsh environments, in: M. Fanun (Ed.) The Role of Colloidal Systems in Environmental Protection, Elsevier, Amsterdam, 2014, pp. 509-526.
11. P. Traverso, E. Canepa, A review of studies on corrosion of metals and alloys in deep-sea environment, Ocean Engineering 87 (2014) 10-15.
12. S.J. Megremis, Corrosion resistance of precious metals for biomedical applications, in: N. Baltzer, T. Copponnex (Eds.) Precious Metals for Biomedical Applications, Woodhead Publishing, Cambridge, 2014, pp. 56-86.
13. Y. Takakubo, A. Berce, R. Trebše, Y. Tamaki, I. Milošev, A. Al-Samadi, V.M. Tiainen, Orton, Y.T. Konttinen, Wear and corrosion in the loosening of total joint replacements (TJRs), in: Y. Yan (Ed.) Bio-Tribocorrosion in Biomaterials and Medical Implants, Woodhead Publishing, Cambridge, 2013, pp. 74-110.

14. L. Reclaru, R.A. Brooks, M. Zuberbühler, P.Y. Eschler, F. Constantin, G. Tomoaia, Evaluation of taper joints with combined fatigue and crevice corrosion testing: Comparison to human explanted modular prostheses, Materials Science and Engineering C 34 (2014) 69-77.
15. P. Hopkins, Assessing the significance of corrosion in onshore oil and gas pipelines, in: M.E. Orazem (Ed.) Underground Pipeline Corrosion, Woodhead Publishing, Cambridge, 2014, pp. 62-84.
16. Y. Bai, Q. Bai, Corrosion and Corroded Pipelines, in: Y. Bai, Q. Bai (Eds.) Subsea Pipeline Integrity and Risk Management, Gulf Professional Publishing, Boston, 2014, pp. 3-25.
17. D. Watkinson, Conservation, corrosion science and evidence-based preservation strategies for metallic heritage artefacts, in: Corrosion and Conservation of Cultural Heritage Metallic Artefacts, P. Dillmann, D. Watkinson, E. Angelini, A. Adriaens (Eds.) Woodhead Publishing, Cambridge, 2013, pp. 9-36.
18. E. McCafferty, Introduction to Corrosion Science, Springer, New York, 2010.
19. V. Cicek, B. Al-Numan, Corrosion types based on mechanism, in: Corrosion Chemistry, John Wiley and Sons Inc., Hoboken, NJ, USA, 2011, pp. 7-14.
20. W.F. Gale, T.C. Totemeier (Eds.), Smithells Metals Reference Book, Eighth edition, Elsevier, Amsterdam, 2004.
21. Y. Tan, Homogeneous Electrode Models and Uniform Corrosion Measurements, in: Heterogeneous Electrode Processes and Localized Corrosion, John Wiley and Sons Inc., Hoboken, NJ, USA, 2012, pp. 1-35.
22. Y.M. Tan, W. Revie, Heterogeneous Electrode Processes and Localized Corrosion, John Wiley and Sons Inc., Hoboken, NJ, USA, 2013.

23. F. Hine, K. Komai, K. Yamakawa, Localized Corrosion, Elsevier Applied Science, London, UK, 1988.
24. Z. Szklarska-Smialowska, Pitting and Crevice Corrosion, NACE International, Houston, TX, USA, 2005.
25. Z.S. Smialowska, Pitting Corrosion of Metals, National Association of Corrosion Engineers, Ca, USA, 1986.
26. E. McCafferty, Introduction to Corrosion Science, Springer, New York, 2010, pp. 263-313.
27. R. Hanifan, The Engineering Language, Momentum Press, New York, USA, 2010.
28. J.M.C. Mol, B.R.W. Hinton, D.H. Van Der Weijde, J.H.W. De Wit, S. Van Der Zwaag, A filiform corrosion and potentiodynamic polarisation study of some aluminium alloys, Journal of Materials Science 35 (2000) 1629-1639.
29. H.P. Hack, Galvanic Corrosion, Issue 978, ASTM International, PA, USA, 1988.
30. R. Francis, Galvanic Corrosion: A Practical Guide for Engineers, Materials and Corrosion, NACE International, Houston, TX, 2002, pp. 138-144.
31. S.A. Shipilov, R. Jones, J.-M. Olive, R.B. Rebak (Eds.) Environment-Induced Cracking of Materials, Volume 1: Chemistry, Mechanics and Mechanisms, Elsevier, Amsterdam, 2007.
32. C. Mansour, E.M. Pavageau, A. Faucher, F. Inada, K. Yoneda, C. Miller, J.L. Bretelle, Flow Accelerated Corrosion of Carbon Steel in the Feedwater System of PWR Plants - Behaviour of Welds and Weld Assemblies, in: J. T. Busby, G. Llevbare, P.L. Andersen (Eds.) 15th International Conference on Environmental Degradation of Materials in Nuclear Power Systems-Water Reactors, John Wiley and Sons Inc., Hoboken, NJ, USA, 2012, pp. 907-919.

33. H. Mazhar, C. Y. Ching, J. S. Cotton, Flow Accelerated Corrosion in Pipe Bends, Lambert Academic Publishing GmbH and Co. KG, Saarbrücken, Germany, 2014.
34. R.F. Steigerwald, Intergranular Corrosion of Stainless Alloys, ASTM International, PA, USA, 1978.
35. A.H. Tuthill, The Nature, Detection, and Prevention of Intergranular Corrosion in 18 Cr-8 Ni stainless steel, Carnegie Institute of Technology, U.S. Naval Postgraduate School, Annapolis, Md, 1946.
36. P.K. Rohatgi, D. Nath, J.K. Kim, A.N. Agrawal, Corrosion and dealloying of cast lead-free copper alloy–graphite composites, Corrosion Science, 42 (2000) 1553-1571.
37. J. Schijve, Fatigue of Structures and Materials, Second edition, Springer, New York, 2009.
38. C.B. Elliott III, M. Moesser, D. W. Hoeppner, The Role of Fretting Corrosion and Fretting Fatigue in Aircraft Rivet Hole Cracking, Quality and Integrity Sign Engineering Center, Salt Lake City, Utah, NASA, 1994.
39. F. Mancia, The effect of environmental modification on the sulphide stress corrosion cracking resistance of 13Cr martensitic stainless steel in H_2S-CO_2-Cl^- systems, Corrosion Science 27 (1987) 1225-1237.
40. R. Lindsay, S.B. Lyon, Shreir's Corrosion: Introduction to Control of Corrosion by Environmental Modification, Elsevier, Amsterdam, 2010.
41. G. Song (Ed.), Corrosion Prevention of Magnesium Alloys, Woodhead Publishing, Cambridge, 2013.
42. L. Yang (Ed.), Techniques for Corrosion Monitoring, Woodhead Publishing, Cambridge, 2008.
43. W. von Baeckmann, G. Franke, D. Funk, C. Gey, H. Gräfen, G. Heim, V. Heinzelmann, K. Horras, B. Isecke, H. Kampermann, B. Leutner, H.-U. Paul, F. Paulekat, W. Prinz, B.

Richter, G. Rieger, H.G. Schöneich, W. Schwenk (Eds.), Handbook of Cathodic Corrosion Protection: Theory and Practice of Electrochemical Protection Processes (Third Edition), Gulf Professional Publishing, Elsevier, Amsterdam, 1997.

44. M. Parker, E. G. Peattie, Pipeline Corrosion and Cathodic Protection, Gulf Professional Publishing, Elsevier, Amsterdam, 1988.
45. V.S. Sastri, Green Corrosion Inhibitors: Theory and Practice, John Wiley and Sons Inc., Hoboken, NJ, USA, 2012.
46. J. Fink, Petroleum Engineer's Guide to Oil Field Fluids, Gulf Professional Publishing, Elsevier, Amsterdam, 2011.
47. Y.I. Kuznetsov, Organic Inhibitors of Corrosion of Metals, Springer, New York, 1996.
48. M. Schlesinger, M. Paunovic (Eds.), Modern Electroplating, John Wiley and Sons Inc., Hoboken, NJ, USA, 2010.
49. G. O. Mallory, J. B. Hajdu (Eds.), Electroless Plating: Fundamentals and Applications, American Electroplaters and Surface Finishers Society INC, Noyes Publication, New York, USA, 1990.
50. P. Maass, P. Peissker (Eds.), C. Ahner (Translator), Handbook of Hot-dip Galvanization, John Wiley and Sons Inc., Hoboken, NJ, USA, 2011.
51. R.E. Lobnig, V. Bonitz, K. Goll, M. Single, W. Villalba, J. Vogelsang, I. Winkels, R. Schmidt, P. Zanger, Development of a new experimental method to determine critical pigment-volume-concentrations using impedance spectroscopy: Solvent based coatings with components typical for commercial organic anticorrosion coatings or with nanoparticles, Progress in Organic Coatings 60 (2007) 1-10.
52. K.M. Skupov, J. Hobbs, J.P. Claverie, Solvent and aqueous-borne polyolefin coatings obtained by catalytic polymerization, Progress in Organic Coatings 65 (2009) 314-321.

53. R.E. Lobnig, V. Bonitz, K. Goll, W. Villalba, R. Schmidt, P. Zanger, J. Vogelsang, I. Winkels, Development of a new experimental method to determine critical pigment-volume-concentrations using impedance spectroscopy: Water-based coatings with components typical for commercial organic anticorrosion coatings, Progress in Organic Coatings 60 (2007) 77-89.
54. M.R. Bagherzadeh, T. Mousavinejad, Preparation and investigation of anticorrosion properties of the water-based epoxy-clay nanocoating modified by Na^{+}-MMT and Cloisite 30B, Progress in Organic Coatings 74 (2012) 589-595.
55. Q. Zhong, M. Rohwerder, Z. Zhang, Study of lubricants and their effect on the anti-corrosion performance as temporarily protective oil coatings, Surface and Coatings Technology 185 (2004) 234-239.
56. Q. Zhong, Corrosion measurements with wire beam electrodes under temporarily protective oil coatings, in: Techniques for Corrosion Monitoring, L. Yang (Ed.), Woodhead Publishing, Cambridge, 2008, pp. 638-657.
57. N. Borcea, Fast, flexible cavity wax application for automotive finishing: New robotic tooling is dramatically streamlining the application of automotive cavity wax, resulting in less waste, better quality, and faster cycle times, Metal Finishing 106 (2008) 28-31.
58. E. Chica, S. Agudelo, N. Sierra, Lost wax casting process of the runner of a propeller turbine for small hydroelectric power plants, Renewable Energy 60 (2013) 739-745.
59. H. Neuder, C. Sizemore, M. Kolody, R. Chiang, C.-T. Lin, Molecular design of in situ phosphatizing coatings (ISPCs) for aerospace primers, Progress in Organic Coatings 47 (2003) 225-232.
60. S. Dalbin, G. Maurin, R.P. Nogueira, J. Persello, N. Pommier, Silica-based coating for corrosion protection of electrogalvanized steel, Surface and Coatings Technology 194 (2005) 363-371.

61. Directive number 2003/53/EC of the European Parliament and Council, Amending for the 26th time Council Directive 76/769/EEC relating to restrictions on the marketing and use of certain dangerous substances and preparations (nonylphenol, nonylphenol ethoxylate and cement), L 178/124-L 178/127, 2003.
62. M.F. Montemor, W. Trabelsi, S.V. Lamaka, K.A. Yasakau, M.L. Zheludkevich, A.C. Bastos, M.G.S. Ferreira, The synergistic combination of bis-silane and $CeO_2 \cdot ZrO_2$ nanoparticles on the electrochemical behaviour of galvanised steel in NaCl solutions, Electrochimica Acta 53 (2008) 5913-5922.
63. M.L. Zheludkevich, R. Serra, M.F. Montemor, M.G.S. Ferreira, Oxide nanoparticle reservoirs for storage and prolonged release of the corrosion inhibitors, Electrochemistry Communications 7 (2005) 836-840.
64. S. Zheng, J. Li, Inorganic–organic sol gel hybrid coatings for corrosion protection of metals, Journal of Sol-Gel Science and Technology 54 (2010) 174-187.
65. P.H. Suegama, H.G. de Melo, A.A.C. Recco, A.P. Tschiptschin, I.V. Aoki, Corrosion behavior of carbon steel protected with single and bi-layer of silane films filled with silica nanoparticles, Surface and Coatings Technology 202 (2008) 2850-2858.
66. H. Wang, R. Akid, Encapsulated cerium nitrate inhibitors to provide high-performance anti-corrosion sol–gel coatings on mild steel, Corrosion Science 50 (2008) 1142-1148.
67. M.F. Montemor, M.G.S. Ferreira, Cerium salt activated nanoparticles as fillers for silane films: Evaluation of the corrosion inhibition performance on galvanised steel substrates, Electrochimica Acta 52 (2007) 6976-6987.
68. F. Deflorian, S. Rossi, M. Fedel, C. Motte, Electrochemical investigation of high-performance silane sol–gel films containing clay nanoparticles, Progress in Organic Coatings 69 (2010) 158-166.

69. W. Trabelsi, P. Cecilio, M.G.S. Ferreira, M.F. Montemor, Electrochemical assessment of the self-healing properties of Ce-doped silane solutions for the pre-treatment of galvanised steel substrates, Progress in Organic Coatings 54 (2005) 276-284.
70. A. Pepe, M. Aparicio, A. Durán, S. Ceré, Cerium hybrid silica coatings on stainless steel AISI 304 substrate, Journal of Sol-Gel Science and Technology 39 (2006) 131-138.
71. W. Trabelsi, E. Triki, L. Dhouibi, M.G.S. Ferreira, M.L. Zheludkevich, M.F. Montemor, The use of pre-treatments based on doped silane solutions for improved corrosion resistance of galvanised steel substrates, Surface and Coatings Technology 200 (2006) 4240-4250.
72. N.C. Rosero-Navarro, A. Durán, S. Ceré, M. Aparicio, Corrosion protection of aluminium alloy AA2024 with cerium doped methacrylate-silica coatings, Journal of Sol-Gel Science and Technology 52 (2009) 31-40.
73. T.W. Cabral AM, R. Serra, M. F Montemor, M. L Zheludkevich, M. G. S. Ferreira, The corrosion resistance of hot dip galvanised steel and AA2024-T3 pre-treated with bis-[triethoxysilylpropyl] tetrasulfide solutions doped with $Ce(NO_3)_3$, Corrosion Science 48 (2006) 3740-3758.
74. M. Schem, T. Schmidt, J. Gerwann, M. Wittmar, M. Veith, G.E. Thompson, I.S. Molchan, T. Hashimoto, P. Skeldon, A.R. Phani, S. Santucci, M.L. Zheludkevich, CeO_2-filled sol-gel coatings for corrosion protection of AA2024-T3 aluminium alloy, Corrosion Science 51 (2009) 2304-2315.
75. K. Aramaki, Self-healing mechanism of a protective film prepared on a $Ce(NO_3)(_3)$-pretreated zinc electrode by modification with $Zn(NO_3)_2$ and Na_3PO_4, Corrosion Science 45 (2003) 1085-1101.
76. K. Aramaki, The inhibition effects of cation inhibitors on corrosion of zinc in aerated 0.5 M NaCl, Corrosion Science 43 (2001) 1573-1588.

77. K. Aramaki, Preparation of self-healing protective films on a zinc electrode treated in a cerium(III) nitrate solution and modified with sodium phosphate and cerium(III) nitrate, Corrosion Science 46 (2004) 1565-1579.
78. M.F. Montemor, W. Trabelsi, M. Zheludevich, M.G.S. Ferreira, Modification of bis-silane solutions with rare-earth cations for improved corrosion protection of galvanized steel substrates, Progress in Organic Coatings 57 (2006) 67-77.
79. R.Z. Zand, K. Verbeken, A. Adriaens, Influence of the cerium concentration on the corrosion performance of Ce-doped silica hybrid coatings on hot dip galvanized steel substrates, International Journal of Electrochemical Science 8 (2013) 548-563.
80. R.Z. Zand, K. Verbeken, A. Adriaens, Evaluation of the corrosion inhibition performance of silane coatings filled with cerium salt-activated nanoparticles on hot-dip galvanized steel substrates, International Journal of Electrochemical Science 8 (2013) 4924-4940.
81. M.F. Montemor, M.G.S. Ferreira, Analytical characterization of silane films modified with cerium activated nanoparticles and its relation with the corrosion protection of galvanised steel substrates, Progress in Organic Coatings 63 (2008) 330-337.
82. M.F. Montemor, R. Pinto, M.G.S. Ferreira, Chemical composition and corrosion protection of silane films modified with CeO_2 nanoparticles, Electrochimica Acta 54 (2009) 5179-5189.
83. A. Phanasgaonkar, V.S. Raja, Influence of curing temperature, silica nanoparticles- and cerium on surface morphology and corrosion behaviour of hybrid silane coatings on mild steel, Surface and Coatings Technology 203 (2009) 2260-2271.
84. Z. Pu, W. J. van Ooij, J. E. Mark, Hydrolysis kinetics and stability of bis(triethoxysilyl)-ethane in water-ethanol solution by FTIR spectroscopy, Journal of Adhesion Science and Technology 11 (1997) 29-47.

85. M.F. Montemor, A.M. Simões, M.G.S. Ferreira, B. Williams, H. Edwards, The corrosion performance of organosilane based pre-treatments for coatings on galvanised steel, Progress in Organic Coatings 38 (2000) 17-26.
86. M. Fedel, Environmentally friendly Hybrid Coatings for Corrosion Protection: Silane Based Pre-Treatments and Nanostructured Waterborne Coatings, PhD thesis, University of Trento, Italy, 2010.
87. D. Wang, G.P. Bierwagen, Sol–gel coatings on metals for corrosion protection, Progress in Organic Coatings 64 (2009) 327-338.
88. J. Wen, G.L. Wilkes, Organic/Inorganic hybrid network materials by the sol-gel approach, Chemistry of Materials 8 (1996) 1667-1681.
89. G. Schottne, Hybrid sol-gel-derived polymers: applications of multifunctional materials 13 (2001) 3422-3435.
90. T.L. Metroke, R.L. Parkhill, E.T. Knobbe, Passivation of metal alloys using sol–gel-derived materials — a review, Progress in Organic Coatings 41 (2001) 233-238.
91. F. Beari, M. Brand, P. Jenkner, R. Lehnert, H.J. Metternich, J. Monkiewicz, H.W. Siesler, Organofunctional alkoxysilanes in dilute aqueous solution: new accounts on the dynamic structural mutability, Journal of Organometallic Chemistry 625 (2001) 208-216.
92. Corrosion Resistance of the Austenitic Chromium Nickel Stainless Steels in Chemical Environments, Report of international Nickel Company (INCO), New York, USA, 1963.
93. A.R. Marder, The metallurgy of zinc-coated steel, Progress in Materials Science 45 (2000) 191-271.
94. X. Zhong, Q. Li, J. Hu, X. Yang, F. Luo, Y. Dai, Effect of cerium concentration on microstructure, morphology and corrosion resistance of cerium–silica hybrid coatings on magnesium alloy AZ91D, Progress in Organic Coatings 69 (2010) 52-56.

95. A.N. Khramov, N.N. Voevodin, V.N. Balbyshev, M.S. Donley, Hybrid organo-ceramic corrosion protection coatings with encapsulated organic corrosion inhibitors, Thin Solid Films 447–448 (2004) 549-557.
96. J.L. S. Zheng, Inorganic-organic sol gel hybrid coatings for corrosion protection of metals, Journal of Sol-Gel Science and Technology 54 (2010) 174-187.
97. M.L. Zheludkevich, R. Serra, M.F. Montemor, K.A. Yasakau, I.M. Miranda Salvado, M.G.S. Ferreira, Nanostructured sol-gel coatings doped with cerium nitrate as pre-treatments for AA2024-T3: Corrosion protection performance, Electrochimica Acta 51 (2008) 208-217.

2

METHODS

2.1. Introduction

This chapter consists of a brief discussion of the techniques used in this work, which comprise: Fourier transform infrared spectroscopy (FTIR) to study the effect of some parameters on the microstructures of the coatings; microscopic techniques including atomic force microscopy (AFM), optical microscopy and scanning electron microscopy with energy-dispersive X-ray spectroscopy (SEM-EDS) to study the morphological and microscopic features of the bare and coated substrates; thickness measurement methods including electromagnetic method to measure the thickness of zinc coating on galvanized steel samples and eddy-current method and SEM to measure the thickness of hybrid coatings and corrosion evaluation tests including neutral salt spray testing and electrochemical corrosion

measurement methods, i.e., potentiodynamic polarization and electrochemical impedance spectroscopy (EIS).

2.2. Fourier transform infrared spectroscopy (FTIR)

2.2.1. Introduction

FTIR spectroscopy is one of the most useful techniques for identifying organic and inorganic materials. The various sampling methods mean that it can be applied to the analysis of a wide range of sample types such as solids, liquids, and gases in a wide spectral range. The analysis of collected FTIR data involves the conversion of an observed interference pattern by using a Fourier transform into an actual spectrum [1-3]. FTIR is a non-destructive technique and provides a precise measurement method without need to any external calibration. This technique improves the quality of infrared spectra and minimizes the time required to obtain data.

This method is based on the identification of functional groups and chemical bonds through observation of their characteristic infrared radiation absorption frequencies. The collective effect produces the FTIR spectrum, which can be used to identify the chemical bonds in the molecules. Each pure material has a unique FTIR spectrum, effectively a molecular fingerprint. Like a fingerprint no two unique molecular structures produce the same infrared spectrum. This makes infrared spectroscopy useful for several types of analysis.

In comparison with the simple spectra of inorganic materials, organic materials have complex spectra with numerous minima and maxima, which can be used to identify the constituent groups of unknown compounds through comparison with a library of known compounds. To identify less-common materials, FTIR can be combined with other

techniques, such as nuclear magnetic resonance, mass spectrometry, emission spectroscopy, and X-ray diffractometry [4, 5].

2.2.2. Fundamental vibrations of molecules

In the absorption spectroscopy techniques, when infrared (IR) light incident on the sample, selectively absorbed by material molecules and converted into their oscillatory energy. The frequencies and intensities of absorbed infrared radiation depend on the various characters, such as chemical structure of the molecule, type of bonds, relative atomic weights, and spatial position of atoms in a molecule, intra- and intermolecular interaction forces. The condition of the material, such as the temperature, the state (solid, liquid, or gas), concentration, pressure, and other materials in a mixture also affect the spectrum [6].

For a molecule to show infrared absorptions it must possess a specific feature, i.e. an electric dipole moment of the molecule must change during the vibration. In other words, the electronic charge distribution from one side of the bond to the other must occur. For example, consider hydrogen chloride, HCl. When HCl vibrates along the bond, the chlorine takes on a slightly more negative charge, and the hydrogen takes on a slightly more positive charge. Consequently, a change in dipole moment of the HCl molecule occurs.

During absorption, various vibration modes can be generated, such as: Stretching vibration which is the increasing or decreasing of the distance between two atoms, Bending vibration is the changes of the position of the atom relative to the original bond axis, Scissoring vibration is the bending of a bent molecule (e.g. H_2O) inward and outward and Rocking vibration is a twist of a bond with several other adjacent atoms. As molecules get more complex, the number of possible modes increases as 3n-6, where n is the number of bonds [4-6].

The intensity of a beam after passing through sample (I), is measured by either absorbance or percent transmittance on the y-axis and by either the wavelength (μm) or wavenumber (cm^{-1}) to measure the position of an infrared absorption on the x-axis.

If the intensity of the primary incident beam on a sample is equal to I_0, the relation between intensity, transmittance and absorbance is as follows [7]:

$$T = I/I0 \qquad \text{(Eq. 2.1)}$$

$$A = \log (I0/I) = -\log T = ecL \qquad \text{(Eq. 2.2)}$$

Where, e is the molar extinction coefficient or molar absorptivity, c is the concentration or the number of molecules of the material being sampled and L is the sample path length. The sample path length term means that a longer or thicker sample will absorb more strongly.

In this work, FTIR was used to examine the influences of cerium and bisphenol A (BPA) as well as the effect of the drying conditions on the microstructures of coatings. The measurements were taken using a Bio-Rad 575C spectrophotometer in the mid-IR range from 4000 to 400 cm^{-1}. All spectra were taken at an incident angle of 45° normal to the surface of the specimen, with a spectral resolution of 4 cm^{-1}. For each measurement, 64 scans were collected.

2.3. Atomic force microscopy (AFM)

Atomic force microscopy (AFM) is part of a microscopy group that called scanning probe microscopy (SPM). SPM has its roots in scanning tunneling microscopy, which measures the topography of surface electronic states as well as charge density, magnetic field, and other surface properties by using tunneling current. SPM research measurements depend

on the interaction between the probe tip and the surface of the conductive or semi conductive sample and includes the viewing of charge density waves [8, 9]. The main limitation of SPM is the requirement of sample conductivity. The atomic force microscope (AFM) was developed to overcome this limitation. This technique can be used for imaging almost any type of surface, including polymers, ceramics, composites, glass, and biological samples. Also, AFM can be applied to a sample in its natural state, in an environment of air, liquid, or vacuum, to generate very-high-resolution topographic images without the need to alter the sample destructively by preparation methods such as drying, coating with metal, or freezing. Additionally, with this technique, directly visualizing the nanometer-sized objects and measuring the dimensions of the surface feature is possible [9-11].

AFMs operate by measuring the interactive force between a tip and the sample surface using special probes that made by a micro-fabricated tip connected to an elastic cantilever. To form a highly magnified 3D image of a surface, the tip is brought close to the sample and raster-scanned over the surface. The force applied to the tip by the surface, results in bending of the cantilever which by measuring the cantilever deflection, it is possible to evaluate the tip–surface interactive force. The forces acting on the tip vary and depending on the sample´s nature, imaging mode and conditions used in the measurements [12].

The main interactions at short probe-sample distances are Van der Waals interactions that are present in all force microscope experiments and arise from the instantaneous polarization of atoms which interact with surrounding atoms [12].

Long-range interactions such as capillary, electrostatic and magnetic are significant further away from the surface which are important in other SPM analyzing methods [12].

During contact with the sample, at short distances (≈ 0.1 nm), the probe mainly senses repulsive Van der Waals forces (contact mode) that lead to the cantilever deflection. As the tip moves further away from the surface (up to 10nm), attractive Van der Waals forces are dominant (non-contact mode).

The total van der Waals potential energy of two atoms, located at a distance *r* from each other can be qualitatively estimated by Lennard-Jones potential equation [13]:

$$V_{LJ} = 4\epsilon\left[\left(\frac{\sigma}{r}\right)^{12} - \left(\frac{\sigma}{r}\right)^{6}\right] = \varepsilon\left[\left(\frac{r_m}{r}\right)^{12} - 2\left(\frac{r_m}{r}\right)^{6}\right] \quad \text{(Eq. 2.3)}$$

The first term of the sum describes short range repulsion and the second term takes into account the long-distance attraction caused, basically, by a dipole-dipole interaction. In this equation V_{LJ} is the intermolecular potential between the two atoms, ε is the potential well depth and a measure of how strongly the two particles attract each other, σ is the finite distance at which the inter-particle potential is zero, *r* is the distance between the particles that measured from the center of one particle to the center of the other particle, and r_m is the distance at which the potential reaches its minimum. At r_m, the potential function has the value -ε. The distances are related as $r_m = 2^{1/6}\,\sigma$ (1.122σ).

AFM images can be gathered in contact, non-contact or tapping mode. In contact mode, the deviation of the cantilever induced by the force between the tip and the sample is monitored by a laser and photodiode to generate an image of the surface. Depending on the sharpness of the tip, the spatial resolution of the technique is 1–20 nm. To prevent damage to the cantilever tip damaging the sample surface, the force between the two should be constant. For this reason, the cantilever tip is maintained at a constant angular deflection that is achieved using a feedback mechanism that adjusts the distance between it and the surface.

The forces applied between the tip and the sample typically ranges from 10^{-11} to 10^{-7} N [8, 9].

In non-contact mode, a small piezo element is mounted under the cantilever to make it oscillate at its resonance frequency. When the distance between the surface and this oscillating cantilever is within 10–100 nm, the oscillation is modified by the interaction forces between the tip and the sample. The changes in the oscillation causes a decrease in resonant frequency and amplitude as well as a phase shift, which are detectable changes that can be used to generate an image of the surface [8, 9].

In tapping mode, similar to non-contact mode, the cantilever is driven to oscillate up and down at near its resonance frequency by a small piezoelectric element mounted in the AFM tip holder. However, the amplitude of this oscillation is greater than 10 nm, typically 100 to 200 nm. The interaction of forces acting on the cantilever when the tip comes close to the surface, cause the amplitude of this oscillation to decrease as the tip gets closer to the sample. An electronic servo uses the piezoelectric actuator to control the height of the cantilever above the sample. The servo adjusts the height to maintain a set cantilever oscillation amplitude as the cantilever is scanned over the sample. A tapping AFM image is therefore produced by imaging the force of the intermittent contacts of the tip with the sample surface [8, 9].

In this work, the microscopic features of the coated substrates were evaluated using AFM. Images were obtained under ambient conditions using a multimode scanning probe microscope (Digital Instruments, USA) equipped with a Nanoscope IIIa controller. 10× 10 μm, 5× 5 μm and 1× 1 μm scans were recorded in tapping mode using a silicon cantilever (OTESPA, Veeco, USA). Nanoscope software (version 4.43r8) was used to analyze the surface roughness, and the recorded images were modified using an automated x-y plane fit.

Also, the microscopic features of the bare substrates were evaluated using a Park systems XE-70 AFM microscope. Images were recorded under ambient conditions in non-contact mode using a PPP-NCHR 10M non-contact cantilever.

2.4. Optical microscopy

Advances in digital imaging and analysis have enabled scientists to carry out faster and more efficient quantitative measurements on specimens ranging from photosensitive caged compounds and synthetic ceramic superconductors to real-time fluorescence microscopy of living cells in their natural environment. The optical microscope which often referred to as the light microscope, with help of digital video, can be used to image very thin optical sections, and confocal optical systems. This type of microscope uses visible light and a system of lenses to produces magnified images of small specimens and there is in two basic configurations: simple microscope and compound microscope [14]:

In simple microscope, a lens or set of lenses uses to enlarge a sample via angular magnification which giving the viewer an erect magnified virtual image. Simple microscope does not have the ability to produce high magnified images.

In compound microscope, a lens that called objective lens, collects light diffracted by the sample and forms a real image. The image is then magnified by eyepieces or oculars which gives the viewer an inverted magnified virtual image of the sample. In more advanced illumination setups of compound microscopes, a condenser lens focuses the light from the illuminator onto a small area of the specimen. Although illumination of the specimen is important, the objective lens is the most critical component of the microscope. Its properties determine depth of focus, resolution, and contrast of the specimen. The eyepiece simply magnify the resolved detail in the real intermediate image formed by the objective, which

permits a detector (eye or camera) to record what has been resolved. Combination of objective and eyepieces lenses allows to produces images with high magnification and reduces chromatic aberration [14, 15].

The first and most critical step in setting up a microscope for optimal resolution involves the mechanics of Köhler illumination which was first described in 1893 by August Köhler. In this method of sample illumination, a collector lens on the lamp housing is adjusted so that it focuses an image of the lamp filament at the front focal plane of the condenser while completely filling the aperture. It provides efficient, bright, and even illumination in the specimen field, minimizes internal stray light, and allows for control of contrast and depth. Under Koehler illumination condition, only the specimen area viewed by a given objective/eyepiece combination is illuminated and no stray light or noise is generated inside the microscope [14].

In this work, the surface characterization of the bare and coated 316L stainless steel samples after immersion in neutral 3.5% NaCl solution, were assessed using an optical microscope Nikon SMZ 800 with operating software NIS Elements D 3.0.

2.5. Scanning electron microscopy with energy dispersive X-ray spectroscopy (SEM-EDS)

Scanning electron microscopy (SEM), a powerful technique for the characterization of materials, is widely used in metallurgy, geology, biology, and medicine. It generates high-magnification images, which allows the analysis of small features, such as individual crystals [16-18].

In a scanning electron microscope a beam of electrons generated by a tungsten filament or field emission gun is accelerated by a high voltage (e.g., 15 kV) before it is passed

through a system of apertures and electromagnetic lenses to produce a narrow electron beam. The electron beam is scanned across the sample's surface by a scan coil. The interaction of the electron beam with the sample causes radiation to be emitted from the sample, which is collected by a detector. Analysis of the detected radiation allows an image of the sample to be constructed or its elemental composition to be determined [16, 17].

There are different types of electron image. The two most common are compiled from the detection of secondary electrons and backscattered electrons. Secondary electrons are those emitted from the atoms occupying the top surface of the sample; their detection can be used to produce a high-resolution image. Backscattered electrons are primary electrons from the incident beam that are reflected from atoms in the solid; the resulting images are of lower resolution than secondary electron images, because the electrons are emitted from within the sample, not its surface [16-18].

The interaction of the primary electron beam with atoms in the sample also causes shell transitions, which lead to the emission of X-rays. The energy of each X-ray is characteristic for its parent element. The analysis of these X-rays constitutes an elemental analysis technique known as energy dispersive X-ray spectroscopy (EDS). EDS can provide qualitative or, with the use of adequate standards, quantitative analysis of elemental composition. It can also be used to form maps or line profiles showing the elemental distribution on a surface [16, 19].

In this study, SEM measurements were performed using an XL30 SEM microscope (Philips, Netherlands) equipped with an EDS spectroscope. The silane coatings were observed before and after EIS measurements. Secondary electron images were collected at 15 and 20 kV.

2.6. Coating thickness measurements

The most commonly used measuring techniques for coating thickness include nondestructive methods such as magnetic induction and eddy current methods and also destructive methods such as cross-sectioning measurement.

The magnetic induction method measures non-magnetic coatings thickness over ferrous substrates and magnetic coatings over non-magnetic substrates. Magnetic gages measure either the magnetic attraction between a magnet and a magnetic material such as steel, or measure the magnetic flux change through a coating to a magnetic steel substrate. In this method, the probe of a magnetic gauge is placed on the point of the surface to be measured. When the probe is positioned, the linear distance between the probe tip that contacts the surface and the base substrate is measured. Magnetic induction instrument uses an alternating magnetic field that generates by a coil inside the measurement probe. A second coil of wire is used to detect changes in magnetic flux. The output of the secondary coil is transferred to a microprocessor where it is viewed as a coating thickness measurement on a digital display [20].

The common types of the magnetic gages are electromagnetic and Pull-Off gages that the last one is the mechanical gage. Mechanical gages measure the strength required to pull a magnet away from magnetic material such as steel. The typical accuracy of this method is $\pm$ 5% in dial-type and $\pm$ 10% in pen-style gages. Electronic gages measure the change in flux density using electronic circuitry and the accuracy of these gages is $\pm$1%. The magnetic induction method is simple, fast and inexpensive. It's also accurate and repeatable, and measurements are instantaneous with a digital display.

Eddy current method measures the thickness of non-conductive coatings over conductive substrates. This method uses a probe that contains a coil which conducting a high frequency alternating current (above 1 MHz) to set-up an alternating magnetic field. When the

probe is brought near a conductive surface, the alternating magnetic field will set up eddy currents on the surface, which results in the impedance change of the probe coil. The substrate characteristics and the distance between the probe-coil and the conductive substrate material affect the magnitude of impedance change. Therefore, coating thickness is determined by the impedance change in the form of a digital reading. Typical tolerance of this method is $\pm$1% [20, 21].

Cross-sectioning measurement is a method to measure the local thickness of coatings by examination of cross-section with a scanning electron microscope. A special cutting tool is used to make a small, V-groove through the coating and into the substrate. This method is destructive and has an uncertainty of less than 10%. This method is used when inexpensive, nondestructive methods are not possible, or as a way of confirming nondestructive results [22].

In this work, the thickness of zinc coating on galvanized steel samples measured by using of an electromagnetic gage (Elcometer 355 probe module, Braine Instruments). The specimens coating thickness is the average of 20 readings at widely dispersed points.

The thickness of hybrid coatings was measured by eddy – current method on 20 points of sample by using of Check line 3000 pro instrument (Germany). Additionally, in some cases, for simultaneously study of microstructure and the thickness of the coated samples, the thickness was measured by cross-sectioning method on 10 points of the cross-section of samples.

2.7. Salt spray test

The salt spray test is an accelerated laboratory corrosion testing method used to evaluate the relative corrosion resistance of bare and coated metallic specimens. Samples are exposed to a salt spray or salt fog atmosphere at an elevated temperature. This method is the

oldest corrosion test that remains in wide usage for the evaluation of the corrosion resistance of finished surfaces or parts. For example, it is used in industrial, marine, automotive, aircraft, and military testing. The test offers numerous advantages; it is inexpensive to conduct and can be used to test bare metal and painted or coated samples. Compared with testing in the natural environment, the assessment duration is short [23, 24].

The most common and widely used standard method is the ASTM B-117 salt spray test standard that specifies the use of a salt solution dispersed into uniform droplets to act on specimens supported or suspended between 15°–30° from the vertical. A typical salt solution would comprise 5% sodium chloride. The temperature within the chamber is maintained at 35 °C. The samples to be tested are inserted into the chamber, and then the salt solution is sprayed over them. The application of a continuous spray ensures that the samples are constantly wet, and thus constantly subject to corrosion [25].

The appearance of corrosion products is evaluated after a test duration that depends on the corrosion resistance of the sample. A more resistant sample would require longer testing than a less resistant sample, which would show signs of corrosion sooner.

The corrosion resistance of the bare and coated substrates was evaluated here in a neutral salt spray test that followed the ASTM B117 [25] procedure using a 5% NaCl solution. Prior to exposure, the back and edges of the plates were covered with adhesive tape. An artificial scratch that reached the substrate was made in the coating to examine possible delamination. Visual assessment of the macroscopic surfaces was carried out at various intervals throughout the total exposure time.

2.8. Potentiodynamic polarization measurements

2.8.1. Electrochemical principles

Corrosion can occur through electrochemical reactions at the interface of a metal surface and an electrolyte. These reactions can be investigated by various electrochemical methods, such as EIS, cyclic voltammetry, and potentiodynamic polarization measurements [23, 26, 27].

Potentiodynamic polarization measurements record the potential versus current to yield information on the corrosion rate, passivity range, pitting tendency, and corrosion protection afforded by coating layers. Testing involves sweeping the potential of a metallic sample in the positive direction at a very low scan rate, thus the metallic sample acts as an anode, which causes it to corrode or to form a passive oxide film [23, 28, 29].

A metallic specimen in contact with a corrosive medium oxidizes, which releases electrons into the metal. A complementary reduction reaction of solution species, such as O_2 or H^+, can remove electrons from the metal which causes developing a potential and occurring the corrosion. This potential is called corrosion potential (E_{corr}) or mixed potential. [23, 28].

Experimental potentiodynamic polarization measurements are characterized by plotting the logarithm of absolute current response with respect to the applied potential. This plot is known as a potentiodynamic polarization plot, in which potentials negative of E_{corr} give rise to cathodic currents, whereas potentials positive of E_{corr} give rise to anodic currents [23, 28].

2.8.2. Polarization resistance

During polarization resistance measurements, a potential range very near to the corrosion potential (± 25 mV about E_{corr}) is swept, and the resulting current is plotted versus the potential. The corrosion current (i_{corr}) is related to the slope of the plot through equation 2.1 [23, 29-31]:

$$\Delta E/\Delta i = \frac{\beta_A \beta_C}{2.3(i_{corr})(\beta_A + \beta_C)} \qquad \text{(Eq. 2.4)}$$

where $\Delta E/\Delta i$ is the slope of the polarization resistance plot with ΔE expressed in volts and Δi is expressed in μA. The slope has units of resistance, hence, polarization resistance. β_A and β_C are respectively the anodic and cathodic Tafel constants, which have units of volts/decade of current. i_{corr} is the corrosion current in microamperes.

The corrosion current can be related directly to the corrosion rate through equation 2.2.

$$\text{Corrosion rate}\left(\text{mpy}\right) = \frac{0.13\ i_{corr}(\text{E.W.})}{\text{d}} \qquad \text{(Eq. 2.5)}$$

Where mpy is the penetration rates ($mm.y^{-1}$ or milli-inch per year), E.W. is the equivalent weight of the corroding species expressed in grams, d is the density of the corroding species (g/cm^3), and i_{corr} is the corrosion current density ($\mu A/cm^2$).

2.8.3. Tafel plots

A Tafel plot of a metallic sample is compiled through anodic and cathodic polarization of the sample by 300 mV from the corrosion potential [23, 29, 32]. The resulting current is plotted on a logarithmic scale as shown in Figure 2.1.

The corrosion current (i_{corr}) is obtained from a Tafel plot by extrapolating the linear portions of the curves to E_{corr}. The anodic and cathodic Tafel plots are described by the Tafel equation [29, 33]:

$$\eta=\beta \log\frac{i}{i_{corr}} \qquad \text{(Eq. 2.6)}$$

where η is the overvoltage (the difference between the potential of the specimen and the corrosion potential), β is the Tafel constant in either mV/decade or V/decade (a decade of current is one order of magnitude), and i_{corr} is the current in μA at overvoltage η. The two Tafel constants, β_A and β_C, are derived from the respective anodic and cathodic portions of the Tafel plot.

In this work, potentiodynamic polarization tests assessed the corrosion of the silane-treated steel substrates in a 3.5 % NaCl solution. An Autolab PG-STAT 20 potentiostat (Metrohm, Switzerland) was used to assess a three-electrode system consisting of an Ag/AgCl KCl_{sat} reference electrode, a platinum mesh counter electrode, and the sample as the working electrode. Potentiodynamic measurements were performed over the range -1500 to 1000 mV versus Ag/AgCl KCl_{sat} at a rate of 1 mV/s. These measurements were performed three times. Tafel extrapolation conducted according to the ASTM Standard G3-89, 2004 [24] was used to determine i_{corr} and E_{corr}.

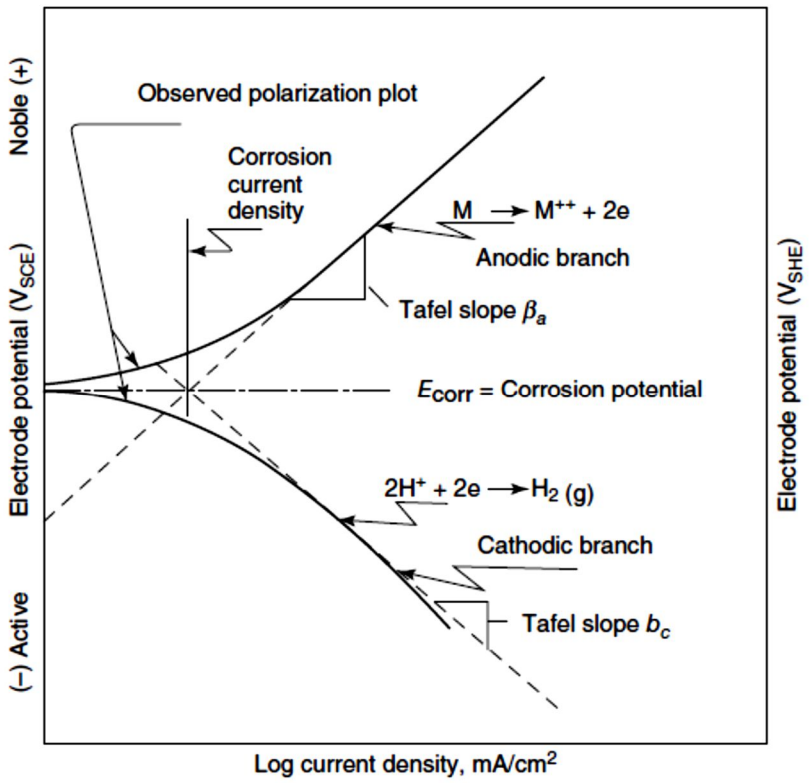

Figure 2.1. Classic Tafel Analysis. (Reprinted with permission from S. Papavinasam, Electrochemical polarization techniques for corrosion monitoring, in: L. Yang (Ed.), Techniques for Corrosion Monitoring, (2008) [34]. Copyright Woodhead Publishing Limited).

2.9. Electrochemical impedance spectroscopy (EIS)

2.9.1. Introduction

EIS, or the ac impedance method, is a powerful technique for the characterization of electrochemical systems and complex interfaces. The method evaluates the response of a system to the application of a small periodic amplitude ac signal over a sufficiently broad range of frequencies. Analysis of the response can provide information about the influence of effective physical and chemical phenomena at the interface, the structure of the sample, and its possible reactions. This method is widely used in the characterization of materials used in coatings, fuel cells, batteries, and semiconductors. It can also be used to assess corrosion phenomena [35-39].

2.9.2. Principles of electrochemical impedance spectroscopy measurements

As mentioned above, electrochemical impedance is usually measured by applying a small-amplitude sinusoidal excitation potential to an electrochemical cell, and then measuring the current or voltage response through the cell. The cell's response is thus pseudo-linear. In a linear (or pseudo-linear) system, the current response to a sinusoidal potential will be sinusoidal at the same frequency but shifted in phase [39], as shown in Figure 2.2.

The excitation signal, expressed as a function of time, has the form [35-40]:

$$E_t = E_0 \sin(\omega t) \qquad \text{(Eq. 2.7)}$$

where E_t is the potential at time t, E_0 is the amplitude of the signal, and ω is the particular frequency. The relationship between ω in radian/s and frequency (f) in hertz is

$$\omega = 2\pi f \qquad \text{(Eq. 2.8)}$$

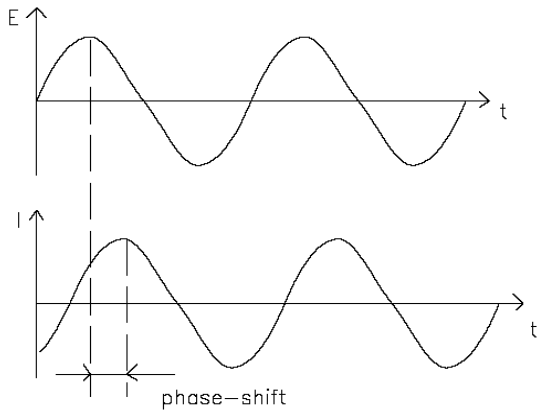

Figure 2.2. Sinusoidal current response in a linear system. (Reprinted with permission from V.F. Lvovich, Fundamentals of Electrochemical Impedance Spectroscopy, in: V.F. Lvovich, Impedance Spectroscopy: Applications to Electrochemical and Dielectric Phenomena, (2012) [41]. Copyright John Wiley and Sons, Inc).

In a linear system, the response signal (i_t) is shifted in phase (φ), and has a different amplitude from i_0

$$i_t = i_0 \sin(\omega t+\varphi) \quad \text{(Eq. 2.9)}$$

The Taylor series expansion for the current is given by

$$\Delta i=\left(\frac{\mathrm{d}i}{\mathrm{d}E}\right)_{E_0,i_0}\Delta E+\frac{1}{2}\left(\frac{\mathrm{d}^2 i}{\mathrm{d}E^2}\right)_{E_0,i_0}\Delta E^2+..... \quad \text{(Eq. 2.10)}$$

If the magnitude of the perturbing signal ΔE is small, then the response can be considered linear in the first approximation. The higher order terms in the Taylor series can be assumed to be negligible. The impedance of the system can then be calculated using Ohm's law as

$$Z(\omega)=\frac{E(\omega)}{i(\omega)} \quad \text{(Eq. 2.11)}$$

This ratio, the impedance ($Z(\omega)$) of the system, is a complex quantity with a magnitude and a phase shift, which depend on the frequency of the signal. Therefore, by varying the frequency of the applied signal the impedance of the system can be obtained as a function of frequency. Electrochemical measurements generally use a frequency range of 100 kHz–0.1 Hz. Like any complex quantity, $Z(\omega)$ can be represented in Cartesian as well as polar coordinates. In polar coordinates, the impedance of the data is represented by

$$Z(\omega)=|Z(\omega)|e^{\omega\varphi} \quad \text{(Eq. 2.12)}$$

where $|Z(\omega)|$ is the magnitude of the impedance and φ is the phase shift. In Cartesian coordinates the impedance is given as,

$$Z(\omega)=Z'(\omega)-j.Z''(\omega) \quad \text{(Eq. 2.13)}$$

where $Z'(\omega)$ is the real part of the impedance, $Z''(\omega)$ is the imaginary part, and $j = \sqrt{-1}$.

2.9.3. Data presentation

The plot of the real part of impedance on the *x*-axis against the imaginary part on the *y*-axis is a Nyquist plot. The *y*-axis is negative, and each point on the plot is the impedance at one frequency. As shown in Figure 2.3, low-frequency data are on the right side of the plot, and higher frequencies are on the left. The impedance can be represented as a vector of length |*Z*|. The angle between this vector and the *x*-axis, known as the phase angle, is *f* (= arg *Z*) [40, 42].

The shape of the Nyquist plot gives important qualitative information about the data from the electrical circuit. The plot often contains one or more portions of a semicircle that are each characteristic of a single time constant. A "time constant" is defined as the time required for the voltage to fall to V_0/e , where V_0 is the capacitor voltage at time = 0. Time constant is given by[35-40]

$$\tau = RC \quad \text{(Eq. 2.14)}$$

Which RC is the simplest circuit that contain a capacitor and a resistor in series.

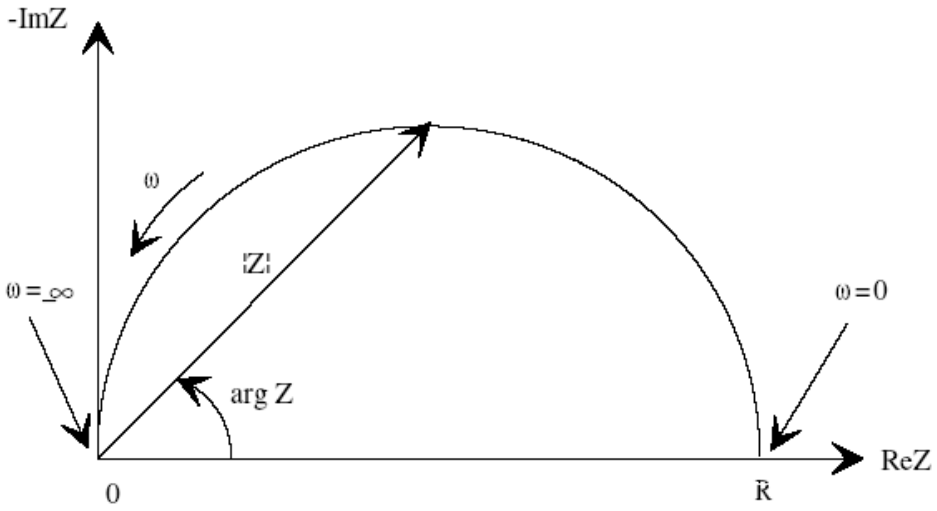

Figure 2.3. A typical Nyquist plot. (Reprinted with permission from V.F. Lvovich, Fundamentals of Electrochemical Impedance Spectroscopy, in: V.F. Lvovich, Impedance Spectroscopy: Applications to Electrochemical and Dielectric Phenomena, (2012) [41]. Copyright John Wiley and Sons, Inc).

Despite their advantages, Nyquist plots lose the frequency dimension of the data, which is their main drawback. This problem can be overcome by labeling the frequencies on the curve. In this way, the absolute value of impedance and the phase shifts can be plotted with respect to frequency in two different plots, resulting in a Bode plot. An example is shown in Figure 2.4. This is a more complete way to present the data [35-40].

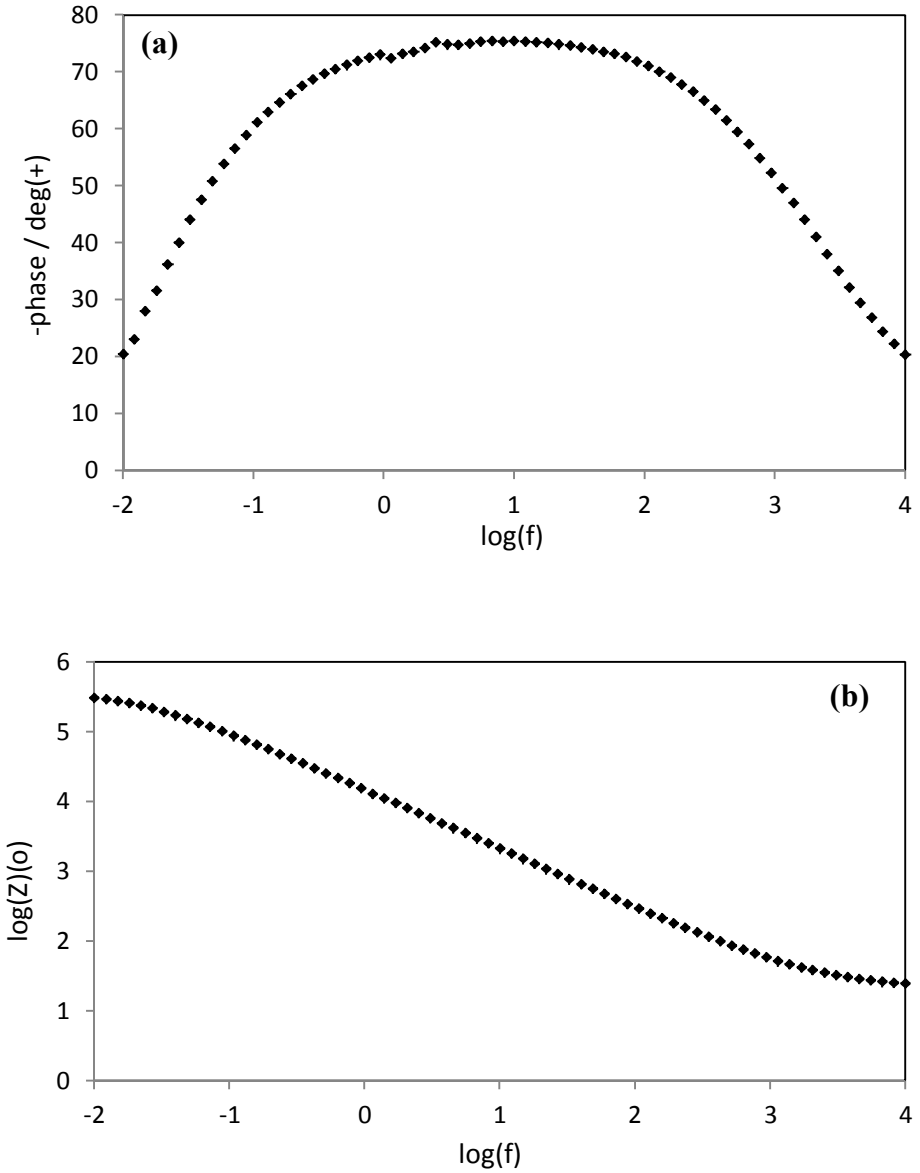

Figure 2.4. A typical Bode plot with one time constant (Reprinted with permission from R. Z. Zand, K. Verbeken and A. Adriaens, Progress in Organic Coatings, 75 (2012) 463 [41]. Copyright Elsevier) .

2.9.4. Electrical circuit elements

EIS data are commonly interpreted by fitting to an equivalent electrical circuit model. These models commonly consist of either passive elements, such as resistors, capacitors, and inductors, or distributed elements, such as a constant phase element or Warburg impedance, that can be combined in series or parallel to give complex equivalent circuits. Each of the

elements is attributable to a physical meaning. For example, most models contain a resistor that represents the cell's solution resistance [35-40].

Resistance (*R*)

The circuit element resistance (*R*) has an impedance of [43]:

$$Z_R = R \qquad \text{(Eq. 2.15)}$$

The impedance of a resistor is independent of frequency and has no imaginary component. With only a real impedance, the current through a resistor is always in phase with the voltage.

Ohmic resistance and polarization resistance (explained in section 2.6.2.) are the two most common examples of the use of resistance to describe electrochemical phenomena.

Ohmic resistance (R_Ω)

The potential drop between the reference electrode and the working electrode is the ohmic resistance, which is a function of the cell geometry and the conductivity of the electrolyte. For a planar electrode with uniform current density across its surface, the ohmic resistance is given by [43]:

$$R_\Omega = \frac{X}{\kappa \mathrm{A}} \qquad \text{(Eq. 2.16)}$$

where X is the distance of the reference electrode from the working electrode, κ is the solution conductivity, and A is the working electrode area.

For a rotating disc electrode, the ohmic resistance is given by

$$R_{\Omega} = \frac{1}{4\kappa R} \qquad \text{(Eq. 2.17)}$$

where R is the radius of the disc.

For more complex geometries, the ohmic resistance is determined experimentally and can be estimated by impedance spectroscopy. In a Nyquist plot, the intersection of the impedance data with the real part of the axis at the high-frequency end gives the ohmic resistance.

Capacitance (*C*)

The circuit element capacitance (C) has an impedance of [43, 44]:

$$Z_{c} = \frac{1}{j\omega C} \qquad \text{(Eq. 2.18)}$$

A capacitor's impedance is a function of frequency and decreases as the frequency is raised. Capacitors also have only an imaginary impedance component. The current through a capacitor is phase shifted 90° with respect to the voltage. Double-layer capacitance and coating capacitance are examples of the use of capacitance to describe electrochemical phenomena.

Double-layer capacitance (C_{dl})

Double-layer capacitance is the storing of electrical energy through the electrical double layer effect, which occurs at the interface between an electrode and an electrolyte. At this interface two layers of ions from the solution will form with opposing polarity if a voltage

is applied. The two layers are separated by a single layer of solvent molecules that adheres to the surface of the electrode and acts like the dielectric of a conventional capacitor. The value of the double-layer capacitance depends on many parameters including electrode potential, temperature, ionic concentrations, types of ions, oxide layers, electrode roughness, and impurity adsorption [43, 44].

Coating capacitance (C_C)

The coating capacitance (C_c) of a polymer-coated substrate is given by follow equation [43, 44]:

$$C_c = \frac{\varepsilon \varepsilon_0 A}{d} \qquad \text{(Eq. 2.19)}$$

where ε is the dielectric constant of the coating, ε_0 is the dielectric constant of vacuum, A is the area of the coating, and d is the thickness of the coating.

Typical dielectric constants of coatings are between 3 and 4; that of water is around 80. The penetration of water into a coating increases its capacitance. Therefore, coating capacitance can be used to measure the water uptake of a coating.

Constant phase element (CPE)

In EIS measurements, the capacitors for heterogeneous surfaces do not behave ideally, and instead act like a constant phase element, represented by Q [43, 44]:

$$Z_Q = \frac{1}{Y_0 (j\omega)^n} \qquad \text{(Eq. 2.20)}$$

where Y_0 is the admittance of an ideal capacitance, and n is an empirical constant between 0 and 1. If n is 1, the CPE behaves as a pure capacitor; if it is 0, the CPE behaves as a pure resistor. For n = 0.5, the CPE is the equivalent of a so-called Warburg element.

Warburg impedance (W)

The Warburg impedance was developed to model the diffusion of ionic species at an interface. Different assumptions can be used to describe the diffusion impedance. Under the assumption of a semi-infinite diffusion layer, the impedance is [43, 44]:

$$Z_{\mathrm{W}} = \frac{1}{Y_0\sqrt{j\omega}} \qquad \text{(Eq. 2.21)}$$

where Y_0 is the diffusion admittance. A Warburg impedance has identical real and imaginary parts, which result in a phase angle of 45°.

Inductance (L)

The impedance of an inductance (L) is given by [43, 44]:

$$Z_{\mathrm{L}} = j\omega \mathrm{L} \qquad \text{(Eq. 2.22)}$$

The impedance of an inductor increases as frequency increases. Inductors have only an imaginary impedance component. As a result, the current through an inductor is phase-shifted –90° with respect to the voltage.

In this work, EIS was carried out to monitor the anticorrosion performance of silane-treated steel substrates in a 3.5% NaCl solution. The measurements were made using an

Autolab PG-STAT20 potentiostat equipped with a frequency response analyzer module. A three-electrode configuration cell was used with a Ag/AgCl KCl_{sat} reference electrode and a platinum mesh counter electrode. Measurements were made at the open-circuit potential at room temperature. The data were obtained as a function of frequency in the frequency range 10^5 to 10^{-2} Hz using a sine wave with peak-to-peak amplitude of 10 mV. Samples were transferred to a fresh solution 30 min before the experiments. Impedance fitting was performed using the appropriate equivalent circuits in Z-view software (Scribner Associates Inc.) and the results presented as graphical figures together with fitting error. For each coating type, triplicate electrodes were prepared. In this work, to investigation the effect of each parameter, three series of different coatings type (for example, A, B C and D) used for EIS measurements. In all series of measurements, the same result was achieved (for example, sample B was the best one in all three measurements) but there was a bit difference in EIS measurements results of different electrodes of each coating type.

References

1. H. Zhou, A. Meng, Y. Long, Q. Li, Y. Zhang, Interactions of municipal solid waste components during pyrolysis: A TG-FTIR study, Journal of Analytical and Applied Pyrolysis, 108, 2014, pp. 19-25.
2. S.F. Maria, L.M. Russell, B.J. Turpin, R.J. Porcja, FTIR measurements of functional groups and organic mass in aerosol samples over the Caribbean, Atmospheric Environment 36, 2002, pp. 5185-5196.
3. C. Coury, A.M. Dillner, ATR-FTIR characterization of organic functional groups and inorganic ions in ambient aerosols at a rural site, Atmospheric Environment 43, 2009, pp. 940-948.

4. J.S. Gaffney, N.A. Marley, D.E. Jones, Fourier transform infrared (FTIR) spectroscopy, in: E.N. Kaufmann (Ed.) Characterization of Materials, John Wiley and Sons Inc., Hoboken, NJ, USA, 2002, pp. 1-33.
5. P.R. Griffiths, J.A. De Haseth, Fourier Transform Infrared Spectrometry, John Wiley and Sons Inc., Hoboken, NJ, USA, 2007.
6. B.H. Stuart, Infrared Spectroscopy: Fundamentals and Applications, John Wiley and Sons, Ltd, Hoboken, NJ, USA,2004.
7. P.R. Griffiths, Beer's Law, in: Handbook of Vibrational Spectroscopy, John Wiley and Sons, Ltd, Hoboken, NJ, USA, 2006.
8. S. Morita, R. Wiesendanger, E. Meyer (Eds.), Noncontact Atomic Force Microscopy, Volume 1, Springer, New York, 2002.
9. S. Morita, F. J. Giessibl, R. Wiesendanger (Eds.), Noncontact Atomic Force Microscopy, Volume 2, Springer, New York, 2009.
10. V. J. Morris, A. R. Kirby, A. P. Gunning, Atomic Force Microscopy for Biologists, 2nd Edition, World Scientific, London, UK, 2009.
11. C. L. Frewin (Ed.), Atomic Force Microscopy Investigations into Biology - From Cell to Protein, InTech, Rijeka, Croatia, 2012.
12. E. Meyer, Atomic force microscopy, Progress in Surface Science, 41, 1992, pp. 3-49.
13. B. Cappella, G. Dietler, Force-distance curves by atomic force microscopy, Surface Science Reports, 34, 1999, pp. 1-104.
14. J. Mertz, Introduction to Optical Microscopy, Roberts, 2010.
15. M. Spencer, Fundamentals of Light Microscopy, Cambridge University Press, 1982.
16. J. Goldstein, D.E. Newbury, D.C. Joy, C.E. Lyman, P. Echlin, E. Lifshin, L. Sawyer, J.R. Michael, Scanning Electron Microscopy and X-ray Microanalysis, Third Edition, Springer, New York, 2003.

17. L. Reimer, Scanning Electron Microscopy: Physics of Image Formation and Microanalysis, Springer, New York, 1998.
18. V. Kazmiruk, Scanning Electron Microscopy, InTech, Rijeka, Croatia, 2012.
19. D.E. Newbury, Advanced Scanning Electron Microscopy and X-Ray Microanalysis, Springer, New York, 1986.
20. ASTM E376-11, Standard Practice for Measuring Coating Thickness by Magnetic-Field or Eddy-Current (Electromagnetic) Testing Methods, ASTM International, West Conshohocken, PA, 2011, www.astm.org.
21. P. May, E. Zhou, Coating Thickness Measurement, in: S. Hinduja, L. Li (Eds.) Proceedings of the 36th International MATADOR Conference, Springer London, 2010, pp. 327-330.
22. P.d. Lima-Neto, A.N. Correia, G.P.d. Silva, Structural and morphological investigations of the electrodeposited Cr and Ni-Cr-P coatings and their electrochemical behaviors in chloride aqueous medium, Journal of the Brazilian Chemical Society, 17, 2006, pp. 1419-1427.
23. S. Papavinasam, Electrochemical polarization techniques for corrosion monitoring, in: L. Yang (Ed.), Techniques for Corrosion Monitoring, Woodhead Publishing Limited, Cambridge, 2008.
24. E. Ramoškienė, M. Gladkovas, M. Šalkauskas, Validation of salt spray corrosion test, in: P. De Bièvre, H. Günzler (Eds.) Validation in Chemical Measurement, Springer, New York, 2005, pp. 121-127.
25. ASTM B117-03 Standard Practice for Operating Salt Spray (Fog) Apparatus, Annual Book of ASTM Standards, 03.02, ASTM International, PA, USA, 2004.
26. V. Viswanathan, H.A. Hansen, J. Rossmeisl, T.F. Jaramillo, H. Pitsch, J.K. Nørskov, Simulating Linear Sweep Voltammetry from First-Principles: Application to

Electrochemical Oxidation of Water on Pt(111) and Pt3Ni(111), The Journal of Physical Chemistry C, 116, 2012, pp. 4698-4704.

27. J.W. Weidner, P.S. Fedkiw, Linear-sweep voltammetry in a cylindrical-pore electrode, Analytical Chemistry, 64, 1992, pp. 449-453.
28. B. Speiser, Linear Sweep and Cyclic Voltammetry, in: Allan J. Bard, M. Stratmann, E. Gileadi et al. (Eds.), Encyclopedia of Electrochemistry, Wiley-VCH Verlag GmbH and Co. KG, Saarbrücken, Germany, 2007.
29. Z. Ahmad, Principles of Corrosion Engineering and Corrosion Control, Elsevier, Amsterdam, 2006.
30. F. Mansfeld, The Polarization Resistance Technique for Measuring Corrosion Currents, in: M. Fontana, R. Staehle (Eds.) Advances in Corrosion Science and Technology, Springer, New york, USA, 1976, pp. 163-262.
31. G. Rocchini, SOFTCOR-DC-1 A Code for Evaluating Polarization Resistance, Corrosion Reviews, 7, 2011, pp. 273-286.
32. A.B. Anderson, Y. Cai, Calculation of the Tafel Plot for H_2 Oxidation on Pt(100) from Potential-Dependent Activation Energies, The Journal of Physical Chemistry B, 108, 2004, pp. 19917-19920.
33. ASTM G3−89 − Standard practice for conventions applicable to electrochemical measurements in corrosion testing, Annual Book of ASTM Standards, 03.02, ASTM International, PA, USA, 2004.
34. E. McCafferty, Validation of corrosion rates measured by the Tafel extrapolation method, Corrosion Science, 47, 2005, pp. 3202-3215.
35. B.T. Mark E. Orazem, Electrochemical Impedance Spectroscopy, John Wiley and Sons, Hoboken, NJ, USA, 2008.

36. A. Lasia, Electrochemical Impedance Spectroscopy and its Applications, Springer, New York, 2014.
37. J. R. Scully, D. C. Silverman, M. W. Kendig, Electrochemical Impedance: Analysis and Interpretation, ASTM International, PA, USA, 1993.
38. E.P. Randviir, C.E. Banks, Electrochemical impedance spectroscopy: an overview of bioanalytical applications, Analytical Methods, 5, 2013, pp. 1098-1115.
39. J.R. Macdonald, Impedance Spectroscopy, Annals of Biomedical Engineering, 20, 1992, pp. 289-305.
40. N.A. Sekushin, Method of presentation of experimental data in impedance spectroscopy, Russian Journal of Electrochemistry, 45, 2009, pp. 1300-1305.
41. V.F. Lvovich, Fundamentals of Electrochemical Impedance Spectroscopy, in: V.F. Lvovich, Impedance Spectroscopy: Applications to Electrochemical and Dielectric Phenomena, John Wiley and Sons Inc., Hoboken, NJ, USA, 2012.
42. N.P. Mark, E. Orazema, B. Tribollet, Enhanced Graphical Representation of Electrochemical Impedance Data, Journal of The Electrochemical Society, 153, 2006, pp. B129-B136.
43. R. Z. Zand, K. Verbeken, A. Adriaens, Corrosion resistance performance of cerium doped silica sol–gel coatings on 304L stainless steel, Progress in Organic Coatings, 75, 2012, pp. 463-473.
44. E. Barsoukov, J. R. Macdonald (Eds.), Impedance Spectroscopy: Theory, Experiment, and Applications, John Wiley and Sons INC., Hoboken, NJ, USA, 2005.

3

Investigation of the corrosion protection performance of silane hybrid coatings on a 316L stainless steel substrate [1]

3.1. Introduction

316L is a low carbon-chromium-nickel-molybdenum austenitic stainless steel with a good strength which combines properties such as acceptable biocompatibility and excellent mechanical resistance with easy fabrication at low cost, that permits its use in many industrial applications, consumer products and temporary orthopedic devices [1, 2]. In general 316L stainless steel presents good anticorrosion properties, however its corrosion resistance is weakened when it is subjected to a medium containing chloride or moisture environment [3,

[1] Reprinted from Progress in Organic Coatings, Volume 72 / Issue 4, Roohangiz Zandi Zand, Kim Verbeken and Annemie Adriaens, The corrosion resistance of 316L stainless steel coated with a silane hybrid nanocomposite coating, 709-715, Copyright (2011), with permission from Elsevier.

4], with a tendency to suffer localized corrosion (e.g. pitting corrosion). The corrosion may result in the loss of aesthetic appearance and structural integrity [5] and can be accompanied by the release of potentially toxic ions, which can be reduced by protective coatings [6-8]. Furthermore, the corrosion of stainless steel welds and joints occurs in the trans passive potential region in highly oxidizing environments of many industrial processes, especially in sulfuric acid media releasing Cr(VI) ions [9]. To resolve all these problems, the application of silane hybrid coatings has been increasingly investigated in the last years [7, 10-12].

Silane films not only ensure the adhesion between metal substrates and organic coatings but they also provide a thin, but efficient, barrier against oxygen diffusion to the metal interface [13, 14]. Recently, silane coatings have attracted the attention of the nanotechnology industry because they provide a highly uniform, robust and reliable coating with lateral resolution on the nanometer scale [15]. A general silane structure is $(XO)_3Si(CH_2)nY$, where XO is a hydrolysable alkoxy group, which can be methoxy (OCH_3), ethoxy (OC_2H_5) or acetoxy ($OCOCH_3$). Y is an organofunctional group such as epoxy, vinyl (C=C) or amino (NH_2) which is responsible for a good adhesion of a silane treated metal surface [16, 17].

3-Glycidoxypropyl-trimethoxysilane (GPTMS) is one of the organo–functional silane molecules that have been used as an effective coupling agent or adhesion promoter in glass/mineral reinforced polymeric composites for decades [16, 18-20]. Also it has been used in transparent abrasion-resistant hybrid coatings for polymers [21-24], metals [25-27] and for gas separation membranes [28, 29].

GPTMS can undergo a variety of reactions during the preparation of a hybrid by a sol–gel route. Hydrolysis of the methoxy groups gives silanol groups, which can subsequently condense to form the silane network. The silicon atom in GPTMS is tri-functional in terms of

the reactive methoxy groups and is therefore able to form a three-dimensional branched siloxane silane network with a nominal stoichiometry $SiO_{1.5}$. The epoxy rings can be opened and polymerized to form a linear poly(ethylene oxide) organic network [29, 30].

Cross-links between the two networks arise either from the preexisting link in the GPTMS molecule, by direct reaction of silanols with epoxy rings, or by condensation of silanols with hydroxyl of the opened epoxy rings. The uncatalyzed ring opening reaction occurs at a useful rate only at elevated temperature and so thermal curing is required [29, 30].

The use of the sol–gel process to prepare highly intermingled inorganic–organic hybrid polymer networks is of current scientific interest since it offers the possibility of tailoring the material properties by variation of the relative composition of the inorganic and organic phases. With such systems, the inorganic and organic networks are formed together (often simultaneously) to achieve homogeneous phase morphologies, which are impossible to produce by the other routes [29].

The present work aims at evaluating the structure and corrosion protection performance of silane sol–gel hybrid coatings deposited on austenitic 316L stainless steel. Sol–gel coatings were prepared from hydrolysis and condensation of 3-glycidoxypropyl-trimethoxysilane (GPTMS) as the precursor and bisphenol A (BPA) as the cross-linking agent in acid catalyzed condition. The effect of the drying method as an effective parameter on the microscopic features and morphology of the silane hybrid coating was examined.

3.2. Sample preparation

The silane solution was prepared by adding 4.084 mL of 3–glycidoxypropyl-trimethoxy silane (GPTMS, Merck) to 0.5 mL aqueous HCl (pH = 2), and stirred in a sealed beaker at room temperature for 20 min at 240 RPM to hydrolyze and condense the silane

precursors. In the next step, 2.111 g of bisphenol A (BPA, Merck) was added to the solution as a cross-linking agent. The BPA was dissolved by mixing the solution for 80 minutes. To accelerate the condensation reaction, 0.0152 mL of 1–methylimidazol (MI, Merck) was added to the solution and stirred for 5 min. A clear, colourless, homogenous solution resulted [31, 32].

The substrate material used for the present investigation was 316L stainless steel alloy, purchased from Watrin-sprl CO. Its chemical composition, analysed by spectro–analysis method, is given in table 3.1. Plates (7 cm ×15 cm ×0.1 cm) were used for the salt spray tests, while coupons (1.13 cm^2 area and 0.1 cm thickness) were used for all other experiments. The substrates were initially degreased with detergent and then polished with 600 and 1200 grit sand papers. The polished samples were rinsed with distilled water and degreased with 1 M NaOH solution at 50°C. Consequently the substrates were neutralized with 0.01 M HCl solution to remove excess of NaOH solution. As a last step, the substrates were cleaned with acetone to remove all dirt and grease and were then air-dried.

Table 3.1. Chemical composition of 304L stainless steel (in mass%).

C	Si	Mn	P	S	Al	Cr	Mo	Ni	Cu	Fe
0.024	0.46	1.22	0.038	0.0048	0.020	16.45	1.95	9.69	0.35	Balance

The cleaned substrates were dipped into the silane solution for a duration of 5–10 s. In order to study the effect of drying method on the microscopic features and morphology of the hybrid coatings, a series of the silane–treated substrates was dried at the ambient temperature

for 2 weeks, denoted as air dried silica hybrid coating (A-SHC), while another series was dried at ambient temperature for 24 h and placed in a furnace to cure at temperatures ranging from 25–130°C curing process with a heating rate of 7.5 °C/min for 90 minutes to extensively crosslink the silane films. This series of the coatings is denoted as thermal cured silica hybrid coating (T-SHC).

3.3. Results and discussion

3.3.1. Characterization

Figure 3.1 shows the FTIR spectra of two series of hybrid films (A-SHC and T-SHC). The most resolved bands are attributed to the vibration frequencies of the glycidoxypropylsiloxane structural fragment. They include the oxiranes methylene bending at 1480 cm^{-1}, the epoxide ring breathing band at 1250 cm^{-1} and the antisymmetric epoxide ring deformation bands at 758 and 902 cm^{-1} [33]. The band of the antisymmetric epoxide ring deformation at 758 and 902 cm^{-1} in the magnified region from 729 to 950 cm^{-1} in panel A, appears to be intense. It allows the monitoring of the chemical reaction of the epoxy functional groups of organosilica-networks coupled with diol crosslinker groups. FTIR spectra of the cured film show the disappearance of this band, which indicates the formation of a cross-linked network under curing. Also the bands centered at 1100 cm^{-1} due to Si–O–Si [34] in the magnified region from 950 to 1200 cm^{-1} in panel B, are intensive as compared to that without curing. All these changes indicate the formation of a denser siloxane network upon thermal curing.

SEM was used to investigate the effect of the drying method on the morphology of the silica hybrid coatings. Figure 3.2 shows typical SEM micrographs of the T-SHC and A-SHC coatings. Cracking during drying is a rare event but could occur when the gel has had insufficient aging and strength. After drying, the coatings were densified by heat treatment.

During this step the residual stress grows until the point of generating some micro−cracks into the coating. Residual stress at the interface comes from the differential thermal expansion of both substrate and film coating.

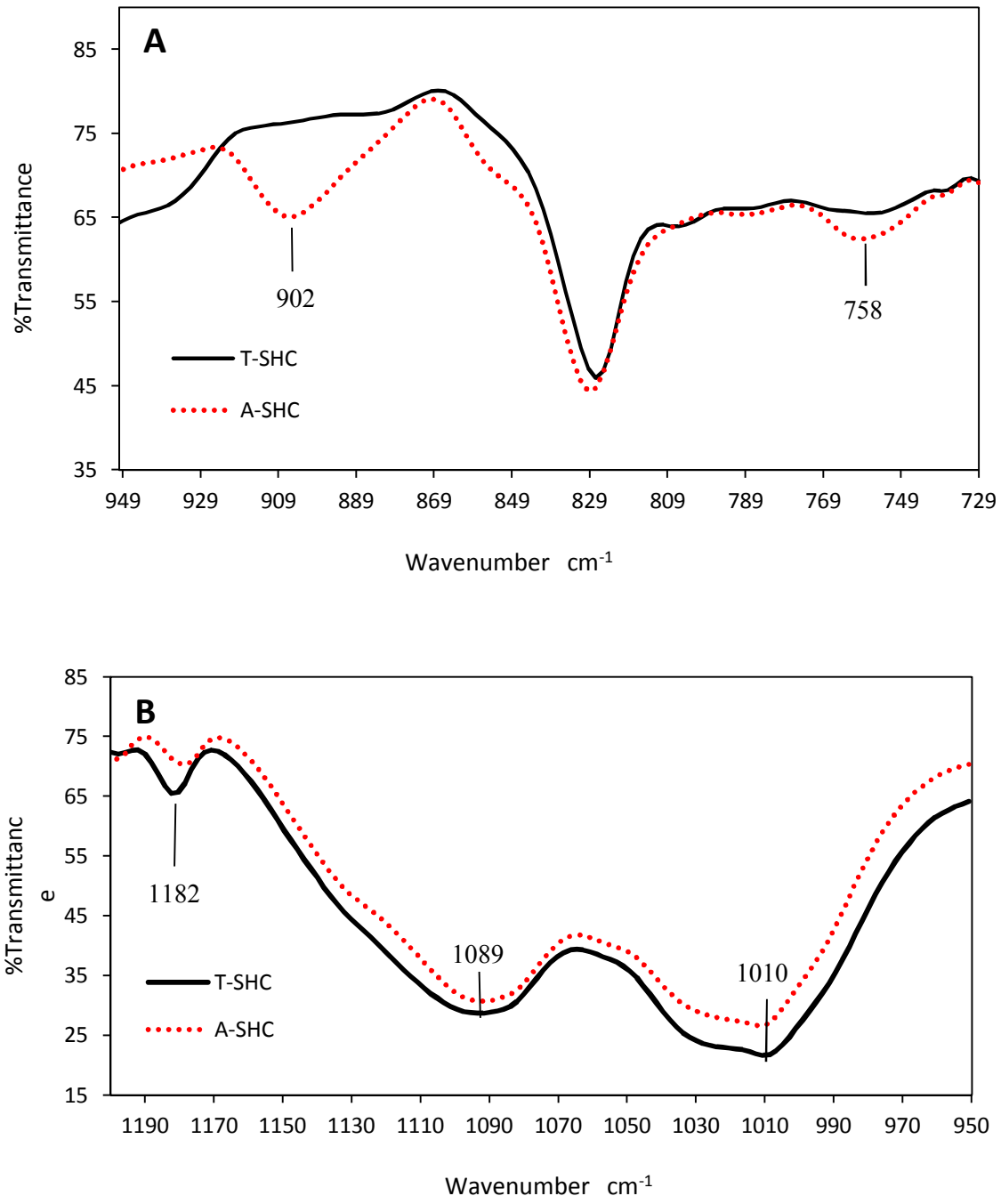

Figure 3.1. FTIR spectra of silane films prepared under two drying condition: air exposed dried film (A-SHC) and thermal cured film (T-SHC); (A) magnified region from 729 to 950 cm^{-1} and (B) magnified region from 950 to 1200 cm^{-1}.

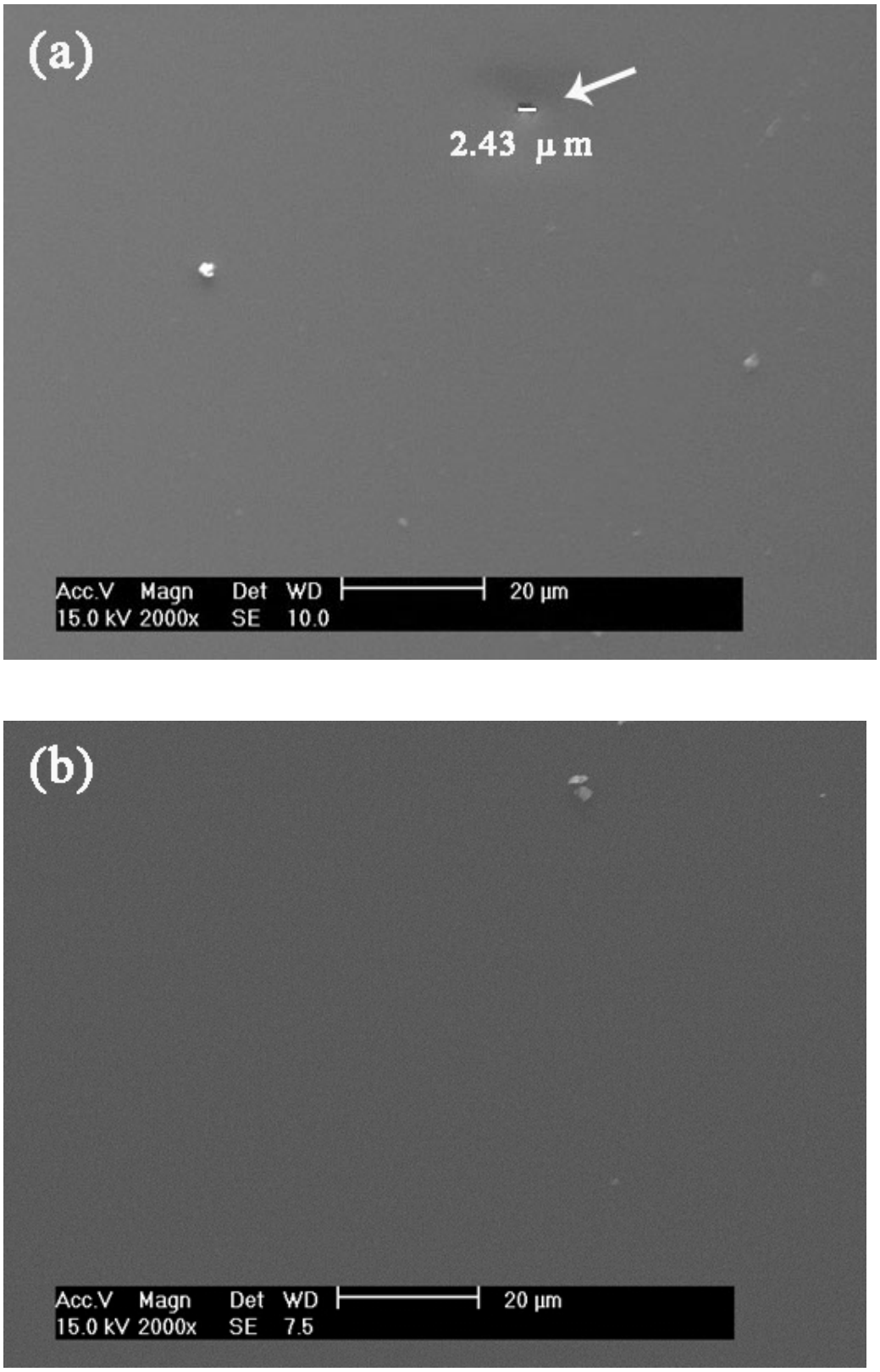

Figure 3.2. Secondary electron images of the coated 316L stainless steel samples prior to polarization test: (a) T-SHC and (b) A-SHC coated SS316L.

However, as soon as the corrosive medium penetrates through the layer and reaches the substrate, an electrochemical reaction takes place, causing an increase of current density [35]. Fortunately, the evaluated coatings did not show such behavior and the surface appearance obtained by SEM characterization did not present any cracks in each of the samples. It seems that both of the coatings are uniform, defect and crack free. However, sample coated with T-SHC coating shows the presence of micro-pore which marked with white arrow in figure 3.2 a.

3.3.2. Corrosion protection performance of the hybrid coating

The corrosion protection performance of the hybrid coatings was studied by linear sweep voltammetry (LSV). Figure 3.3 presents the potentiodynamic polarization curves of the bare and A-SHC and T-SHC coated 316L stainless steel substrates recorded after 3 h of immersion in a neutral 3.5% NaCl solution. Table 3.2 summarizes the electrochemical parameters obtained from these measurements.

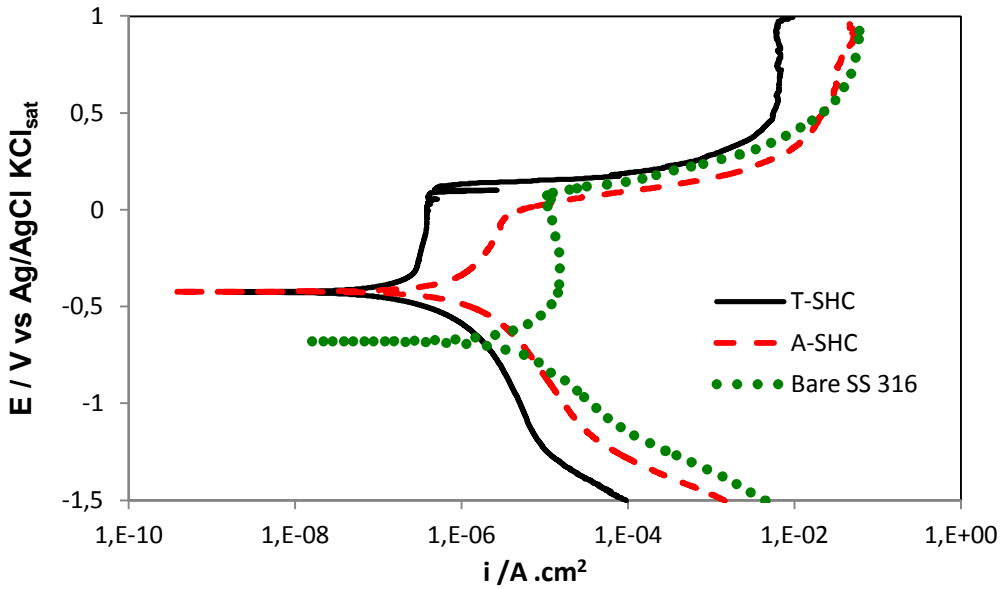

Figure 3.3. Potentiodynamic polarization curves of the A-SHC and T-SHC coated and bare 316L stainless steel in a 3.5 % NaCl solution.

In comparison to the bare sample, the T-SHC coated sample shows a decrease in the corrosion current density, Icorr, around 10−8 A cm^{-2}. In addition its potential is shifted to a higher value (−0.424 V). This coated sample shows an anodic behavior with limited current density in the range of +0.55 V over its E_{corr}, before the potential exceeds the breakdown potential. This behavior was improved by the protective barrier characteristic of the coating, as reported before [30]. However, the A-SHC coated sample into this solution did not significantly improve the corrosion resistance, but it showed some characteristics in the anodic current zone. In this way, the A-SHC coated sample presents a range of anodic potential at +0.4 V over the E_{corr}, before the point of the breakdown potential was reached. As a comparative result, the uncoated sample presented a continuous potential range characterized by a control mechanism of equilibrium in the oxidation and reduction reactions. Also a wide passive plateau in the potential characteristic of stainless steel was observed.

Table 1. Summary of the electrochemical parameters (corrosion potential, corrosion current, cathodic and anodic slopes) obtained from the polarization measurements in a 3.5 % NaCl solution.

Sample	E_{corr} (V)	I_{corr} (A.cm^{-2})	B_c (V/dec)	B_a (V/dec)
Bare SS316L	-0.564	1.35×10^{-6}	0.204	0.142
A-SHC	-0.423	2.84×10^{-7}	0.152	0.111
T-SHC	-0.424	7.63×10^{-8}	0.175	0.091

Figure 3.4 shows the scanning electron micrographs for the bare and coated 316L stainless steel samples after potentiodynamic polarization in a neutral 3.5% NaCl solution. After the anodic polarization, a localized corrosion is observed for all samples, consisting of small cracks (Figures 3.4a and c) and pits (Figures 3.4e) of different sizes. A closer inspection

shows that the region surrounding some of the cracks and pits is damaged (see figures 3.4b, d and f). This may indicate a preferential localized attack, occurring after the electric potential exceeded the breakdown potential. This localized attack has resulted in debonding, delaminating and lifting of the coating from the substrate, possibly due to the hydrolysis reactions at the interface. Additionally, the diffusion of the oxidant ions speeds up and the corrosion rate increases causing an accumulation of the corrosion products at the interface, promoting the formation of bulges and even leading to micro-cracks as can be seen in figure 3.4a and d. As the quantity of corrosion products increases, the protective coating is lost by the fact that the film peels off. Fractures of the coatings derived by the increasing of sweep over-potential initially grow from small cracking points or pitting in the coating. On the other hand, increasing towards higher potential promotes the cracking and peeling of the coating [35]. However, the coated samples show a higher corrosion resistance described by the E_{corr} and i_{corr} values (Table 3.2), as reported before.

The traditional salt spray coating corrosion resistance evaluation technique was used to investigate the corrosion performance of the sol–gel films. Pictures of the T-SHC and A-SHC coated 316L stainless steel plates after 600 h of salt spray exposure are shown in figure 3.5; along with bare plates as control (taped areas were cropped from the picture). It can be clearly seen that silane-treated surfaces do not exhibit any sign of corrosion and still retain their originally shiny surfaces. The bare panel, in contrast, exhibits early signs of corrosion. Therefore, these data confirm the good corrosion protection for a long term, of the silane sol–gel coatings.

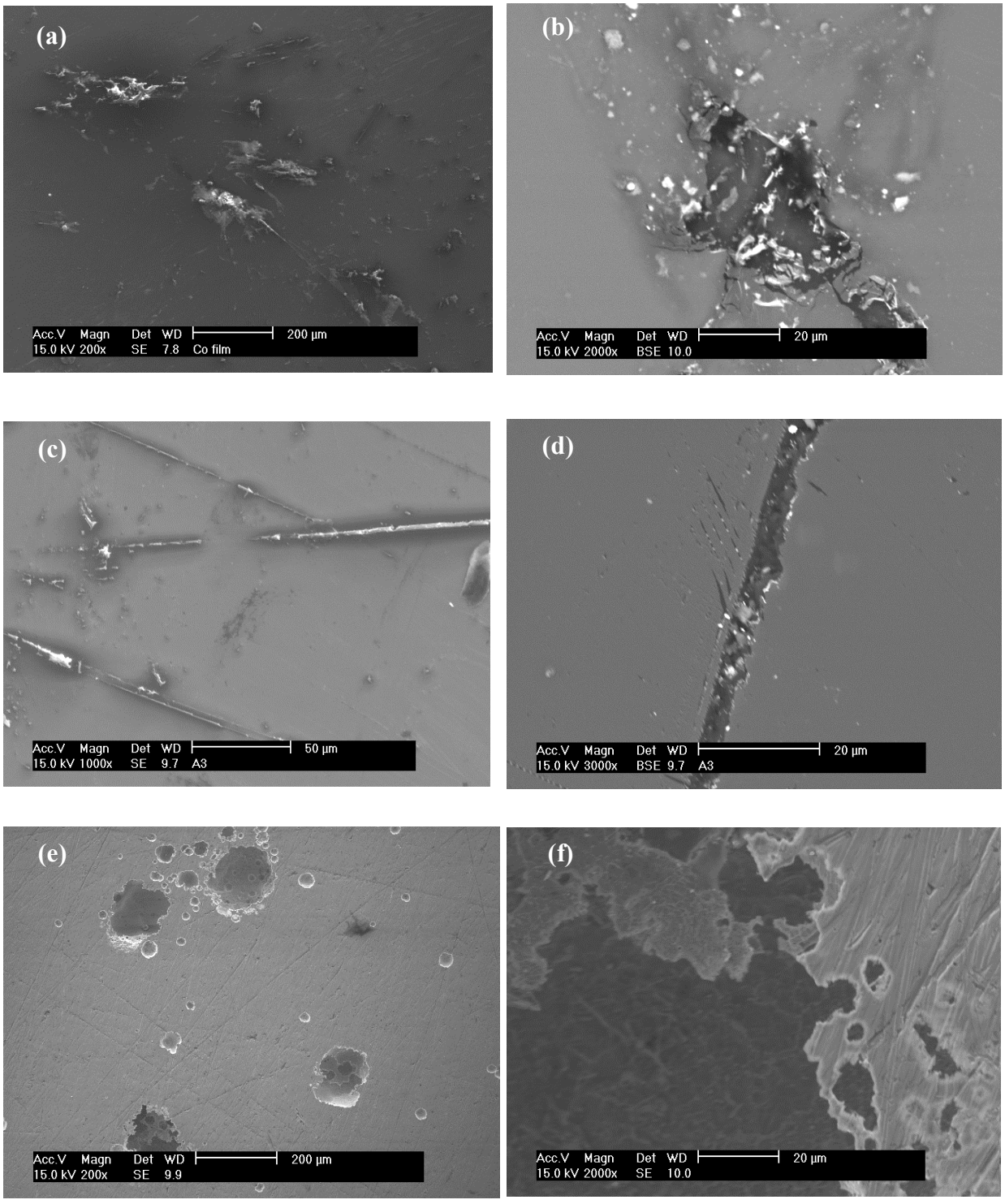

Figure 3.4. Secondary electron images of the bare and coated 316L stainless steel samples after potentiodynamic polarization test in neutral 3.5% NaCl solution with different magnifications: (a) and (b) T-SHC, (c) and (d) A-SHC and (e) and (f) bare SS316L.

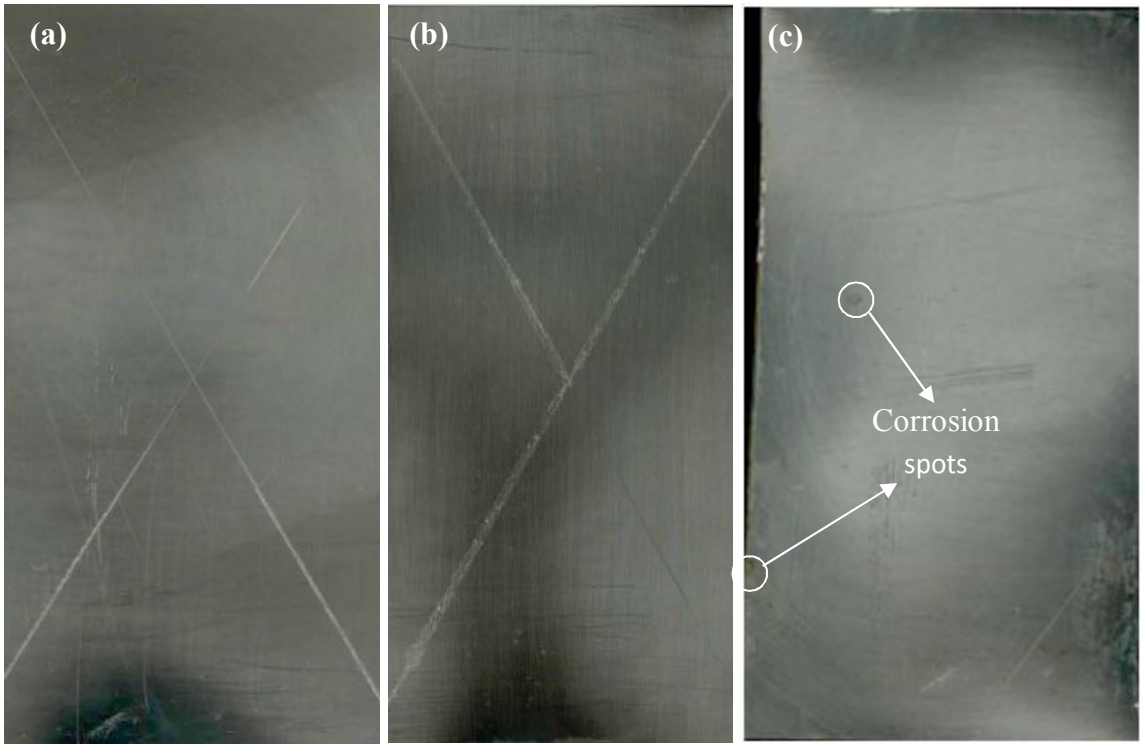

Figure 3.5. Photograph of A-SHC (a) and T-SHC (b) coated and bare (c) 316L stainless steel samples after 600 hours of exposure in the salt spray chamber.

Figure 3.6 shows the optical microscopic images for the bare and T-SHC coated 316L stainless steel samples after immersion test in a neutral 3.5% NaCl solution. After 360h (15days) of immersion, a localized corrosion is observed for the bare samples, consisting of small pits (Figure 3.6a) of different sizes. For the T-SHC coated sample, after 5h immersion, coatings appear crack-free and transparent in such a way that the polishing marks on the underlying metal substrates are visible through the coatings (Figure 3.6b). After 360h immersion, the surface of the coating is found to contain a few heterogeneities (Figure 3.6c). These heterogeneities are probably due to the precipitation of insoluble corrosion products or defects in the coating, which marked with black arrows in figure 3.6 c.

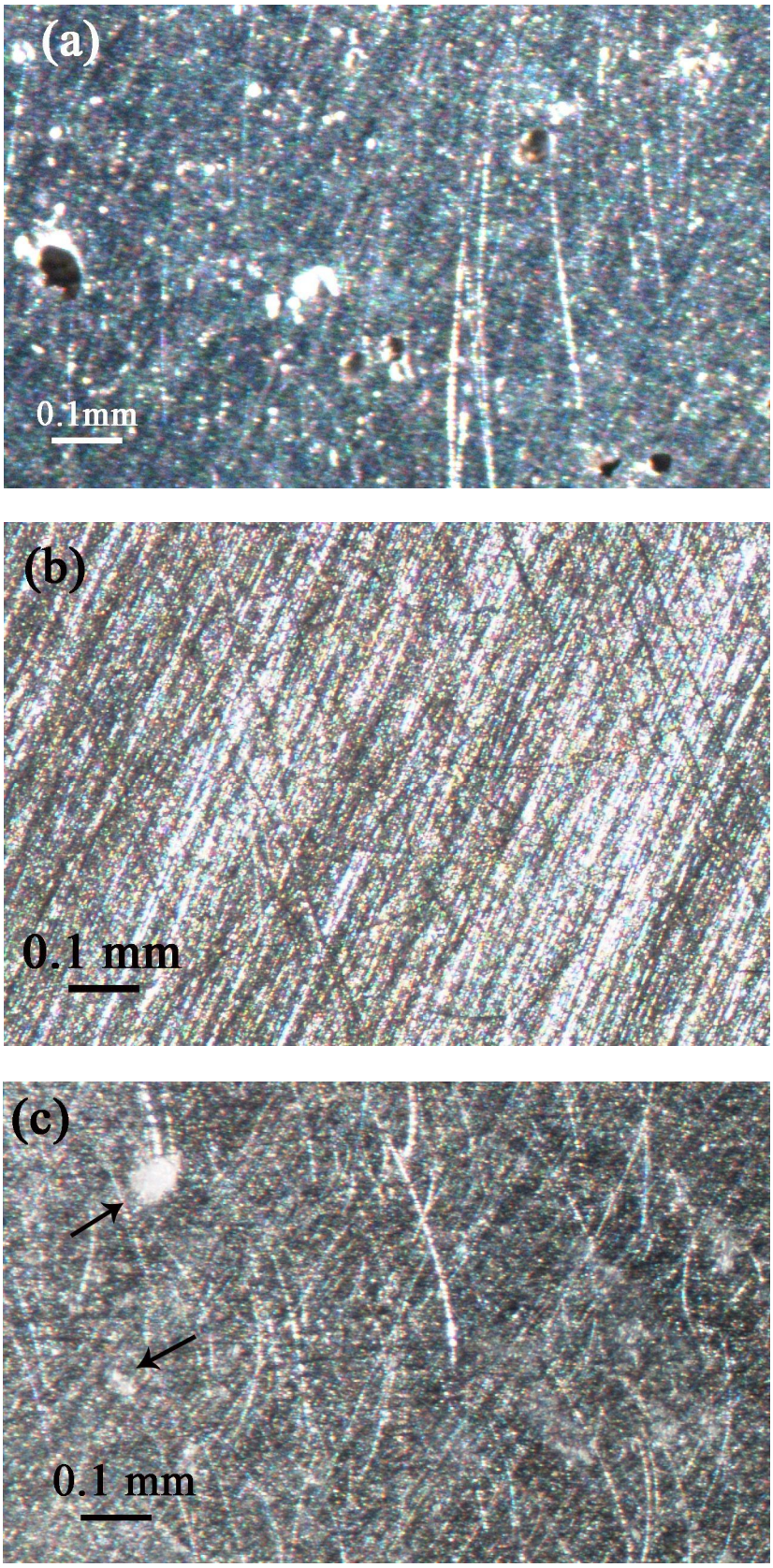

Figure 3.6. Optical microscopic images of the bare and T-SHC coated 316L stainless steel samples after immersion in neutral 3.5% NaCl solution: (a) bare sample after 360h (15days) immersion and (b) and (c) coated sample after 5 and 360h immersion.

Figure 3.7 presents the impedance spectra obtained for the bare and thermal cured hybrid coated 316L substrates (T-SHC) during immersion in a 3.5% NaCl solution for a period of 43 days. For the bare sample, the EIS spectrum obtained after 360 h (15days) of immersion is characterized by two overlapping time constants at a frequency around 10 rad s^{-1} and another one at lower frequencies (around 1 rad s^{-1}). The time constant at higher frequencies can be assigned to the presence of an oxide/hydroxide film existing on the bare 316L substrate, whereas the time constant at lower frequencies can be assigned to corrosion activity. The total impedance of the bare substrate after 360 h of immersion is lower than 10^5 $\Omega.cm^2$. At this stage, the bare surface shows a significant quantity of corrosion products (as shown in figure 3.6 a).

For the coated substrate, during 5 to 888 h (37 days) of immersion the spectra are also characterized by the presence of two time constants. The high frequency time constant appears at 10^4 rad s^{-1} and the low frequency time constant develops around 10^{-1} rad s^{-1}. After 1032 h (43 days) of immersion the spectra are characterized by the presence of three time constants. The first time constant appears at 10^4 rad s^{-1}, the second one appears at 3.16 rad s^{-1} and the last one develops around 0.05 rad s^{-1}.

The results show a significant shift in the high frequency impedance during 5 to 360 h (15days) of immersion which is most probably associated with water uptake through the pores/defects present in the films (as shown in figure 3.2a). The access of aggressive species induces localised corrosion activity. This is followed by precipitation of insoluble corrosion products (as shown in figure 3.6c), which block the pores/defects at the coating/substrate interface leading to increasing the high frequency impedance during 360 – 1032h immersion.

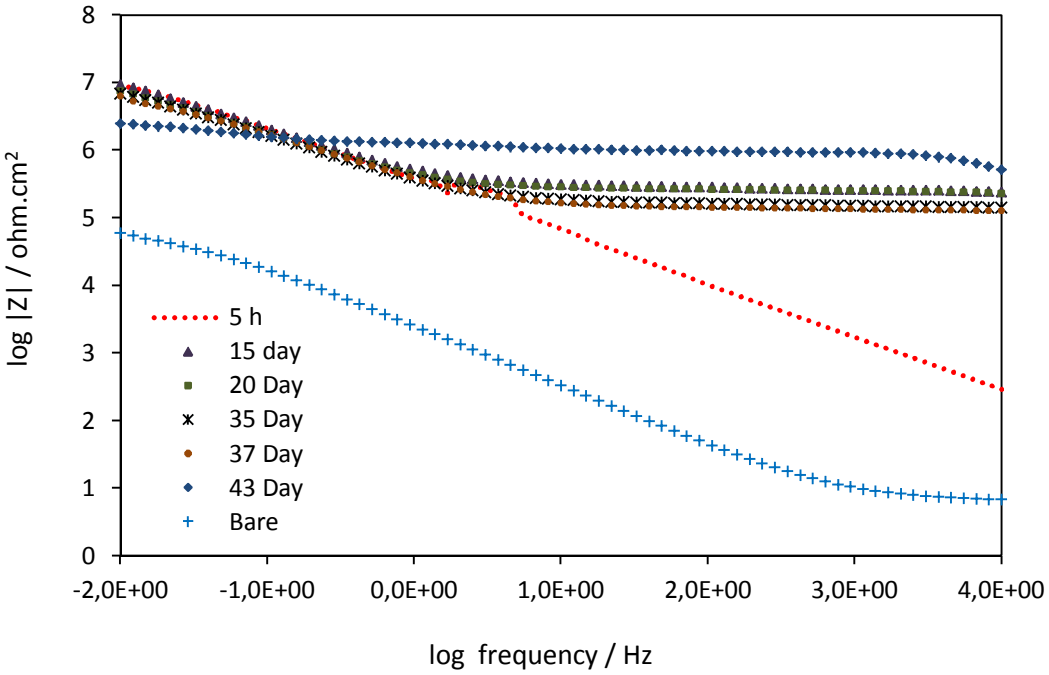

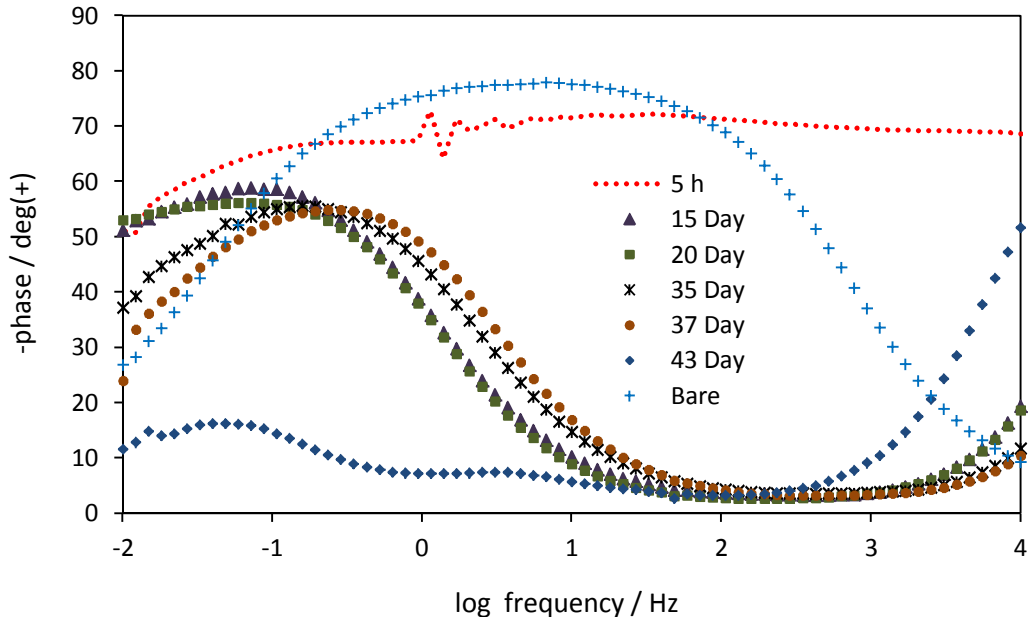

Figure 3.7. EIS Bode plots obtained for bare and T-SHC coated 316L stainless steel substrates after different immersion times in 3.5% NaCl solution.

The results also show that the hybrid coating increases the low frequency impedance of the system by about two orders of magnitude, in comparison to the bare sample. Moreover, for the coated sample, the total impedance values starts to decrease slightly as a function of immersion time and reaches a value of 6.727 $\Omega.cm^2$ at the end of 37 days of immersion. The first signs of corrosion activity were detected between 37th and 43th days of immersion. Nevertheless, the impedance values are more than 1.5 order of magnitude higher than those for the bare sample. These results indicate the protective nature of silane hybrid coating.

A more detailed interpretation of the EIS results can be made by numerical fitting of the experimental data to the equivalent circuits depicted in figure 3.8. Because the phase angle plots revealed two or three time constants at different immersion times, two different equivalent circuits were used to fit the data. The equivalent circuit shown in figure 3.8a was used to model the EIS results of T-SHC coated samples during 5 to 888 h (37 days) of immersion. The equivalent circuit shown in figure 3.8b was used to model the EIS results of sample during 1032 h (43 days) of immersion.

Thus, for the equivalent circuits shown in figure 3.8, R_s is interpreted as the resistance of the electrolyte; CPE_{Coat} ($0.66 < n_{coat} < 0.96$) and R_{Coat} represent the capacitance and resistance of the hybrid coatings, respectively; CPE_{oxide} ($0.76 < n_{oxide} < 0.8$) and R_{oxide} represent the capacitance and resistance of the metal oxide layer over the metal surface , respectively; CPE_{dl} ($n_{dll} = 0.79$) is the capacitance of the electrochemical double layer at the metal/electrolyte interface; and R_{polar} is the polarization resistance of the corrosion process. In these equivalent circuits, constant phase elements (CPE) were used instead of pure capacitors, because of the non-ideal character of the corresponding response. This is due to presence of silicon particles which give rise to a certain surface roughness and inhomogeneity's. The true

capacitances can be calculated from the respective CPE parameters, as described elsewhere [36].

(a)

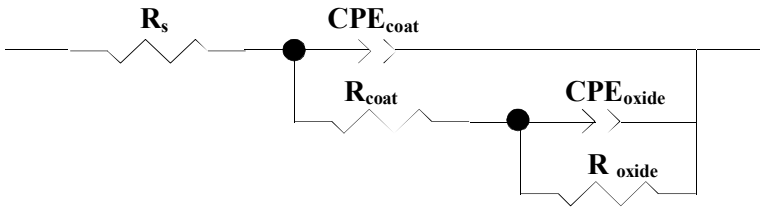

(b)

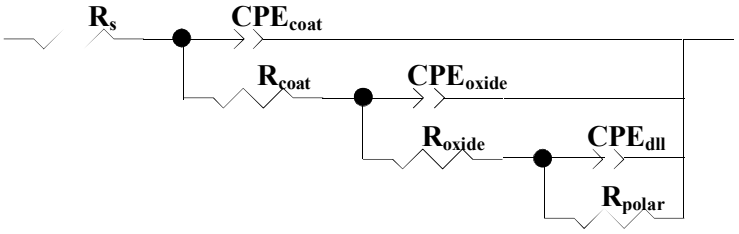

Figure 3.8. Equivalent circuits used for the numerical fitting of the EIS data during immersion in a 3.5% NaCl solution.

The variation of the fitted parameters (resistances and capacitances) with immersion time using the equivalent circuits of figure 3.8 is shown in figure 3.9. Values are shown with the errors from the numerical fitting (10^{-3} < Chi-squared < 10^{-2}). The change of the T-SHC coated sample capacitances during immersion is presented in figure 3.9a. Generally the capacitance of dielectric films depends on the amount of absorbed water [37], thus increases in capacitance values are associated to water uptake [38]. During 360 h of immersion, CPE_{coat} showed a pronounced decrease and then remains almost constant which reflects the stability and the good barrier properties of the coating.

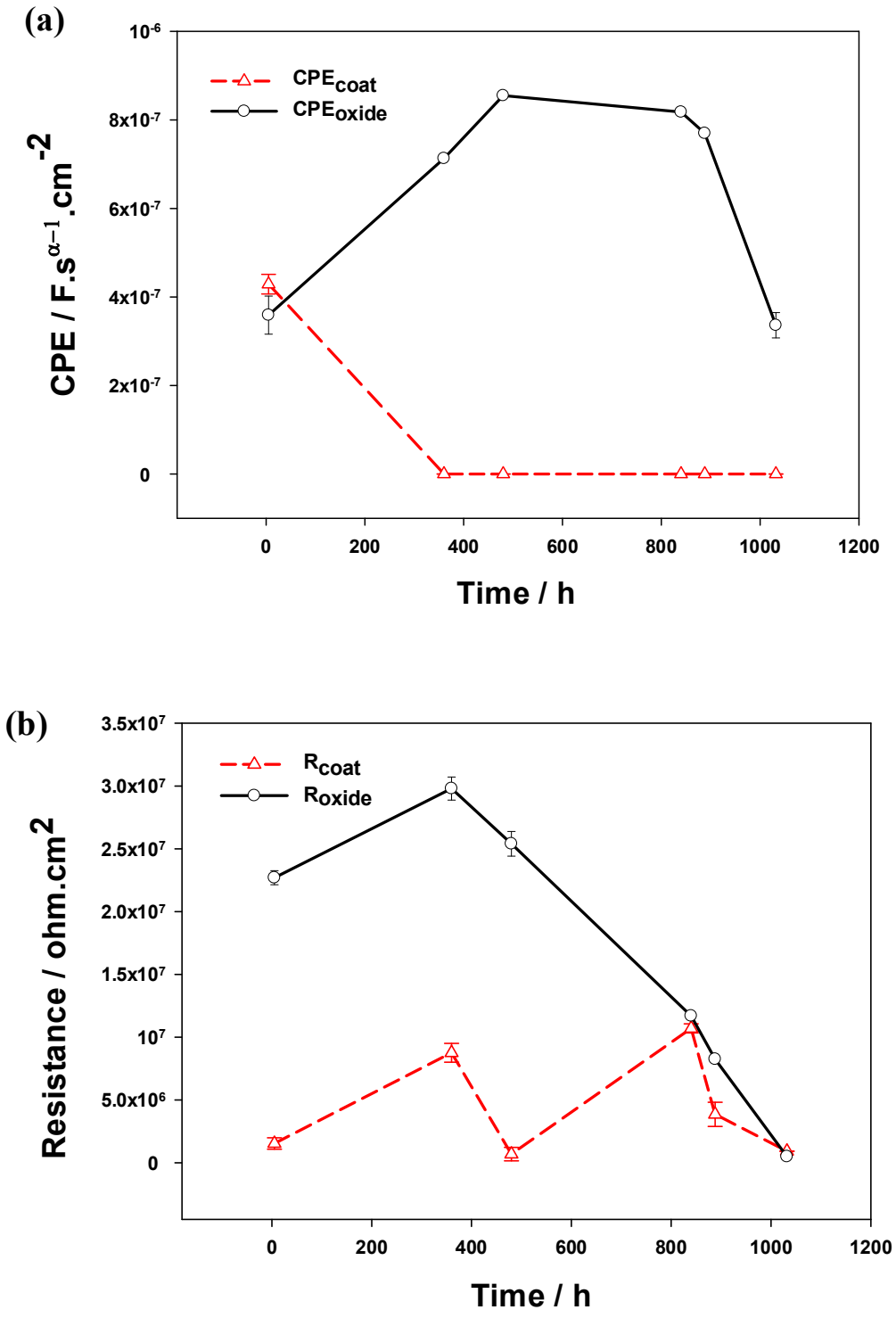

Figure 3.9. Evolution of the fitted parameters (capacitances and resistances) with immersion time using the equivalent circuits of figure 3.8 during immersion in a 3.5 % NaCl solution.

In contrast, The CPE associated with the metal oxide layer (CPE_{oxide}), exhibit significantly faster growth during 480h immersion as a result of water uptake through the pores/defects present in the films [39]. Since the corrosion activity occurred in localized areas, it is likely that the precipitation of the insoluble and passive corrosion products occurred at these locations, thereby decreasing the corrosion activity at the coating/substrate interface leading to a partial recovery of the coating barrier properties. This precipitation is translated in a decrease in oxide capacitance after the increase due to water uptake.

The evolution of the T-SHC coated sample resistances, is shown in figure 3.9b. The coating resistance (R_{coat}), shows some fluctuations, with a rapid drop and later recovery after 360 h and 840 h of immersion suggesting the formation of some pores or the enlargement of smaller pores in the sol–gel layer [40]. In contrast, the resistance of metal oxide layer (R_{oxide}), shows a maxima at 360h immersion that follow by gradual decreasing during 1032h immersion due to water uptake through the pores/defects in the coating and localized corrosion activity at the coating/substrate interface.

3.4. Conclusions

In this study, the corrosion protective behavior of hybrid coatings based on 3-glycidoxypropyl-trimethoxysilane (GPTMS) as the precursor and bisphenol A (BPA) as the cross-linking agent as an "environmentally friendly" corrosion resistant protection system on 316L stainless steel substrates were studied. Additionally, the effect of drying method on microscopic features and morphology of the hybrid coatings was evaluated. The results of the FTIR analysis indicated the formation of a denser siloxane network upon thermal curing. In addition the SEM analyses confirm the formation of a transparent and homogenous film without any defect and micro crack especially cured at 130°C. The results of the electrochemical analyses as well as salt spray test highlight the good barrier properties of the

silane film. The pretreatment of 316L stainless steel with silane hybrid coating leads to the formation of a surface film that performs as a physical barrier on metal substrate. The presence of the silane film increases the anodic polarization of the system and its total impedance relative to the bare substrate. These results indicate the protective nature of silane hybrid coating.

References

1. B.B. I. Olefjord, and U. Jelvestam, Surface composition of stainless steels during anodic dissolution and passivation studied by ESCA, Journal of Electrochemical Society., 132, 1985, pp. 2854-2861.
2. M.R. A. Turnbull, A. Willetts, S. Zhou, Corrosion and electrochemical behaviour of 316L stainless steel in acetic acid solutions, Corrosion Science, 45, 2003, pp. 1051-1072.
3. M.A.M. Ibrahim, S.S. Abd El Rehim, M.M. Hamza, Corrosion behavior of some austenitic stainless steels in chloride environments, Materials Chemistry and Physics, 115, 2009, pp. 80-85.
4. Y. Tsutsumi, A. Nishikata, T. Tsuru, Pitting corrosion mechanism of Type 304 stainless steel under a droplet of chloride solutions, Corrosion Science, 49, 2007, pp. 1394-1407.
5. S. Bhattacharyya, M.B. Das, S. Sarkar, Failure analysis of stainless steel tubes in a recuperator due to elevated temperature sulphur corrosion, Engineering Failure Analysis, 15, 2008, pp. 711-722.
6. M.P. Ryan, D.E. Williams, R.J. Chater, B.M. Hutton, D.S. McPhail, Why stainless steel corrodes, Nature, 415, 2002, pp. 770-774.
7. D.A. López, N.C. Rosero-Navarro, J. Ballarre, A. Durán, M. Aparicio, S. Ceré, Multilayer silica-methacrylate hybrid coatings prepared by sol–gel on stainless steel

316L: Electrochemical evaluation, Surface and Coatings Technology, 202, 2008, pp. 2194-2201.

8. I. De Graeve, J. Vereecken, A. Franquet, T. Van Schaftinghen, H. Terryn, Silane coating of metal substrates: Complementary use of electrochemical, optical and thermal analysis for the evaluation of film properties, Progress in Organic Coatings, 59, 2007, pp. 224-229.
9. I. Betova, M. Bojinov, T. Laitinen, K. Mäkelä, P. Pohjanne, T. Saario, The transpassive dissolution mechanism of highly alloyed stainless steels: I. Experimental results and modelling procedure, Corrosion Science, 44, 2002, pp. 2675-2697.
10. J. Ballarre, D.A. López, N.C. Rosero, A. Durán, M. Aparicio, S.M. Ceré, Electrochemical evaluation of multilayer silica–metacrylate hybrid sol–gel coatings containing bioactive particles on surgical grade stainless steel, Surface and Coatings Technology, 203, 2008, pp. 80-86.
11. J. Ballarre, E. Jimenez-Pique, M. Anglada, S.A. Pellice, A.L. Cavalieri, Mechanical characterization of nano-reinforced silica based sol–gel hybrid coatings on AISI 316L stainless steel using nanoindentation techniques, Surface and Coatings Technology, 203, 2009, pp. 3325-3331.
12. H.B. Lu, Y. Hu, M.H. Gu, S.C. Tang, H.M. Lu, X.K. Meng, Synthesis and characterization of silica–acrylic–epoxy hybrid coatings on 430 stainless steel, Surface and Coatings Technology, 204, 2009, pp. 91-98.
13. P.H. Suegama, H.G. de Melo, A.A.C. Recco, A.P. Tschiptschin, I.V. Aoki, Corrosion behavior of carbon steel protected with single and bi-layer of silane films filled with silica nanoparticles, Surface and Coatings Technology, 202, 2008, pp. 2850-2858.

14. M. Fedel, M. Olivier, M. Poelman, F. Deflorian, S. Rossi, M.E. Druart, Corrosion protection properties of silane pre-treated powder coated galvanized steel, Progress in Organic Coatings, 66, 2009, pp. 118-128.
15. M.F. Montemor, A.M. Cabral, M.L. Zheludkevich, M.G.S. Ferreira, The corrosion resistance of hot dip galvanized steel pretreated with Bis-functional silanes modified with microsilica, Surface and Coatings Technology, 200, 2006, pp. 2875-2885.
16. W. van Ooij, D. Zhu, V. Palanivel, J.A. Lamar, M. Stacy, Overview: The Potential of silanes for chromate replacement in metal finishing industries, Silicon Chemistry, 3, 2006, pp. 11-30.
17. D. Zhu, W.J.v. Ooij, Enhanced corrosion resistance of AA 2024-T3 and hot-dip galvanized steel using a mixture of bis-[triethoxysilylpropyl]tetrasulfide and bis-[trimethoxysilylpropyl]amine, Electrochimica Acta, 49, 2004, pp. 1113-1125.
18. E.P. Plueddemann, Silane Coupling Agents, 2nd ed., Plenum Press, New York, 1991.
19. K.L. Mittal (Ed.), Silanes and Other Coupling Agents, VSP, Utrecht, 1992.
20. K.L.Mittal (Ed.), Silanes and Other Coupling Agents, Vol. 2, VSP, Utrecht, 2000.
21. C.A. Glotfelter, R.P. Ryan, US Patent 5,120,811, 1992.
22. H. Schmidt, B. Seiferling, G. Phillip, K. Deichmann, in: J.D. Mackenzie, D.R. Ulrich (Eds.), Ultrastructure processing of Advanced Ceramics, Wiley and Sons INC.,, New York, 1988, pp. 651–660.
23. S. Amberg-Schwab, E. Arpac, W. Glaubitt, K. Rose, G. Schottner, U. Schubert, in: P. Vincenzini (Ed.), High Performance Ceramic Films and Coatings, Elsevier, Amsterdam, 1991, pp. 203–208.
24. R.P. Winkler, E. Arpac, H. Schirra, S. Sepeur, I. Wegner, H. Schmidt, Aqueous wet coatings for transparent plastic glazing, Thin Solid Films, 351, 1999, pp. 209-211.

25. G.W. Wagner, S. Sepeur, R. Kasemann, H. Schmidt, Novel Corrosion Resistant Hard Coatings for Metal Surfaces, Key Engineering Materials, 150, 1998, pp. 193–198.
26. R.H. Chung, US Patent 4,486,504, pp. 1984 .
27. M. Pilz, H. Römich, Sol-Gel Derived Coatings for Outdoor Bronze Conservation, Journal of Sol-Gel Science and Technology, 8, 1997, pp. 1071-1075.
28. M.L. Sforça, I.V.P. Yoshida, S.P. Nunes, Organic–inorganic membranes prepared from polyether diamine and epoxy silane, Journal of Membrane Science, 159, 1999, pp. 197-207.
29. S.R. Davis, A.R. Brough, A. Atkinson, Formation of silica/epoxy hybrid network polymers, Journal of Non-Crystalline Solids, 315, 2003, pp. 197-205.
30. R. Zandi-zand, A. Ershad-langroudi, A. Rahimi, Organic–inorganic hybrid coatings for corrosion protection of 1050 aluminum alloy, Journal of Non-Crystalline Solids, 351, 2005, pp. 1307-1311.
31. R. Zandi Zand, K. Verbeken, A. Adriaens, Corrosion resistance performance of cerium doped silica sol–gel coatings on 304L stainless steel, Progress in Organic Coatings, 75, 2012, pp. 463-473.
32. R. Zandi Zand, K. Verbeken, A. Adriaens, The corrosion resistance of 316L stainless steel coated with a silane hybrid nanocomposite coating, Progress in Organic Coatings, 72, 2011, pp. 709-715.
33. A.N. Khramov, V.N. Balbyshev, N.N. Voevodin, M.S. Donley, Nanostructured sol–gel derived conversion coatings based on epoxy- and amino-silanes, Progress in Organic Coatings, 47, 2003, pp. 207-213.
34. S.M. Hosseinalipour, A. Ershad-langroudi, A.N. Hayati, A.M. Nabizade-Haghighi, Characterization of sol–gel coated 316L stainless steel for biomedical applications, Progress in Organic Coatings, 67, 2010, pp. 371-374.

35. G. Carbajal-de La Torre,- M. A. Espinosa-Medina, A. Martinez-Villafane, J. G. Gonzalez-Rodriguez, V. M. Castano, Study of ceramic and hybrid coatings produced by the sol-gel method for corrosion protection, The Open Corrosion Journal 2, 2009, pp. 197-203.
36. G.J. Brug, A.L.G. van den Eeden, M. Sluyters-Rehbach, J.H. Sluyters, The analysis of electrode impedances complicated by the precense of a constant phase element, Journal of Electroanalytical Chemistry, 176 (1984) 275-295.
37. M.L. Zheludkevich, R. Serra, M.F. Montemor, K.A. Yasakau, I.M.M. Salvado, M.G.S. Ferreira, Nanostructured sol–gel coatings doped with cerium nitrate as pre-treatments for AA2024-T3: Corrosion protection performance, Electrochimica Acta, 51, 2005, pp. 208-217.
38. M.F. Montemor, M.G.S. Ferreira, Cerium salt activated nanoparticles as fillers for silane films: evaluation of the corrosion inhibition performance on galvanised steel substrates, Electrochimica Acta, 52, 2007, pp. 6976-6987.
39. M.F. Montemor, R. Pinto, M.G.S. Ferreira, Chemical composition and corrosion protection of silane films modified with CeO_2 nanoparticles, Electrochimica Acta, 54, 2009, pp. 5179-5189.
40. Z.Y. X. Liu, T. Romeo, J. Weber, T. Scheuermann, S. Moulton, G. Wallace, Biofunctionalized anti-corrosive silane coatings for magnesium alloys, Acta Biomaterialia, 9, 2013, pp. 8671-8677.

Effects of cerium ions and bisphenol A on the microstructure and the corrosion protection of silane hybrid coatings on 304L stainless steel [1]

4.1. Introduction

AISI 304 stainless steel as an corrosion resistant alloy is widely used in different industrial fields because of its mechanical and corrosion inhibition properties [1] but is, nevertheless, susceptible to localized corrosion in the presence of chlorides or other aggressive ions [2, 3]. Several strategies are applicable to increase the corrosion resistance of steel. A first one is to alloy the material. On the one hand, one can opt to add small amounts of for example Cu, P, Si or Cr to form a protective layer [4]. Weathering steels, i.e. structural

[1] Reprinted from Progress in Organic Coatings, Volume 75 / Issue 4, Roohangiz Zandi Zand, Kim Verbeken and Annemie Adriaens, Corrosion resistance performance of cerium doped silica sol–gel coatings on 304L stainless steel, 463-473, Copyright (2012), with permission from Elsevier.

high strength alloy steels with improved atmospheric corrosion properties are commonly known as COR-TEN steels, which is their original US brand name. On the other hand, a significant addition of chromium to the steel makes it resist rust, or stain "less" than other types of steel. The chromium in the steel combines with the oxygen in the atmosphere to form a thin, invisible layer of chrome containing oxide, called the passive film. As an alloying element, molybdenum is more effective in increasing the pitting corrosion resistance as is expressed by the so-called PREN value (pitting resistance equivalent number) [5]:

$$PREN=\%\ Cr+3.3\%\ Mo+16\%N \qquad \text{(Eq 4.1)}$$

A second strategy to improve the corrosion resistance is the use of coatings. Metallic coatings are an option as they create a barrier between the base metal and the corrosive environment. Moreover, they might even offer additional resistance by cathodic protection, as is for example realized by galvannealing or galvanizing steel sheet. Non-metallic coatings with the incorporation of corrosion inhibitors are an alternative option. Different inhibitors are possible and chromium (VI) compounds, mainly chromates, are the most common substances used and their efficiency/cost ratio has made them standard corrosion inhibitors. However, the hexavalent chromium species are responsible for several diseases including DNA damage and cancer, which is the main reason for banning chromium (VI) containing anticorrosion coatings in Europe since 2007 [6-9]. For this reason, different initiatives have been launched to develop "green" alternative coatings.

The development of hybrid organic–inorganic sol–gel coatings sintered at low temperatures represents a good alternative for coatings containing chromates [10]. They offer increased toughness and are thicker than conventional chemical conversion coatings [1, 8, 9, 11]. However, the sol–gel coatings may contain pores, cracks and areas of low cross-link densities, through which the corrosion initiators can be diffused to the coating/metal interface.

The corrosion process usually begins in such areas. Normally, the sol–gel coatings cannot stop the development of the corrosion process when the defects appear, due to the lack of self-healing properties [8, 11-13]. Lately attempts have been made to enhance the protective effect of silanes by combining them with other corrosion protection systems such as silica nano-particles or corrosion inhibitors [13-18].

Lanthanides ions, such as Ce^{3+}, Y^{3+}, La^{3+}, Pr^{3+}, Nd^{3+}, seem to fulfill the basic requirements for alternative corrosion inhibitors [19, 20]. These elements form insoluble hydroxides and have a low toxicity since their ingestion or inhalation is not considered harmful to health. In addition, lanthanides are economically competitive products, as some of them in particular cerium are relatively abundant in nature [8, 11, 21].

Cerium doped sol–gel coatings have been actively investigated during the last decades [1, 6, 13, 21-23]. The first work on cerium conversion layers for aluminum alloys was carried out by Hinton et al. [24]. Cerium was later tested for the corrosion protection of aluminum and steel based alloys [25, 26] as well as galvanized steel in aqueous sodium chloride solution [27, 28]. It is claimed that, similarly to the pure sol–gel coatings, the cerium doped ones also can form a dense barrier, which hinders the penetration of electrolyte toward the metallic substrates. The important difference between them is that cerium doped sol–gel coatings can supply self-healing abilities, which can automatically repair the corroded areas, thereby providing a long-term corrosion protection [1, 6, 22]. The modification of hybrid sol–gel coatings by adding cerium was successfully tested for improvement of corrosion protection of aluminum [29, 30], zinc [31, 32] and mild steel substrates [33].

The present work focuses on a detailed study of organic–inorganic hybrid coatings obtained by dip coating 304L stainless steel specimens in an organically modified silica sol made from the hydrolysis and condensation of 3-glycidoxypropyltrimethoxysilane (GPTMS)

as the precursor in acid catalyzed condition. Coatings prepared from epoxy silanes and propyltrimethoxy silane using HCl as a catalyst, show a good corrosion protection but are at the same time very brittle and form cracks by bending. For this reason, Kasemann et.al [34] introduced an organic chain to connect the epoxy group. Diols were chosen for this purpose. The epoxy functions can react to polyethylenoxide chains or can be connected by polyaddition reaction with the aromatic diol (bisphenol A) in the presence of a basic catalyst (1-methylimidazole) (see figure 4.1). In this work, the influence of the addition of cerium ions and bisphenol A (BPA) as a cross-linking agent on the microscopic features, morphology as well as the corrosion resistance of the coatings is examined.

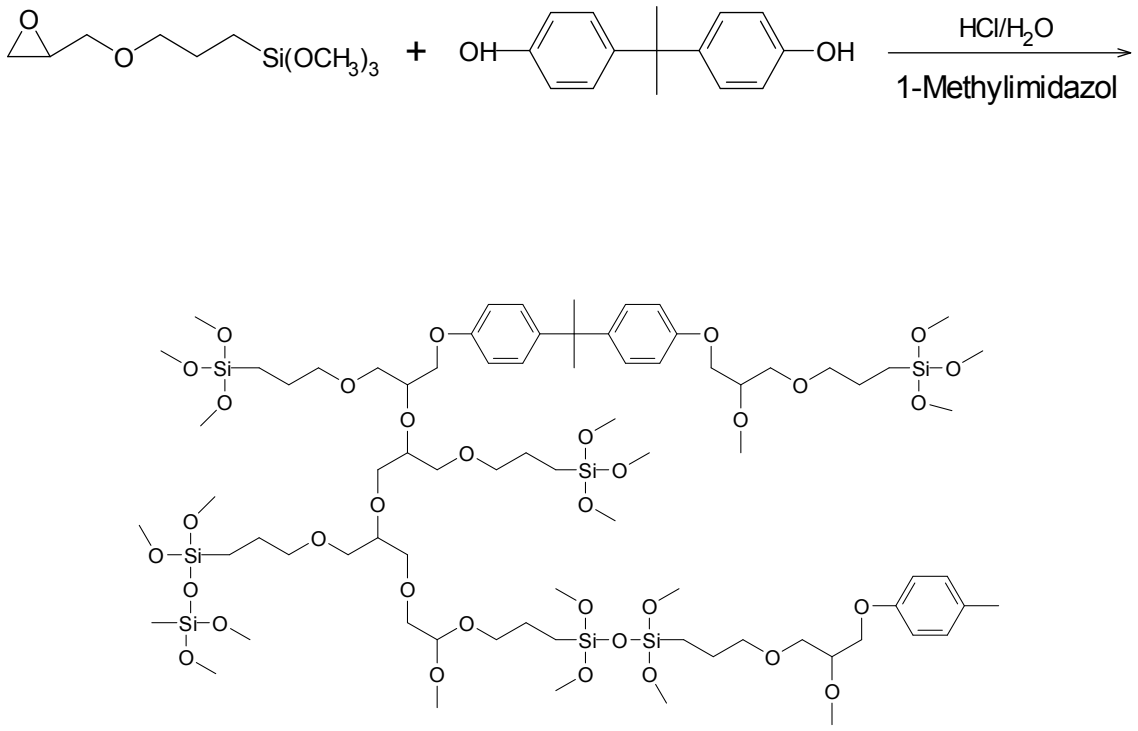

Figure 4.1. Simplified schematic of bonding mechanism between Bisphenol A and the epoxy function of GPTMS [34].

4.2. Sample preparation

The reference sol was prepared by adding stoichiometric amounts of the silane precursor, GPTMS, and the organic crosslinking agent, BPA, into HCl-acidified water (pH 2). The H2O/Si mole ratio was 0.5 and was chosen according to a previous study [35]. The solution was stirred at room temperature for 80 min at a rate of 240 rpm. Then 1-methylimidazol, MI, was added to accelerate the condensation reaction after hydrolysis. The MI/Si mole ratio was 0.01. The solution was again stirred for 10 min at room temperature. The result was a clear and colorless homogenous solution. This sol will be called "silica hybrid coating" (A). In the case of cerium doped coating, cerium nitrate hexahydrate was added to the mixture of GPTMS and acid prior to the addition of BPA and 1-methylimidazol. The Ce/Si mole ratio was 0.2. The solution was stirred at room temperature for 10 min at a rate of 240 rpm. Then BPA was added to the mixture and dissolved by mixing the solution for 80 min. 1-methylimidazol was added to the solution and the sol was again stirred for 10 min. The result was a brown homogenous solution. This type of coating is referred to as "cerium doped silica hybrid coating" (B). In order to study the effect of BPA on the microscopic features, morphology and corrosion performance of the cerium doped silica hybrid coating, another (B) coating was prepared with the identical chemical composition and procedure, excluding BPA (BPA = 0). The result was a colorless homogenous solution. This coating is referred to as "non BPA cerium doped silica hybrid coating" (C).

The substrate material used for the present investigation is a 304L stainless steel alloy. Its chemical composition, analysed by spectro–analysis method, is given in table 4.1. Sheets (7 cm × 15 cm × 0.1 cm) were used for the salt spray tests, while coupons (1.13 cm^2 area and 0.1 cm thickness) were used for all other experiments. The substrates were successively abraded with 600 and 1200 grits emery paper and degreased with acetone in an ultrasonic bath for 10 min. Chemical etching was performed by dipping the samples into the 1 molar NaOH

solution for 5 min at 50 ◦C. After rinsing in tap water and then in deionized water, the 304L samples were air-dried. The cleaned substrates were dipped for 1 min in different silane solutions. The coated samples were dried at room temperature for 24 h, which was followed by 25–130°C curing process with a heating rate of 7.5 °C/min for 90 minutes to initiate extensive cross-linking in the hybrid films [10]. The coating thickness was measured by eddy-current method (Check line 3000 pro, Germany).

Table 4.1. Chemical composition of 304L stainless steel (in mass%).

C	Si	Mn	P	S	Al	Cr	Mo	Ni	Cu	Fe
0.017	0.41	1.75	0.032	0.0050	0.0049	17.65	0.25	8.59	0.45	Balance

4.3. Results and discussion

Magnified FTIR spectra of the silane hybrid coating (SHC, sample A) and the cerium-doped silane hybrid coating (Ce-SHC, sample B) in the regions 500 to 1300 cm^{-1} (Figure 4.2a) and 2800 to 4000 cm^{-1} (Figure 4.2b) show main features that include bands corresponding to Si–O–Si sequences, OH groups, and $–CH_2$ groups.

- The strong peaks between 1000 and 1200 cm^{-1} are associated with the Si–O–Si/C–O–C asymmetric bond stretching vibration [13], which is the structural backbone of the hybrid material [13]. The high-frequency band near 1020 cm^{-1} is assignable to the antisymmetric stretching of oxygen atoms. The bands at intermediate frequencies around 750–800 cm^{-1} are attributable to the symmetric stretching of the oxygen atoms.
- The $–CH_2$ group incorporated into the silica group is indicated by the two weak absorption peaks at about 2930 cm^{-1} and 2950 cm^{-1}, which can be assigned to symmetric and

asymmetric stretching of the $–CH_2$ bonds present on the silicon moiety [36]. The presence of this hydrocarbon unit reveals a certain degree of planarization of the coating macromolecular chains. The intensities of the 1087 cm^{-1} band and the 780 and 2950 cm^{-1} shoulders increase in the Ce-doped sample (B), demonstrating that the incorporation of cerium nitrate leads to improved condensation.

- The broad band centered near 3400 cm^{-1} is assigned to residual Si–OH stretching vibrations and hydrogen-bonded water [14], which possibly formed during the hydrolysis of the alkoxy groups of GPTMS.

The effects of bisphenol A, an aromatic diol, on the cross-linking of organo-silica networks via the chemical coupling of the aromatic diol and epoxy-functionalities were also studied by FTIR spectroscopy. Cerium-doped silica hybrid coatings with and without BPA (Ce-SHC, BPA=0) (B and C) were analyzed. The magnified spectral regions of interest are 500 to 1300 cm^{-1} (Figure 4.3a) and 2800 to 4000 cm^{-1} (Figure 4.3b). The bands due to asymmetric epoxide ring deformation at 758 and 902 cm^{-1} in sample C, are of similar intensity, which allows monitoring of the coupling reaction between the epoxy functionalities of the organo-silica networks and the diol cross-linkers. These bands almost disappear in the FTIR spectra of sample B, indicating the chemical bonding of organo-silica networks in a cross-linked network [15]. The bands due to Si–O–Si in sample C (centered at 1100 cm^{-1}) become more intense and broader relative to those in sample B. This is attributable to the direct connection of epoxy silanes and propyl trimethoxy silane in sample C, which resulted in the formation of a very brittle film.

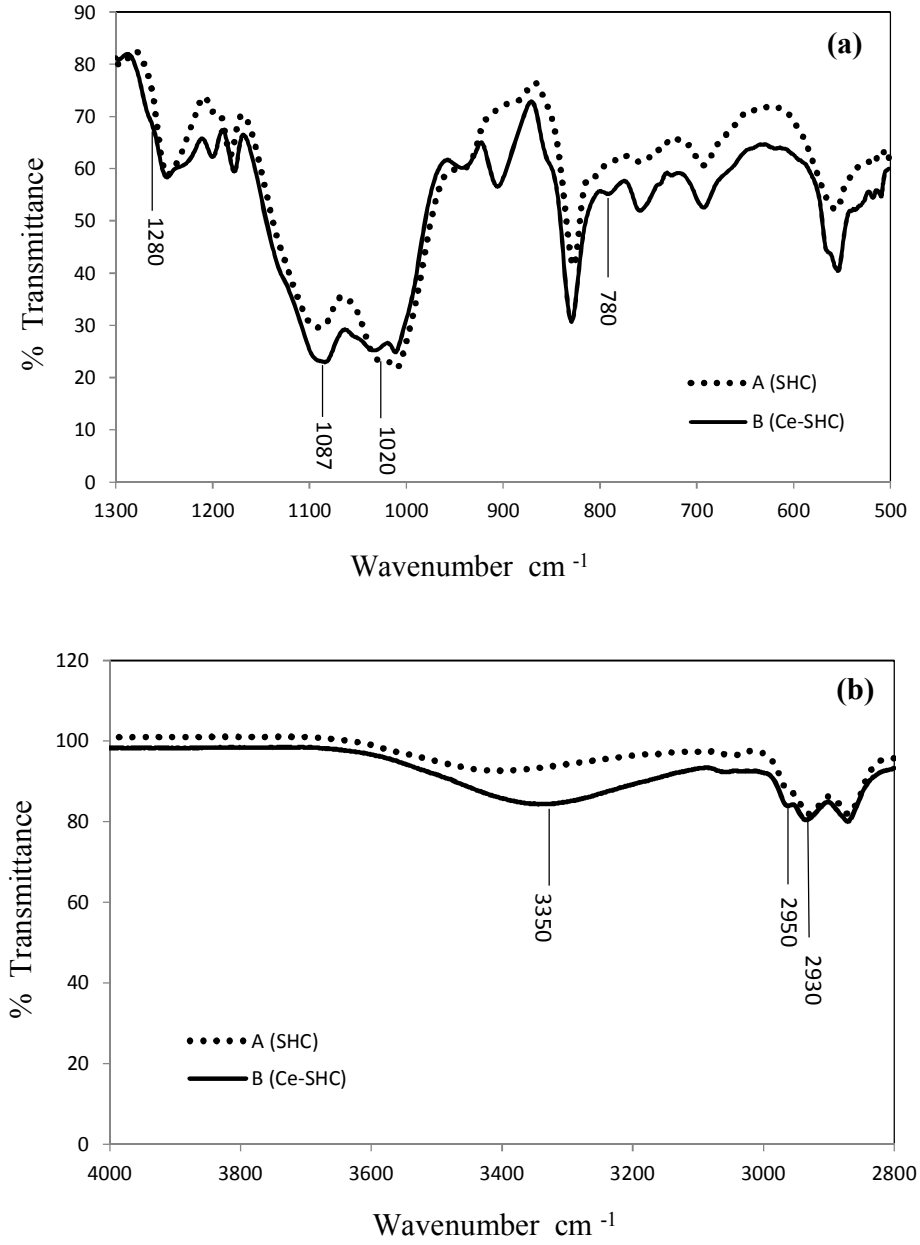

Figure 4.2. FTIR spectra of 304L SS substrates pre-treated with silane hybrid (A) and cerium nitrate-doped silane hybrid (B) coatings: (a) magnified region from 500 to 1300 cm^{-1} and (b) magnified region from 2800 to 4000 cm^{-1}.

A standard corrosion resistance evaluation using salt spray was used to assess the three sol–gel film coatings. Photographs after 2000 hours of salt spray exposure (figure 4.4) illustrate that the silane hybrid coating (A) (average thickness 19 ± 7 μm) and the cerium-doped silane hybrid coating (B) (average thickness 58 ± 12 μm) did not show any signs of

blistering, delamination, or corrosion. The samples retained their original shiny surfaces. However, the Ce-doped silica hybrid coating without BPA (C) (average thickness 57 ± 4 μm) showed limited resistance to the salt spray; it exhibited blistering and delamination after exposure for 148 hours. The first signs of corrosion appeared after exposure for 1600 hours.

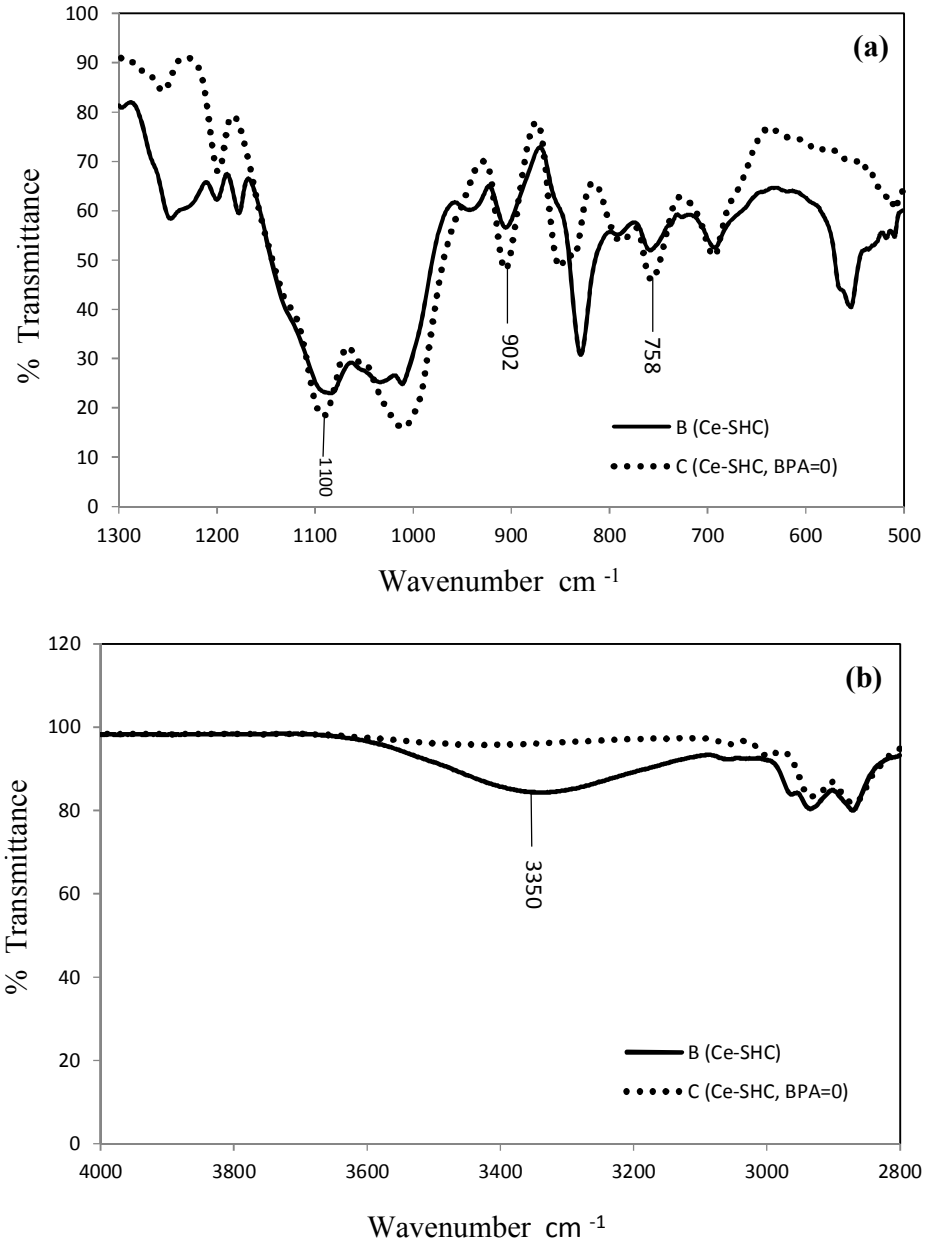

Figure 4.3. FTIR spectra of the 304L stainless steel substrate coated with Ce-doped silica hybrid coating (sample B) and non BPA Ce-doped silica hybrid coating (sample C): (a) magnified region from 500 to 1300 cm−1 and (b) magnified region from 2800 to 4000 cm−1.

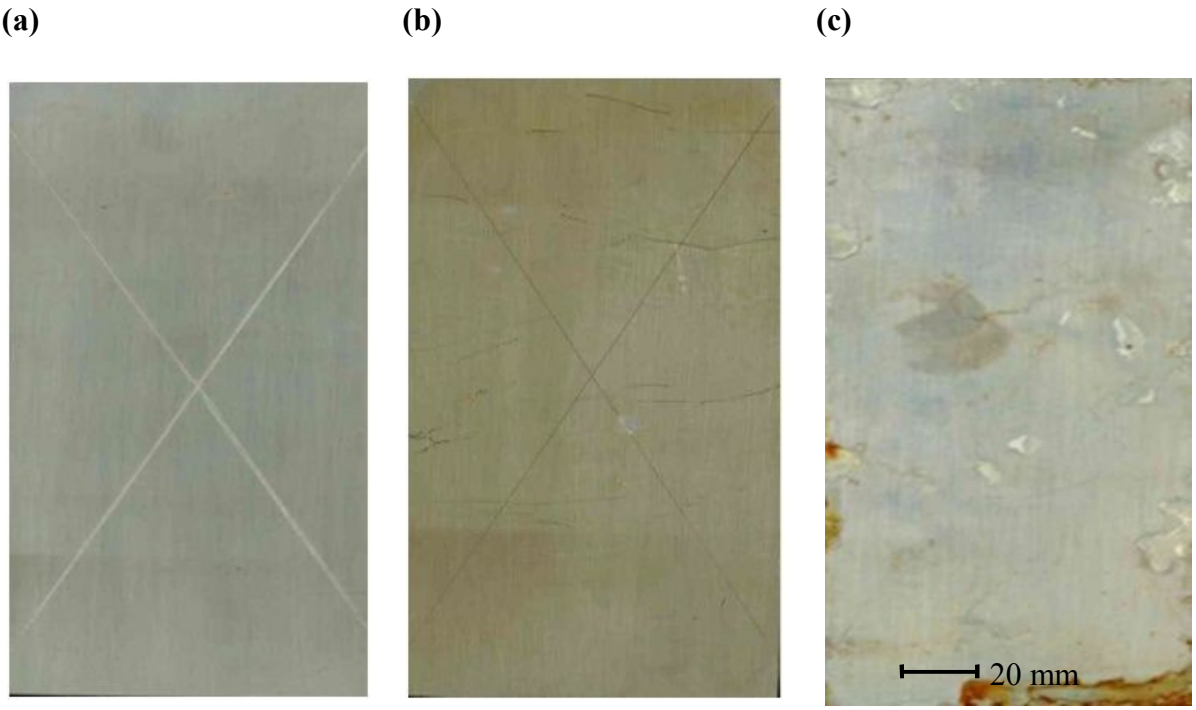

Figure 4.4. Photographs of (a) silica hybrid coated, (b) Ce-doped silica hybrid coated and (c) non BPA Ce-doped silica hybrid coated stainless steel samples after 2000 h of exposure in the salt spray chamber.

Potentiodynamic polarization measurements were carried out to estimate the effects of cerium and BPA on the corrosion resistance of the silane hybrid coatings. Potentiodynamic polarization curves (figure 4.5) were recorded after the bare and pre-treated 304L SS substrates with the three coatings (A–C) were immersed for 3 hours in a neutral 3.5 % NaCl solution. Table 4.2 lists the electrochemical parameters derived from these curves.

The limiting current density for oxygen reduction and the anodic current density for all the coated specimens were lower than those for the uncoated 304L SS. This suggests that the corrosion protection was due to both the blockage of the surface with the reduction of oxygen and metal dissolution in the pores of the coating layers. Sample (A) showed a decreased corrosion current density, i_{corr}, of around 2.30×10^{-8} A cm^{-2}. Its corrosion potential (−0.414 V)

is more positive than that of the bare sample. Nevertheless, Figure 4.5 shows a very limited passive region of approximately −0.269 V to −0.030 V over its corrosion potential.

Table 4.2. Electrochemical parameters obtained from the polarization measured in a 3.5 % NaCl solution.

Sample	E_{corr} (V)	i_{corr} (A cm^{-2})	b_c (V/dec)	b_a (V/dec)	Passive area (V)
Bare 304L SS	-0.690	3.97×10^{-6}	0.331	0.243	-0.326 to -0.086
A: SHC	-0.414	2.30×10^{-8}	0.264	0.103	-0.269 to -0.030
B: Ce-SHC	-0.389	4.48×10^{-8}	0.297	0.100	-0.233 to 0.308
C: Ce-SHC(BPA=0)	-0.427	5.10×10^{-7}	0.315	0.101	-0.312 to 0.181

The addition of cerium ions in coating B led to further reductions of corrosion current density and corrosion potential. A distinct passive region emerges that extends over a several hundred mV range of 0.233 V to +0.308 V over the E_{corr}.

The poor performance of the coating C that lacked BPA may have been due to the permeability of the coating, which occurred due to cracks or porosity. This permeability allowed the aggressive electrolyte to reach the metal surface and initiate corrosion, indicating that the omission of a cross-linker can significantly affect the corrosion resistance of cerium-doped silane hybrid coatings.

SEM images of the bare and coated 304L SS samples recorded after potentiodynamic polarization testing in a neutral 3.5 % NaCl solution (Figure 4.6) each show localized corrosion. Exfoliation of the corrosion products, cracks (Figure 4.6a–c), and pits (Figure 4.6d) of different sizes are visible. The damage around some of the cracks and pits (Figure 4.6a–d) indicates preferential localized attack, which occurred after the applied potential exceeded the breakdown potential.

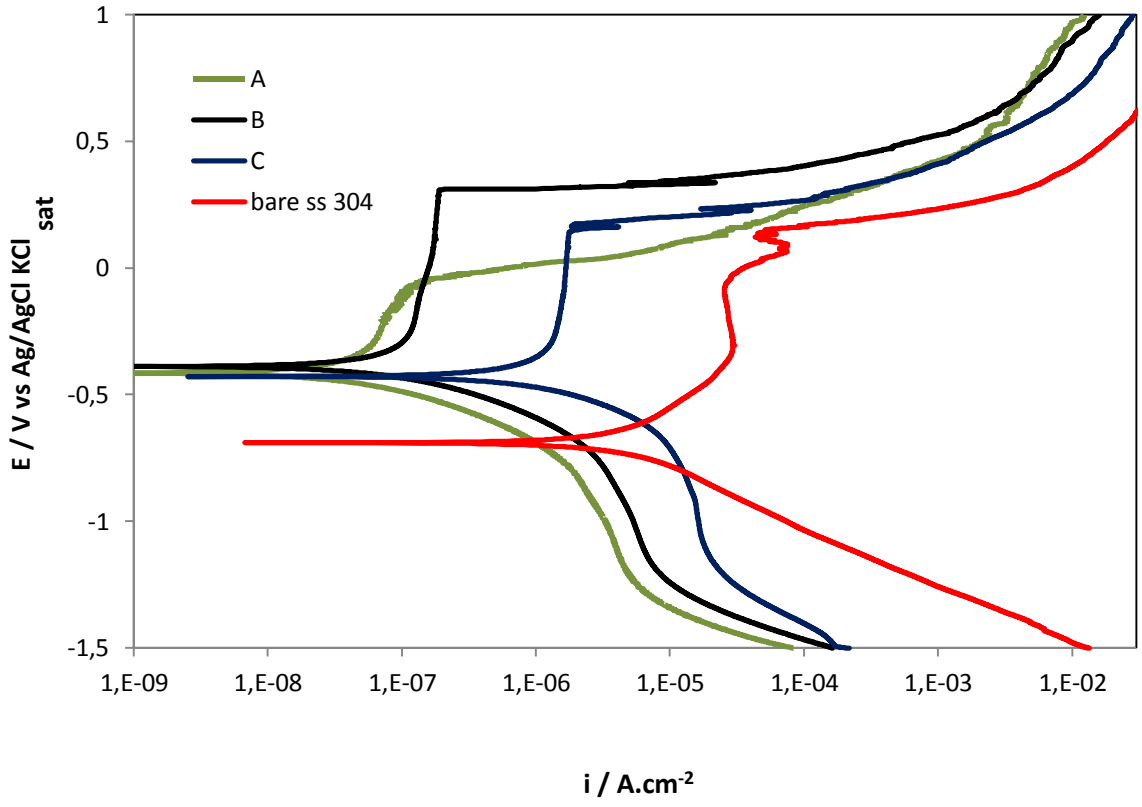

Figure 4.5. Potentiodynamic polarization curves of the (A)–(C) coated and bare 304L stainless steel in a 3.5% NaCl solution.

This localized attack promoted the hybrid film to deteriorate and delaminate, possibly due to hydrolysis reactions at the interface. The diffusion of oxidant ions and the corrosion rate both increased, causing an accumulation of corrosion products at the interface, which promoted the formation of the defects and micro-cracks that are shown in Figure 5a–c. Samples A and B showed improved corrosion resistance, as suggested by the E_{corr} and i_{corr} values (Table 4.2).

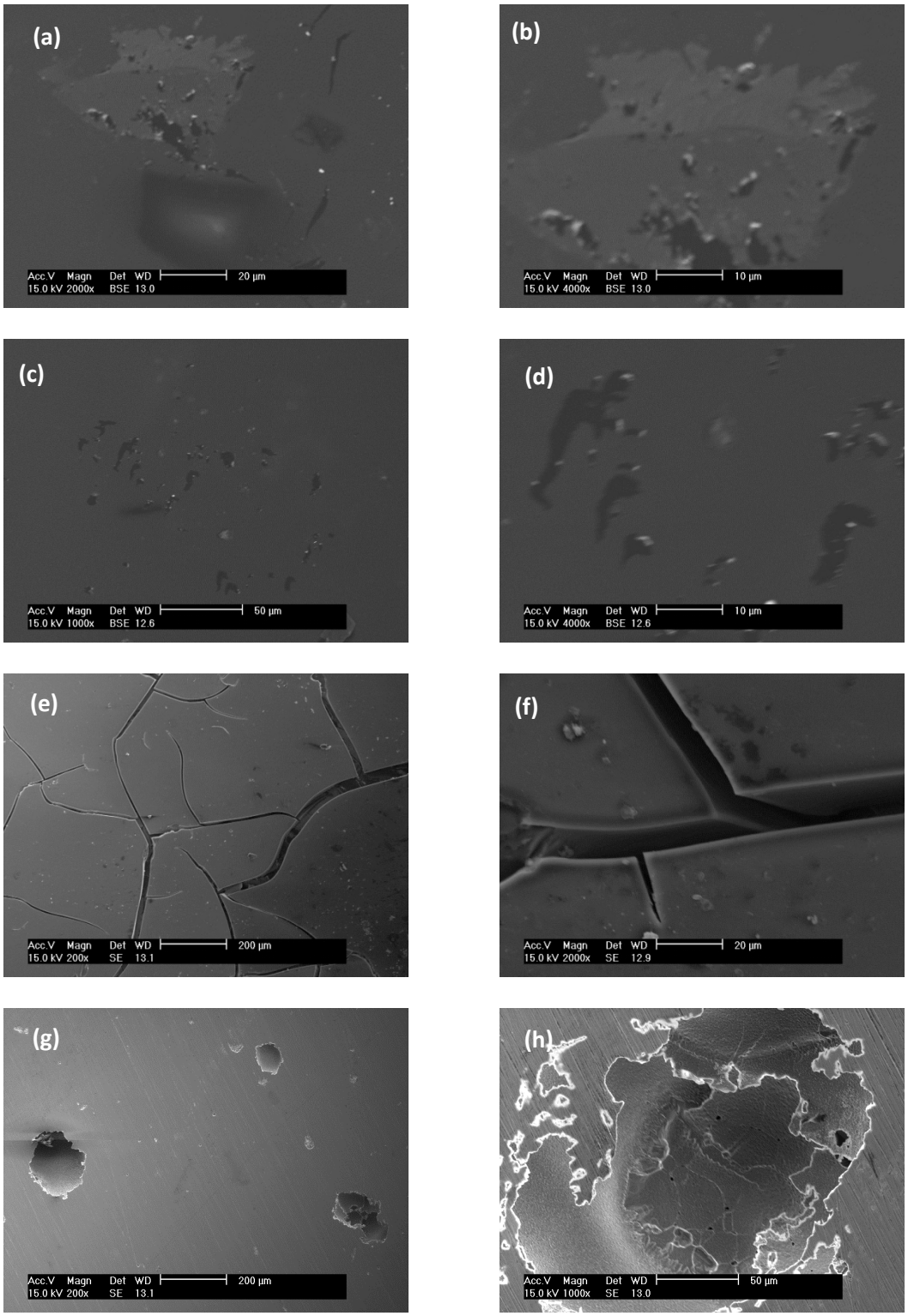

Figure 4.6. Scanning electron micrographs of the bare and coated 304L stainless steel samples after potentiodynamic polarization in a neutral 3.5% NaCl solution with different magnifications: (a and b) sample A, (c and d) sample B, (e and f) sample C and (g and h) bare 304L stainless steel.

Impedance spectra were recorded for the bare and coated 304L SS substrates after immersion for 3 hours in a 3.5 % NaCl solution (Figure 4.7). The uncoated sample showed an EIS spectrum characterized by two time constants. The time constant at higher frequencies develops around 47.86 rad s^{-1} was assigned to the presence of an oxide/hydroxide film on the substrate, and that at lower frequencies develops around 0.059 rad s^{-1} was due to corrosion activity. The total impedance of the substrate was below 5.86×10^5 Ω cm^2. Significant amounts of corrosion products were observed.

Samples A and B also showed two time constants: one at higher frequencies (around 10^4 rad s^{-1}), attributed to the presence of the silane layer, and a lower frequency constant (0.034 rad s^{-1}) due to the metal oxide layer over the metal surface. The Bode phase angle plot for sample C shows a different time constant at middling frequencies (around 26.85 rad s^{-1}) that can be attributed to cracking and corrosion activity at the surface of the substrate. This likely resulted from the absence of the cross-linker (BPA) causing brittleness in the film, which led to micro cracks and delamination of the film.

Both the silane hybrid coating (A) and the cerium-doped silane hybrid coating (B) showed low-frequency system impedances that were about one order of magnitude greater than those shown by the bare sample and sample C (Figure 4.7b). This was probably due to the coating blocking the aggressive electrolyte from reaching the reactive metal surface. The lower impedance shown by sample C was due to the creation of defects and cracks in the coating, which allowed the diffusion of the aggressive electrolyte to the substrate.

EIS of samples A and B evaluated their barrier properties and inhibition mechanisms. Phase angle plots and bode modulus and for samples A (Figure 4.8) and B (Figure 4.9) were recorded at intervals while the samples were immersed in a 3.5 % NaCl solution for 22 days.

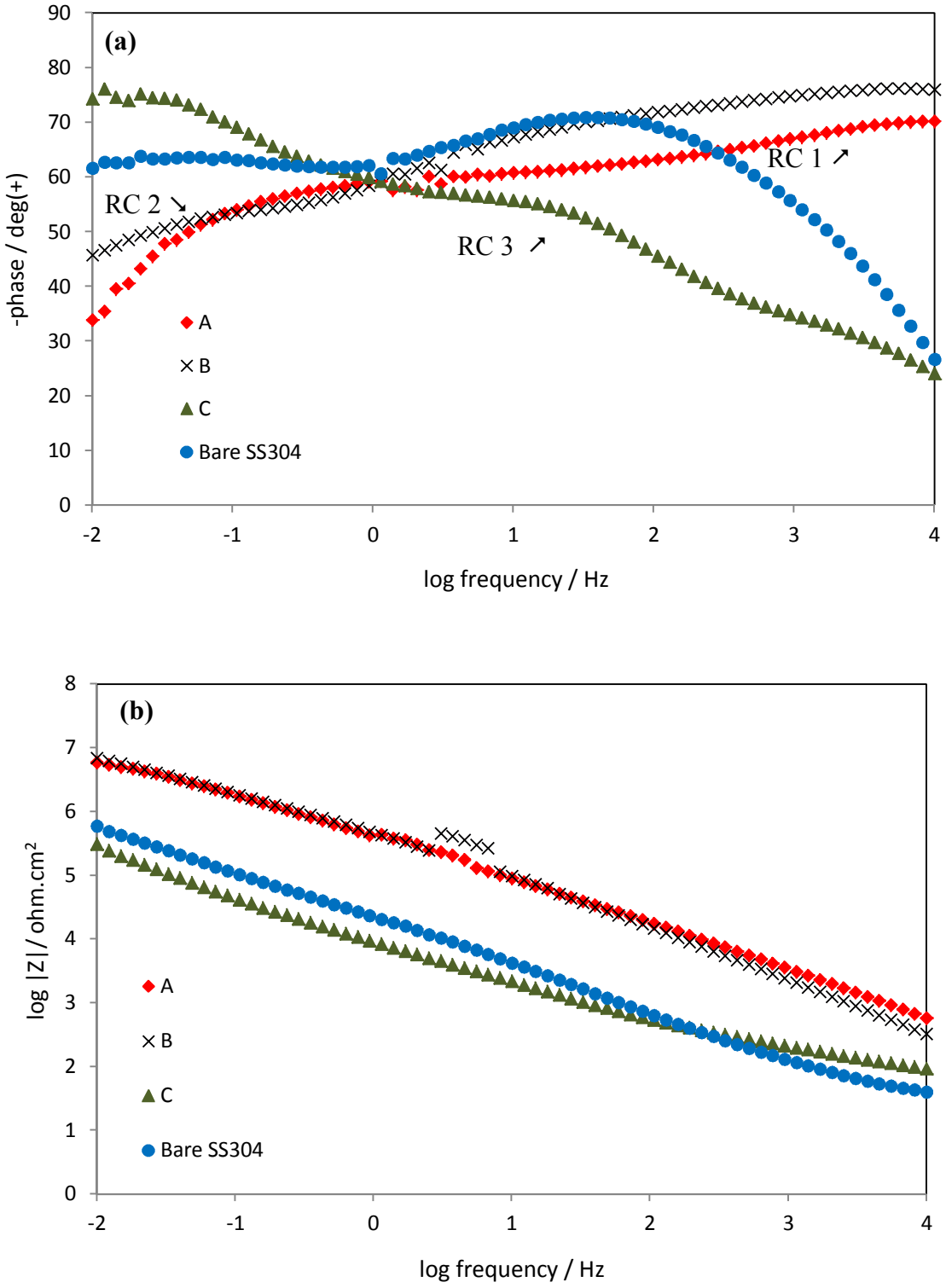

Figure 4.7. EIS Bode plots (a) φ vs log freq and (b) log |Z| vs log freq for bare and (A)–(C) coated 304L stainless steel substrates after 3 h of immersion in a 3.5% NaCl solution.

Impedance measurements of the non-inhibited system (A) display a slight evolution of the barrier properties associated with the hybrid coating. This behavior is related to water uptake, which occurred during the first days of immersion in the electrolyte. After 22 days, the non-inhibited system displayed lower barrier effects.

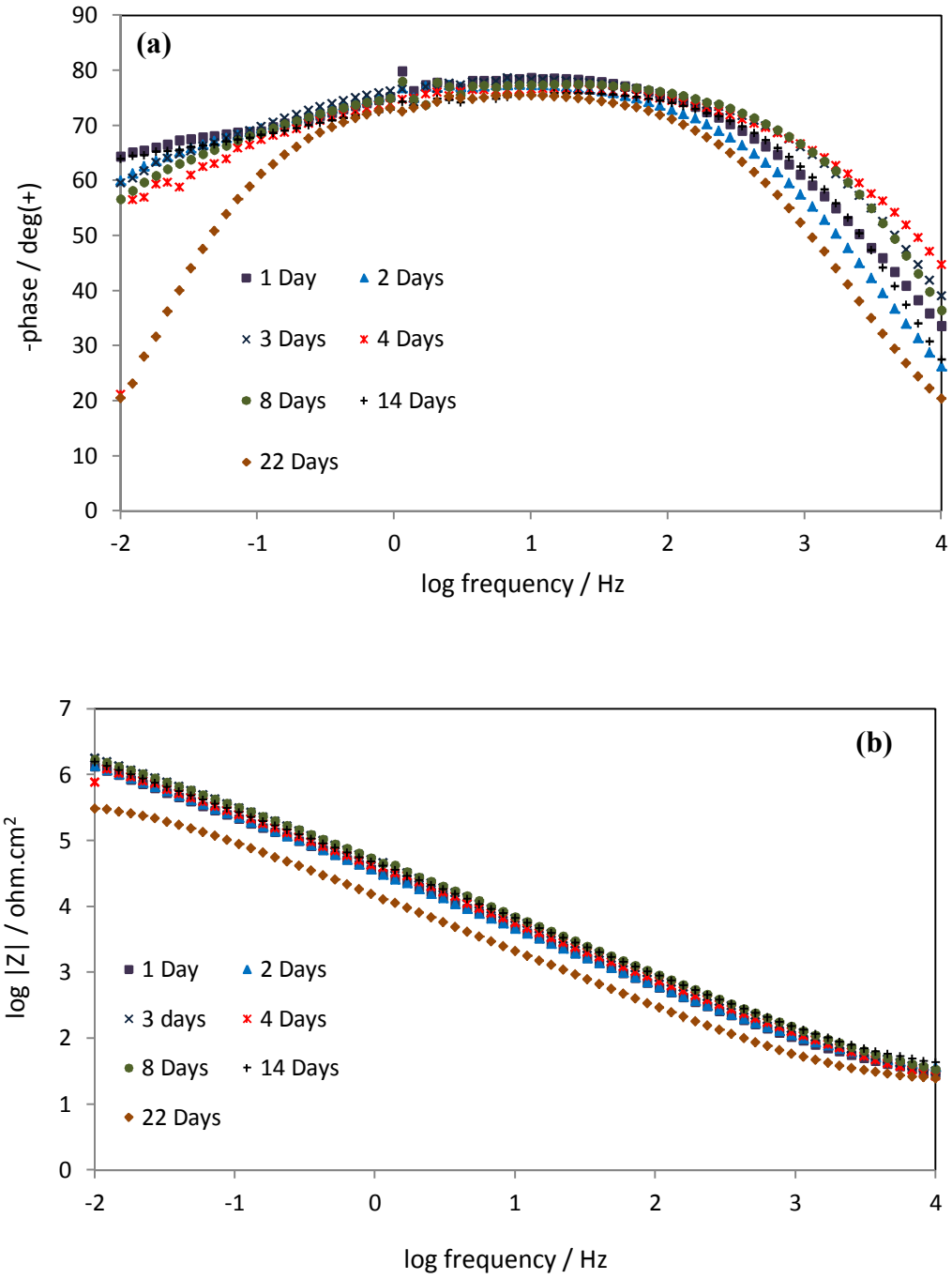

Figure 4.8. EIS Bode plots (a) φ vs log freq and (b) log |Z| vs log freq for silica hybrid coated (sample A) 304L stainless steel substrates at different immersion times in a 3.5% NaCl solution.

The system containing cerium species (B) offered better protection than the non-inhibited (A) system and its barrier properties remained constant for longer. The inhibited system showed slower electrochemical evolution than the non-inhibited one because the inhibiting effect of cerium ions slowed the corrosion kinetics.

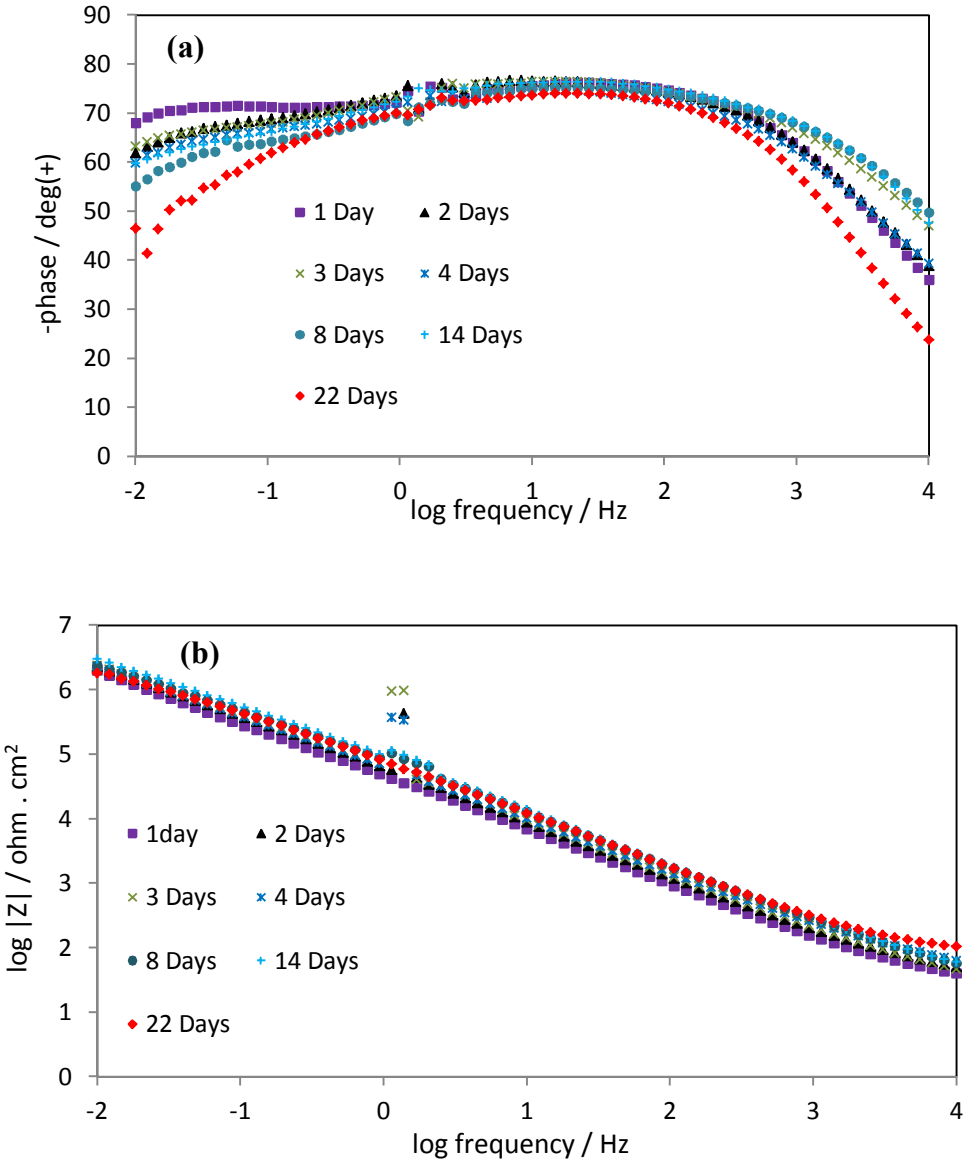

Figure 4.9. EIS Bode plots (a) φ vs log freq and (b) log |Z| vs log freq for Ce doped silica hybrid coated (sample B) 304L stainless steel substrates at different immersion times in a 3.5% NaCl solution.

The corrosion features of the samples were further explored through analysis of the EIS spectra analysis using equivalent electric circuits. To simulate the impedance plots, the constant phase element (CPE) was used instead of an "ideal" capacitor to explain the deviations from the −1 slope in the Bode modulus plot.

The impedance response of sample A after immersion for 22 days suggests non-ideal dielectric capacitive behavior, which includes the electrolyte resistance (R_s), polarization resistance (R_{po}) of the corroded areas, and the non-ideal capacitance of the coating (CPE_c) (Figure 4.10a). The equivalent circuit shown in Figure 4.11a, models sample B after similar immersion. It consists of similar elements: R_s, CPE_c, and R_{po}, related to porosity or defects to the passage of the electrolyte. The extra parameters included in the circuits (CPE_{Ox} and R_{Ox}) represent the presence of a metal oxide layer between the metal surface and the electrolyte, which led corrosion products to the pores. CPE_{Ox} is related to the non-ideal capacitance of the metal oxide layer and R_{Ox} is related to the resistance of the metal oxide layer. Table 4.3 lists the fitting parameters for the models presented in Figure 4.10a and 4.11a. The lower polarization resistance shown by the system containing sample A is associated with water uptake through the pores and/or defects in the coating. It is likely linked to an increase of exposed area.

The electrochemical parameters derived from the polarization curves, together with the EIS results, reveal the persistent protection offered by the cerium-doped silane hybrid coatings. Increased immersion would likely lead to the release of cerium from the defects in the coatings. The cerium would then produce insoluble hydroxides when it reacts with hydroxyl groups from cathodic reactions [16, 37]. These hydroxides, together with the corrosion products, decrease the cathodic current and, therefore, reduce the overall corrosion rate [16].

(a)

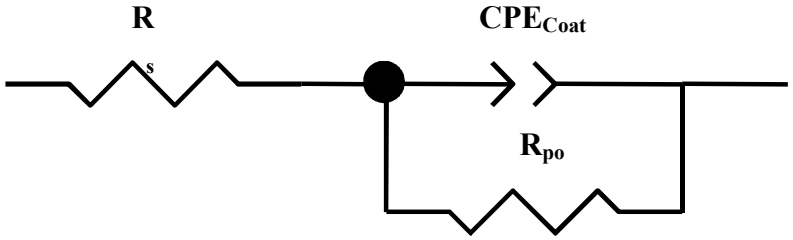

(b)

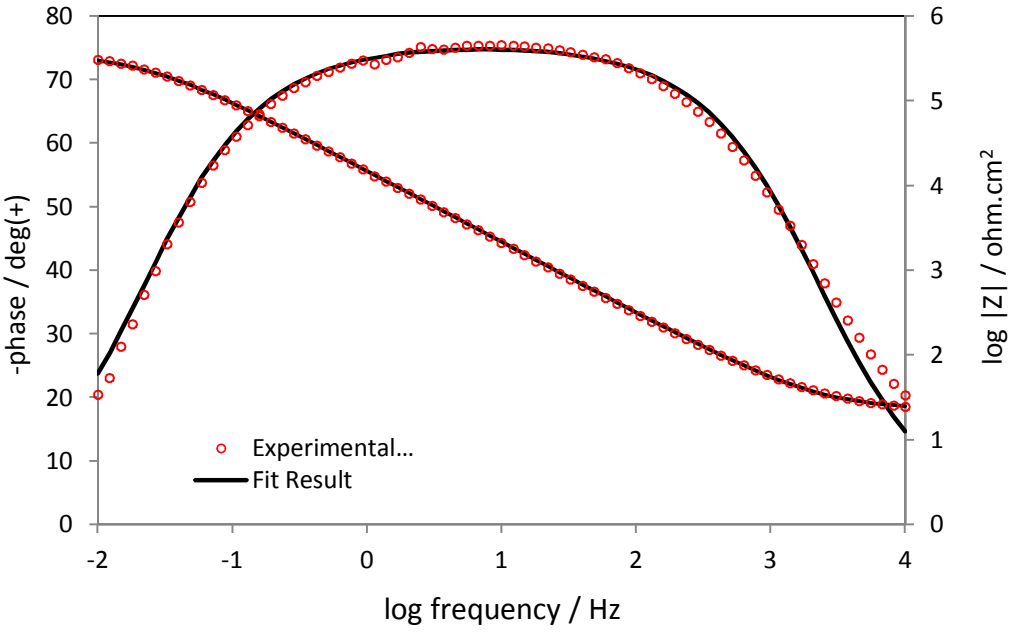

Figure 4.10. (a) Equivalent circuit used for modeling and (b) bode plots with respective fittings for 304L stainless steel substrate protected with the silica hybrid coating (sample A) after 22 days immersion in 3.5% NaCl solution.

(a)

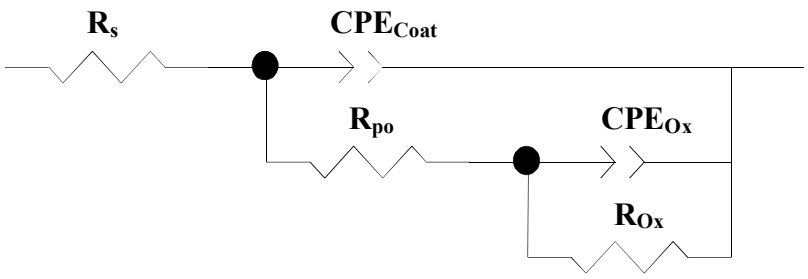

(b)

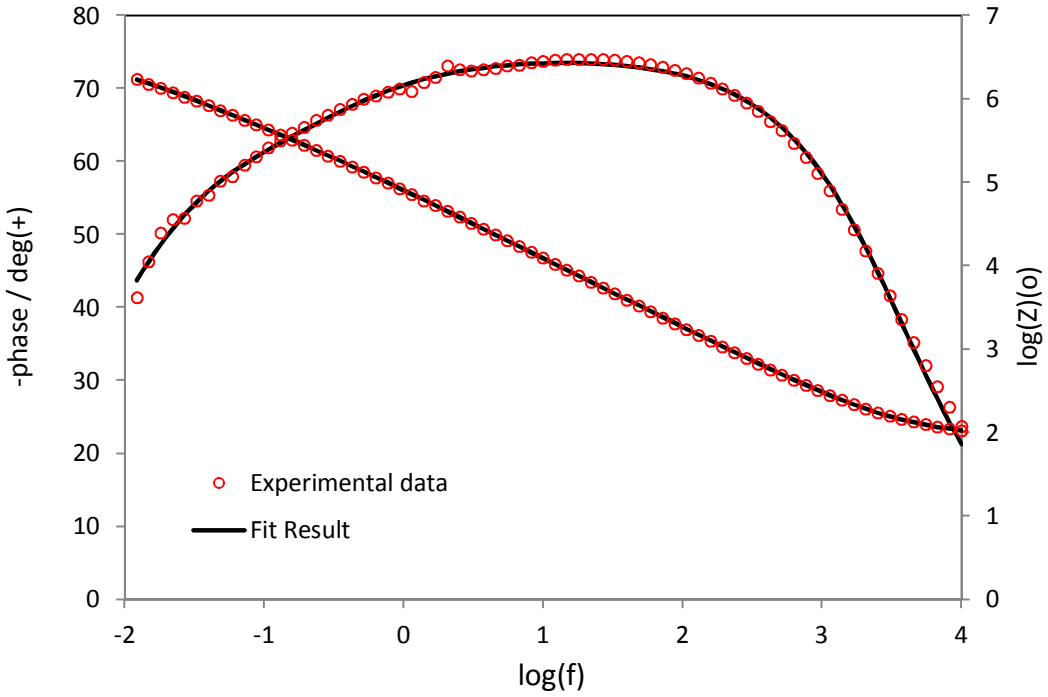

Figure 4.11. (a) Equivalent circuit used for modeling and (b) bode plots with respective fittings for 304L stainless steel substrate protected with the Ce doped silica hybrid coating (sample B) after 22 days immersion in 3.5% NaCl solution.

Table 4.3. Parameters obtained from fitting data for 304L SS with silica hybrid (A) and Ce-doped silica hybrid (B) coatings after immersion for 22 days in a 3.5 % NaCl solution.

Sample	R_s (Ω cm^2)	*C_{Coat} (F.cm^{-2})	n_c	R_{po} (Ω cm^2)	C_{Ox} (F.cm^{-2})	n_{Ox}	R_{Ox} (Ω cm^2)	Goodness
A: SHC	22.59 $\pm 5\times10^{-1}$	1.96×10^{-5} $\pm 7.8\times10^{-8}$	0.839 $\pm 1\times10^{-3}$	3.67×10^{5} $\pm 5\times10^{3}$	-	-	-	2.06×10^{-3}
B: Ce-SHC	22.59 $\pm 5\times10^{-1}$	3.25×10^{-6} $\pm 1.5\times10^{-8}$	0.828 $\pm 8\times10^{-4}$	9.45×10^{5} $\pm 7.8\times10^{4}$	3.09×10^{-6} $\pm 1.68\times10^{-7}$	0.70 $\pm 4.8\times10^{-2}$	2.8×10^{6} $\pm 2.4\times10^{5}$	4.30×10^{-4}

* Equivalent capacitance calculated based on Brug et al. equation: $C_{eff} = [QR_e^{(1-\alpha)}]^{1/\alpha}$, Where Q represents the differential capacity of the interface, α is the exponent of the CPE and R_e is the Ohmic resistance [38].

4.4. Conclusions

Silica based hybrid organic–inorganic coatings with the incorporation of cerium ions were synthesized via a sol–gel method to protect 304L stainless steel substrate against corrosion. Three types of samples were produced by means of dip coating technique: a non-inhibited silica hybrid coating, an inhibited silica coating containing cerium and an inhibited silica coating containing cerium but without cross-linking agent (BPA). The latter one was used to study the effect of the cross-linking on the morphology and the corrosion protection properties of prepared samples. Results of FTIR and SEM analyses confirm the formation of crack-free silica hybrid coatings with Si–O–Si structural backbone and CH_2 group incorporated into silica network which results in the formation of a transparent and homogenous film. Cracks are observed in the linear cross-linked cerium doped silica hybrid coating due to lack of cross-linking agent, which causes the formation of very brittle and crack full coating with poor corrosion resistance.

The corrosion protection performance of the films was evaluated by natural salt spray, potentiodynamic polarization and EIS techniques. The results show that the presence of the cerium ion has significantly improved the corrosion protection properties of the silica hybrid coatings. This effect is due to both increases in the barrier properties as well as the corrosion inhibition ability. Thus cerium doped silica hybrid coatings protect the 304L stainless steel surface effectively and can be used as a pre-treatment for corrosion protection.

References

1. A. Pepe, M. Aparicio, A. Durán, S. Ceré, Cerium hybrid silica coatings on stainless steel AISI 304 substrate, Journal of Sol-Gel Science and Technology, 39, 2006, pp. 131-138.
2. H. P. Leckie, H. H. Uhlig, Environmental factors affecting the critical potential for pitting in 18–8 stainless steel, Journal of The Electrochemical Society, 113, 1966, pp. 1262-1267.
3. N.J. Laycock, R.C. Newman, Localised dissolution kinetics, salt films and pitting potentials, Corrosion Science, 39, 1997, pp. 1771-1790.
4. S. Vervynckt, K. Verbeken, B. Lopez, J.J. Jonas, Modern HSLA steels and role of non-recrystallisation temperature, International Materials Reviews, 57, 2012, pp. 187-207.
5. The Salt Spray Test and Its Use in Ranking Stainless Steels, International Stainless Steel Forum,, May 2008.
6. X. Zhong, Q. Li, J. Hu, X. Yang, F. Luo, Y. Dai, Effect of cerium concentration on microstructure, morphology and corrosion resistance of cerium–silica hybrid coatings on magnesium alloy AZ91D, Progress in Organic Coatings, 69, 2010, pp. 52-56.
7. D. Shchukin, H. Möhwald, M. Ferreira, S. Guerreiro, M. Zheludkevich, Corrosion inhibiting pigment comprising nanorres, Patent WO2007/104457 A1, 2007.

8. N.C. Rosero-Navarro, L. Paussa, F. Andreatta, Y. Castro, A. Durán, M. Aparicio, L. Fedrizzi, Optimization of hybrid sol–gel coatings by combination of layers with complementary properties for corrosion protection of AA2024, Progress in Organic Coatings, 69, 2010, pp. 167-174.
9. B.P. Mosher, C. Wu, T. Sun, T. Zeng, Particle-reinforced water-based organic–inorganic nanocomposite coatings for tailored applications, Journal of Non-Crystalline Solids, 352, 2006, pp. 3295-3301.
10. R. Zandi Zand, K. Verbeken, A. Adriaens, The corrosion resistance of 316L stainless steel coated with a silane hybrid nanocomposite coating, Progress in Organic Coatings, 72, 2011, pp. 709-715.
11. N.P. Tavandashti, S. Sanjabi, Corrosion study of hybrid sol–gel coatings containing boehmite nanoparticles loaded with cerium nitrate corrosion inhibitor, Progress in Organic Coatings, 69, 2010, pp. 384-391.
12. T.L. Metroke, R.L. Parkhill, E.T. Knobbe, Passivation of metal alloys using sol–gel-derived materials — a review, Progress in Organic Coatings, 41, 2001, pp. 233-238.
13. A. Phanasgaonkar, V.S. Raja, Influence of curing temperature, silica nanoparticles- and cerium on surface morphology and corrosion behaviour of hybrid silane coatings on mild steel, Surface and Coatings Technology, 203, 2009, pp. 2260-2271.
14. M. Quinet, B. Neveu, V. Moutarlier, P. Audebert, L. Ricq, Corrosion protection of sol–gel coatings doped with an organic corrosion inhibitor: Chloranil, Progress in Organic Coatings, 58, 2007, pp. 46-53.
15. V. Palanivel, D. Zhu, W.J. van Ooij, Nanoparticle-filled silane films as chromate replacements for aluminum alloys, Progress in Organic Coatings, 47, 2003, pp. 384-392.

16. L.S. Kasten, J.T. Grant, N. Grebasch, N. Voevodin, F.E. Arnold, M.S. Donley, An XPS study of cerium dopants in sol–gel coatings for aluminum 2024-T3, Surface and Coatings Technology, 140, 2001, pp. 11-15.
17. M.F. Montemor, A.M. Cabral, M.L. Zheludkevich, M.G.S. Ferreira, The corrosion resistance of hot dip galvanized steel pretreated with bis-functional silanes modified with microsilica, Surface and Coatings Technology, 200, 2006, pp. 2875-2885.
18. H. Schmidt, G. Jonschker, S. Goedicke, M. Mennig, The sol-gel process as a basic technology for nanoparticle-dispersed inorganic-organic composites, Journal of Sol-Gel Science and Technology, 19, 2000, pp. 39-51.
19. M.G. A. Caglieri, O. Acampa, R. Antreoli, M.V. Vettori, M. Corradi, P. Apostoli, A. Mutti, The effect of inhaled chromium on different exhaled breath condensate biomarkers among chrome-plating workers, Environmental Health Perspectives, 11, 2006, pp. 542-546.
20. P.T. Anatas, T.C. Williamson, Green chemistry: An overview, In Green Chemistry: Designing Chemistry for the Environment, P.T. Anatas, T.C. Williamson (Eds.), American Chemical Society Symposium Series, 626, American Chemical Society, Washington DC, 1996, pp. 1-17.
21. A. Nazeri, P.P. Trzaskoma-Paulette, D. Bauer, Synthesis and properties of cerium and titanium oxide thin coatings for corrosion protection of 304 stainless steel, Journal of Sol-Gel Science and Technology, 10, 1997, pp. 317-331.
22. A. Pepe, M. Aparicio, S. Ceré, A. Durán, Preparation and characterization of cerium doped silica sol–gel coatings on glass and aluminum substrates, Journal of Non-Crystalline Solids, 348, 2004, pp. 162-171.

23. M. Garcia-Heras, A. Jimenez-Morales, B. Casal, J.C. Galvan, S. Radzki, M.A. Villegas, Preparation and electrochemical study of cerium–silica sol–gel thin films, Journal of Alloys and Compounds, 380, 2004, pp. 219-224.
24. L. Wilson, B.R.W. Hinton, A method of forming a corrosion resistant coating, Patent WO 88/06639, 1988.
25. B. Hinton, New approaches to corrosion inhibition with rare earth metal salts, Corrosion 89, paper 170, NACE International, New Orleans, 17-21 April, 1989.
26. B. Hinton, K. Shankar, P. T. M. Salagaras, L. Wilson, G. Devereaux, Control of corrosion on aluminum alloys with corrosion prevention compounds, Paper 135, Vol. 3, Proceedings of the 13th International Corrosion Congress, Melbourne, Australia, 25-29 November, 1996.
27. W. Trabelsi, P. Cecilio, M.G .S. Ferreira, M.F. Montemor, Electrochemical assessment of the self-healing properties of Ce-doped silane solutions for the pre-treatment of galvanised steel substrates, Progress in Organic Coatings, 54, 2005, pp. 276-284.
28. M.F. Montemor, A.M. Simões, M.G.S. Ferreira, Composition and corrosion behaviour of galvanised steel treated with rare-earth salts: the effect of the cation, Progress in Organic Coatings, 44, 2002, pp. 111-120.
29. H. Wang, R. Akid, A room temperature cured sol–gel anticorrosion pre-treatment for Al 2024-T3 alloys, Corrosion Science, 49, 2007, pp. 4491-4503.
30. L.E.M. Palomino, P.H. Suegama, I.V. Aoki, Z. Pászti, H.G. de Melo, Investigation of the corrosion behaviour of a bilayer cerium-silane pre-treatment on Al 2024-T3 in 0.1 M NaCl, Electrochimica Acta, 52, 2007, pp. 7496-7505.
31. W. Trabelsi, P. Cecílio, M.G.S. Ferreira, K. Yasakau, M.L. Zheludkevich, M.F. Montemor, Surface evaluation and electrochemical behaviour of doped silane pre-

treatments on galvanised steel substrates, Progress in Organic Coatings, 59, 2007, pp. 214-223.

32. M.F. Montemor, W. Trabelsi, M. Zheludevich, M.G.S. Ferreira, Modification of bis-silane solutions with rare-earth cations for improved corrosion protection of galvanized steel substrates, Progress in Organic Coatings, 57, 2006, pp. 67-77.
33. H. Wang, R. Akid, Encapsulated cerium nitrate inhibitors to provide high-performance anti-corrosion sol–gel coatings on mild steel, Corrosion Science, 50, 2008, pp. 1142-1148.
34. H.S. R. Kasemann, Coating for mechanical and chemical protection based on organic-inorganic sol-gel nanocomposites, New Journal of Chemistry, 18, 1994, pp. 1117–1123.
35. R. Zandi-Zand, Investigation of corrosion, abrasion and weathering resistance in hybrid nanocomposite coatings based on epoxy-silica, Thesis, Azad University- Tehran North Branch, 2005.
36. W.J. Van Ooij, D. Zhu, M. Stancy, A. Seth, T. Mugada, J. Gandhi, P. Paomi, Corrosion protection properties of organofunctional silanes —An overview, Tsinghuax Science Technology, 10, 2005, pp. 639–664.
37. M.A.M. Ibrahim, S.S. Abd El Rehim, M.M. Hamza, Corrosion behavior of some austenitic stainless steels in chloride environments, Materials Chemistry and Physics, 115, 2009, pp. 80-85.
38. G.J. Brug, A.L.G. van den Eeden, M. Sluyters-Rehbach, J.H. Sluyters, The analysis of electrode impedances complicated by the precense of a constant phase element, Journal of Electroanalytical Chemistry, 176 (1984) 275-295.

5

Electrochemical assessment of the self-healing properties of silane hybrid coatings modified with cerium nitrate and cerium oxide nanoparticles on 304L stainless steel [1]

5.1. Introduction

Pre-treatments based on functional silane coatings present prime technological interest as they provide different chemical functionalities on a wide range of substrates either metallic or non-metallic. The silane coatings are usually uniform, robust and reliable, presenting a lateral resolution in the nanometer regime [1-6]. The good barrier properties of the silane coatings are due to the formation of a dense –Si–O–Si– network, which hinders the

[1] Published as full paper in International Journal Electrochemical Science, Volume 7, Roohangiz Zandi Zand, Kim Verbeken and Annemie Adriaens, Electrochemical Assessment of the Self-Healing Properties of Cerium Doped Sol-Gel Coatings on 304L Stainless Steel Substrates, 9592 – 9608, (2012).

penetration of aggressive species towards the metallic substrate. Thus, the effectiveness of the pre-treatments based on silane coatings is strongly dependent on the barrier properties of the film [7-10]. These barrier properties can be enhanced in order to make the silane coatings even more effective. Such goal can be achieved by the addition of small amounts of chemicals possessing specific corrosion inhibition properties, preferentially self-healing properties [11].

Recently, a new research trend in sol–gel processes has been oriented towards the development of sol–gel coatings doped with environmentally friendly inhibitors, such as cerium compounds [11-16]. These systems try to combine the "barrier protection" effect of sol–gel coatings with the "corrosion inhibition" effect of the cerium ions [8, 16]. Corrosion is inhibited by cerium ions that migrate through the coating to the location of the attack (a defect in the coatings) and then react to passivate the site. Thus, cerium ions act as cathodic inhibitors at active sites through precipitation of insoluble cerium hydroxide at local regions of high pH [16, 17].

The corrosion inhibition properties of cerium compounds have been widely discussed in literature. Pepe et al. [12, 13], for instance, studied the role of incorporating cerium ions in hybrid silica sol-gel coatings prepared with tetraethylorthosilicate ($Si(OC_2H_5)_4$, TEOS) and methyltriethoxysilane ($SiCH_3(OC_2H_5)_3$, MTES) doped with cerium salts on AISI 304 stainless steel and aluminum substrates. Results have shown an improvement of the corrosion protection in NaCl solutions. The explanation for this behavior can be found in the reaction of cerium (III and IV) and chromium (in the case of stainless steel) ions with the hydroxyls groups to the precipitation of cerium and chromium oxide/hydroxide on cathodic areas that can act as a barrier for the subsequent entrance of the oxygen to the reactive sites. Schem et al. [17] studied the electrochemical behavior of aluminum alloy 2024-T3 treated with hybrid sol-gel coating containing cerium oxide nanoparticles. Their studies indicate a general

beneficial effect of incorporation of ceria nanoparticles, although the performance of the coated alloy depends on the nanoparticle content. The electrochemical polarisation behavior revealed that the coating decreased the anodic current density by about seven orders of magnitude compared with the uncoated alloy, with high breakdown potentials in chloride-containing solution.

Montemor et al. [18] investigated the role of CeO_2 nanoparticles used as fillers for hybrid silane coatings applied on galvanized steel substrates. Electrochemical impedance (EIS) and scanning vibrating electrode technique (SVET) measurements showed that the modified coatings have improved barrier properties and highlight the corrosion inhibition effect of ceria nanoparticles activated with Ce(III) ions.

In previous work (chapter 4) it was reported that silane coatings modified with cerium nitrate hexahydrate provide very good barrier properties and improve the corrosion protection in comparison to non-modified silane coatings, when applied on 304L stainless steel substrates. The cerium inhibited system shows a slower electrochemical evolution than the non-inhibited one, because the inhibition effect of cerium ions slows down the corrosion kinetics.

Also cerium doped sol–gel coatings can supply self-healing abilities, which can automatically repair the corroded areas, thereby providing long-term corrosion protection. Self–healing can be defined as the partial recovery of the protective properties of the coated system when damaged [9, 18]. The most suitable way to evaluate self-healing ability is via the application of an artificial defect on the surface and monitoring of the electrochemical behavior using electrochemical impedance spectroscopy [9, 18].

In this regard, in the present work, the self-healing ability of cerium modified sol-gel coatings on 304L stainless steel substrates was investigated by monitoring the electrochemical behavior of the coated samples before and after defect application. Cerium nitrate and cerium oxide nanoparticles were used as cerium sources and the electrochemical behavior of the sol-gel coatings doped with cerium nitrate was compared with that of sol-gel coatings containing cerium oxide nanoparticles. In this study, the coated samples were immersed in the electrolyte for one week and after this period a defect in the form of a scratch was made on the surface using a needle. The diameter of the circular defect was around 1 mm. Electrochemical impedance measurements (EIS) and potentiodynamic polarization tests were carried out to monitor the corrosion performance of intact and scratched silane-treated 304L stainless steel substrates.

5.2. Sample preparation

304L stainless steel was used as substrate. In this study, sheets (7 cm × 15 cm × 0.1 cm) were used for the salt spray tests, while coupons (1.13 cm^2 area and 0.1 cm thickness) were used for all other experiments. The substrates were successively polished with 600 and 1200 grit emery paper, degreased with acetone in an ultrasonic bath for 10 min. Chemical etching was performed by dipping the samples into an alkaline solution (1 M NaOH solution) for 5 min at 50ºC. After rinsing in tap water and then in deionized water, the cleaned substrates were air-dried.

The silane solution was prepared by adding 4.084 mL of 3-glicidoxypropyltrimethoxy silane or GPTMS (Merck) to 0.5 mL of HCl-acidified water (pH = 2) (H_2O/Si mole ratio = 0.5 (23)). The solution was placed in a sealed beaker and stirred at room temperature for 20 min at a rate of 240 rpm to hydrolyse and condensate the silane precursors. $Ce(NO_3)_3.6H_2O$ (Fluka) and CeO_2 nanoparticles (10 wt % in water, particle size < 25 nm, Sigma Aldrich)

were used as sources of cerium and were added at the end of this step of synthesis, followed by stirring for 10 min. The Ce/Si mole ratio in both cases was 0.1. In a following step, 2.111 g of bisphenol A (BPA) (Merck) was added to the solutions as a cross-linking agent (BPA/Si mole ratio = 0.5). The latter has shown to have a significant effect on the morphology and corrosion resistance of the coating [19]. BPA was dissolved by mixing the solution for 80 minutes. To accelerate the condensation reaction, 0.0152 mL of 1-methylimidazol (MI) (Merck) (MI/Si mole ratio = 0.01) was added to the solution, followed by stirring for 5 min. The result in both cases ($Ce(NO_3)_3.6H_2O$ and CeO_2 solution) was a clear and colorless homogenous solution. Finally, the cleaned substrates were dipped for 1 min in the silane solutions. The coated specimens were left to dry at room temperature for 24 hours, which was followed by a 25–130°C curing process with a heating rate of 7.5 °C/min for 90 minutes to initiate extensive cross-linking in the hybrid films [20]. The coating thickness was measured by eddy-current method (Check line 3000 pro, Germany).

5.3. Results and discussion

Figure 5.1 presents AFM topographic images recorded on the bare and coated 304L stainless steel specimens with the sol-gel coatings modified with $Ce(NO_3)_3.6H_2O$ and CeO_2 nanoparticles respectively. AFM images of the bare 304L stainless steel sample (Figure 5.1a, b), show a heterogeneous and scratched surface with an RMS surface roughness of 127.165 that can be ascribed to polishing with emery paper. These images reveal some grains (crystal structure) of chromium in different sizes as well as distinct arrays (growth grains) along the scratches. These images used as reference to investigate the effect of cerium modified silane hybrid coating on microstructure and roughness of 304L stailess steel substrates.

The AFM images of the sol-gel coating modified with $Ce(NO_3)_3.6H_2O$ (Figures 5.1c) reveal a the formation of crack and defect free coating with RMS (root mean square) surface

roughness of 0.227 nm. Interestingly, the rather low color contrast in the AFM image, suggests a limited heterogeneity of the coating thickness. In addition, no agglomerates are present on the surface.

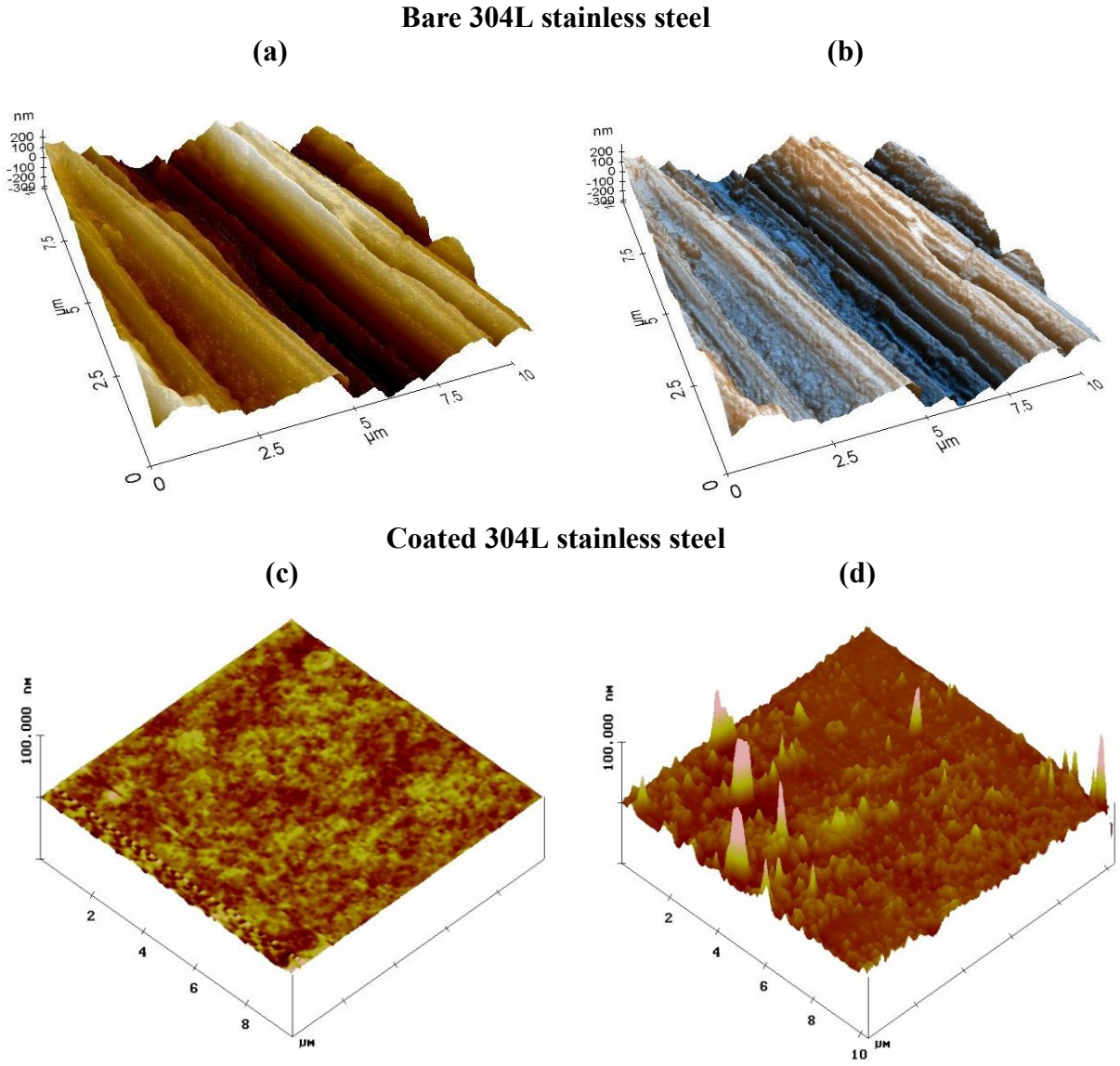

Figure 5.1. AFM topographic images of the bare (a, b, in different colors) and coated 304L stainless steel with the sol-gel coatings modified with $Ce(NO_3)_3.6H_2O$ (c) and CeO_2 nanoparticles (d). AFM images for the bare and coated specimens recorded in non-contact and tapping mode, respectively.

In case of the sol-gel coating modified with CeO_2 nanoparticles (Figures 5.1d), the nano-sized particles incorporated into the film matrix are clearly defined in these scans. The distribution of the nanoparticles is relatively uniform and the RMS roughness is 2.145 nm. Several particles in the hybrid matrix show a larger diameter and seem to result from agglomerates of smaller ones. Furthermore, there is a sharper color contrast in this image suggesting stronger height differences. Interestingly, the color contrast is uniformly distributed throughout the image, again suggesting heterogeneity of the coating thickness.

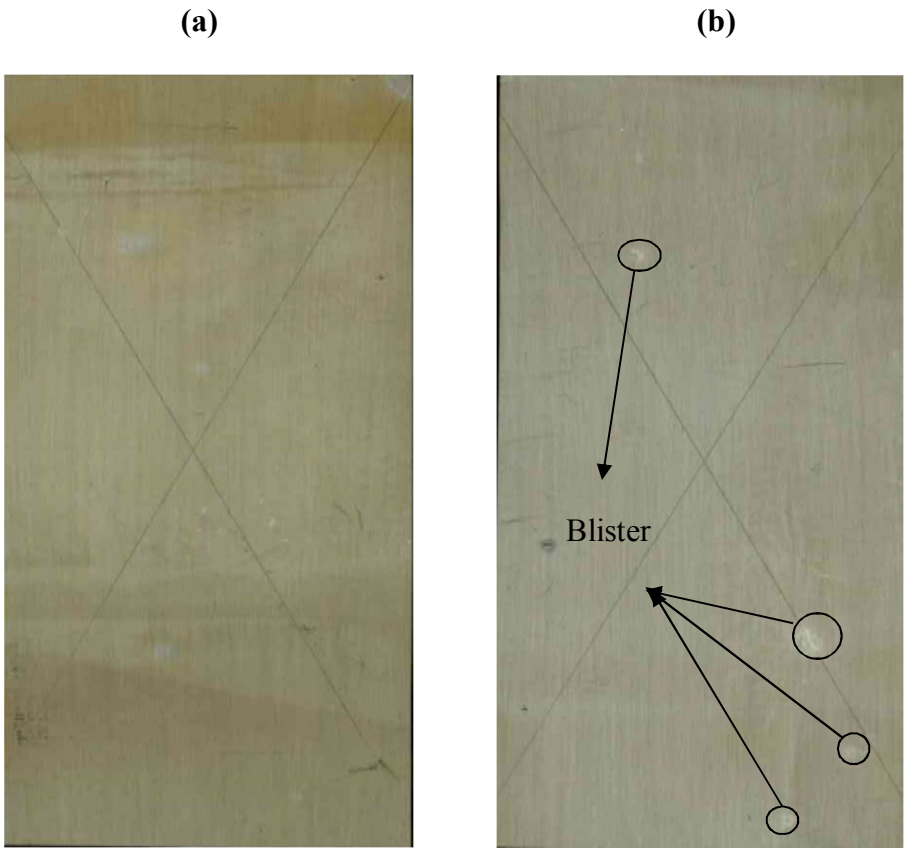

Figure 5.2. Photographs of the 304L stainless steel surfaces coated with the sol-gel coatings modified with $Ce(NO_3)_3.6H_2O$ (a) and CeO_2 nanoparticles (b) after 2000 hours of salt spray exposure.

Photographs of the 304L SS pre-treated with $Ce(NO_3)_3.6H_2O$ and CeO_2 nanoparticle modified coatings after 2000 hours of salt spray exposure (Figure 5.2) show that the coatings gave different levels of protection. Coating modified with $Ce(NO_3)_3.6H_2O$ (average thickness of the coating= 61 $\pm$ 12 μm) (Figure 5.2a) did not blister or delaminate and retained its originally shiny surface, while coating modified with CeO_2 nanoparticles (average thickness of the coating= 61 $\pm$ 14 μm) (Figure 5.2b), exhibited slight blistering around the scratched area (circles in the figure). Overall, good long-term corrosion protection appears to have been achieved by the silane sol–gel coating modified with $Ce(NO_3)_3 \cdot 6H_2O$.

Impedance spectra for the coating modified with $Ce(NO_3)_3.6H_2O$, both with and without an applied defect, were recorded at intervals during immersion (Figure 5.3a). The impedance at low frequencies (LF) shown by the pristine sample was close to 1.95×10^6 Ω cm^2 during the first hours of immersion. After immersion for 3 days, it dropped slightly (1.6×10^6 Ω cm^2). This was associated with water uptake through pores and/or defects in the coating. Longer immersion (3 to 7 days) led impedance at LF to increase rapidly and remain high that can be ascribed to blocking the pores or defects by insoluble precipitation of cerium oxide or hydroxide (self-healing properties of cerium ions). This insoluble precipitation can be formed by releasing the cerium ions near the defects and its reaction with OH^- ions from the cathodic reactions.

After immersion for 7 days, a defect was induced on the coating to create a corroding area. The impedance at LF markedly decreased 1 hour after application of the defect (close to 1.19×10^5 Ω cm^2). This was an expected consequence of the damage. Further immersion for 1 day led the impedance at LF to increase further to 1.6×10^6 Ω cm^2. Yet longer immersion led the LF impedance to decrease slightly. This change is attributable to the self-healing effects of $Ce(NO_3)_3 \cdot 6H_2O$ on the areas of corrosion [21]. The self-healing originated from the release of

cerium near the defect. The cerium then produced insoluble hydroxides by its reaction with hydroxyl groups from cathodic reactions [19]. These hydroxides, together with the corrosion products, decreased the cathodic current and consequently reduced the overall corrosion rate.

The shape of the phase angle plot (Figure 5.3b) indicates two time constants before and after the application of the defect. The high-frequency process (around 10^3 before and 10^2 rad s^{-1} after defect application) is attributable to the response of the silane film; the low-frequency time constant (around 10^{-1} rad s^{-1} before and after defect application) is due to the response of the processes occurring between the metal oxide over the substrate and electrolyte.

The coating modified with CeO_2 nanoparticles showed a different trend. The total impedance of the system was lower than that of the $Ce(NO_3)_3.6H_2O$ modified sol–gel film. Impedance decreased rapidly with increased immersion, both before and for 5 days after the application of the defect (Figure 5.4a). Impedance increased 7 days after the application of the defect, suggesting that the coating was still providing some protection.

The EIS spectra show two time constants before and after the application of the defect (Figure 5.4b). Increased immersion led the low-frequency time constant (around 10^{-1} rad s^{-1}) to lose its prominence, while the high-frequency time constant (around 10^3 rad s^{-1}) remained well defined. After the application of the defect, the phase angle plot shows two overlapped time constant; one at high frequencies (around 3.16 rad s^{-1}), which is attributable to the response of the silane film and another one at the low-frequencies (around 1 rad s^{-1}), which is ascribable to corrosion on the substrate, although no coating degradation was observed for the sol–gel coating containing CeO_2 nanoparticles.

(a)

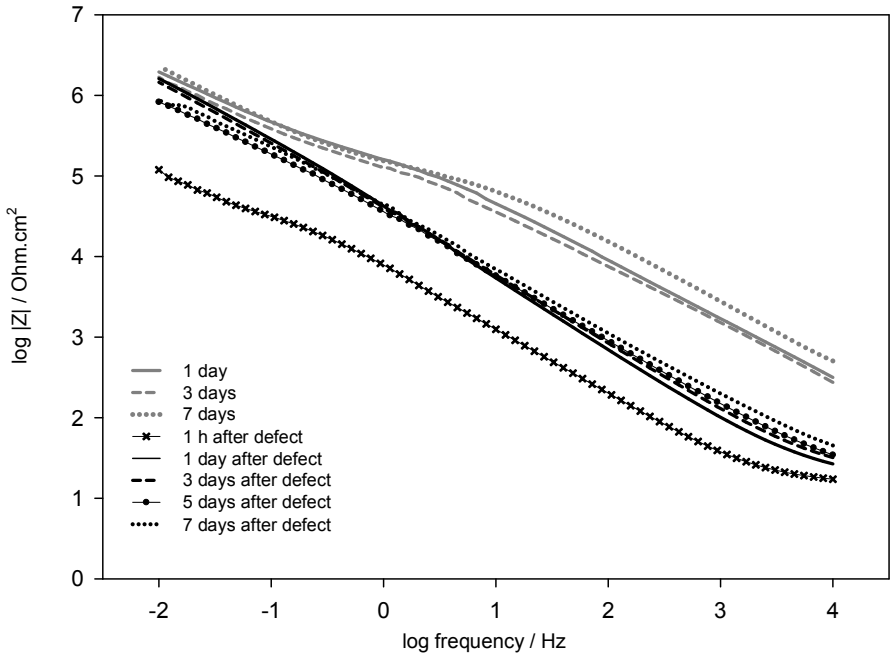

(b)

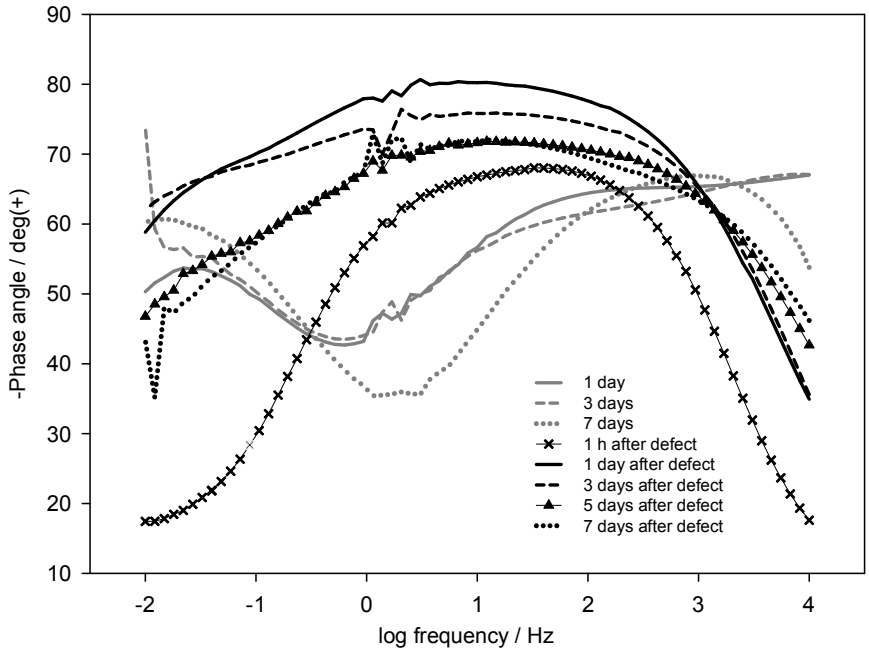

Figure 5.3. EIS Bode modulus (a) and phase angle (b) plots obtained on the 304L stainless steel sample pre-treated with the silane film modified with cerium nitrate. Spectra were obtained during immersion in a 3.5% NaCl solution, before and after the application of the defect.

(a)

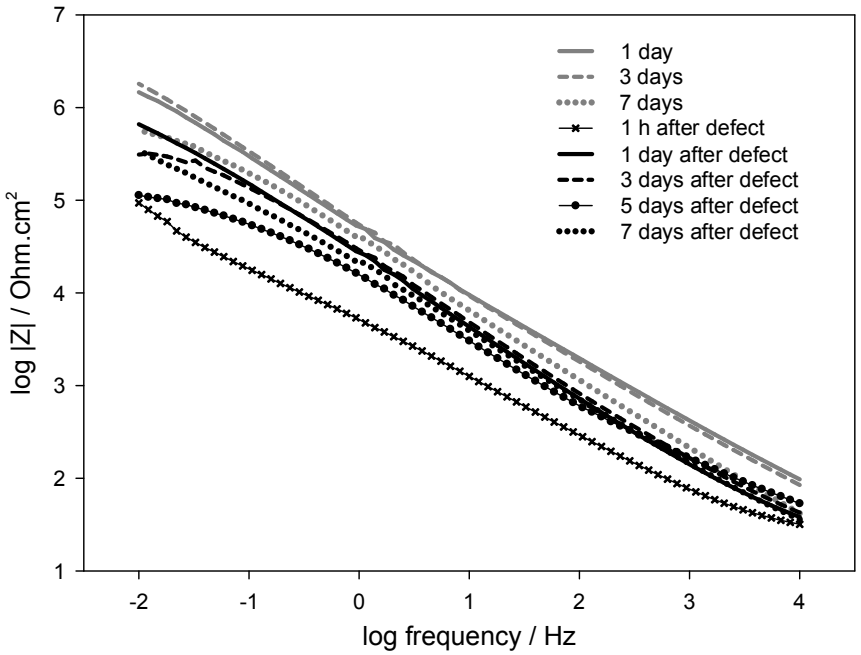

(b)

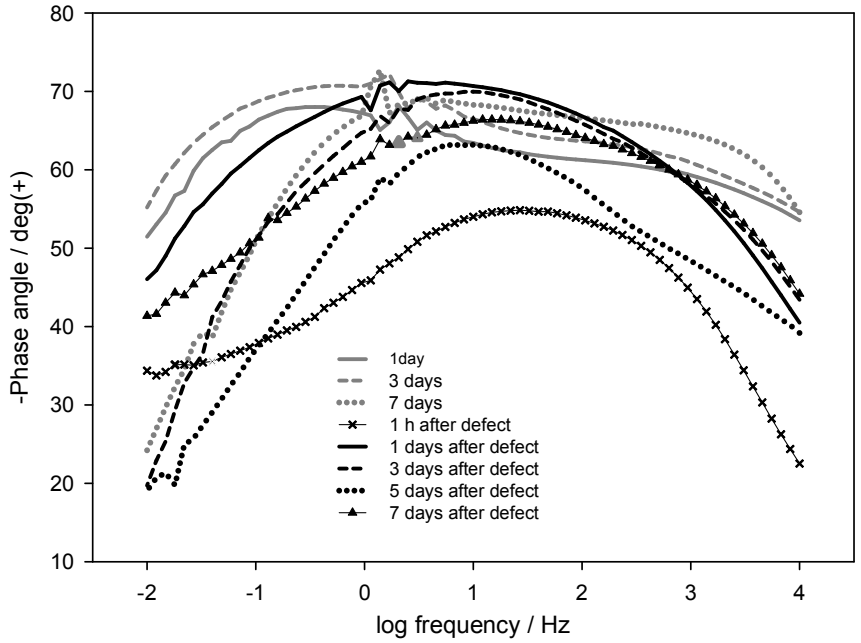

Figure 5.4. EIS Bode modulus (a) and phase angle (b) plots obtained on the 304L stainless steel sample pre-treated with the silane film containing CeO_2 nanoparticles. Spectra were obtained during immersion in 3.5% NaCl solution, before and after defect application.

The EIS measurements were further analyzed by fitting the experimental plots to equivalent electrical circuits (EECs), while taking into consideration the number of time constants and the quality of the fits [22]. The equivalent circuit for the $Ce(NO_3)_3.6H_2O$ and CeO_2 modified coating (Figure 5.5) consists of: the electrolyte resistance, R_s; the non-ideal capacitance of the coating, CPE_{coat} ($0.67 < n_{coat} < 0.88$); the resistance to the passage of the electrolyte presented by pores or defects, R_{po}; the non-ideal capacitance of the oxide layer between the metal surface and the electrolyte, which soaks the corrosion products near the pores, CPE_{oxide} ($0.62 < n_{coat} < 0.95$); and the oxide resistance of the metal oxide layer over the metal surface, R_{oxide}.

In this equivalent circuit, constant phase elements were used instead of pure capacitors, because of the non-ideal character of the corresponding response with phase shifts differing from –90°. The true capacitances can be calculated from the respective CPE parameters, as described in chapter 2, section 2.7.4.

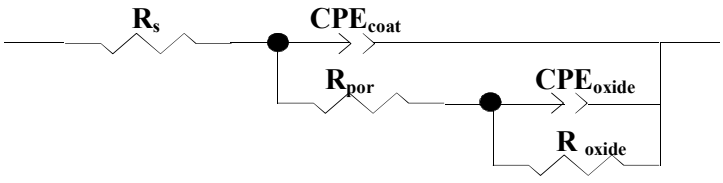

Figure 5.5. Equivalent circuit used for the numerical fitting of the EIS data during immersion in a 3.5% NaCl solution.

Figures 5.6 – 5.8 depict the evolution of the parameters used in the numerical simulation of the experimental results. Values are shown with the errors from the numerical fitting. The system modified with cerium nitrate showed a high-frequency resistance that

decreased slightly during the first hours of immersion before the application of the defect (Figure 5.6), following the development of conductive pathways inside the silane film. The resistance remained nearly constant (around 1.32×10^5 Ω cm^2) during immersion for 7 days. The high-frequency CPE values were around 9.5×10^{-7} F. cm^{-2} and decreased slightly with time. The low-frequency behavior was characterized by a resistance that increased from 8.25×10^6 Ω cm^2 during the first hours of immersion to 161×10^6 Ω cm^2 after immersion for 7 days. Its CPE values were around 2.70×10^{-6} F. cm^{-2} and remained nearly constant during the 7 days of immersion.

The high-frequency resistance increased 1 day after the application of the defect (1.30×10^6 Ω cm^2); it subsequently decreased slightly until the end of the experiment. The CPE values were around 4.7×10^{-6} F. cm^{-2} and increased with time.

1 day after defect application, the low-frequency resistance increased slightly from 4.06×10^6 Ω cm^2 to 6.05×10^6 Ω cm^2 3 days after defect application and then decreased slightly until the end of the experiment. The CPE values decreased from 2.70×10^{-6} F cm^{-2} 1 day after defect application to 1.81×10^{-6} F. cm^{-2} 3 days after defect application and then increased significantly until the end of the experiment.

The system modified with CeO_2 showed slightly decreased high frequency resistance during immersion for 4 days that followed by slightly increasing after 7 days of immersion before the application of the defect (Figure 5.7). This can be ascribed to cerium oxide or hydroxide blocking the pores or defects [9, 21]. The CPE values were around 6.74×10^{-6} F. cm^{-2} and remained nearly constant during the 7 days of immersion. At low frequencies, resistance increased with time during 7 days immersion, indicating that cerium oxide/hydroxide formed with the release of CeO_2 from the sol–gel matrix [9, 23].

Correspondingly, the CPE values pass through a maximum after 3 days of immersion and then decreased slightly during 7 days immersion.

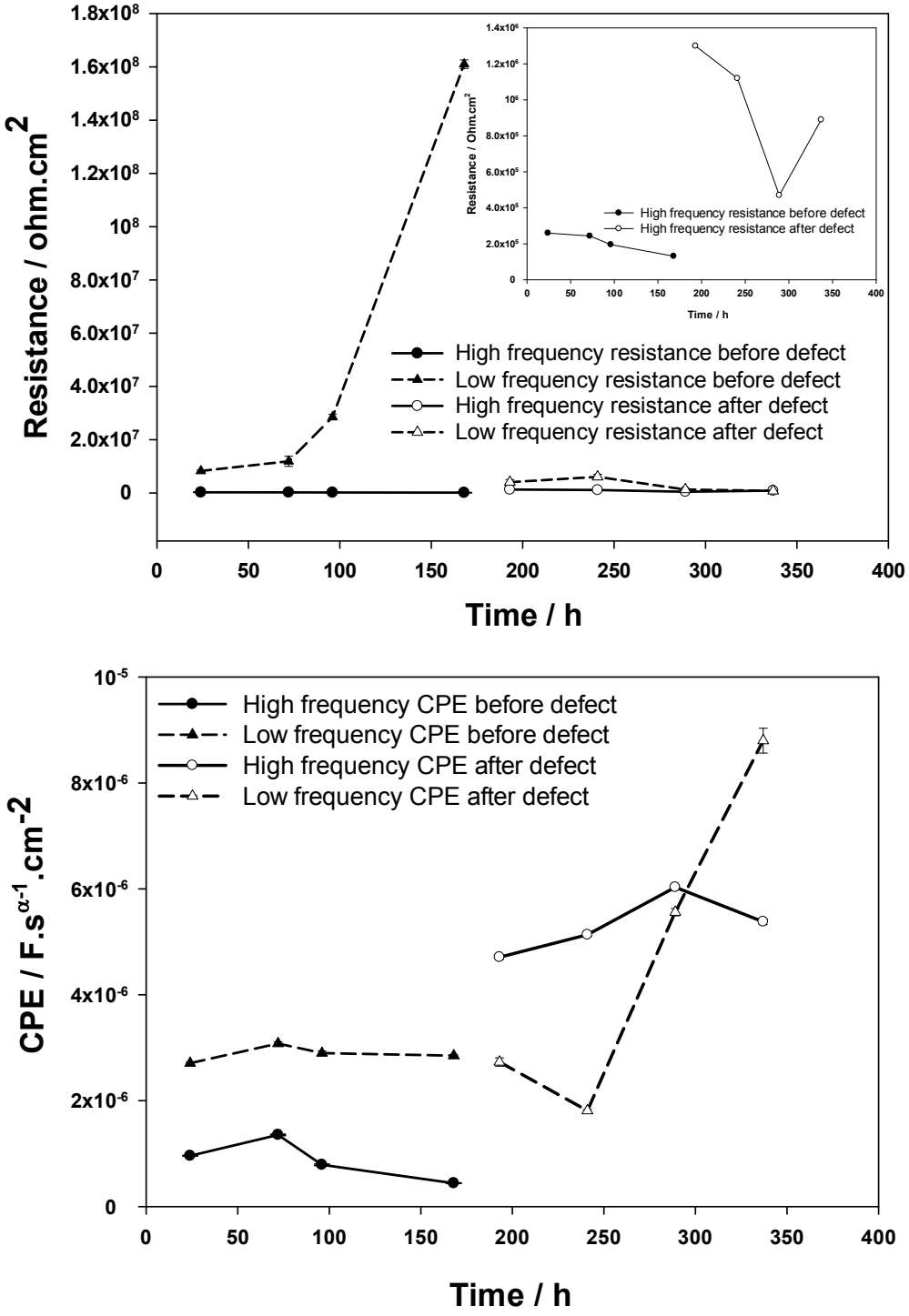

Figure 5.6. Evolution of the fitting parameters for the sol-gel coating modified with cerium nitrate before and after defect application. Values were obtained by numerical fitting, using the equivalent circuit depicted in figure 5.5, (10^{-4} < Chi-squared < 10^{-3}).

After the application of the defect, the sample showed slightly decreasing high frequency resistance and increasing correspondingly CPE values for the duration of the immersion test, indicating degradation of the coating (Figure 5.8). At low frequencies, 2days after the application of the defect, the resistance decreased significantly which followed by nearly constant values until the end of the experiment. The CPE values reached a maximum during the 5 days after the application of the defect which followed by rapidly decreasing until the end of the experiment owing to saturation of electrolyte in the sol–gel film.

The electrochemical tests showed that modification of the silane sol–gel coating with cerium ions resulted in a protective coating with barrier properties and/or corrosion inhibiting activity. The improved barrier properties were correlated with increases of reactive silanol groups ($–Si(OH)_3$) and condensed species that could increase the viscosity of the silane solution and the coating thickness [7].

Further assessment of the mechanisms associated with the electrochemical behavior of these systems was conducted through potentiodynamic polarization measurements. The curves obtained from the scratched samples after 1 hour of immersion are depicted in Figure 5.8. Table 5.1 lists the electrochemical parameters obtained from these measurements.

The $Ce(NO_3)_3$-doped sol–gel coating showed a lower corrosion current density, i_{corr}, (around 1.36×10^{-7} A cm^{-2}) than the sol–gel coating containing CeO_2 nanoparticles, and its potential was shifted higher (−0.408 V). This coated sample shows a passivation range of approximately −0.340 V to +0.013 V over its corrosion potential. This behavior was improved by the barrier properties of the coating [19].

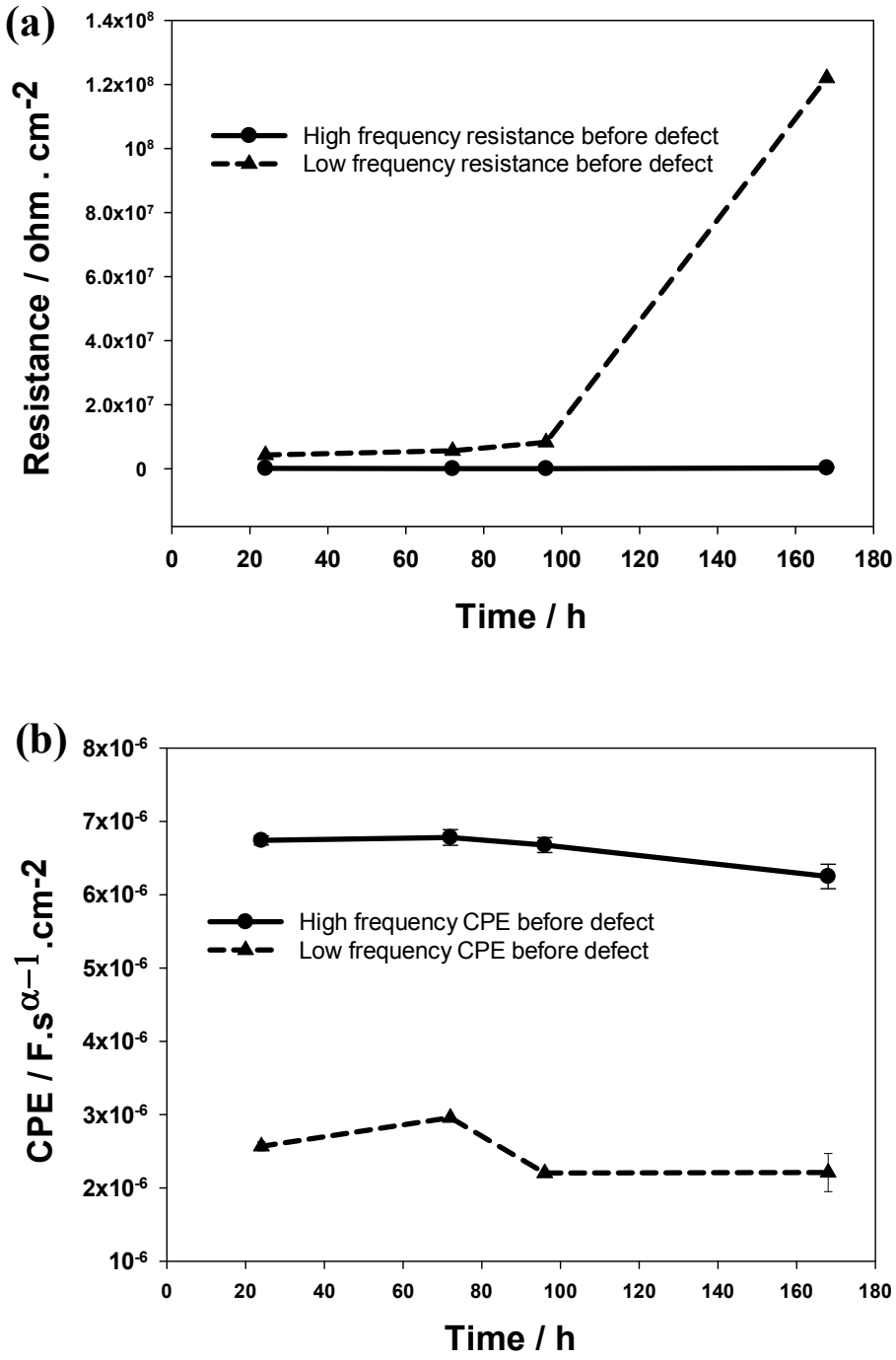

Figure 5.7. Evolution of the resistance (a) and capacitance (b) for the sol-gel coating containing CeO_2 nanoparticles before defect application, during immersion in a 3.5% NaCl solution. Values were obtained by numerical fitting, using the equivalent circuit depicted in figure 5.5, (10^{-4} < Chi-squared < 10^{-3}).

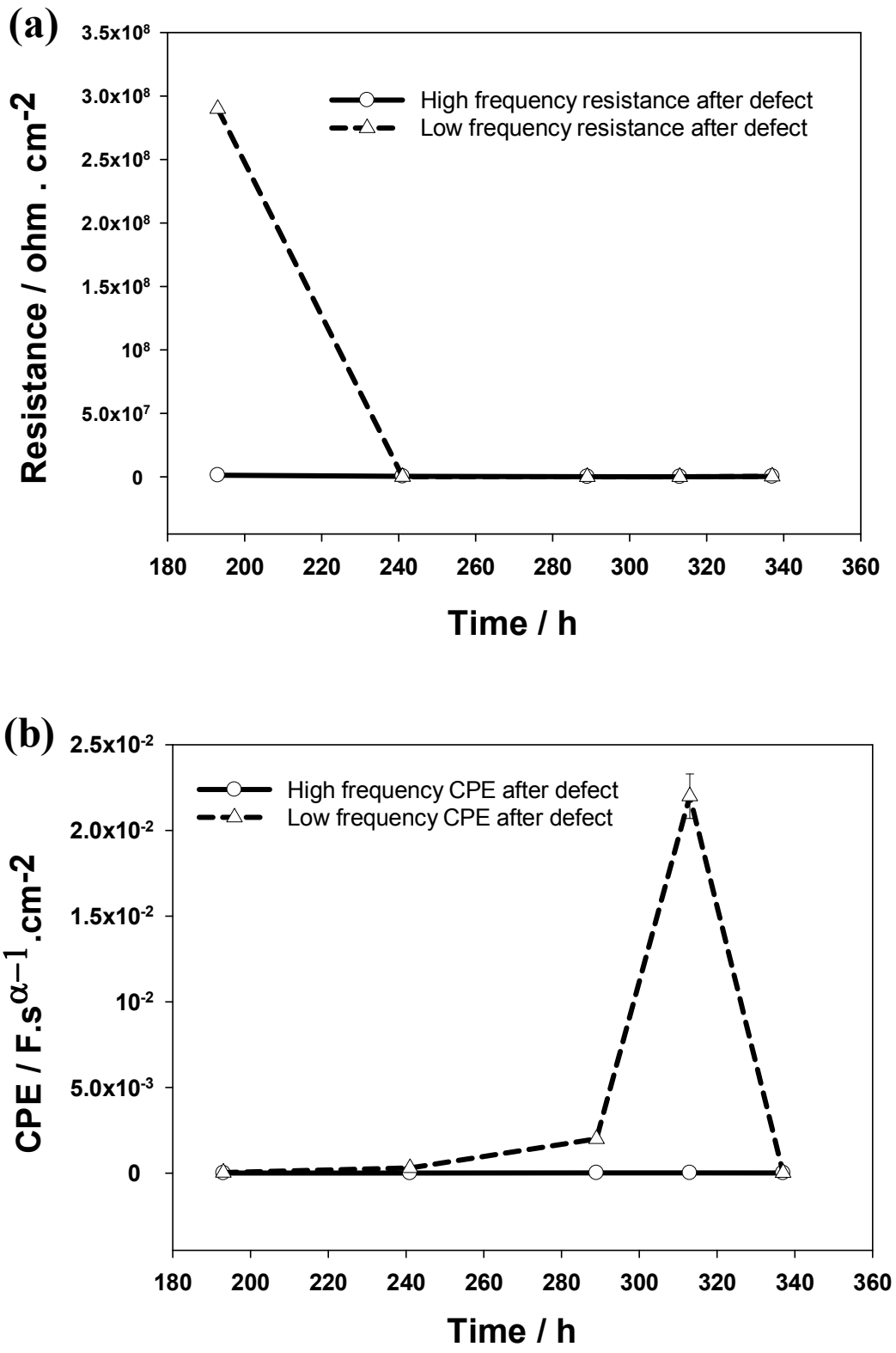

Figure 5.8. Evolution of the resistance (a) and capacitance (b) for the sol-gel coating containing CeO_2 nanoparticles after defect application, during immersion in a 3.5% NaCl solution. Values were obtained by numerical fitting, using the equivalent circuit depicted in figure 5.5, (10^{-4} < Chi-squared < 10^{-3}).

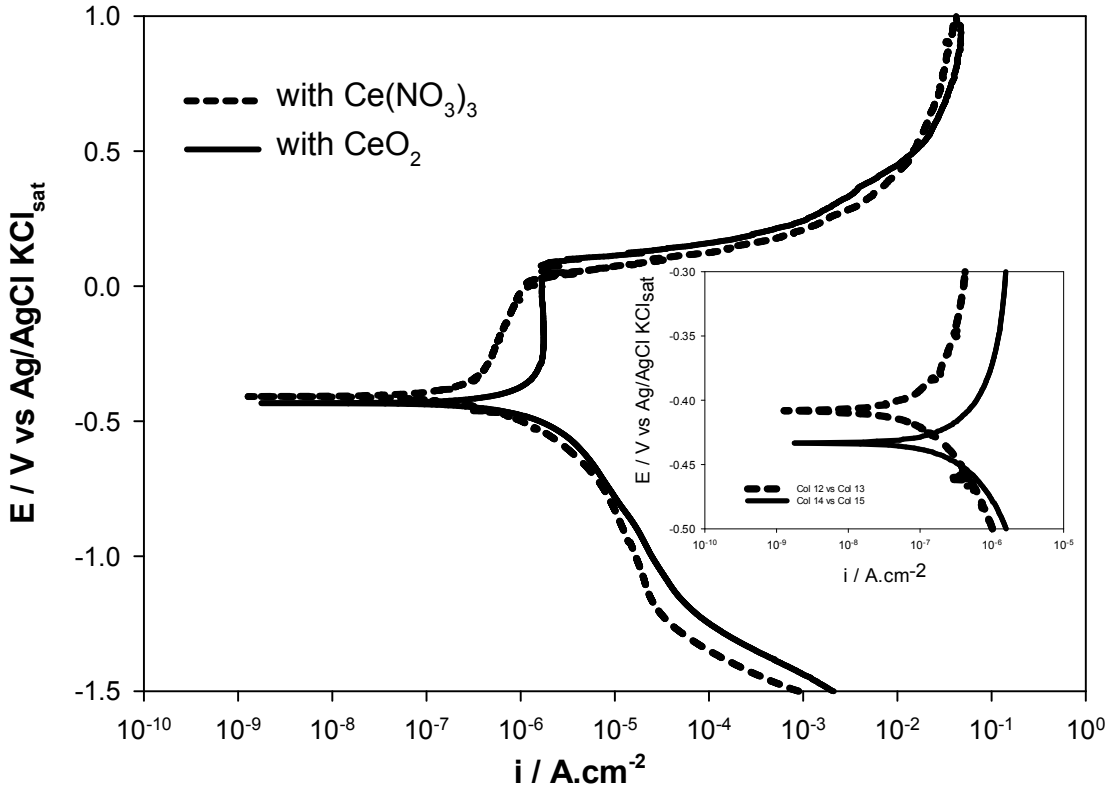

Figure 5.8. Potentiodynamic polarization curves of the sol-gel coating modified with cerium nitrate and sol-gel coating containing CeO_2 nanoparticles obtained after 1 hour immersion in a 3.5 % NaCl solution. For comparative purposes a plot is also inserted, in which the potential is depicted as the difference between the imposed potential and the corrosion potential. This approach allows a better separation of the anodic and cathodic polarization effects.

Coating containing CeO_2 presented a continuous potential range characterized by a control mechanism of equilibrium in the oxidation and reduction reactions. It also showed a wide passive plateau of −0.403 V to +0.092 V above the corrosion potential.

The d.c. polarization results show that the presence of the cerium compounds favorably shifted the corrosion potential, decreased the anodic currents, and altered the

kinetics of the anodic processes [19]. These effects were much more marked for $Ce(NO_3)_3$-doped coatings than for coating containing CeO_2.

Table 5.1. Summary of the electrochemical parameters obtained from the polarization measured in a 3.5% Nacl solution.

sample	E_{corr} (V)	i_{corr} (A cm^{-2})	b_c (V/dec)	b_a (V/dec)	Passive area (V)
With $Ce(NO_3)_3$	-0.408	1.361×10^{-7}	0.187	0.950	-0.340 to 0.013
With CeO_2	-0.434	4.993×10^{-7}	0.230	0.116	-0.403 to 0.092

5.4. Conclusion

Pre-treatments based on the use of organofunctional silane solutions modified with a corrosion inhibitor can benefit from additional active corrosion protection when an appropriate inhibitor is used. Cerium nitrate and cerium oxide are demonstrated here as possible additives which can provide a self-healing ability in combination with their good barrier properties of the sol-gel films.

Microscopic observations confirm the formation of transparent cerium modified sol-gel films without any defects and cracks. The results reveal the formation of a comparatively smooth nanostructure surface with a small heterogeneity in coating thickness in the sol-gel coatings modified with $Ce(NO_3)_3.6H_2O$. Also these results confirm the integral maintaining the surface morphology of the sol-gel coatings modified with CeO_2 nanoparticles, after short time corrosion tests (14 days immersion in 3.5% NaCl solution).

Corrosion tests results indicate that the CeO_2 nanoparticles have good corrosion inhibition properties on scratched surfaces due to ability to complex other species, therefore contributing for the stabilization of the passive film. In this way, these particles have an anodic inhibition mechanism.

The positive impact, in the barrier properties, corrosion inhibition and self –repair of defects, is significantly improved with modification of the silane solution with cerium nitrate solution. The cerium ions have the ability to change the silane solution chemistry, promoting the formation of reactive silanol group and also of more condensed species. The cerium nitrate provides the best corrosion protection either in intact sol-gel films or in the presence of scratches.

References

1. R.L. Twite, G.P. Bierwagen, Review of alternatives to chromate for corrosion protection of aluminum aerospace alloys, Progress in Organic Coatings, 33, 1998, pp. 91-100.
2. A. Franquet, C. Le Pen, H. Terryn, J. Vereecken, Effect of bath concentration and curing time on the structure of non-functional thin organosilane layers on aluminium, Electrochimica Acta, 48, 2003, pp. 1245-1255.
3. D. Zhu, W.J. van Ooij, Corrosion protection of AA 2024-T3 by bis-[3-(triethoxysilyl)propyl]tetrasulfide in sodium chloride solution, Part 2: mechanism for corrosion protection, Corrosion Science, 45, 2003, pp. 2177-2197.
4. A.M. Beccaria, L. Chiaruttini, The inhibitive action of metacryloxypropylmethoxysilane (MAOS) on aluminium corrosion in NaCl solutions, Corrosion Science, 41, 1999, pp. 885-899.

5. A.M. Beccaria, G. Padeletti, G. Montesperelli, L. Chiaruttini, The effect of pretreatments with siloxanes on the corrosion resistance of aluminium in NaCl solution, Surface and Coatings Technology, 111, 1999, pp. 240-246.
6. D. Zhu, W.J.v. Ooij, Enhanced corrosion resistance of AA 2024-T3 and hot-dip galvanized steel using a mixture of bis-[triethoxysilylpropyl]tetrasulfide and bis-[trimethoxysilylpropyl]amine, Electrochimica Acta, 49, 2004, pp. 1113-1125.
7. F. Deflorian, S. Rossi, M. Fedel, C. Motte, Electrochemical investigation of high-performance silane sol–gel films containing clay nanoparticles, Progress in Organic Coatings, 69, 2010, pp. 158-166.
8. A.M. Cabral, W. Trabelsi, R. Serra, M.F. Montemor, M.L. Zheludkevich, M.G.S. Ferreira, The corrosion resistance of hot dip galvanised steel and AA2024-T3 pre-treated with bis-[triethoxysilylpropyl] tetrasulfide solutions doped with $Ce(NO_3)_3$, Corrosion Science, 48, 2006, pp. 3740-3758.
9. M.F. Montemor, M.G.S. Ferreira, Cerium salt activated nanoparticles as fillers for silane films: Evaluation of the corrosion inhibition performance on galvanised steel substrates, Electrochimica Acta, 52, 2007, pp. 6976-6987.
10. H. Wang, R. Akid, Encapsulated cerium nitrate inhibitors to provide high-performance anti-corrosion sol–gel coatings on mild steel, Corrosion Science, 50, 2008, pp. 1142-1148.
11. W. Trabelsi, P. Cecilio, M.G.S. Ferreira, M.F. Montemor, Electrochemical assessment of the self-healing properties of Ce-doped silane solutions for the pre-treatment of galvanised steel substrates, Progress in Organic Coatings, 54, 2005, pp. 276-284.
12. A. Pepe, M. Aparicio, A. Durán, S. Ceré, Cerium hybrid silica coatings on stainless steel AISI 304 substrate, Journal of Sol-Gel Science and Technology, 39, 2006, pp. 131-138.

13. A. Pepe, M. Aparicio, S. Ceré, A. Durán, Preparation and characterization of cerium doped silica sol–gel coatings on glass and aluminum substrates, Journal of Non-Crystalline Solids, 348, 2004, pp. 162-171.
14. W. Trabelsi, E. Triki, L. Dhouibi, M.G.S. Ferreira, M.L. Zheludkevich, M.F. Montemor, The use of pre-treatments based on doped silane solutions for improved corrosion resistance of galvanised steel substrates, Surface and Coatings Technology, 200, 2006, pp. 4240-4250.
15. N.N. Voevodin, N.T. Grebasch, W.S. Soto, F.E. Arnold, M.S. Donley, Potentiodynamic evaluation of sol–gel coatings with inorganic inhibitors, Surface and Coatings Technology, 140, 2001, pp. 24-28.
16. N.C. Rosero-Navarro, S.A. Pellice, A. Durán, S. Ceré, M. Aparicio, Corrosion protection of aluminium alloy AA2024 with cerium doped methacrylate-silica coatings, Journal of Sol-Gel Science and Technology, 52, 2009, pp. 31-40.
17. M. Schem, T. Schmidt, J. Gerwann, M. Wittmar, M. Veith, G.E. Thompson, I.S. Molchan, T. Hashimoto, P. Skeldon, A.R. Phani, S. Santucci, M.L. Zheludkevich, CeO_2-filled sol–gel coatings for corrosion protection of AA2024-T3 aluminium alloy, Corrosion Science, 51, 2009, pp. 2304-2315.
18. M.F. Montemor, R. Pinto, M.G.S. Ferreira, Chemical composition and corrosion protection of silane films modified with CeO_2 nanoparticles, Electrochimica Acta, 54, 2009, pp. 5179-5189.
19. R. Zandi Zand, K. Verbeken, A. Adriaens, Corrosion resistance performance of cerium doped silica sol–gel coatings on 304L stainless steel, Progress in Organic Coatings, 75, 2012, pp. 463-473.

20. R. Zandi Zand, K. Verbeken, A. Adriaens, The corrosion resistance of 316L stainless steel coated with a silane hybrid nanocomposite coating, Progress in Organic Coatings, 72, 2011, pp. 709-715.
21. H. Shi, F. Liu, E. Han, Corrosion behaviour of sol–gel coatings doped with cerium salts on 2024-T3 aluminum alloy, Materials Chemistry and Physics, 124, 2010, pp. 291-297.
22. M.L. Zheludkevich, R. Serra, M.F. Montemor, K.A. Yasakau, I.M.M. Salvado, M.G.S. Ferreira, Nanostructured sol–gel coatings doped with cerium nitrate as pre-treatments for AA2024-T3: Corrosion protection performance, Electrochimica Acta, 51, 2005, pp. 208-217.
23. V. Moutarlier, B. Neveu, M.P. Gigandet, Evolution of corrosion protection for sol–gel coatings doped with inorganic inhibitors, Surface and Coatings Technology, 202, 2008, pp. 2052-2058.

6

Influence of cerium concentration on the microstructural features and corrosion protection of the cerium-doped silane hybrid coatings on hot-dip galvanized steel substrates [1]

6.1. Introduction

Cerium doped sol–gel coatings are actively investigated for the surface pre-treatment of metals and alloys. Positive results have been obtained with aluminium and its alloys [1-4], magnesium and its alloys [5, 6] and steel [7-12]. Similar as pure sol–gel coatings, the cerium doped ones can also form a dense barrier, which hinders the penetration of electrolyte towards the metal surface. The important difference between them is that cerium doped sol–gel

[1] Published as full paper in International Journal Electrochemical Science, Volume 8, Roohangiz Zandi Zand, Kim Verbeken and Annemie Adriaens, Influence of the Cerium Concentration on the Corrosion Performance of Ce-doped Silica Hybrid Coatings on Hot Dip Galvanized Steel Substrates, 548-563, (2013).

coatings display self-healing abilities, which can automatically repair the damaged areas, providing a long-term corrosion protection [13].

Also cerium–silica hybrid coatings have been investigated as prospective pre-treatments for many metallic substrates. For instance, Trabelsi [14] and Zhong et al. [13] studied the electrochemical behaviour of Ce-doped silane hybrid coatings on galvanized steel and magnesium alloy AZ91D, respectively. They found that the protective behaviour of the pre-treatments based on Ce-doped silane solutions depends on the dopant concentration. The results also suggest that there is an optimum concentration of dopant as higher or lower concentrations lead to a negative effect in the coating barrier properties. Garcia-Heras and co-workers [15] investigated the electrochemical properties of cerium–silica sol–gel thin films on zinc panels. They found that the critical concentration of the anticorrosive pigment (Ce^{3+} salts) was in the 0.2–0.6 range (wt.%). Above this concentration, defects were observed in the sol–gel film. Rosero-Navarro and co-workers [1] studied the effects of Ce-containing sol–gel coatings reinforced with SiO_2 nanoparticles on the protection of AA2024. The results show that the incorporation of cerium ions in the coating induced an inhibition action. However, the interaction of the cerium pigments with the silica network usually leads to significant shortcomings in the coating stability and the activities of the cerium pigments [16]. Therefore, the cerium concentration has to be carefully controlled to overcome these shortcomings as much as possible.

A few studies have reported on the effect of the cerium concentration on the properties of the coatings [14, 17]. Information on the influence of the cerium concentration on morphology and anticorrosion performance remains, however, still limited in the literature and hence needs further investigation. Therefore, the present work investigates the effect of the cerium concentration on the morphology and anticorrosion performance of cerium–silica

hybrid coatings on hot dip galvanized steel substrates (HDG) pre-treated with 3-glycidoxypropyltrimethoxysilane (GPTMS) solutions doped with cerium nitrate.

6.2. Sample preparation

The silane solution was prepared by adding 4.084 mL of 3-glicidoxypropyltrimethoxy silane or GPTMS (Merck) to 0.5 mL of HCl-acidified water (pH = 2) (H_2O/Si mole ratio = 0.5 [18]). The solution was placed in a sealed beaker and stirred at room temperature for 20 min at a rate of 240 rpm to hydrolyse and condensate the silane precursors. $Ce(NO_3)_3.6H_2O$ (Fluka) was used as cerium source and was added at the end of this step of synthesis, followed by stirring for 10 min. The Ce/Si mole ratio was 0.000, 0.001, 0.005, 0.010, 0.050 and 0.100, respectively. In a following step, 2.111 g of bisphenol A (BPA) (Merck) was added to the solutions as a cross-linking agent (BPA/Si mole ratio = 0.5). The latter has shown to have a significant effect on the morphology and corrosion resistance of the coating [7]. BPA was dissolved by mixing the solution for 80 minutes. To accelerate the condensation reaction, 0.0152 mL of 1-methylimidazol (MI) (Merck) (MI/Si mole ratio = 0.01) was added to the solution, followed by stirring for 5 min. The result was a clear and colourless homogenous solution.

The metallic substrate consisted of hot dip galvanized steel coupons (1.13 cm^2 area and 0.1 cm thickness for the SEM measurements and electrochemical tests) and plates (7 cm × 15 cm × 0.1 cm for the salt spray tests). The zinc coating has a weight of approximately 140 g/m^2 and a thickness of approximately 10 µm, measured by Elcometer 355 probe module (Braine Instruments). The galvanized steel specimens were degreased using an alkaline cleaner. Following the cleaning, the substrates were washed with distilled water, dried in air and immersed in the silane solution for 60 s. The coated specimens were dried at room temperature for 24 hours and subsequently submitted to a 25–130°C curing process with a

heating rate of 7.5 °C/min for 90 minutes to initiate extensive cross-linking in the hybrid films [11]. The coating thickness was measured by eddy-current method (Check line 3000 pro, Germany).

6.3. Results and discussion

Microstructural observation of the non-doped and the 0.05 M cerium nitrate-modified silane hybrid coatings before immersion in a 3.5 % NaCl solution revealed smooth surfaces without any cracks or defects (Figure 6.1). However, the non-doped coating showed several agglomerations (Figure 6.1a), which may be ascribed to the relatively high viscosity of the sol solution [19]. The heterogeneities in the coating might lead to regions more prone to corrosion.

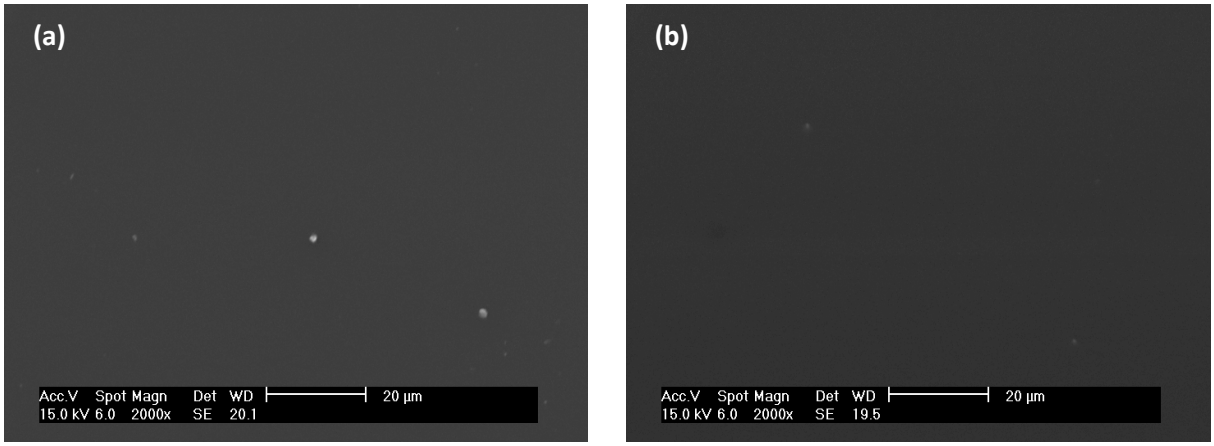

Figure 6.1. Scanning electron micrographs of cerium-silica coatings doped with (a) 0.000 M and (b) 0.05 M cerium nitrate on HDG steel samples prior to immersion in a 3.5% NaCl solution.

After immersion for 72 hours in a 3.5 % NaCl solution, localized corrosion was observed for all coatings (for the 0.050 M sample). Exfoliation of the corrosion products and cracks of different sizes were observed. These localized attacks could promote the

deterioration and delamination of the films, and were possibly due to hydrolysis reactions at the interface. Corrosion was enhanced by the diffusion of the oxidant ions, which caused corrosion products to accumulate at the interface and promoted the formation of defects and micro-cracks [20, 21].

The coating prepared using 0.050 M cerium nitrate remained homogenous and crack-free after immersion for 120 hours (not shown). Further immersion for a total 144 hours led to the appearance of cracks. Comparison of the specimens after immersion for 144 hours (Figure 6.2) suggests that the lowest and highest tested concentrations of cerium reduced corrosion inhibition in the sol–gel matrix and weakened the coatings.

Non-doped coating (average thickness: 2.7 ± 0.2 μm), showed limited resistance in the neutral salt spray test. Corrosion was visible to the naked eye after exposure for 120 hours. Coatings doped with 0.005 and 0.010 M cerium nitrate (average thickness: 5.5 ± 0.2 and 7.6 ± 0.2 μm, respectively) showed corrosion after 168 hours, while coatings containing 0.001 and 0.100 M cerium nitrate (average thickness: 6.4 ± 0.2 and 11.5 ± 0.2 μm, respectively) showed corrosion after 240 hours. The best performance in the salt spray test, with respect to general and localized corrosion, was shown by coating containing 0.050 M cerium nitrate (average coating thickness: 8.4 ± 0.2 μm). Corrosion was detected after 336 hours of exposure.

Non-doped coating showed delamination, which increased rapidly during exposure to the salt spray. The coatings that incorporated cerium nitrate also showed increasing delamination during exposure, but with markedly reduced rates; for example, the coatings with 0.001 M and 0.050 M cerium nitrate showed comparatively little delamination after exposure to the neutral salt spray for 336 hours. Images of the specimens after salt spray testing for 336 hours are shown in figure 6.3.

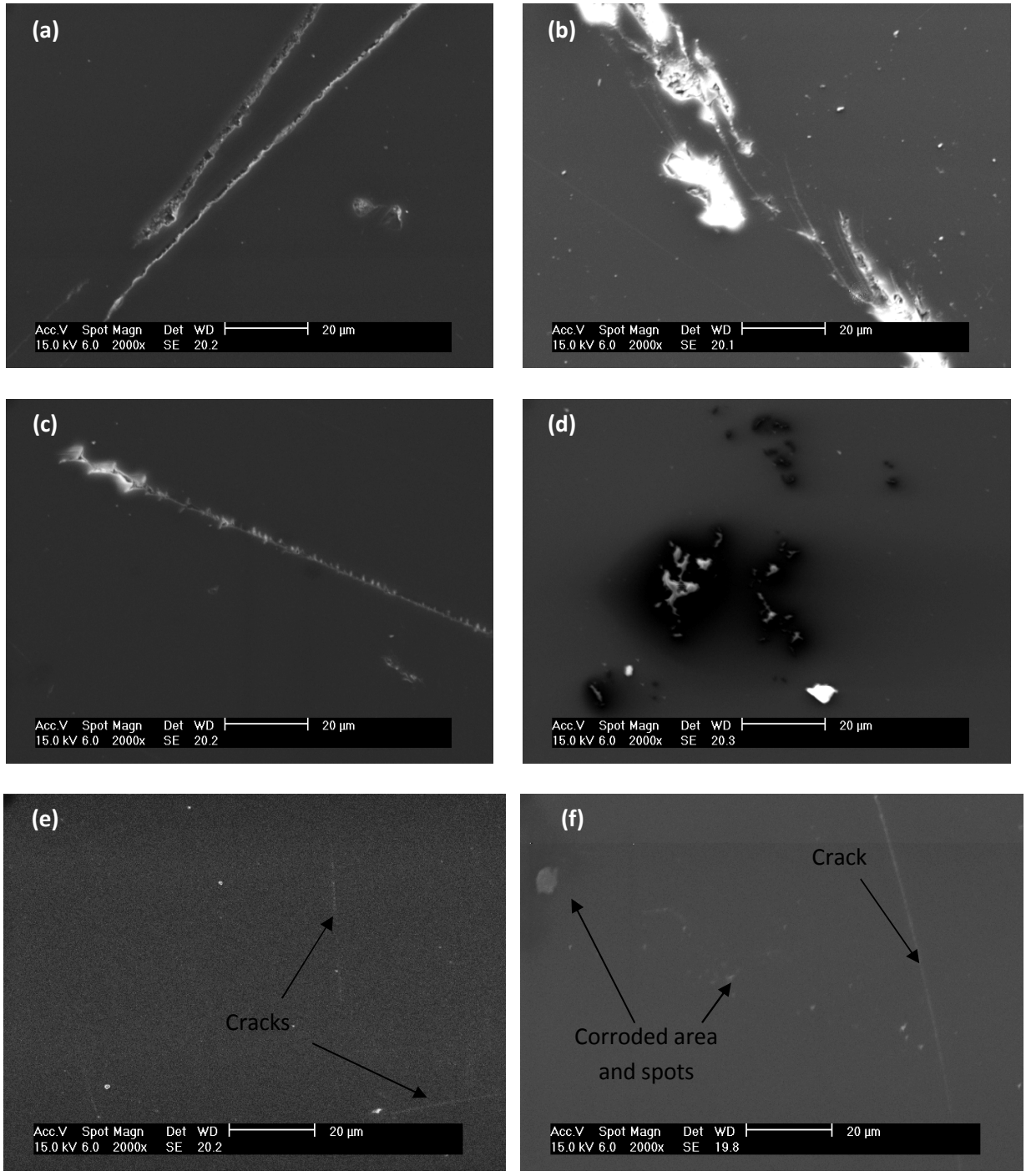

Figure 6.2. Scanning electron micrographs of cerium-silica coatings doped with (a) 0.000 M , (b) 0.001 M, (c) 0.005 M, (d) 0.01 M, (e) 0.05 M and (f) 0.1 M cerium nitrate on HDG steel samples after 144 hours immersion in 3.5% NaCl solution.

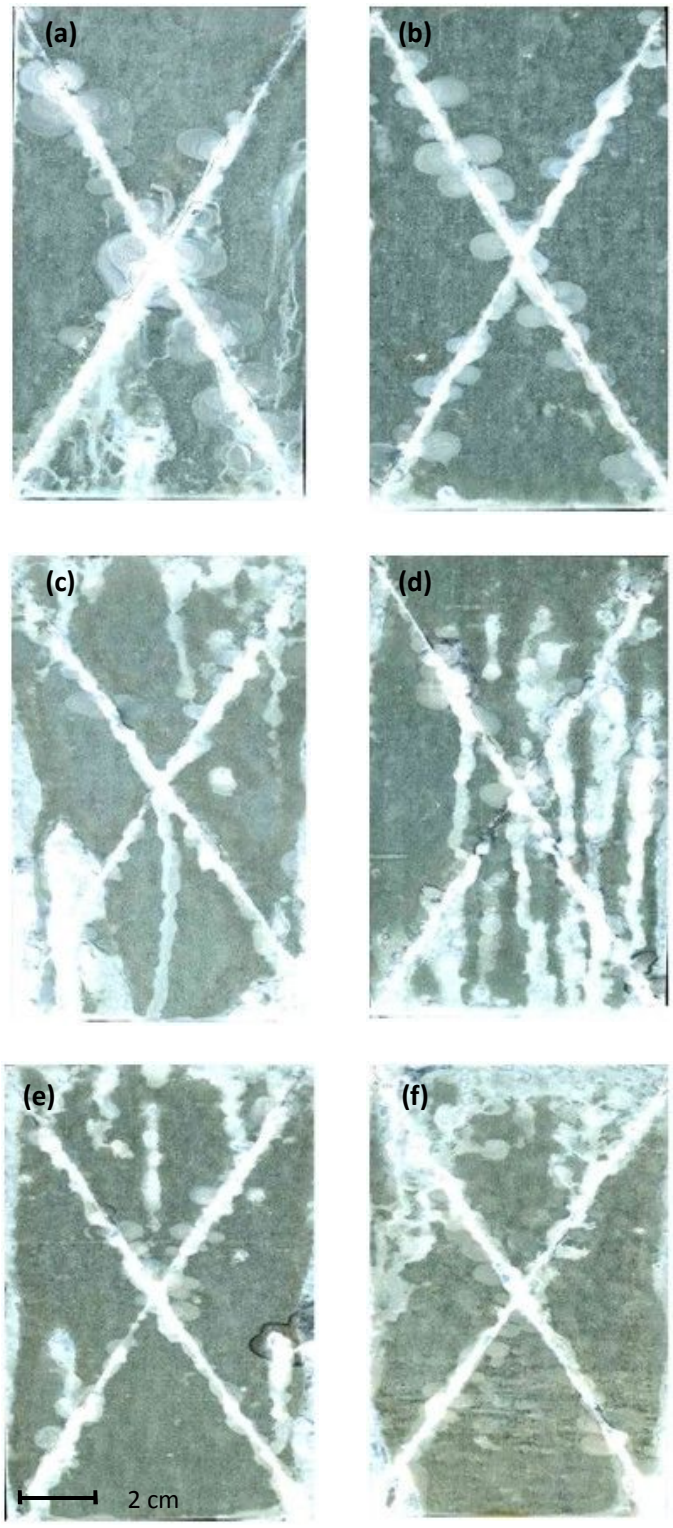

Figure 6.3. Photographs of cerium-silica coatings doped with (a) 0.000 M, (b) 0.001 M, (c) 0.005 M, (d) 0.01 M, (e) 0.05 M and (f) 0.1 M cerium nitrate on HDG steel samples after 336 hours of salt spray exposure.

The different corrosion behaviors of the five samples containing cerium nitrate can be modeled using hybrid networks with limited capacities for inhibitor uptake. A low concentration of inhibiting cerium nitrate leads to improved barrier properties and, therefore, to improved uniform corrosion protection. Increased cerium nitrate content leads to increased porosity, which reduces the barrier properties of the coating and so lowers the protection against corrosion [9, 15, 19, 22].

Corrosion near the scratch behaved differently from the uniform corrosion elsewhere. Increasing the cerium concentration significantly reduced delamination. For instance, the coatings with 0.050 M and 0.1 M cerium nitrate showed less delamination near the scratch than those with lower cerium nitrate contents. The limited delamination in the presence of higher concentrations of cerium nitrate suggests the presence of a corrosion-inhibiting species.

Impedance spectra of the six HDG samples were recorded after 24 hours of immersion in a 3.5 % NaCl solution (Figure 6.4a). The impedance at low frequencies (LF) initially increased with increasing cerium nitrate concentration from 0.000 to 0.050 M. However, above this critical concentration, impedance at LF reduced slightly.

The shape of the phase angle plot in figure 6.4b indicates the presence of two time constants. The high-frequency time constant (around 10^4 rad s^{-1}) is attributable to the response of the silane film, and low-frequency time constant (around 0.316 rad s^{-1}) to the response of processes between the metal oxide layer over the substrate and electrolyte.

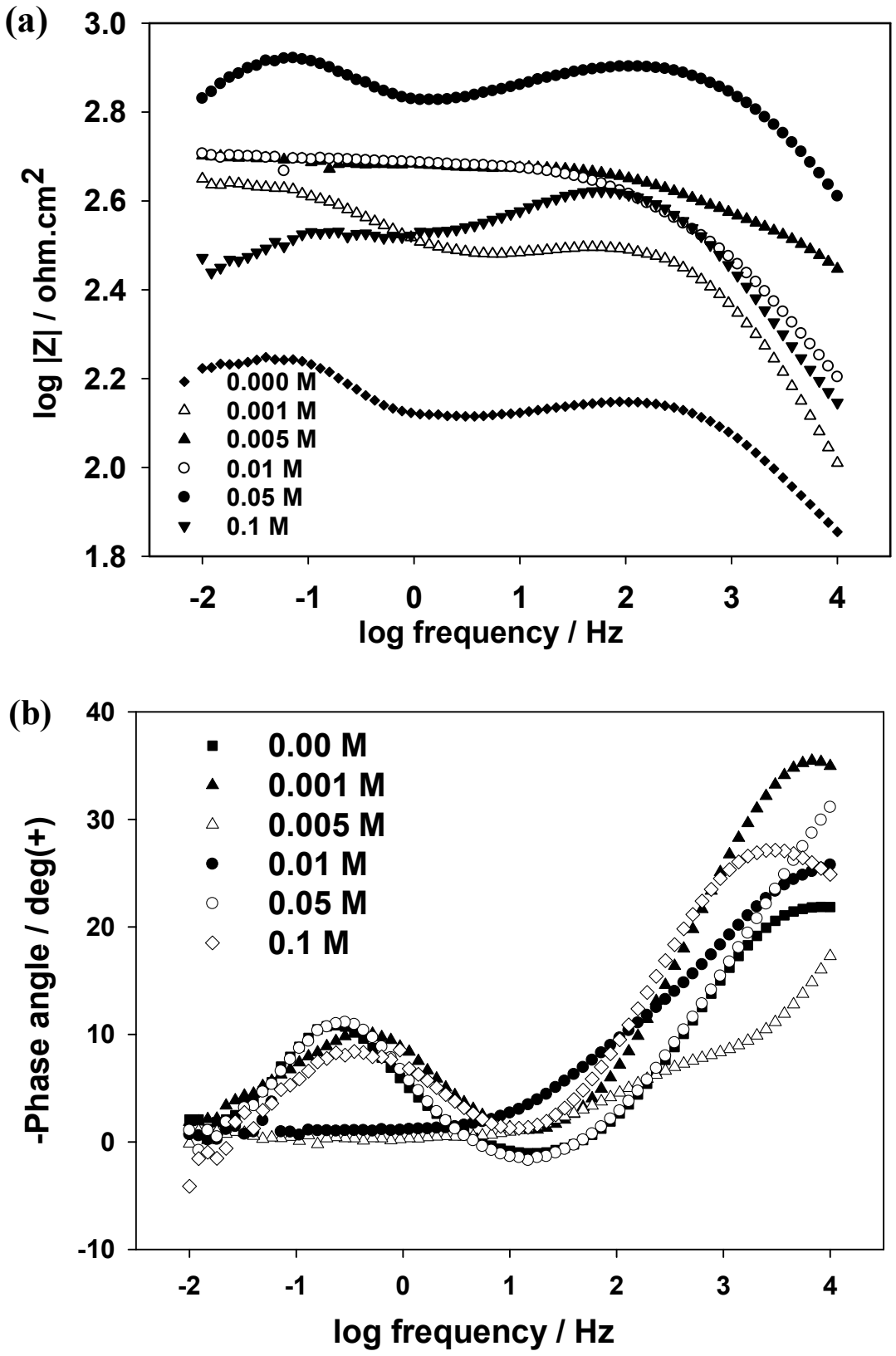

Figure 6.4. EIS Bode modulus (a) and phase angle (b) plots obtained on the HDG steel samples pre-treated with the cerium-silica coatings doped with different concentrations of cerium nitrate. Spectra were obtained after 24 hours of immersion in a 3.5% NaCl solution.

EIS Bode modulus (Figure 6.5a) and phase angle (Figure 6.5b) plots of the various coatings after immersion for 144 hours in a 3.5 % NaCl solution consistently show clear decreases of impedance at LF. This can be attributed to the hydrolytic degradation of the coatings. The impedance at LF of coatings doped with cerium nitrate (except 0.05 M) dropped to less than 300 Ω cm^2. However, the exception, doped with 0.05 M cerium nitrate, retained higher impedance at LF of 337 Ω cm^2. The dependence of corrosion resistance on the cerium concentration indicates the significance of controlling the cerium concentration for optimal protection [13, 14].

The EIS results can be interpreted by numerical fitting using the equivalent circuit depicted in figure 6.6. In this equivalent circuit, R_S is the resistance of the electrolyte; CPE_{coat} ($0.61 < n_{oxide} < 0.84$) and R_{coat} represent the capacitance and resistance of the hybrid coating, respectively and CPE_{oxide} ($0.63 < n_{oxide} < 92$) and R_{oxide} represent the capacitance and resistance of the metal oxide layer over the metal surface, respectively. The variation of the fitted parameters (resistances and capacitances) with immersion time using the equivalent circuits of figure 6.6 is shown in figure 6.7 and 6.8. Values are shown with the errors from the numerical fitting ($10^{-4} <$ Chi-squared $< 10^{-2}$).

The evolution of the properties of the coatings during immersion was assessed by plotting their capacitance and resistance (Figure 6.7). The coatings doped with 0.005 and 0.050 M cerium nitrate had the lowest capacitance during the 144 hours of immersion, demonstrating that they were of the greatest thickness (Figure 6.7a). During immersion, capacitance remained largely consistent, with only a small increase, associated with electrolyte uptake, visible after 24 hours. Increased cerium nitrate doping significantly influenced the capacitance of the coatings, which was raised by about an order of magnitude in the coating with 0.100 M cerium nitrate.

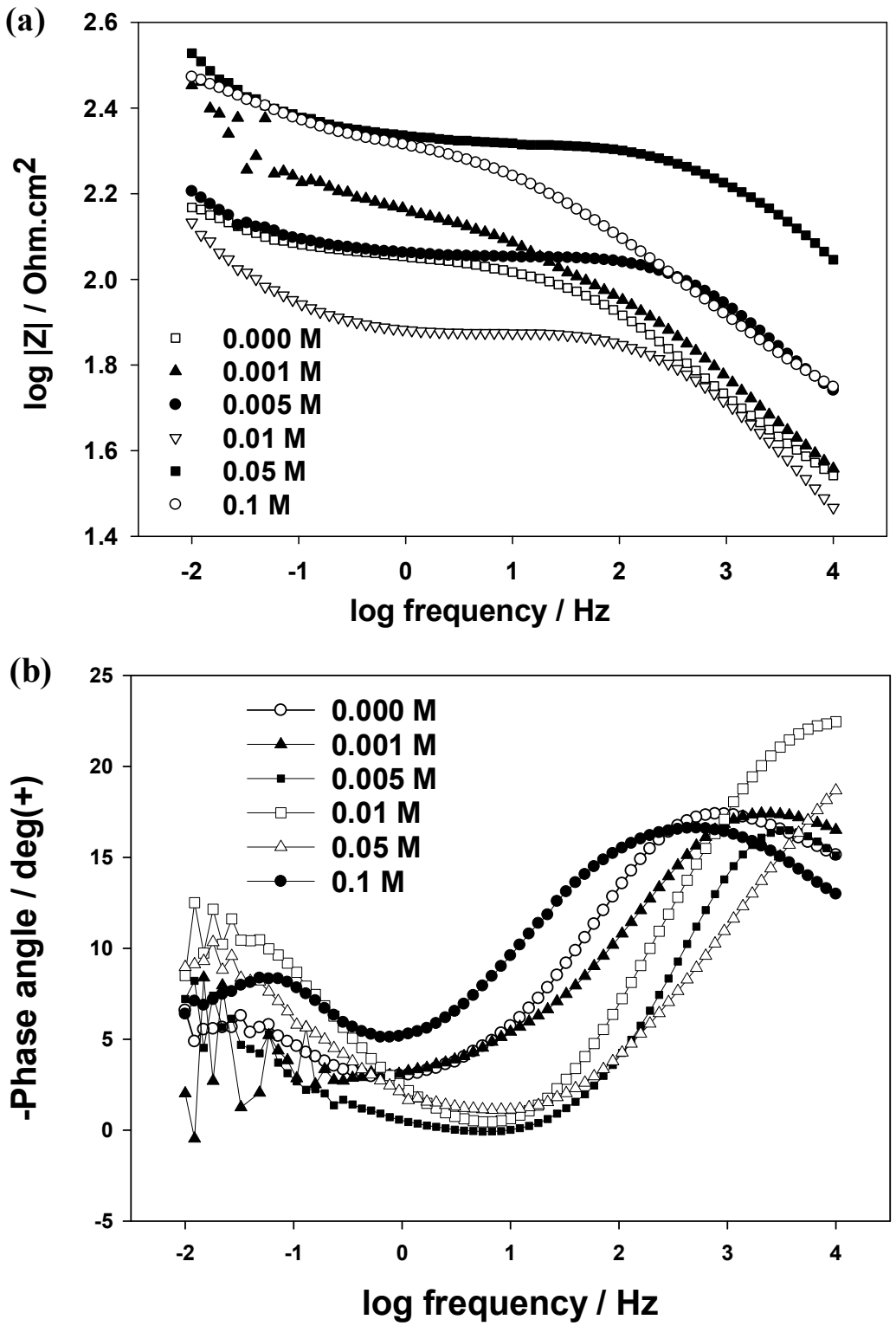

Figure 6.5. EIS Bode modulus (a) and phase angle (b) plots obtained on the HDG steel samples pre-treated with the cerium-silica coatings doped with different concentrations of cerium nitrate. Spectra were obtained after 144 hours of immersion in a 3.5% NaCl solution.

This increase was due to a decrease of the coating thickness and/or a higher porosity, either of which would increase conductivity [14]. During immersion of the coating containing 0.100 M cerium nitrate, film capacitance significantly increased because of water uptake. This was due to the reduced barrier properties of the highly loaded film, which is in accordance with previous results of cerium-doped silane coatings on aluminum alloys (reported by Schem) [19] and on galvanized steel (reported by Trabelsi) [14].

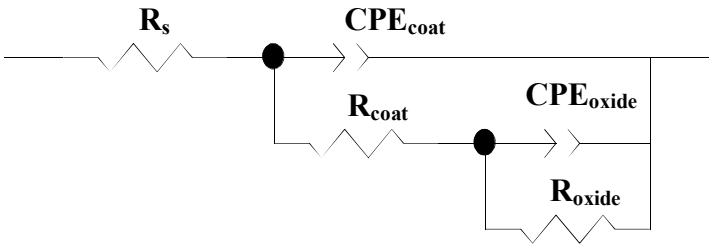

Figure 6.6. The equivalent circuit used for numerical fitting of the EIS data during immersion in a 3.5% NaCl solution.

The evolution of the coating resistance (Figure 6.7b) is an important characteristic of the barrier properties of a protective layer [14, 19]. Upon initial immersion, the highest resistance was shown by the coating containing 0.050 M cerium nitrate. A small increase of coating resistance occurred during the first 24 hours of immersion, probably due to swelling of the matrix and consequent closing of nano/micro pores [19]. Resistance subsequently decreased slowly during the remainder of the 144 hour immersion test, reflecting the stability and good barrier properties of the coating. In contrast, the coatings containing the lowest concentrations of cerium nitrate (0.000 to 0.005 M) rapidly lost their barrier properties; resistance decreased throughout the immersion test. This fast decrease was related to the

formation of new defects and pores in the coatings [19]. The behaviors of resistance and capacitance suggest that there is an optimum level of cerium nitrate doping for the silane solutions [14].

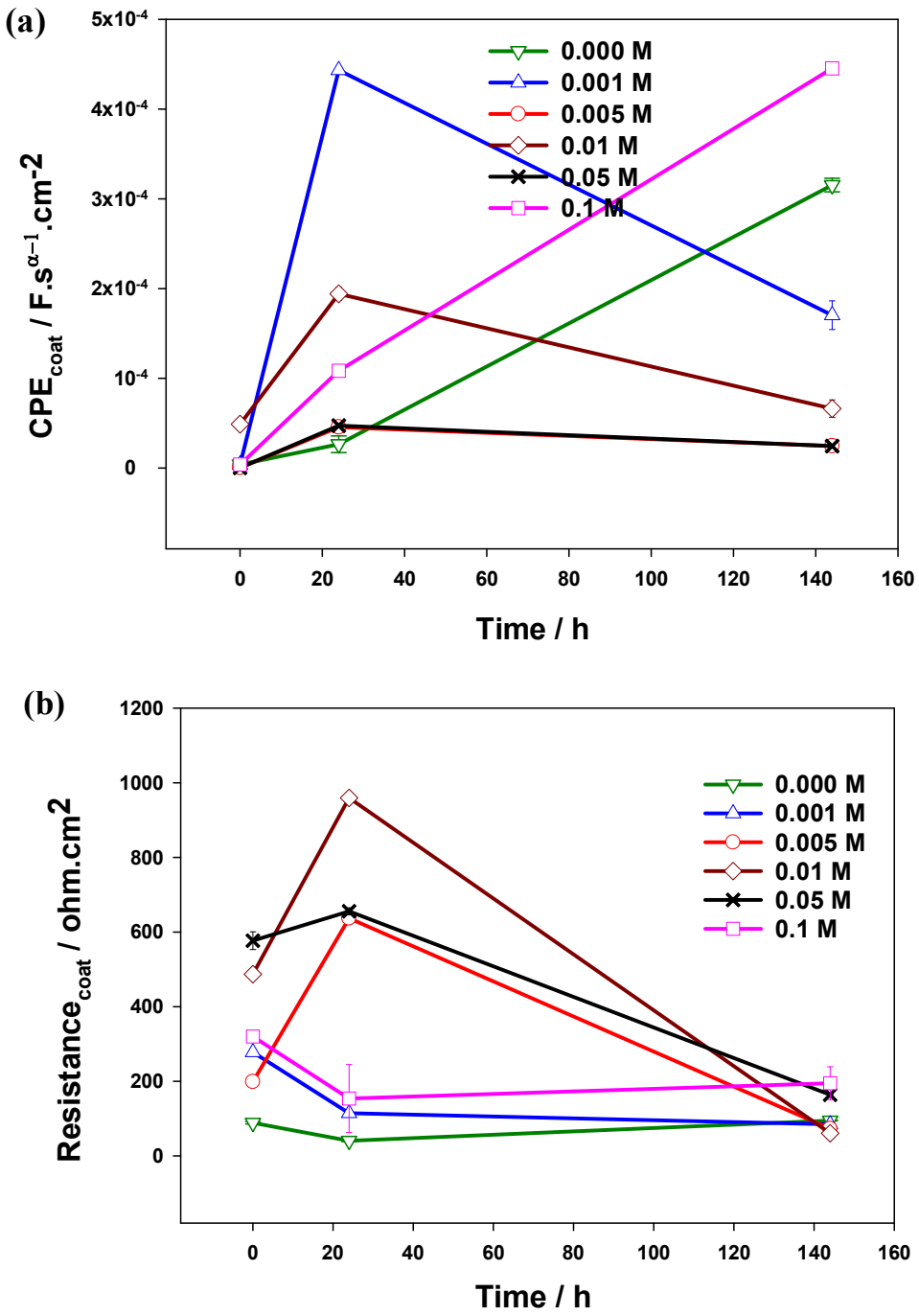

Figure 6.7. Evolution of the coating capacitance (a) and coating resistance (b) during immersion in a 3.5% NaCl solution. Values were obtained by numerical fitting using the equivalent circuit depicted in figure 6.6.

The concentration of cerium nitrate also affected parameters characteristic of the corrosion process between the metal oxide layer and electrolyte; which is associated with the development of a time constant in the low-frequency range of the EIS spectra. Over the first 24 hours of immersion, metal oxide resistance, increased as cerium content increased from 0.000 to 0.050 M (Figure 6.8a). Greater doping led to a significant reduction of metal oxide resistance. All coatings showed decreasing resistance during immersion for 144 hours, although the highest resistances were shown by the coating doped with 0.050 M cerium nitrate. This behavior indicates the good resistance of the doped coating against the onset of corrosion [14].

The metal oxide capacitance (Figure 6.8b) of all the coatings increased during the immersion test. The EIS results also show that the coatings doped with 0.000 and 0.001 M cerium nitrate corroded soonest, with the first signs of corrosion detected after 24 h. The others coatings showed corrosion after 96 hours (except for that containing 0.05 M cerium nitrate). These results are in good agreement with the observations of coating resistance, and indicate that there is an optimal level of cerium doping. The coating with the highest concentration of cerium nitrate showed lower barrier properties, and so allowed corrosion [14].

Potentiodynamic polarization measurements were carried out to estimate the effects of cerium concentration on the corrosion resistance of the coatings (Figure 6.9). The corrosion current (i_{corr}) and corrosion potential (E_{corr}) were determined by Tafel extrapolation [13, 23], and show the effects of the different doping levels (Table 6.1). There are two significant differences between the curves of the non-doped coating and that containing 0.050 M cerium nitrate: E_{corr} shifted to a greatly less negative value and cathodic current density (A/cm^2) markedly reduced.

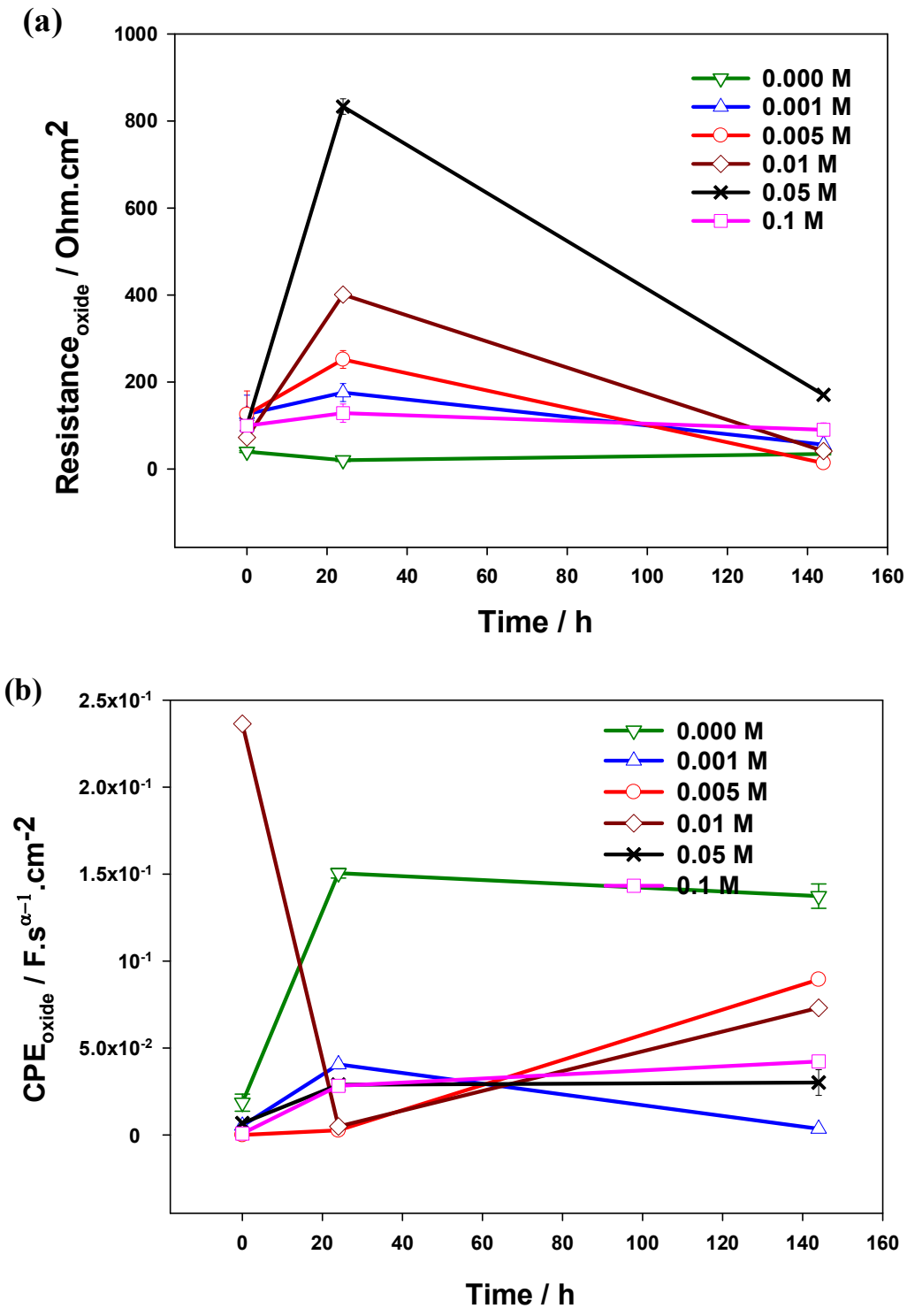

Figure 6.8. Evolution of the metal oxide resistance (a) and capacitance (b) during immersion in a 3.5% NaCl solution. Values were obtained by numerical fitting using the equivalent circuit depicted in figure 6.6.

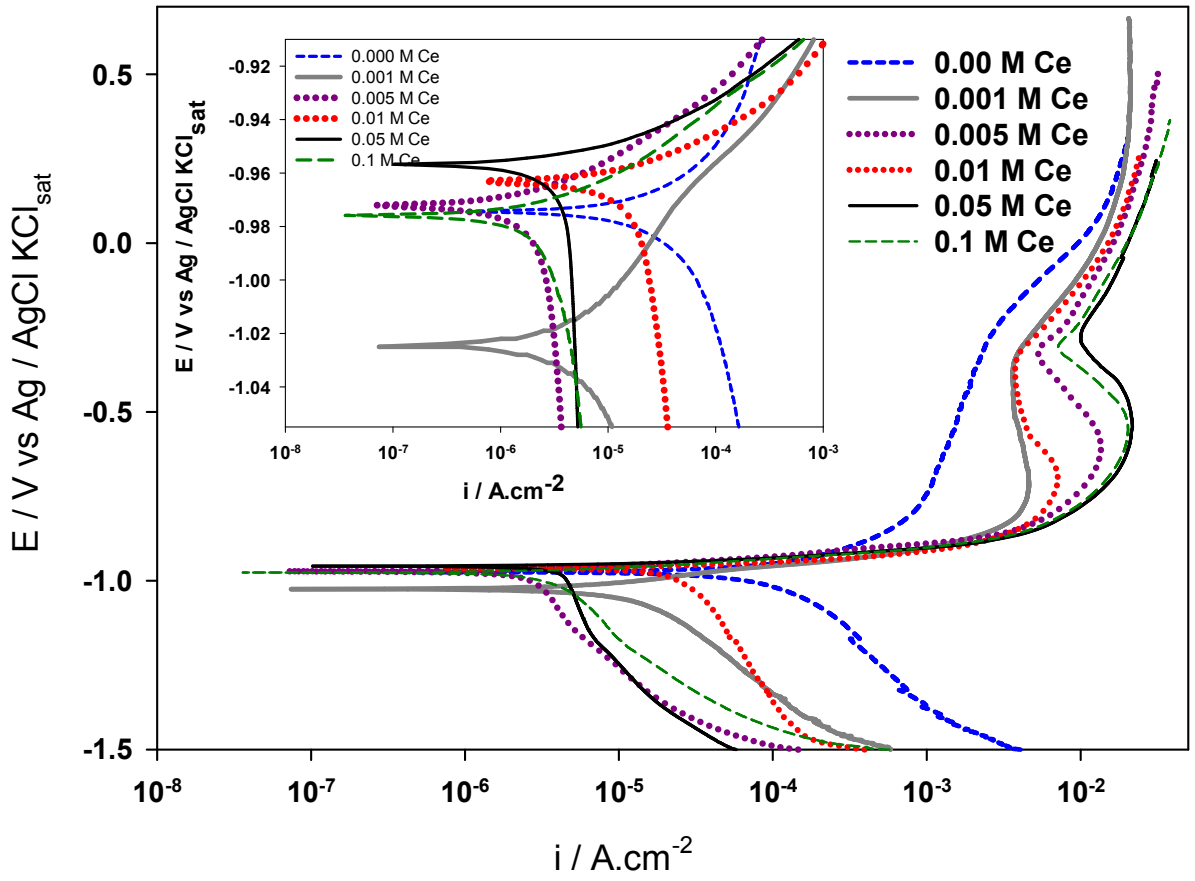

Figure 6.9. Potentiodynamic polarization curves of the cerium-silica coatings doped with different concentrations of cerium nitrate obtained after 1 hour immersion in a 3.5 % NaCl solution. For comparative purposes a plot is also inserted, in which the potential is depicted as the difference between the imposed potential and the corrosion potential. This approach allows a better separation of the anodic and cathodic polarization effects.

The difference in E_{corr} directly reflects the degree of coverage of the coating over the entire substrate [24]. Good coverage provides a continuous nano-porous coating layer, which causes E_{corr} to shift to a more positive value. The reduction of cathodic current density is attributable to the inhibition of the cathodic reaction at the corrosion site, particularly the oxygen reduction reaction [24, 25]. Similar behavior has been reported by Zhong et al. [13] for the magnesium alloy AZ91D in 3.5 % NaCl solution after the addition of cerium nitrate.

Their results suggest that Ce^{3+} ions react in a first stage with OH^- ions, which are generated in the cathodic zones of the alloy, leading to the formation of localized areas rich in cerium. These are then involved in blocking the cathodic sites, which is reflected in the reduced corrosion rate. Hence, such a reaction, which leads to the corrosion of steel, appears to be retarded by a silica coating containing an inhibitor of 0.05 M cerium nitrate.

Table 6.1. Summary of the electrochemical parameters obtained from the polarization measured in a 3.5 % NaCl solution.

sample	E_{corr} (V)	i_{corr} (A cm^{-2})	b_c (V/dec)	b_a (V/dec)	Passive area (V)
0.000 M	-0.974	3.577×10^{-5}	0.06	0.093	-0.792 to -0.241
0.001 M	-1.025	3.484×10^{-6}	0.043	0.057	-0.815 to -0.348
0.005 M	-0.972	1.184×10^{-6}	0.017	0.066	-0.829 to -0.320
0.01 M	-0.963	6.013×10^{-6}	0.014	0.027	-0.838 to -0.341
0.05 M	-0.957	1.749×10^{-6}	0.047	0.0096	-0.864 to -0.289
0.1 M	-0.976	1.020×10^{-6}	0.016	0.027	-0.840 to -0.304

6.4. Conclusion

Pre-treatments of hot dip galvanized steel based on the use of 3-glycidoxypropyltrimethoxysilane (GPTMS) and bisphenol A (BPA) doped with different concentrations of cerium nitrate reveal a relatively smooth surface morphology without cracks or defects before the corrosion test. After the corrosion test the morphology of the coatings depend on the cerium nitrate concentration. The results confirm that very low and very high cerium concentrations lead to a lack of corrosion inhibition in the sol-gel matrix. The optimum concentration of cerium nitrate is 0.050 M. These coatings resist for 336 hours the

salt spray exposure with only a reduced corrosion near the artificial scratch and uniform corrosion, compared to the silane coating without cerium nitrate.

Upon addition of cerium nitrate as dopant, the silane coating shows improved barrier properties, coating resistance and a decrease in coating capacitance. Incorporation of 0.05 M cerium nitrate reduces the cathodic current density by two orders of magnitude and shifts the voltage to more positive values compared with the non-doped silane coated substrate during polarization in a 3.5 % NaCl solution.

References

1. N.C. Rosero-Navarro, S.A. Pellice, A. Durán, M. Aparicio, Effects of Ce-containing sol–gel coatings reinforced with SiO_2 nanoparticles on the protection of AA2024, Corrosion Science, 50, 2008, pp. 1283-1291.
2. K.A. Yasakau, M.L. Zheludkevich, O.V. Karavai, M.G.S. Ferreira, Influence of inhibitor addition on the corrosion protection performance of sol–gel coatings on AA2024, Progress in Organic Coatings, 63, 2008, pp. 352-361.
3. M.L. Zheludkevich, R. Serra, M.F. Montemor, K.A. Yasakau, I.M.M. Salvado, M.G.S. Ferreira, Nanostructured sol–gel coatings doped with cerium nitrate as pre-treatments for AA2024-T3: corrosion protection performance, Electrochimica Acta, 51, 2005, pp. 208-217.
4. A. Pepe, M. Aparicio, S. Ceré, A. Durán, Preparation and characterization of cerium doped silica sol–gel coatings on glass and aluminum substrates, Journal of Non-Crystalline Solids, 348, 2004, pp. 162-171.
5. M.F. Montemor, M.G.S. Ferreira, Cerium salt activated nanoparticles as fillers for silane films: evaluation of the corrosion inhibition performance on galvanised steel substrates, Electrochimica Acta, 52, 2007, pp. 6976-6987.

6. M.F. Montemor, M.G.S. Ferreira, Analytical and microscopic characterisation of modified bis-[triethoxysilylpropyl] tetrasulphide silane films on magnesium AZ31 substrates, Progress in Organic Coatings, 60, 2007, pp. 228-237.
7. R. Zandi Zand, K. Verbeken, A. Adriaens, Corrosion resistance performance of cerium doped silica sol–gel coatings on 304L stainless steel, Progress in Organic Coatings, 75, 2012, pp. 463-473.
8. H. Wang, R. Akid, Encapsulated cerium nitrate inhibitors to provide high-performance anti-corrosion sol–gel coatings on mild steel, Corrosion Science, 50, 2008, pp. 1142-1148.
9. A. Phanasgaonkar, V.S. Raja, Influence of curing temperature, silica nanoparticles- and cerium on surface morphology and corrosion behaviour of hybrid silane coatings on mild steel, Surface and Coatings Technology, 203, 2009, pp. 2260-2271.
10. A.M. Cabral, W. Trabelsi, R. Serra, M.F. Montemor, M.L. Zheludkevich, M.G.S. Ferreira, The corrosion resistance of hot dip galvanised steel and AA2024-T3 pre-treated with bis-[triethoxysilylpropyl] tetrasulfide solutions doped with $Ce(NO_3)_3$, Corrosion Science, 48, 2006, pp. 3740-3758.
11. R. Zandi Zand, K. Verbeken, A. Adriaens, The corrosion resistance of 316L stainless steel coated with a silane hybrid nanocomposite coating, Progress in Organic Coatings, 72, 2011, pp. 709-715.
12. R. Zandi Zand, K. Verbeken, A. Adriaens, Electrochemical assessment of the self-healing properties of cerium doped sol-gel coatings on 304L stainless steel substrates, International Journal of Electrochemical Science, 7, 2012, pp. 9592-9608.
13. X. Zhong, Q. Li, J. Hu, X. Yang, F. Luo, Y. Dai, Effect of cerium concentration on microstructure, morphology and corrosion resistance of cerium–silica hybrid coatings on magnesium alloy AZ91D, Progress in Organic Coatings, 69, 2010, pp. 52-56.

14. W. Trabelsi, P. Cecilio, M.G.S. Ferreira, M.F. Montemor, Electrochemical assessment of the self-healing properties of Ce-doped silane solutions for the pre-treatment of galvanised steel substrates, Progress in Organic Coatings, 54, 2005, pp. 276-284.
15. M. Garcia-Heras, A. Jimenez-Morales, B. Casal, J.C. Galvan, S. Radzki, M.A. Villegas, Preparation and electrochemical study of cerium–silica sol–gel thin films, Journal of Alloys and Compounds, 380, 2004, pp. 219-224.
16. M.L. Zheludkevich, D.G. Shchukin, K.A. Yasakau, H. Möhwald, M.G.S. Ferreira, Anticorrosion coatings with self-healing effect based on nanocontainers impregnated with corrosion inhibitor, Chemistry of Materials, 19, 2007, pp. 402-411.
17. N.C. Rosero-Navarro, L. Paussa, F. Andreatta, Y. Castro, A. Durán, M. Aparicio, L. Fedrizzi, Optimization of hybrid sol–gel coatings by combination of layers with complementary properties for corrosion protection of AA2024, Progress in Organic Coatings, 69, 2010, pp. 167-174.
18. R. Zandi-Zand, Investigation of corrosion, abrasion and weathering resistance in hybrid nanocomposite coatings based on epoxy-silica, Thesis, Azad University- Tehran North Branch, 2005.
19. M. Schem, T. Schmidt, J. Gerwann, M. Wittmar, M. Veith, G.E. Thompson, I.S. Molchan, T. Hashimoto, P. Skeldon, A.R. Phani, S. Santucci, M.L. Zheludkevich, CeO_2-filled sol–gel coatings for corrosion protection of AA2024-T3 aluminium alloy, Corrosion Science, 51, 2009, pp. 2304-2315.
20. W. Trabelsi, P. Cecílio, M.G.S. Ferreira, K. Yasakau, M.L. Zheludkevich, M.F. Montemor, Surface evaluation and electrochemical behaviour of doped silane pre-treatments on galvanised steel substrates, Progress in Organic Coatings, 59, 2007, pp. 214-223.

21. S. Dalbin, G. Maurin, R.P. Nogueira, J. Persello, N. Pommier, Silica-based coating for corrosion protection of electrogalvanized steel, Surface and Coatings Technology, 194, 2005, pp. 363-371.
22. J. Ballarre, E. Jimenez-Pique, M. Anglada, S.A. Pellice, A.L. Cavalieri, Mechanical characterization of nano-reinforced silica based sol–gel hybrid coatings on AISI 316L stainless steel using nanoindentation techniques, Surface and Coatings Technology, 203, 2009, pp. 3325-3331.
23. ASTM G 3 - 89; Standard practice for conventions applicable to electrochemical measurements in corrosion testing, Annual Book of ASTM Standards, 03.02, ASTM International, PA, USA, 2004.
24. T. Sugama, Cerium acetate-modified aminopropylsilane triol: a precursor of corrosion-preventing coating for aluminum-finned condensers, Journal of Coatings Technology and Research, 2, 2005, pp. 649-659.
25. M. Hosseini, H. Ashassi-Sorkhabi, H.A.Y. Ghiasvand, Corrosion protection of electro-galvanized steel by green conversion coatings, Journal of Rare Earths, 25, 2007, pp. 537-543.

7

Evaluation of corrosion inhibition by silane coatings filled with cerium salt-activated nanoparticles on hot-dip galvanized steel substrates [1]

7.1. Introduction

Zinc coatings are predominantly used for an improved aqueous corrosion resistance of steel by two mechanisms, namely barrier and galvanic protection. On the one hand, the zinc coating serves as a barrier between the steel substrate and the corrosive environment. Consequently zinc will be attacked before steel. On the other hand, since zinc is less noble, i.e. more anodic than iron at ambient conditions, it will also offer galvanic protection as zinc will sacrificially corrode to protect the steel substrate, even if steel is exposed at cut edges or

[1] Published as full paper in International Journal Electrochemical Science, Volume 8, Roohangiz Zandi Zand, Kim Verbeken and Annemie Adriaens, Evaluation of the Corrosion Inhibition Performance of Silane Coatings Filled with Cerium Salt-Activated Nanoparticles on Hot-Dip Galvanized Steel Substrates, 4924-4940, (2013).

at scratches. Typical processing methods used to apply Zn-based coatings include hot-dip galvanizing (HDG), thermal spraying and electro deposition. HDG is the immersion of a steel compound in a molten bath of zinc or a zinc-alloy. Both batch and continuous processing methods are industrially available [1]. An extensive overview of the metallurgy of zinc coated steels can be found in the review of Marder [2].

The corrosion resistance of HDG steel can be improved by the application of coatings [2]. One approach to improve corrosion resistance of HDG steel is based on hybrid organic–inorganic coatings [3, 4]. This approach combines the advantages of the inorganic and organic components. The organic constituent provides flexibility, reduces defectiveness, and improves the compatibility with the polymer coatings, while the inorganic part is responsible for the superior adhesion to the metal surface and the high ductility. Moreover, these coatings can be applied at relatively low temperatures.

The anticorrosive properties of hybrid organic–inorganic coatings can be improved by the incorporation of nanoparticles in the coating [5-10]. The nanoparticles can be synthesized in the films, as demonstrated for sol–gel coatings [9, 11], or they can be added to the pre-treatment solutions [12]. The corrosion resistance of Mg alloys, pre-treated with sol–gel coatings containing ZrO_2 and CeO_2 nanoparticles, has been investigated previously, and it was reported that the CeO_2 component provided enhanced corrosion protection, while ZrO_2 imparted corrosion resistance and wear resistance [13].

Van Ooij and co-workers [14] reported that bis-sulfur silane films could be thickened and strengthened by loading them with silica particles. However, when the bis-sulfur silane film was heavily loaded with silica, it tended to form a porous film, which promoted electrolyte intrusion and premature film delamination. The addition of SiO_2 nanoparticles to silane films electrodeposited on aluminum also revealed beneficial effects, and a “critical

content" of nanoparticles was proposed [15]. The results obtained in these studies focused mainly on the role of the nanoparticles in the barrier properties of the film, and little attention was given at the role of the nanoparticles in the electrochemical processes involved in the corrosion processes of metallic substrates [11].

Ceria nanoparticles are versatile materials that have found applications in many different fields, including catalysis [16], semiconductores [17], sensors [18, 19], biomaterials [20], cosmetics [7], and coatings [21, 22]. With respect to coatings, ceria nanoparticles have shown to improve wear and corrosion resistance in acidic media [22]. NiAl intermetallic coatings containing CeO_2, in comparison with the coating without CeO_2, exhibited higher hardness, an improved elastic modulus, fewer defects, and decreased porosity [23]. Ce_2O_3–CeO_2 layers showed a pronounced stabilizing effect on the passive state of steel and its corrosion resistance in a sulfuric acid medium, which allows these coated steels to be used as construction materials for reactors neutralizing sulfuric acid-containing emissions [24]. It has also been reported that nano-CeO_2 and nano-SiO_2 particles increased the thermal stability of Ni–W–P alloy coatings at high temperatures, and improved their micro-hardness [25].

Previous work has reported the protective nature of silane coatings modified with CeO_2 nanoparticles and cerium nitrate (chapter 5). The results demonstrated that ceria nanoparticles were very effective fillers; they led to improved barrier properties in the silane coatings, and improved the corrosion inhibition. It was established that the positive impact on both the barrier properties and the corrosion inhibition was significantly improved by modifying the silane solution with cerium nitrate. The presence of cerium nitrate reinforced the barrier properties of the silane films, reducing the corrosion activity and improved self-healing the corroded areas.

The present work reports and discusses the protective behavior of silane films loaded with CeO_2 nanoparticles. The nanoparticles were activated with cerium ions to improve the corrosion resistance of the galvanized steel substrates.

7.2. Sample preparation

Ceria nanoparticles (10 wt% in water, particle size < 25 nm, Sigma Aldrich) were ultrasonically dispersed in an aqueous solution of cerium nitrate (Fluka), to obtain concentrations of 0.025 M for the nanoparticles, and 0.025 M for the cerium nitrate. This aqueous dispersion was then used to prepare what will be called the "silane solution containing activated CeO_2 nanoparticles" in the remaining part of the chapter.

Another set of ceria nanoparticles was ultrasonically dispersed in water at a concentration of 0.05 M. This aqueous dispersion was used to prepare what will be called the "silane solution containing CeO_2 nanoparticles" in the remaining part of the chapter.

The silane solution was prepared by adding 4.084 mL of 3-glicidoxypropyltrimethoxy silane or GPTMS (Merck) to 0.5 mL of HCl-acidified water (pH = 2) (H_2O/Si mole ratio = 0.5 [26]). The solution was placed in a sealed beaker and stirred at room temperature for 20 min at a rate of 240 rpm, to hydrolyze and condensate the silane precursors. The aqueous dispersion of ceria nanoparticles was added at the end of this synthesis step, and this was followed by stirring for 10 min. In the following step, 2.111 g of bisphenol A (BPA) (Merck) was added to the solutions as a cross-linking agent (BPA/Si mole ratio = 0.5). The latter has been shown to realize a significant effect on the morphology and improvement of the corrosion resistance of coatings [27]. The BPA was dissolved by mixing the solution for 80 minutes. To accelerate the condensation reaction, 0.0152 mL of 1-methylimidazol (MI)

(Merck) (MI/Si mole ratio = 0.01) was added to the solution, which was followed by stirring for 5 min. The result was a clear and colorless homogenous solution.

Identical silane solutions were prepared with and without cerium nitrate, to obtain the so-called "cerium modified and non-modified silane coatings". The Ce/Si mole ratio was 0.05.

The metallic substrate consisted of hot dip-galvanized steel coupons (1.13 cm^2 area and 0.1 cm thickness for the AFM, SEM, and electrochemical tests) and plates (7 × 15 × 0.1 cm for the salt spray tests). The galvanized steel specimens after degreasing, as explained in chapter 6, immersed in the silane solution for 60 s. The coated specimens were dried at room temperature for 24 h, and subsequently submitted to a 25–130°C curing process with a heating rate of 7.5 °C/min for 90 minutes, to initiate extensive cross-linking in the hybrid films [28]. The coating thickness was measured by cross-sectioning method.

7.3. Results and discussion

AFM images of the bare and coated HDG substrates with both non-modified and cerium-modified silane coatings presented in Figure 7.1. AFM images of the bare HDG steel sample (Figure 7.1a, b), show a heterogeneous surface with an RMS surface roughness of 57.025. These images reveal some grains (crystal structure) of zinc in different sizes as well as distinct arrays (growth grains). These images used as reference to investigate the effect of hybrid coating on microstructure and roughness of galvanized steel substrates.

AFM image of non-modified silane coating (Figure 7.1c) shows formation of a defect and crack free coating with an RMS surface roughness of 0.608 nm. Also, the image reveals some large particles that likely resulted from the agglomeration of smaller silica particles on the surface [29, 30].

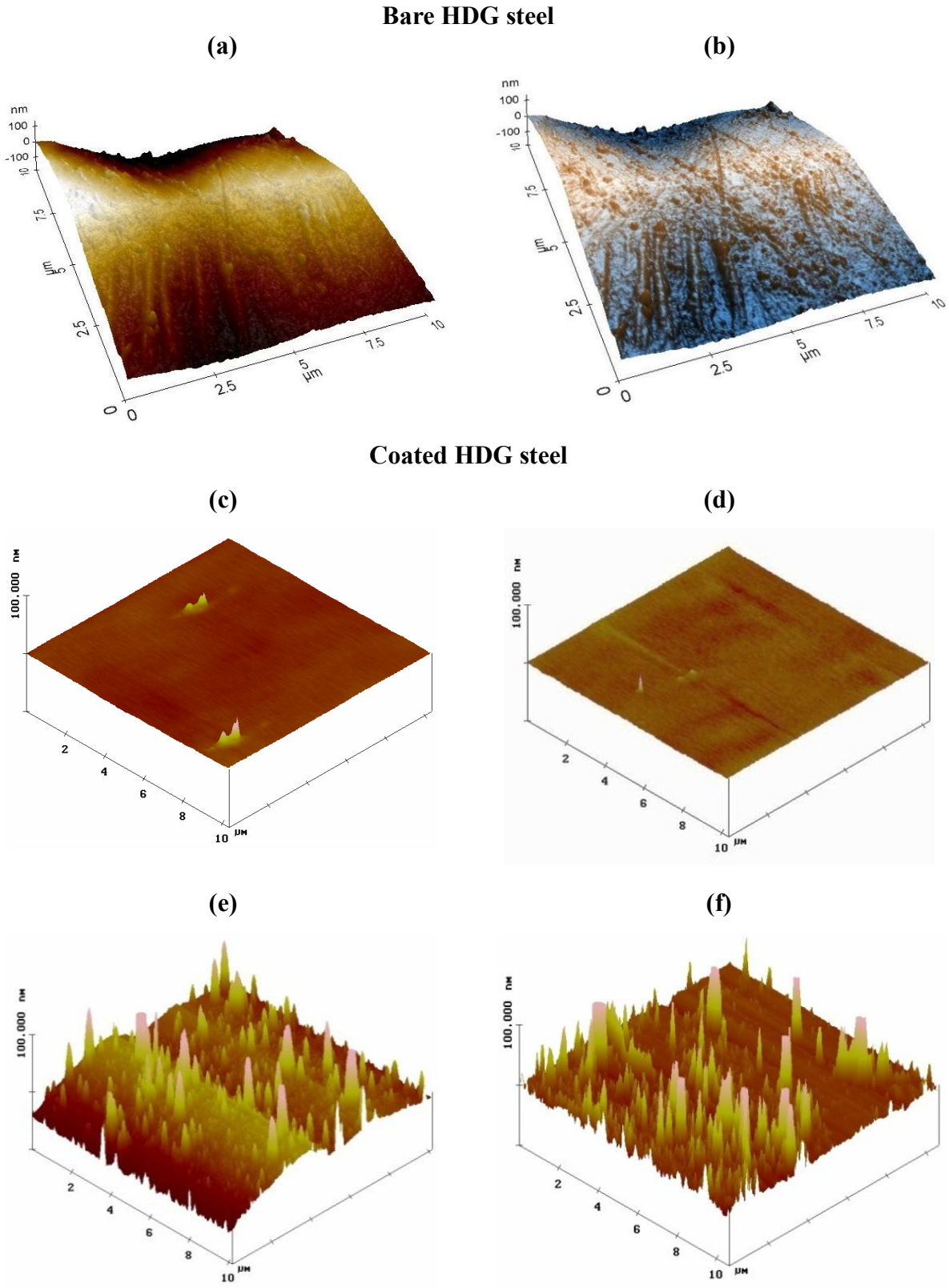

Figure 7.1. AFM topographic images of the bare (a, b; in different color scales) and coated HDG steel samples with blank silane (c), $Ce(NO_3)_3.6H_2O$ (d), CeO_2 nanoparticles (e), and CeO_2 + $Ce(NO_3)_3.6H_2O$ (f). AFM images for the bare and coated specimens recorded in non-contact and tapping mode respectively.

The silane coating modified with $Ce(NO_3)_3$, also, showed a defect and crack free surface without any agglomerates with an RMS surface roughness of 0.402 nm (Figure 7.1 d).

AFM image of the coating modified with non-activated CeO_2 nanoparticles (Figure 7.1e) shows a number of CeO_2 nanoparticles uniformly distributed in the silane coating, which had an RMS roughness of 8.421 nm. Also, some agglomerates were visible in the image. The sharper color contrast of the topographic image suggests larger height differences. The color contrast was uniformly distributed throughout the image, indicating heterogeneity of the coating thickness. Similar observations were reported by Phanasgaonkar et al. [29].

AFM image of the silane film filled with activated CeO_2 nanoparticles (Figure 7.1f) reveals a number of CeO_2 nanoparticles uniformly distributed in the silane coating, which had an RMS roughness of 6.210 nm. The image shows that the outer surface layers of this coating contained nanometer-scale particles and agglomerates. These results suggest that the addition of cerium ions altered the surface morphology of the coating modified with non-activated CeO_2 nanoparticles.

SEM revealed the effects of the CeO_2 nanoparticles on the microstructure and qualitative chemical composition of the various silane coatings. Figure 7.2a shows the surface of the typical blank silane coating prior to immersion in a 3.5 % NaCl solution. It appears uniform and defect- and crack-free. However, several white agglomerates appeared in the coating matrix, which were identified by EDX as being Si-rich (Figure 7.2b). It is likely that these features were clusters of nanoparticles formed in the outermost layers of the silane film 1, 39. The coatings doped with cerium nitrate (Figure 7.2c) and non-activated cerium oxide nanoparticles (Figure 7.2d) contained particles of many different sizes. These particles were equally distributed in the coatings, and no micro-scale pores or cracks were observed. The silane film filled with CeO_2 nanoparticles activated with cerium ions showed fewer and

smaller silica agglomerations than the blank silane film (Figure 7.2e). EDX analysis of this region (Figure 7.2f) clearly showed the presence of cerium and silicon peaks, indicating that the addition of activated CeO_2 nanoparticles led to the decomposition of the silane chains and a reduction in the size of the particles in the sols [29, 31].

The thicknesses of the silane films were also determined using SEM. The silane coatings modified with cerium nitrate and non-activated cerium oxide nanoparticles showed thicknesses of approximately 2.16 and 4.97 μm, respectively. Thickness increased to approximately 6.77 μm for the coating filled with CeO_2 nanoparticles activated with cerium ions. All modified films were thicker than the blank silane film (approximately 1.89 μm), suggesting that thicker or better cross-linked coatings formed in the presence of the activated ceria nanoparticles, as also observed by Montemor et al. [13] and Garcia-Heras et al. [32]. This modification of the coating matrix could improve the resistance to oxidation of the substrate [29].

SEM images of the non-modified and cerium-modified silane coatings obtained after electrochemical impedance spectroscopy testing (Figure 7.3) indicate the ability of the sol–gel coatings to protect the HDG substrates. All the coatings showed localized corrosion after immersion for 144 h in a 3.5 % NaCl solution: exfoliation of the corrosion products and cracks of different sizes were observed. These localized attacks promoted the deterioration and delamination of the hybrid film, possibly due to hydrolysis reactions at the interface.

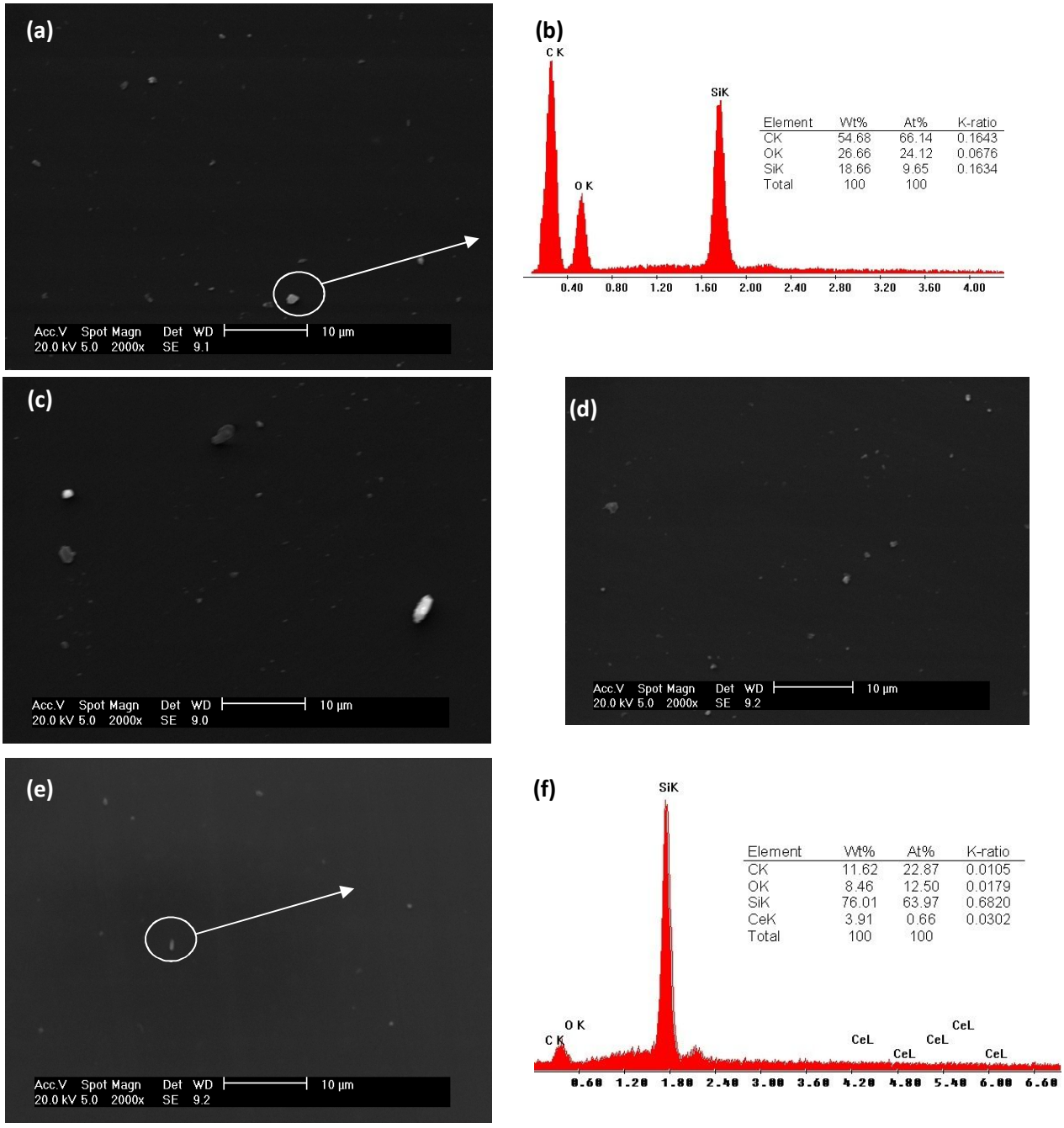

Figure 7.2. Scanning electron micrographs (a, c, d, e) and EDX spectrum obtained from the indicated regions (b, f) of the HDG steel samples coated with blank silane (a, b), $Ce(NO_3)_3.6H_2O$ (c), CeO_2 nanoparticles (d), and $CeO_2 + Ce(NO_3)_3.6H_2O$ (e, f) prior to immersion in a 3.5% NaCl solution.

Additionally, the diffusion of the oxidant ions became faster, and the corrosion rate increased, causing an accumulation of corrosion products at the interface, and at the same time promoting the formation of defects and micro-cracks [33].

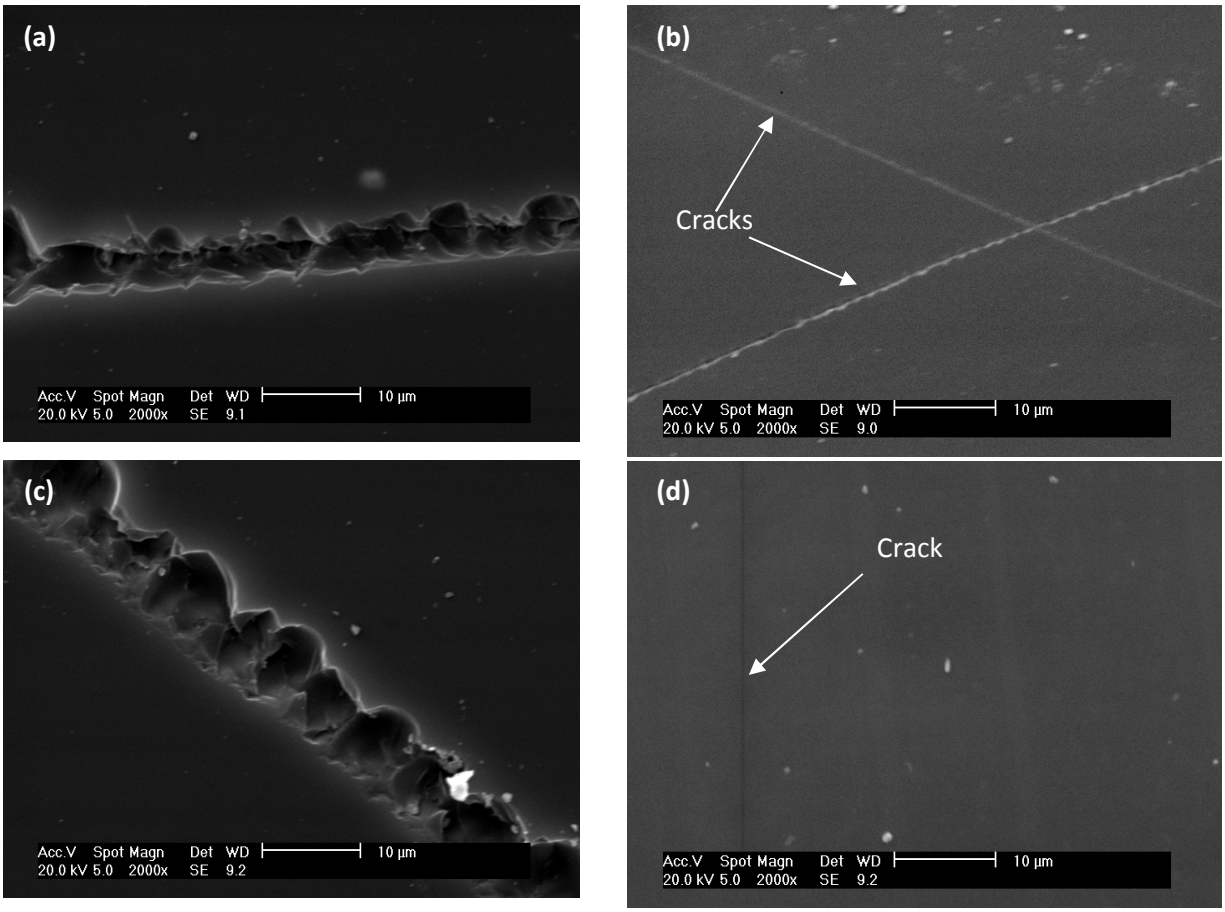

Figure 7.3. Scanning electron micrographs of the HDG steel samples coated with blank silane (a), $Ce(NO_3)_3.6H_2O$ (b), CeO_2 nanoparticles (c), and CeO_2 + $Ce(NO_3)_3.6H_2O$ (d) after 144 h of immersion in a 3.5% NaCl solution.

However, the SEM results showed that the barrier properties of the films containing the activated nanoparticles (Figure 7.3d) were improved, likely as a consequence of the increased film thickness. The presence of the cerium ions also promoted the formation of reactive silanol groups in the silane molecules, leading to a higher degree of cross-linking,

higher silicon content, and, therefore, more homogeneous films with better barrier properties, as has been confirmed by Montemor et al. [13].

To detect possible differences among the differently modified silane films, 144 h salt spray tests were performed (Figure 7.4). At the initial stages of exposure, all coatings showed the sacrificial dissolution of zinc in the artificially scratched area. The breakdown of the coating layers progressed with time; eventually the zinc coatings degraded, resulting in the formation of white rust [34].

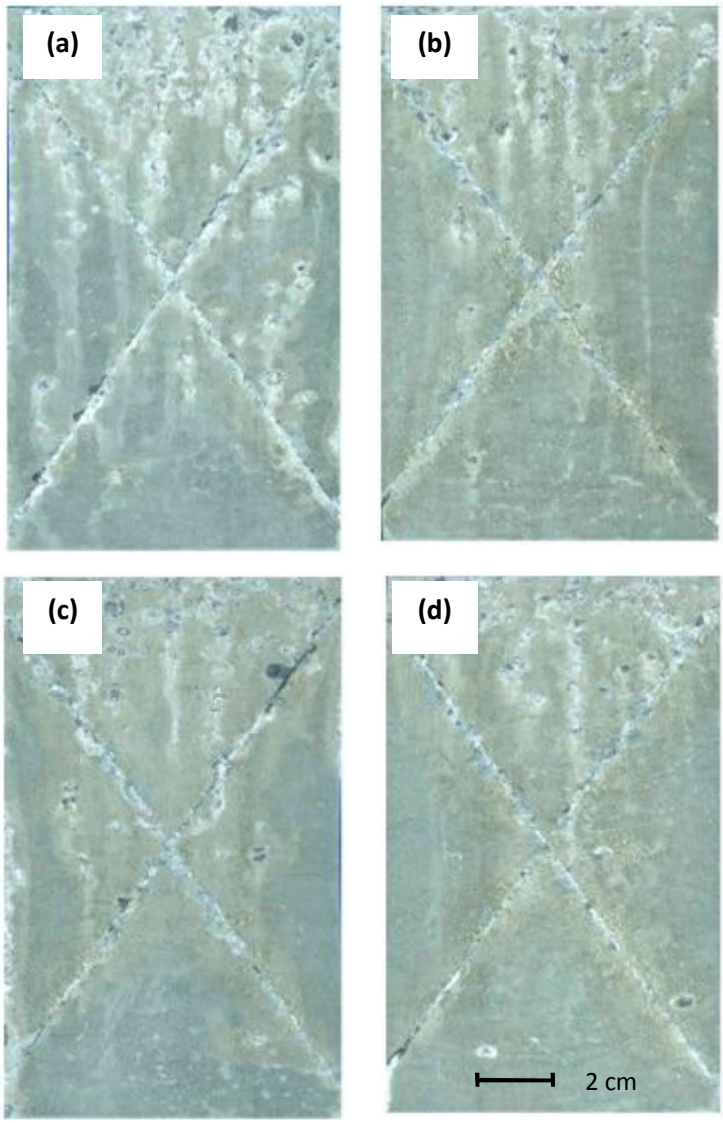

Figure 7.4. Photographs of the HDG steel samples coated with blank silane (a), $Ce(NO_3)_3.6H_2O$ (b), CeO_2 nanoparticles (c), and CeO_2 + $Ce(NO_3)_3.6H_2O$ (d), after 144 h of salt spray exposure.

For the blank silane-coated substrate, delamination increased rapidly during salt spray exposure. The modified silane coatings still showed increased delamination during exposure, but at markedly reduced rates. For example, the silane coating filled with activated CeO_2 nanoparticles suffered comparatively little delamination after exposure for 144 h, indicating its stability and barrier properties.

EIS spectra of the coated galvanized steel substrates show that the non-modified-silane-coated sample (Figure 7.5a) exhibited lower impedance than that with the $Ce(NO_3)_3$-modified coating (Figure 7.5c). Furthermore, in the presence of cerium nitrate, total impedance remained approximately constant for the duration of the 144 h test in a 3.5 % NaCl solution. This was due to both the better barrier properties and the corrosion inhibition abilities [27].

EIS Bode plots obtained for the silane coatings filled with non-activated and activated CeO_2 nanoparticles (Figure 7.5e and g) show that total impedance was lower for the system containing nano-activated CeO_2. The addition of cerium ions led to a significant increase in impedance. For example, after immersion for 24 h, the total impedance of the system containing activated CeO_2 was more than two orders of magnitude higher than that of the system filled with non-activated CeO_2. This finding has also been noted previously [10, 11], and was attributed to the likelihood of nanoparticles agglomerating and creating large defects in the coating, which promotes the uptake of the aggressive solution, and therefore promotes corrosion. The activation of the nanoparticles with cerium ions enhanced the protective properties of the modified silane films by increasing the thickness of the film and/or reducing its porosity [13].

The shape of the phase angle plot indicated the presence of two time constants (Figure 7.5b, d, f, h): one attributable to a high-frequency (around 10^4 rad s^{-1}) response of the silane

film and one to a low-frequency (around 10^{-1} rad s^{-1}) response of the processes occurring between the metal oxide over the substrate and electrolyte.

A more detailed interpretation of the EIS results can be made by numerical fitting, using the equivalent circuit depicted in Figure 7.6. In this equivalent circuit, constant phase elements were used instead of pure capacitors, because of the non-ideal character of the corresponding response with phase shifts differing from –90°.

The true capacitances can be calculated from the respective CPE parameters, as described in chapter 2, section 2.7.4. Thus, for the equivalent circuit shown in Figure 7.6, R_s is the resistance of the electrolyte; CPE_{coat} ($0.61 < n_{coat} < 0.76$) and R_{coat} represent the capacitance and resistance of the hybrid coating, respectively; CPE_{oxide} ($0.68 < n_{coat} < 0.98$) and R_{oxide} represent the capacitance and resistance of the metal oxide layer over the metal surface, respectively. The variation of the fitted parameters (resistances and capacitances) with immersion time using the equivalent circuits of figure 7.6 is shown in figure 7.7 and 7.8. Values are shown with the errors from the numerical fitting ($10^{-4} <$ Chi-squared $< 10^{-2}$).

Figure 7.7 shows the evolution of the resistance and capacitance of the coatings during immersion in a 3.5 % NaCl solution. The high-frequency resistance values (Figure 7.7a) generally decreased during the first hours of immersion owing to the development of conductive pathways inside the blank silane film [35]. During early immersion, the highest resistance was shown by the coating modified with $Ce(NO_3)_3$, whose resistance then dropped sharply after a few hours. The high-frequency resistance of the coating with non-activated CeO_2 nanoparticles reached a maximum, and then started to decrease. The initial increase of the high-frequency resistance in the last two systems was attributed to swelling of the matrix and the consequent closing of nano/micro pores [36].

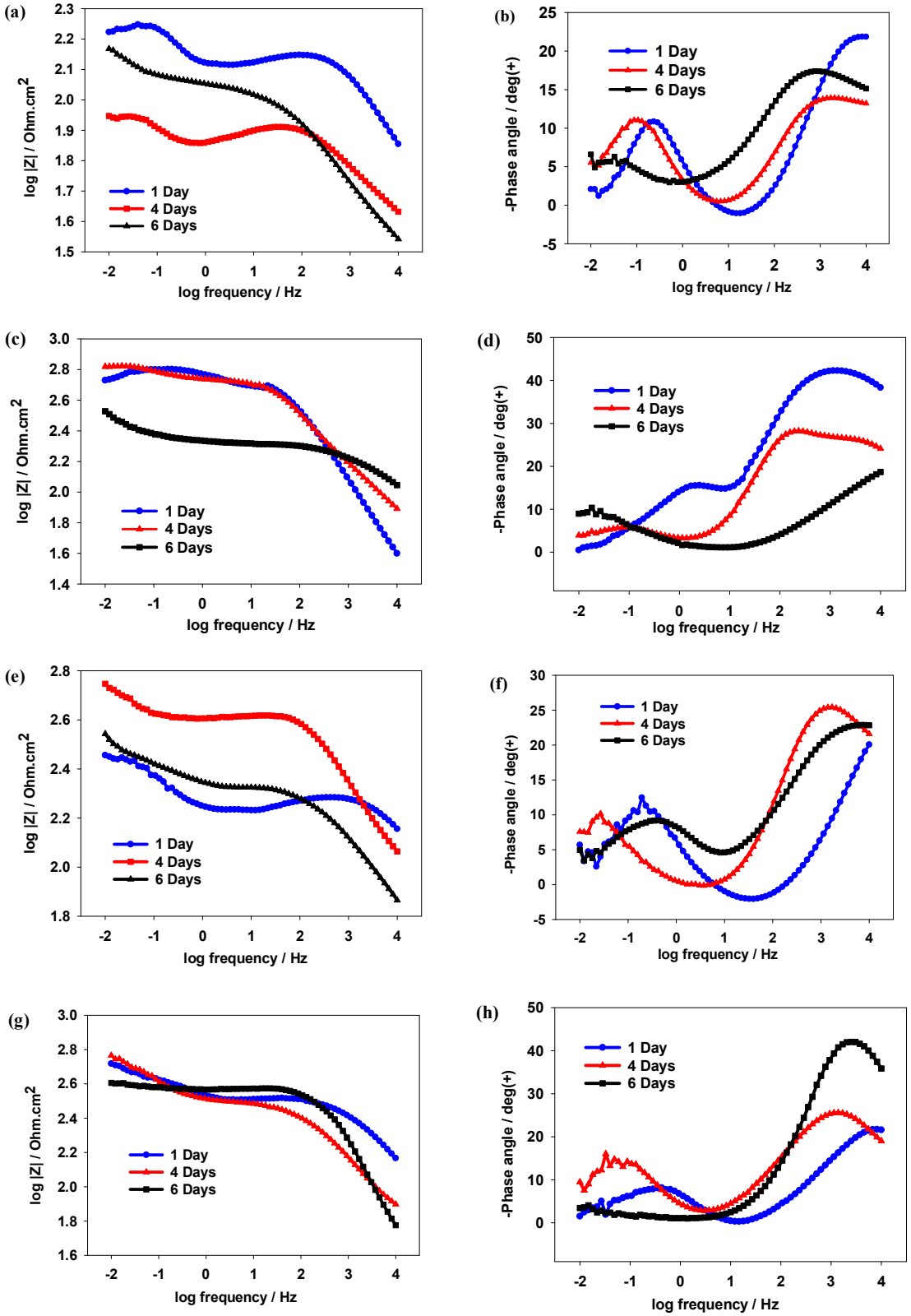

Figure 7.5. EIS Bode modulus (a, c, e, g) and phase angle (b, d, f, h) plots obtained on the HDG steel samples pre-treated with the blank silane coating (a, b), $Ce(NO_3)_3.6H_2O$ (c, d), CeO_2 nanoparticles (e, f), and CeO_2 + $Ce(NO_3)_3.6H_2O$ (g, h) during 144 h of immersion in a 3.5% NaCl solution.

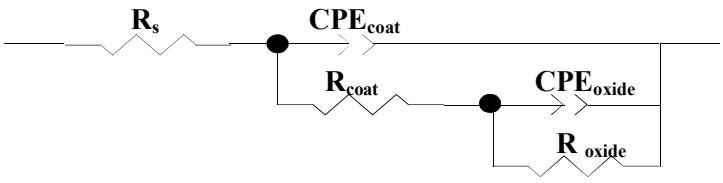

Figure 7.6. Equivalent circuit used for the numerical fitting of the EIS data during immersion in a 3.5% NaCl solution.

The high-frequency resistance of the system filled with activated CeO_2 nanoparticles increased more gradually. The initial EIS response was nearly capacitive over the entire frequency range, and the resistance remained above 233 Ω cm^2. Its continued slow increase over the 144 h test led to a significant overall increase. Compared with the blank silane film, the modified silane films showed significantly improved barrier properties.

The evolution of capacitance during the immersion test is shown in figure 7.7b. Coating filled with activated CeO_2 nanoparticles showed the lowest capacitance of the four considered systems, and it was the thickest of the coatings. Its capacitance remained relatively consistent during the immersion, with only a small increase after 96 h, which was associated with the uptake of electrolyte [11, 36]. In contrast, the blank silane film showed significantly increased film capacitance after 96 h of immersion. This was due to water uptake, which was facilitated by the reduced barrier properties of the film [11].

The evolution of the high-frequency fitting parameters indicated that the addition of nanoparticles reinforced the barrier properties of the film. The addition of cerium to the nanoparticles markedly influenced the capacitance and resistance of the coatings, and the systems filled with cerium-activated CeO_2 nanoparticles showed the best protection. These results are in accordance with those of Schem et al. regarding aluminum alloys with silane

coatings filled with CeO_2 nanoparticles [36], and those of Montemor et al. regarding galvanized steel with silane coatings doped with Ce salt-activated nanoparticles [11].

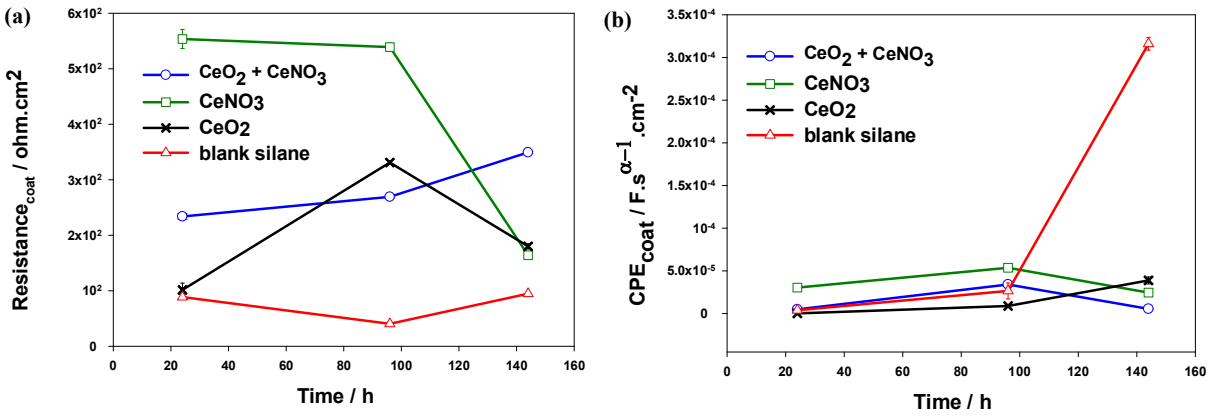

Figure 7.7. Evolution of the coating resistance (a), and coating capacitance (b), during immersion in a 3.5% NaCl solution. Values were obtained by numerical fitting, using the equivalent circuit depicted in figure 7.6.

The evolution of the fitting parameters associated with the low-frequency behavior of the EIS spectra (Figure 7.8) gives information on the electrochemical activity at the silane–zinc interface. For the system pre-treated with the blank silane coating, the initial CPE values (Figure 7.8a) were of the order of 0.0187 F cm^{-2}. During 96 h of immersion, CPE values increased and then stabilized at approximately 0.1402 F cm^{-2}. This agreed with the evolution of the low-frequency resistance (Figure 7.8b) of the blank silane film, which gradually decreased during this period, from 39.81 Ω cm^2 to 20.24 Ω cm^2, before stabilizing at approximately 34.42 Ω cm^2.

The systems modified with CeO_2 behaved distinctly. In the absence of cerium ions, after 96 h, the CeO_2-filled system showed CPE values of approximately 0.0438 F cm^{-2}; its resistance increased from 92.54 Ω cm^2 during the first hour of immersion to approximately 166.20 Ω cm^2. After 144 h, CPE and resistance had increased slightly to 0.0129 F cm^{-2} and 106.60 Ω cm^2, respectively. The activation with cerium ions had significant effects on both the low-frequency CPE and the resistance. During immersion for 96 h, the CPE values of sample filled with activated CeO_2 nanoparticles were below 9.7601×10^{-3} F cm^{-2}, and the resistances increased to over 318.80 Ω cm^2. Resistance gradually decreased during the immersion test. Resistance and CPE eventually approached the values shown by the silane coating modified with $Ce(NO_3)_3$. The low-frequency resistance increased during immersion, indicating that cerium oxide/hydroxide was stably formed with the release of $Ce(NO_3)_3$ from the sol–gel matrix [37]. The low-frequency resistance reached close to 170.62 Ω cm^2 after 144 h, indicating the continuous accumulation of cerium oxide/hydroxide during immersion. In addition, the CPE increased gradually to approximately 0.0301 F cm^{-2} after 144 h, four orders of magnitude lower than the value measured for the blank silane coating, suggesting that the inhibition products had filled the originally electrolyte-saturated pores at the coating–substrate interface [37].

In some cases, the low-frequency resistance increased after a few hours, accompanied by a decrease in CPE. Because corrosion was localized, the precipitation of the insoluble and passive corrosion products likely occurred at these locations, decreasing the corrosion activity at the interface [11]. In fact, the most pronounced changes were observed for the blank silane film, which presented the poorest barrier properties and was therefore the most prone to early corrosion attack, as was observed by Montemor et al. [11].

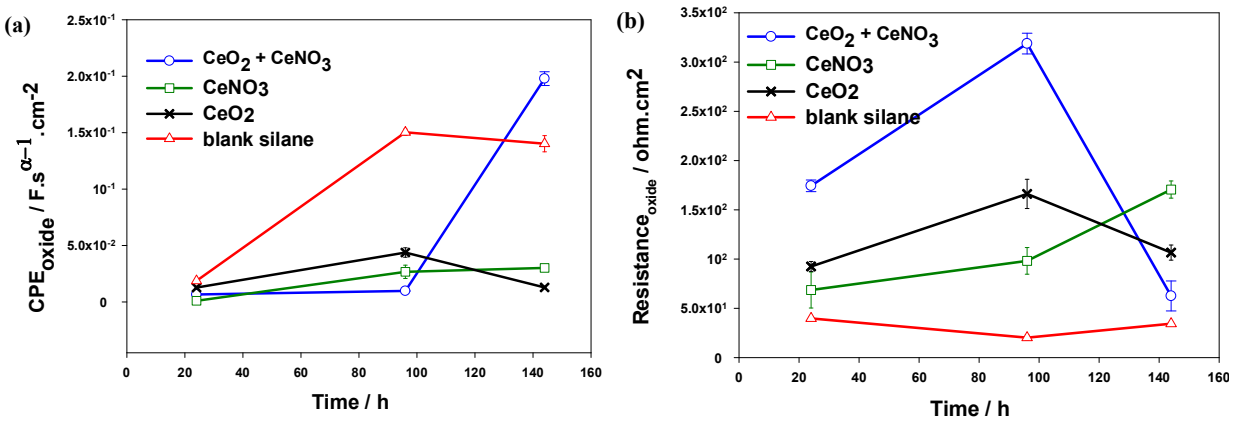

Figure 7.8. Evolution of the metal oxide layer capacitance (a) and resistance (b) during immersion in a 3.5% NaCl solution. Values were obtained by numerical fitting using the equivalent circuit depicted in figure 7.6.

Polarization curves were recorded after 1 h of immersion in the electrolyte (Figure 7.9). Parameters (i_{corr} and E_{corr}) derived from the curves (Table 7.1) indicate the different effects of the cerium modification on the silane coatings. The shifting of the cathodic polarization curves to lower current densities indicates the enhanced protection at the cathodic sites offered by coating containing activated CeO_2. The corrosion potential of sample containing activated CeO_2 nanoparticles (−0.934 V) is indicative of its notably greater corrosion resistance when compared with blank silane coating (−0.974 V), Cerium nitrate modified coating (−0.959 V), and coating containing non-activated CeO_2 (−0.987 V).

The poor performance displayed by blank silane coatings and coating containing non activated CeO_2 may have been attributable to permeability associated with cracks or porosity, which allowed the aggressive electrolyte to come into contact with the metal surface, thus initiating corrosion [35]. These results are consistent with the SEM micrographs, which show cracks and delamination in these coatings after immersion for 144 h in 3.5% NaCl solution

(Figure 7.3). Similar behavior has been reported by Montemor et al. [11] for galvanized steel substrates in 0.005 M NaCl solution.

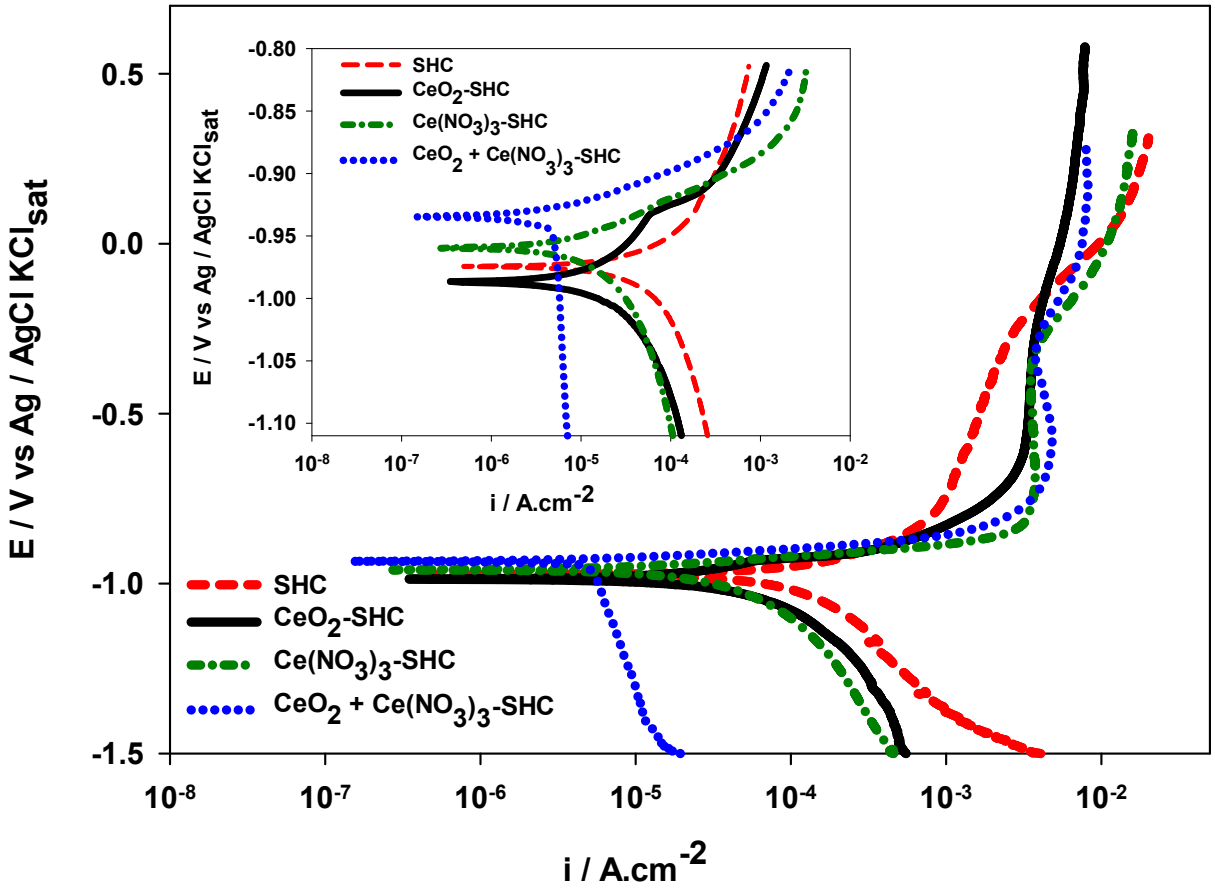

Figure 7.9. Potentiodynamic polarization curves for the HDG steel samples coated with blank silane, $Ce(NO_3)_3.6H_2O$, CeO_2 nanoparticles, and CeO_2 + $Ce(NO_3)_3.6H_2O$, obtained after 1 h of immersion in a 3.5% NaCl solution. For comparative purposes, the inset shows a plot in which the potential is depicted as the difference between the imposed potential and the corrosion potential. This approach allows a better separation of the anodic and cathodic polarization effects.

Table 7.1. Summary of the electrochemical parameters obtained from the polarization, measured in a 3.5% NaCl solution.

Sample	E_{corr} (V)	i_{corr} (A cm^{-2})	b_c (V/dec)	b_a (V/dec)	Passive area (V)
Blank silane	-0.974	3.577×10^{-5}	0.06	0.093	-0.792 to -0.241
$Ce(NO_3)_3$	-0.959	3.224×10^{-6}	0.022	0.022	-0.832 to -0.320
CeO_2	-0.987	4.904×10^{-6}	0.031	0.026	-0.677 to -0.262
CeO_2 + $Ce(NO_3)_3$	-0.934	1.116×10^{-6}	0.015	0.012	-0.809 to -0.327

7.4. Conclusion

Pre-treatments of hot dip-galvanized steel based on the use of 3-glycidoxypropyltrimethoxysilane (GPTMS) and bisphenol A (BPA) filled with activated CeO_2 nanoparticles revealed the formation of a comparatively smooth nanostructured surface, with low heterogeneity in the coating thickness. Microscopic observations also confirmed that the complete surface morphology of the silane coating filled with activated CeO_2 nanoparticles was maintained after short-term corrosion tests (144 h immersion in 3.5% NaCl solution). These coatings resisted the salt spray exposure for 144 h, with reduced corrosion near an artificial scratch, and uniform corrosion otherwise, which contrasted with the blank silane coating.

Upon the addition of activated CeO_2 nanoparticles as a dopant, the silane coating showed improved barrier properties and coating resistance, and a decrease in coating capacitance. The incorporation of activated CeO_2 nanoparticles reduced the cathodic current density by two orders of magnitude, and shifted the voltage to more positive values (compared with the blank silane-coated substrate) during polarization in a 3.5% NaCl solution.

References

1. I.A. Kartsonakis, A.C. Balaskas, E.P. Koumoulos, C.A. Charitidis, G.C. Kordas, Incorporation of ceramic nanocontainers into epoxy coatings for the corrosion protection of hot dip galvanized steel, Corrosion Science, 57, 2012, pp. 30-41.
2. A.R. Marder, The metallurgy of zinc-coated steel, Progress in Materials Science, 45, 2000, pp. 191-271.
3. A.M.P. Simões, R.O. Carbonari, A.R. Di Sarli, B. del Amo, R. Romagnoli, An environmentally acceptable primer for galvanized steel: formulation and evaluation by SVET, Corrosion Science, 53, 2011, pp. 464-472.
4. J.B. Bajat, V.B. Mišković-Stanković, J.P. Popić, D.M. Dražić, Adhesion characteristics and corrosion stability of epoxy coatings electrodeposited on phosphated hot-dip galvanized steel, Progress in Organic Coatings, 63, 2008, pp. 201-208.
5. M. Taryba, S.V. Lamaka, D. Snihirova, M.G.S. Ferreira, M.F. Montemor, W.K. Wijting, S. Toews, G. Grundmeier, The combined use of scanning vibrating electrode technique and micro-potentiometry to assess the self-repair processes in defects on "smart" coatings applied to galvanized steel, Electrochimica Acta, 56, 2011, pp. 4475-4488.
6. B. Ramezanzadeh, M.M. Attar, Studying the effects of micro and nano sized ZnO particles on the corrosion resistance and deterioration behavior of an epoxy-polyamide coating on hot-dip galvanized steel, Progress in Organic Coatings, 71, 2011, pp. 314-328.
7. M.F. Montemor, R. Pinto, M.G.S. Ferreira, Chemical composition and corrosion protection of silane films modified with CeO_2 nanoparticles, Electrochimica Acta, 54, 2009, pp. 5179-5189.
8. M.F. Montemor, M.G.S. Ferreira, Analytical and microscopic characterisation of modified bis-[triethoxysilylpropyl] tetrasulphide silane films on magnesium AZ31 substrates, Progress in Organic Coatings, 60, 2007, pp. 228-237.

9. M.L. Zheludkevich, R. Serra, M.F. Montemor, K.A. Yasakau, I.M.M. Salvado, M.G.S. Ferreira, Nanostructured sol–gel coatings doped with cerium nitrate as pre-treatments for AA2024-T3: corrosion protection performance, Electrochimica Acta, 51, 2005, pp. 208-217.
10. M.F. Montemor, W. Trabelsi, M. Zheludevich, M.G.S. Ferreira, Modification of bis-silane solutions with rare-earth cations for improved corrosion protection of galvanized steel substrates, Progress in Organic Coatings, 57, 2006, pp. 67-77.
11. M.F. Montemor, M.G.S. Ferreira, Cerium salt activated nanoparticles as fillers for silane films: evaluation of the corrosion inhibition performance on galvanised steel substrates, Electrochimica Acta, 52, 2007, pp. 6976-6987.
12. M.F. Montemor, A.M. Cabral, M.L. Zheludkevich, M.G.S. Ferreira, The corrosion resistance of hot dip galvanized steel pretreated with Bis-functional silanes modified with microsilica, Surface and Coatings Technology, 200, 2006, pp. 2875-2885.
13. M.F. Montemor, M.G.S. Ferreira, Analytical characterization of silane films modified with cerium activated nanoparticles and its relation with the corrosion protection of galvanised steel substrates, Progress in Organic Coatings, 63, 2008, pp. 330-337.
14. V. Palanivel, D. Zhu, W.J. van Ooij, Nanoparticle-filled silane films as chromate replacements for aluminum alloys, Progress in Organic Coatings, 47, 2003, pp. 384-392.
15. L. Liu, J.-M. Hu, J.-Q. Zhang, C.-N. Cao, Improving the formation and protective properties of silane films by the combined use of electrodeposition and nanoparticles incorporation, Electrochimica Acta, 52, 2006, pp. 538-545.
16. M. Aresta, A. Dibenedetto, C. Pastore, C. Cuocci, B. Aresta, S. Cometa, E. De Giglio, Cerium(IV) oxide modification by inclusion of a hetero-atom: a strategy for producing efficient and robust nano-catalysts for methanol carboxylation, Catalysis Today, 137, 2008, pp. 125-131.

17. L.L. Kovalenko, O.I. V'yunov, A.G. Belous, Semiconducting barium titanate doped with oxygen-free compounds, Journal of the European Ceramic Society, 19, 1999, pp. 965-968.
18. A. Trinchi, Y.X. Li, W. Wlodarski, S. Kaciulis, L. Pandolfi, S. Viticoli, E. Comini, G. Sberveglieri, Investigation of sol–gel prepared CeO_2–TiO_2 thin films for oxygen gas sensing, Sensors and Actuators B: Chemical, 95, 2003, pp. 145-150.
19. N. Izu, T. Itoh, W. Shin, I. Matsubara, N. Murayama, The effect of hafnia doping on the resistance of ceria for use in resistive oxygen sensors, Sensors and Actuators B: Chemical, 123, 2007, pp. 407-412.
20. Y. Yang, J.L. Ong, J. Tian, Deposition of highly adhesive ZrO_2 coating on Ti and CoCrMo implant materials using plasma spraying, Biomaterials, 24, 2003, pp. 619-627.
21. S.M.A. Shibli, F. Chacko, Development of nano CeO_2-incorporated high performance hot-dip zinc coating, Surface and Coatings Technology, 202, 2008, pp. 4971-4975.
22. S. Zhang, M. Li, J.H. Yoon, T.Y. Cho, C.G. Lee, Y. He, The comparative study on microstructure and properties of nano-CeO_2 and Sm_2O_3 particulate reinforced nickel-based composites by laser deposition, Applied Surface Science, 254, 2008, pp. 7446-7452.
23. Y. Wang, Z. Wang, Y. Yang, W. Chen, The effects of ceria on the mechanical properties and thermal shock resistance of thermal sprayed NiAl intermetallic coatings, Intermetallics, 16, 2008, pp. 682-688.
24. D. Nickolova, E. Stoyanova, D. Stoychev, I. Avramova, P. Stefanov, Protective effect in sulfuric acid media of alumina and ceria oxide layers electrodeposited on stainless steel, Surface and Coatings Technology, 202, 2008, pp. 1876-1888.

25. R. Xu, J. Wang, L. He, Z. Guo, Study on the characteristics of Ni–W–P composite coatings containing nano-SiO_2 and nano-CeO_2 particles, Surface and Coatings Technology, 202, 2008, pp. 1574-1579.
26. R. Zandi-Zand, Investigation of corrosion, abrasion and weathering resistance in hybrid nanocomposite coatings based on epoxy-silica, Thesis, Azad University- Tehran North Branch, 2005.
27. R. Zandi Zand, K. Verbeken, A. Adriaens, Corrosion resistance performance of cerium doped silica sol–gel coatings on 304L stainless steel, Progress in Organic Coatings, 75, 2012, pp. 463-473.
28. R. Zandi Zand, K. Verbeken, A. Adriaens, The corrosion resistance of 316L stainless steel coated with a silane hybrid nanocomposite coating, Progress in Organic Coatings, 72, 2011, pp. 709-715.
29. A. Phanasgaonkar, V.S. Raja, Influence of curing temperature, silica nanoparticles- and cerium on surface morphology and corrosion behaviour of hybrid silane coatings on mild steel, Surface and Coatings Technology, 203, 2009, pp. 2260-2271.
30. M.F. Montemor, W. Trabelsi, S.V. Lamaka, K.A. Yasakau, M.L. Zheludkevich, A.C. Bastos, M.G.S. Ferreira, The synergistic combination of bis-silane and CeO_2–ZrO_2 nanoparticles on the electrochemical behaviour of galvanised steel in NaCl solutions, Electrochimica Acta, 53, 2008, pp. 5913-5922.
31. X. Zhong, Q. Li, J. Hu, X. Yang, F. Luo, Y. Dai, Effect of cerium concentration on microstructure, morphology and corrosion resistance of cerium–silica hybrid coatings on magnesium alloy AZ91D, Progress in Organic Coatings, 69, 2010, pp. 52-56.
32. M. Garcia-Heras, A. Jimenez-Morales, B. Casal, J.C. Galvan, S. Radzki, M.A. Villegas, Preparation and electrochemical study of cerium–silica sol–gel thin films, Journal of Alloys and Compounds, 380, 2004, pp. 219-224.

33. R.Z. Zand, K. Verbek, A. Adriaens A, Influence of the cerium concentration on the corrosion performance of Ce-doped silica hybrid coatings on hot dip galvanized steel substrates, International Journal of Electrochemical Science, 8, 2013, pp. 548-563.
34. S.M.A. Shibli, F. Chacko, CeO_2–TiO_2 mixed oxide incorporated high performance hot dip zinc coating, Surface and Coatings Technology, 205, 2011, pp. 2931-2937.
35. V. Moutarlier, B. Neveu, M.P. Gigandet, Evolution of corrosion protection for sol–gel coatings doped with inorganic inhibitors, Surface and Coatings Technology, 202, 2008, pp. 2052-2058.
36. M. Schem, T. Schmidt, J. Gerwann, M. Wittmar, M. Veith, G.E. Thompson, I.S. Molchan, T. Hashimoto, P. Skeldon, A.R. Phani, S. Santucci, M.L. Zheludkevich, CeO_2-filled sol–gel coatings for corrosion protection of AA2024-T3 aluminium alloy, Corrosion Science, 51, 2009, pp. 2304-2315.
37. H. Shi, F. Liu, E. Han, Corrosion behaviour of sol–gel coatings doped with cerium salts on 2024-T3 aluminum alloy, Materials Chemistry and Physics, 124, 2010, pp. 291-297.

8

Effects of ceria nanoparticle concentration on the morphology and corrosion resistance of cerium–silane hybrid coatings on electro-galvanized steel substrates [1]

8.1. Introduction

Electroplated zinc coatings are employed as active galvanic protection for steel. However, zinc is highly reactive, and high corrosion rates of this coating are observed when exposed, both indoors and out. Therefore, a post-treatment is required to increase the lifetime of zinc coatings [1]. In current industrial practice, particularly in the automotive industry, this

[1] Reprinted from Materials Chemistry and Physics, Volume 145, Roohangiz Zandi Zand, Kim Verbeken, Victoria Flexer and Annemie Adriaens, Effects of ceria nanoparticle concentrations on the morphology and corrosion resistance of cerium–silane hybrid coatings on electrogalvanized steel substrates, 450-460, Copyright (2014), with permission from Elsevier.

treatment consists of immersion in a chemical bath containing hexavalent chromium salts, forming an anti-corrosive layer over plated zinc. However, this type of anti-corrosive system presents a serious drawback due to the high toxicity of hexavalent chromium salts [2]. As a consequence, the European Community decided to ban the use of Cr(VI) in the car industry from July 1st 2007 on, to avoid environmental contamination either during the processing, use or recycling of coated sheets [3].

The need to replace the chromate-based surface treatments promoted the investigation of several classes of new pre-treatment systems. Among these, pre-treatments based on organosilanes attracted considerable interest, as they provide the formation of a thin organic coating that confers surface functionalisation [4, 5]. The silane pre-treatment creates a dense, oxygen-rich coating that generates a protective physical barrier [5]. The major drawback of silane pre-treatments is their inert character with respect to corrosion. The silane coating alone does not provide any active protection when aggressive species reach the metallic surface and initiate corrosion [4, 6, 7].

To overcome this limitation, a new challenge is to modify the bulk properties of silane coatings by adding "active" anti-corrosion species. These modifications should further improve the corrosion resistance of the layer, or introduce a self-healing capability in the silane coating [4, 8, 9].

Among the most effective anti-corrosion species, rare-earth salts offer good corrosion inhibition properties in addition to environmental friendliness [10]. Cerium nitrate has been successfully tested for corrosion protection of galvanized steel substrates, either as a conversion film [11-13] or as a corrosion inhibitor through addition to the silane formulation [10, 14-16]. The results revealed improved corrosion protection of galvanized steel substrates.

Another approach to improve the corrosion protection of silane coatings is based on the addition of oxide nanoparticles. Van Ooij et al. [17] reported that bis-sulfur silane films could be thickened and strengthened by loading them with silica particles. However, when the bis-sulfur silane film was heavily modified with silica, it tended to form a porous film, which promoted electrolyte intrusion and premature film delamination.

Montemor et al. [8, 18] reported a new approach, consisting of the modification of bis {triethoxysilylpropyl} tetrasulfide silane (BTESPT) with nanoparticles, such as CeO_2, SiO_2 or CeO_2-ZrO_2. In some cases, to obtain a synergistic effect and improved corrosion resistance, the nanoparticles were initially activated with cerium nitrate. Results demonstrated that the ceria nanoparticles are a very effective filler, leading to both improved barrier properties of the silane coatings and improved corrosion resistance. Furthermore, the protective behavior depends on the concentration of nanoparticles, and the activation of the nanoparticles with cerium ions leads to the formation of thicker and more protective silane films.

A number of studies have examined the effect of cerium nitrate concentration on the properties of coatings [6, 14, 19, 20]. However, information concerning the influence of the CeO_2 nanoparticle concentration on the morphology, microstructure, and anti-corrosion performance is still limited in the literature, and hence requires further investigation.

Previous work (chapter 7) has reported and discussed the anti-corrosion behavior of 3–glycidoxypropyltrimethoxy silane (GPTMS) modified with CeO_2 nanoparticles. The nanoparticles were activated with cerium nitrate to improve the corrosion resistance of the galvanized steel substrates. Based on the corrosion test results, the effect of the nanoparticles on the barrier properties of the silane films immersed in NaCl solution are ranked as follows: CeO_2+$Ce(NO_3)_3$ > Ce $(NO_3)_3$ > CeO_2 > blank silane film. These results demonstrate that the

cerium activated nanoparticles strongly improve the barrier properties of the silane coatings, and present a better anti-corrosion performance when compared with other coatings.

The objective of this work was to investigate the effect of the CeO_2 nanoparticle concentration on the morphology, microstructure, and anti-corrosion performance of the silane coatings modified with activated CeO_2 nanoparticles on an electro-galvanized steel substrate.

8.2. Sample preparation

Ceria nanoparticles (10 wt% in water, particle size < 25 nm, Sigma Aldrich, St. Louis, USA) were activated by ultrasonic dispersion in an aqueous solution of cerium nitrate (Fluka, Buchs, Switzerland). Three sets of aqueous solutions with different molar ratios of $CeO_2/Ce(NO_3)_3$ were prepared, which were then used to prepare the silane solutions marked as (A), (B), and (C) (Table 8.1).

The silane solution was prepared by adding 4.084 mL of 3–glycidoxypropyl-trimethoxy silane or GPTMS (Merck, New Jersey, USA) to 0.5 mL of HCl-acidified water (pH = 2) (H_2O/Si mole ratio = 0.5 [21]). The solution was placed in a sealed beaker and stirred at room temperature for 20 min at a rate of 240 rpm to hydrolyze and condensate the silane precursors. The aqueous dispersion of ceria nanoparticles was added at the end of this synthesis step, followed by stirring for 10 min. The total Ce/Si mole ratio was 0.05 [14]. In the next step, 2.111 g of bisphenol A (BPA) (Merck) was added to the solution as a cross-linking agent (BPA/Si mole ratio = 0.5). The latter has been shown to realize a significant effect on the morphology and improvement of the corrosion resistance of coatings [22]. The BPA was dissolved by mixing the solution for 80 minutes. To accelerate the condensation reaction, 0.0152 mL of 1–methylimidazol (MI) (Merck) (MI/Si mole ratio = 0.01) was added

to the solution, which was followed by stirring for 5 min. The result was a clear, colorless, homogenous solution.

The metallic substrate consisted of electro-galvanized steel coupons (1.13 cm^2 area and 0.1 cm thickness for the AFM, SEM, and electrochemical tests) and plates (7 × 15 × 0.1 cm for the salt spray tests). The zinc coating had a weight of approximately 112 g/m^2, and a thickness of approximately 8 μm. The galvanized steel specimens were degreased using an alkaline cleaner. After cleaning, the substrates were washed with distilled water, dried in air, and immersed in the silane solution for 60 s. The coated specimens were dried at room temperature for 24 h, and subsequently submitted to a 25–130°C curing process with a heating rate of 7.5 °C/min for 90 minutes, to initiate extensive cross-linking in the hybrid films [23]. The coating thickness was measured by eddy-current method (Check line 3000 pro, Germany).

Table 8.1. Molar ratio (mol%) of CeO_2 nanoparticles and cerium nitrate in the aqueous dispersion of activated ceria nanoparticles.

Set	Molar ratio (mol%)	
	CeO_2 Nanoparticles	Ce $(NO_3)_3.6H_2O$
A	0.0375	0.0125
B	0.0250	0.0250
C	0.0125	0.0375

8.3. Results and discussion

The surface morphology of the doped silane coatings was assessed by AFM. Figure 8.1 shows the morphology and evolution of the surface roughness of the doped silane coatings

before immersion in 3.5 % NaCl solution. The AFM scans reveal the formation of crack and defect free coatings.

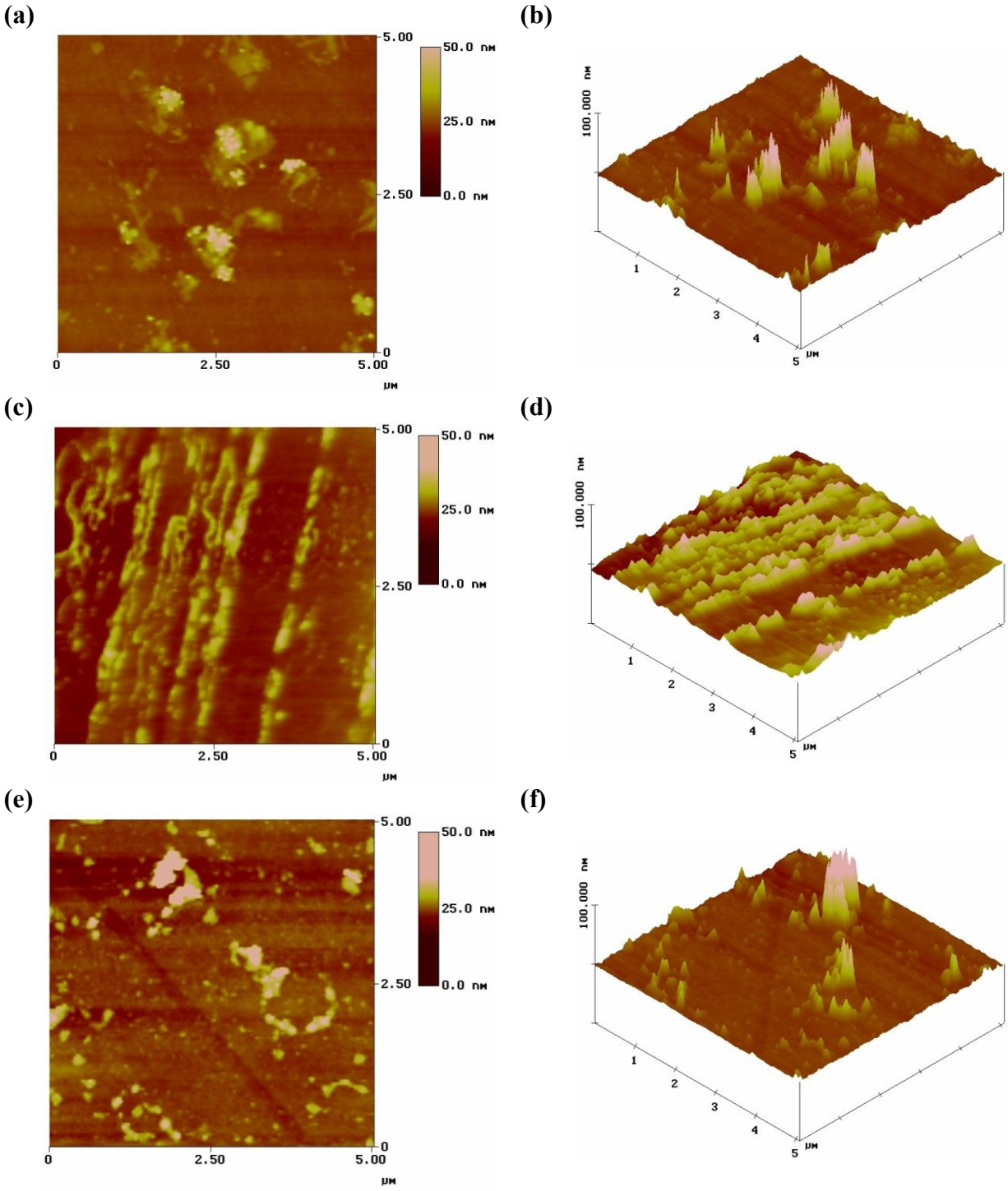

Figure 8.1. AFM top-view (a, c, e) and topographic images (b, d, f) of electro-galvanized steel samples coated with A (a, b), B (c, d), and C (e, f) Ce-modified silane coatings, prior to immersion in a 3.5 % NaCl solution.

However, the surface of the coatings are slightly less uniform, and contain some particles and heterogeneities. The single nanoparticles cannot be clearly seen in the topography images (b, d, f), however, the top view images (a, c, e) show the presence of agglomerates and very small nanoparticles. These nanoparticles appear to be 50–100 nm in diameter. The size difference between the known dimensions of the added nanoparticles and the values measured by AFM can be explained by the presence of a silane layer on the top of the nanoparticles. Thus, AFM measures the convexity of the surface caused by the underlying nanoparticles [4, 24].

As well as single nanoparticles, some agglomerates (ranging from 150 to 400 nm) are visible on the topography maps, and these likely resulted from the agglomeration of smaller nanoparticles on the surface [15, 24]. This observation is consistent with the findings of Montemor et al. [25] and Phanasgaonkar et al. [24] in the AFM scans of microsilica-modified silane coatings. The root mean square (RMS) surface roughness of the topographic images is 3.570, 2.776, and 3.224 nm for the (A), (B), and (C) coatings, respectively. The differences in roughness are caused by the addition of the different contents of nanoparticulate oxide to the silane solution during synthesis.

After immersion in the 3.5 % NaCl solution, the morphology of the coatings changed. The AFM scans reveal that the outer layers of the coatings were released during immersion in the aggressive solution. This release changed the morphology of outer surfaces, which became closer to that of an oxide film. After 456 h of immersion (Figure 8.2), coating (C) still presents an oxide type structure; however, coatings (A) and (B) show signs of corrosion. The oxide type layer on coating (C) constitutes a protective silicon oxide rich-barrier where cerium ions are entrapped. As soon as the corrosion process is initiated, the cerium ions, either Ce^{4+} or Ce^{3+}, can precipitate, hindering the corrosion process. The presence of Ce^{4+} has

also been reported in the literature [26], and it is suggested that this ion results from oxidation of Ce^{3+} in the presence of H_2O_2 that is formed in an intermediate step of the reduction of oxygen.

The secondary electron images depicted in figure 8.3 show the microstructural features of the different surface coatings before and after immersion in 3.5 % NaCl solution. The micrographs reveal the presence of some important features on the different coatings. Figures 8.3a and c show the (A) and (B) silane coating surfaces prior to immersion in a 3.5 % NaCl solution. The coatings reveal the presence of a few micro- and nano-sized holes in the coatings, which may have contributed to the early deterioration of the coatings observed in the AFM scans after immersion. The occurrence of such coating defects is undesirable, since they may serve as initiators for pit corrosion through reduced coating thickness and/or as the initiation sites of fatigue cracks. In the case of coating (C), the uniform coating appeared to be free of defects and cracks. However, several white agglomerates appeared in the coating matrix, which, in accordance with our previous EDX results [15], are silicon rich (Figure 8.3e). It is likely that these features were clusters of nanoparticles that formed in the outermost layers of the silane film [20, 27].

After 456 h of immersion, the surface of the coatings reveals the presence of zinc corrosion products. The density of these corrosion products is higher on coatings (A) and (B) (Figures 8.3b and d). Furthermore, the structure of the substrate is most deteriorated when treated with coating (A). In the case of coatings (B) and (C) (Figures 8.3d and f), the surface has non-attacked areas and the corrosion products are likely to have grown through defects on the surface films.

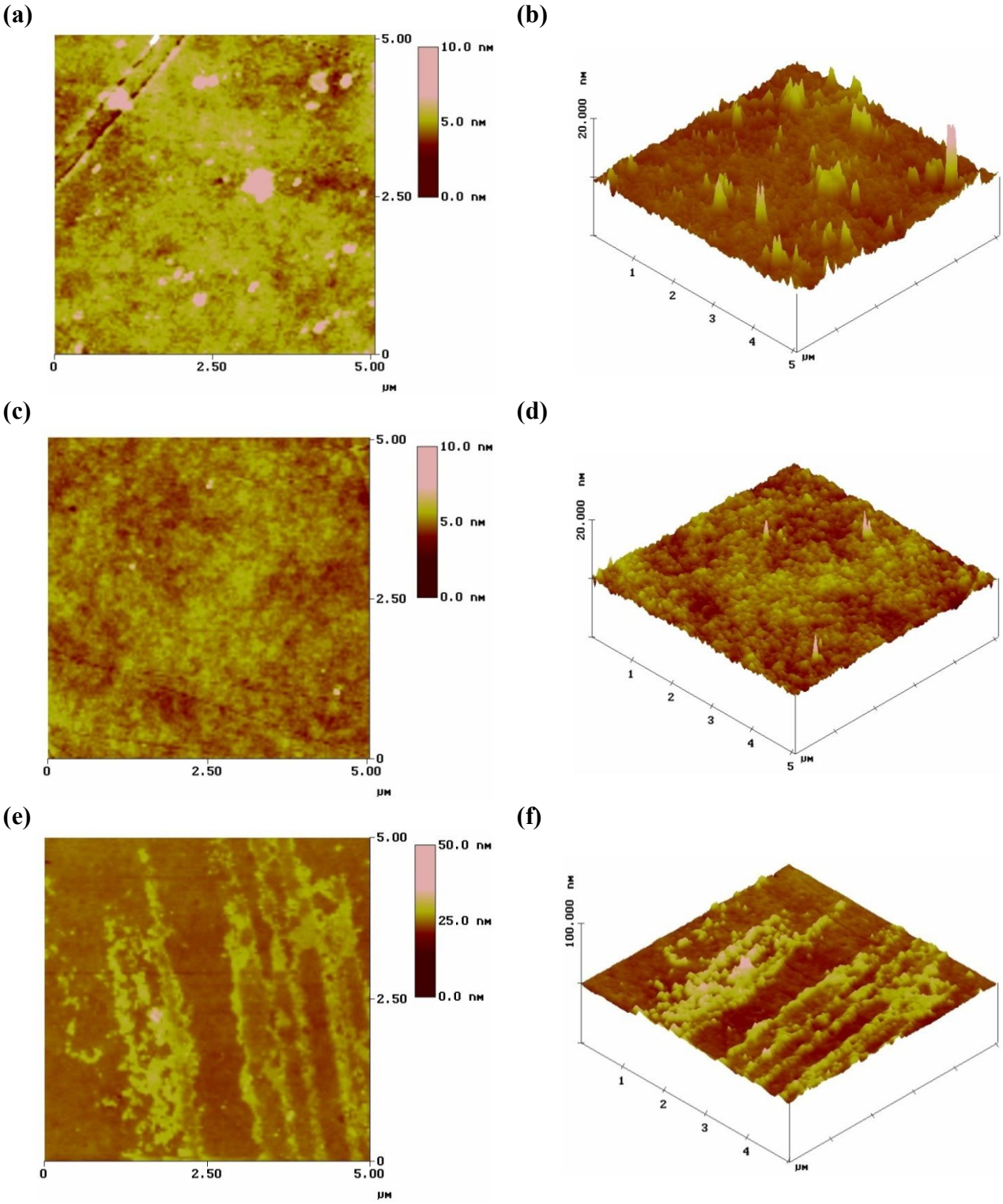

Figure 8.2. AFM top-view (a, c, e) and topographic images (b, d, f) of electro-galvanized steel samples coated with A (a, b), B (c, d), and C (e, f) Ce-modified silane coatings, after 456 h immersion in a 3.5 % NaCl solution.

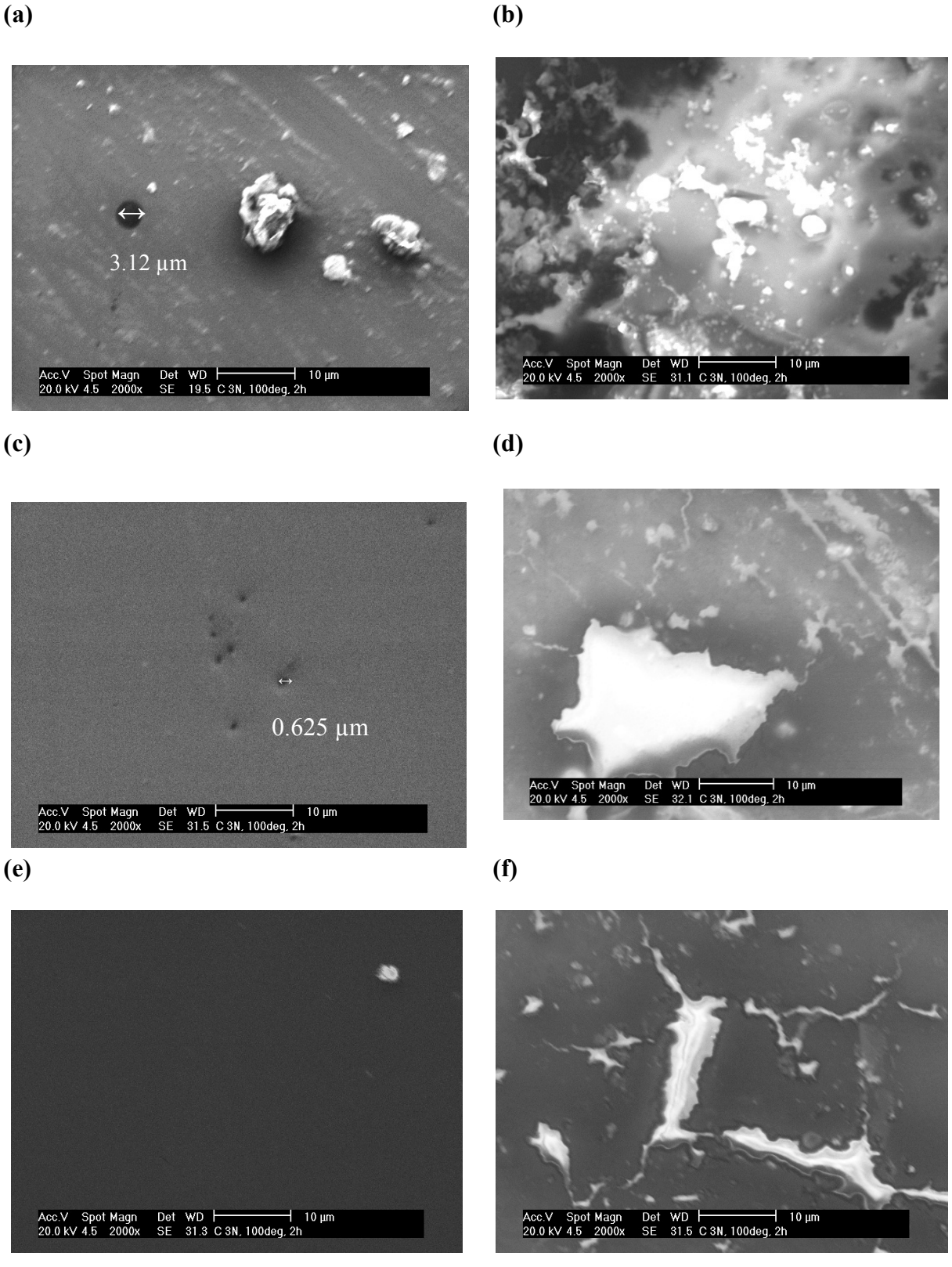

Figure 8.3. Secondary electron micrographs of the electro-galvanized steel samples coated with silane coatings A (a, b), B (c, d), and C (e, f) before (a, c, e) and after (b, d, f) 456 h of immersion in a 3.5 % NaCl solution.

The microscopic results account for the greater durability of the silane coating doped with lower contents of activated CeO_2 nanoparticles (coating C). The addition of small amounts of activated nanoparticles to the silane solution improves the protective properties of the coating, making it more resistant to deterioration under immersion in NaCl solutions. The SEM and AFM results confirm that coating (C) is less prone to corrosive attack.

An evaluation of different formulations of $CeO_2/Ce(NO_3)_3$ silane solutions was performed to investigate the dependence of corrosion resistance on the composition of the silane-based layer. To achieve this, samples coated with various silane solutions were exposed to salt spray to compare the relative corrosion performance of different coatings. This allows to define the optimum $CeO_2/Ce(NO_3)_3$ formulation in terms of corrosion resistance. Figure 8.4 summarizes the results obtained after 192 and 288 h of exposure.

The results show that the corrosion resistance strongly depends on the composition of the silane coating. After 192 h of exposure, all coatings showed delamination, in addition to the sacrificial dissolution of zinc around the scratched area (Figures 8.4a–c). However, upon decreasing the ceria nanoparticle versus cerium nitrate ratio, the degree of delamination was significantly reduced. For example, near the artificial scratch, the delamination is not pronounced for the silane coating containing the lowest fraction of ceria nanoparticles (coating C) (Figure 8.4c).

As the salt spray analysis progressed, the breakdown of the coating layers in (A) and (B) (average coating thickness: 56 ± 10 and 52 ± 12 μm, respectively) progressed, and this was followed by degradation of the zinc coatings, resulting in the formation of white rust (Figures 8.4d–f) [28]. For silane coating (C) (average coating thickness: 61 ± 12 μm), comparatively little delamination was observed after exposure to the neutral salt spray for 288 h (Figure 8.4f). This indicates the stable nature and barrier protection characteristics of the

coating. In addition, the limited delamination in the presence of the lowest concentration of ceria nanoparticles suggests the presence of a corrosion-inhibiting species.

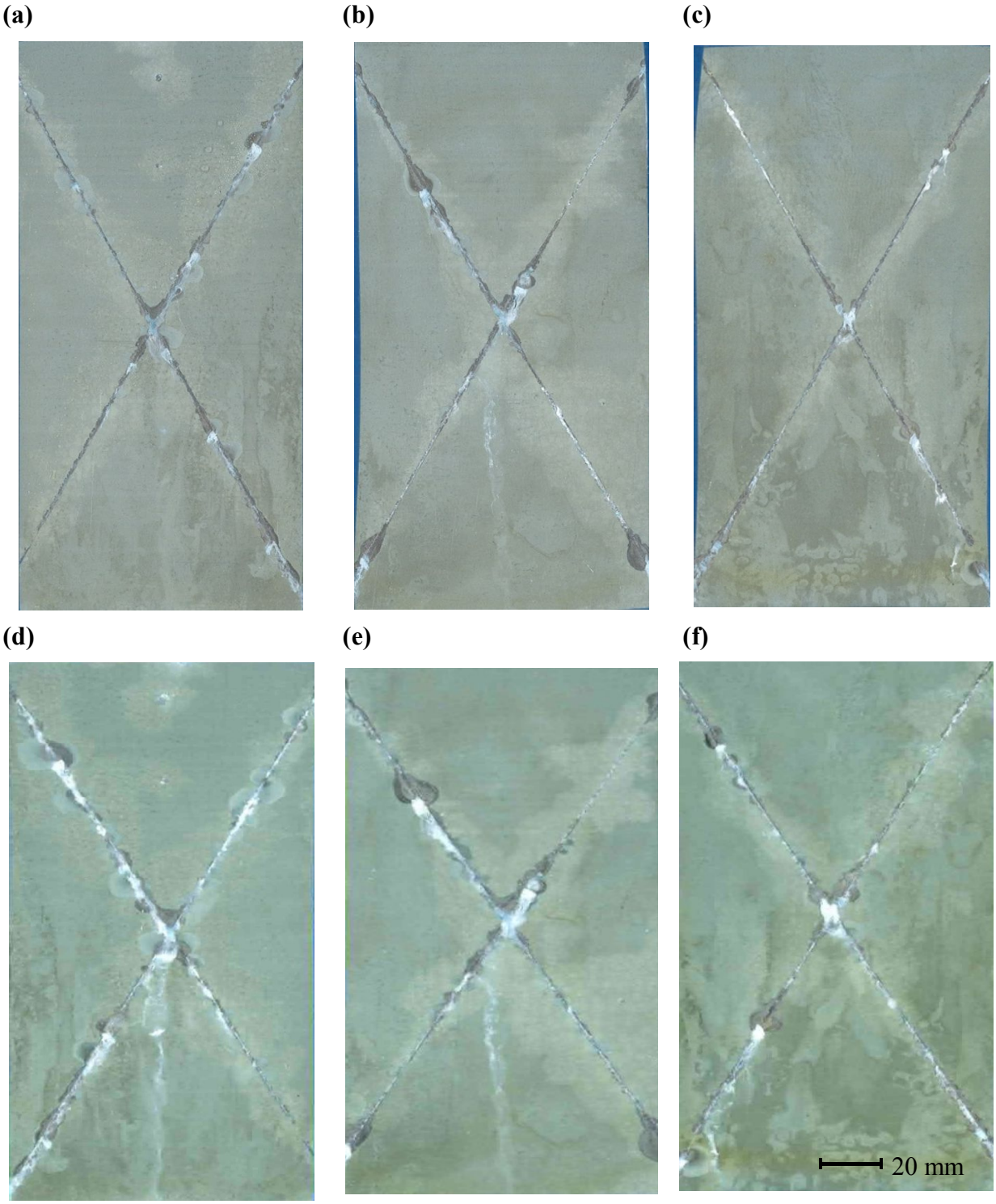

Figure 8.4. Photographs of electro-galvanized steel samples coated with silane coatings A (a, d), B (b, e), and C (c, f), after 192 h (a, b, c) and 288 h (d, e, f) of salt spray exposure.

Figure 8.5 depicts the electrochemical impedance results obtained from the silane films filled with different $CeO_2/Ce(NO_3)_3$ molar ratios during 456 h of immersion in a 3.5 % NaCl solution. The low-frequency impedance values depend upon the concentration of nanoparticles. During the first hours of immersion, for silane films (B) and (C), the low-frequency resistance values (LF) are similar (706.317 and 644.693 $\Omega.cm^2$, respectively), but there is a distinct drop, of around four orders of magnitude, for silane film (A). After 24 h of immersion, a drop in the LF impedance values is observed for all coatings, which can be associated with water uptake through the pores, and/or defects in the coatings [29]. However, after 72 h of immersion, impedance values at LF show a pronounced increase. With further increase of immersion time, a small drop in the LF impedance values is observed.

This increase in impedance value can be attributed to the self-healing effect of cerium on the corrosion spots [30]. This effect can originate from the release of cerium near the coating defects. Subsequently, cerium produces insoluble hydroxides by its reaction with hydroxyl groups from cathodic reactions [22]. These hydroxides, together with corrosion products, decrease the cathodic current and consequently reduce the overall corrosion rate.

The results show that the impedance values were higher for silane film (C), which contained the lowest concentration of CeO_2 nanoparticles. Furthermore, for this coating, the impedance values at LF remained approximately constant during the 456 h in 3.5 % NaCl solution. The EIS results suggest that the concentration of nanoparticles has an important influence on the barrier properties of the silane films. The films with lower concentrations show better barrier properties. This trend has been recognized in the literature [8, 18], and has been attributed to the fact that nanoparticles are likely to agglomerate and to create large defects in the coating, thereby promoting the uptake of the aggressive solution and resulting in corrosion.

The shape of the phase angle plot indicates the presence of two time constants (Figures 8.5b, d, f), which were attributed to the response of the silane film (high-frequency time constant, around 10^4 rad s^{-1}) and the response of the processes occurring between the metal oxide layer over the substrate and electrolyte (low-frequency time constant, around 10^{-1} rad s^{-1}).

A more detailed interpretation of the EIS results can be made by numerical fitting, using the equivalent circuit depicted in figure 8.6. In this equivalent circuit, constant phase elements (CPE) were used instead of pure capacitors, because of the non-ideal character of the corresponding response with phase shifts differing from –90°. The true capacitances can be calculated from the respective CPE parameters, as described in chapter 2, section 2.7.4. Electrical Circuit Elements. Thus, for the equivalent circuit shown in figure 8.6, R_s is the resistance of the electrolyte; CPE_{coat} ($0.68 < n_{coat} < 0.82$) and R_{coat} represent the capacitance and resistance of the hybrid coating, respectively; CPE_{oxide} ($0.64 < n_{coat} < 0.92$) and R_{oxide} represent the capacitance and resistance of the metal oxide layer over the metal surface , respectively. The variation of the fitted parameters (resistances and capacitances) with immersion time using the equivalent circuits of figure 8.6 is shown in figure 8.7 and 8.8. Values are shown with the errors from the numerical fitting ($10^{-4} <$ Chi-squared $< 10^{-2}$).

Figure 8.7 shows the evolution of the coating properties (i.e., the resistance and capacitance) as a function of immersion time. The silane coating (C) that contains the smallest amount of ceria nanoparticles has the lowest capacitance of the three systems examined over the 456 h of immersion, demonstrating the greatest thickness of this coating (Figure 8.7a). In addition, during immersion, the capacitance yields relatively consistent values, with only a small increase after 24 h of immersion, associated with electrolyte uptake [8, 31, 32].

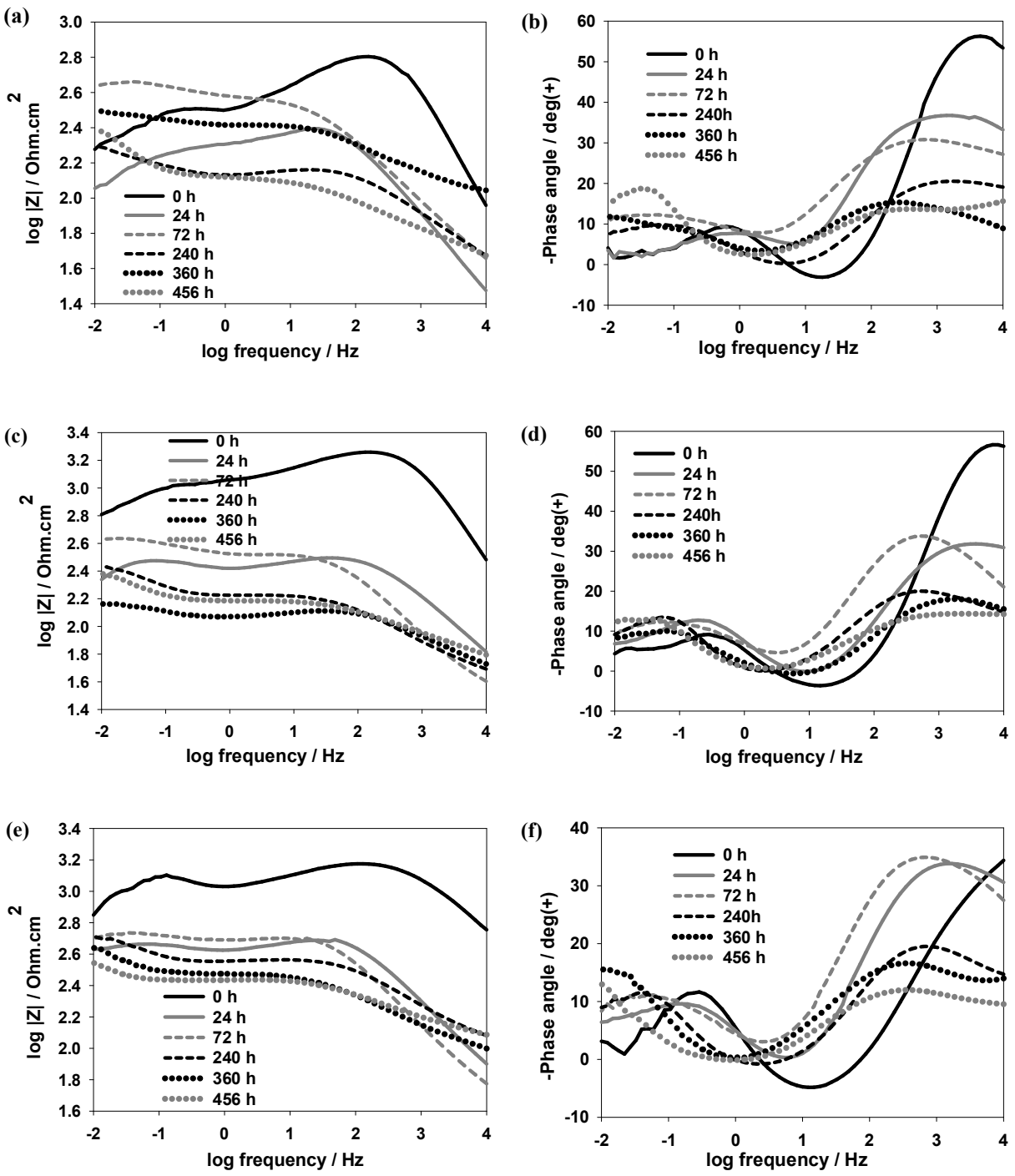

Figure 8.5. FEIS Bode graphs for impedance modulus (log|Z|: a, c, e) and phase angle (-φ: b, d, f) obtained for electro-galvanized steel samples pre-treated with silane coatings A (a, b), B (c, d), and C (e, f), during 0 h to 456 h of immersion in a 3.5% NaCl solution (immersion times as specified in each figure legend).

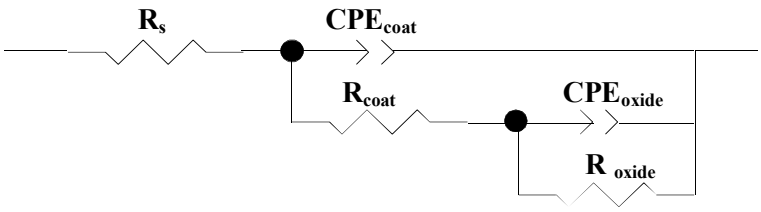

Figure 8.6. Equivalent circuit used for the numerical fitting of the EIS data obtained during immersion in a 3.5% NaCl solution.

The addition of ceria amount influences markedly the capacitance of the coatings. The capacitance data point at 456 hours of immersion shows to be twice as high for coating (B) in comparison to coating (C). The increased capacitance of the layer originates from the reduced thickness of the doped film. The capacitance of the coating is further increased in coating (A). During immersion of this specimen, a significant increase of film capacitance is observed, as a result of water uptake due to the reduced barrier properties of the film [31, 32].

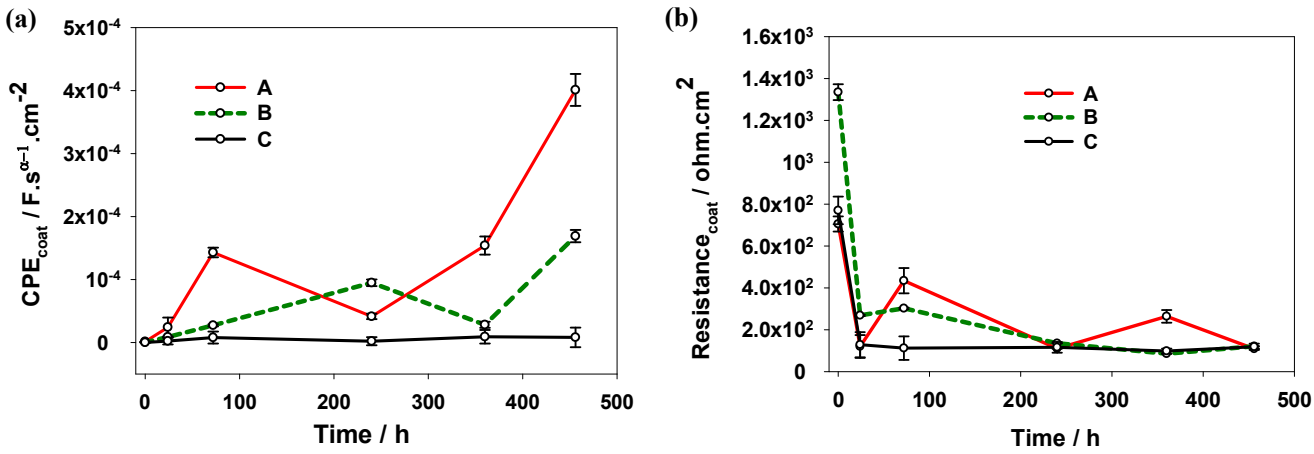

Figure 8.7. Evolution of the coating capacitance (a) and coating resistance (b) during immersion in a 3.5 % NaCl solution. Values were obtained by numerical fitting, using the equivalent circuit depicted in figure 8.6.

The evolution of the coating resistance, which is a fundamental characteristic of the barrier properties of a protective layer, is shown in figure 8.7b. At the commencement of immersion, the highest resistance is observed for coating (B), which is one order of magnitude higher than that of coatings (A) and (C). A significant decrease of the coating resistance occurs over the first 24 h of immersion, due to the development of conductive pathways inside the silane films [5, 9, 32]. Subsequently, the coating resistance remains almost constant in coating (C) over immersion for 456 h, reflecting the stability of the coating and good barrier properties. In contrast, for coatings (A) and (B), the high-frequency resistance passes through a maximum, and then starts to decrease. The initial increase of the high-frequency resistance values in the latter systems was attributed to swelling of the matrix and the consequent closing of nano/micro pores [31].

Thus, analysis of the resistance and capacitance evolution of the silane films shows a very important drop of the barrier properties when higher concentrations of ceria nanoparticles are introduced to the silane matrix. Even the uniform distribution and the absence of particle agglomeration do not protect against the increased water uptake and the decreased coating resistance. Therefore, the introduction of a large amount of ceria is likely to result in shrinkage of the hybrid matrix. These results are in agreement with the work of Schem et al. on aluminum alloys with a silane coating filled with CeO_2 nanoparticles [31].

The concentration of ceria nanoparticles also affects the parameter characteristics of the corrosion process that are associated with the development of a time constant in the low-frequency range of the EIS spectra. Figure 8.8 shows the temporal evolution of the metal oxide layer resistance (R_{oxide}) and capacitance (CPE_{oxide}) values during immersion. Upon arrival of the electrolyte at the substrate, the R_{oxide} and CPE_{oxide} are associated with both the zinc oxide layer and cerium oxide/hydroxide, due to the inhibition reaction. Thus, higher

R_{oxide} values indicate a corrosion-resistant oxide/hydroxide layer due to the reaction of cerium salts with the metal oxide layer over the substrate. With the breakdown of this protective layer due to attack by aggressive species, the R_{oxide} values decreased with time [31, 33].

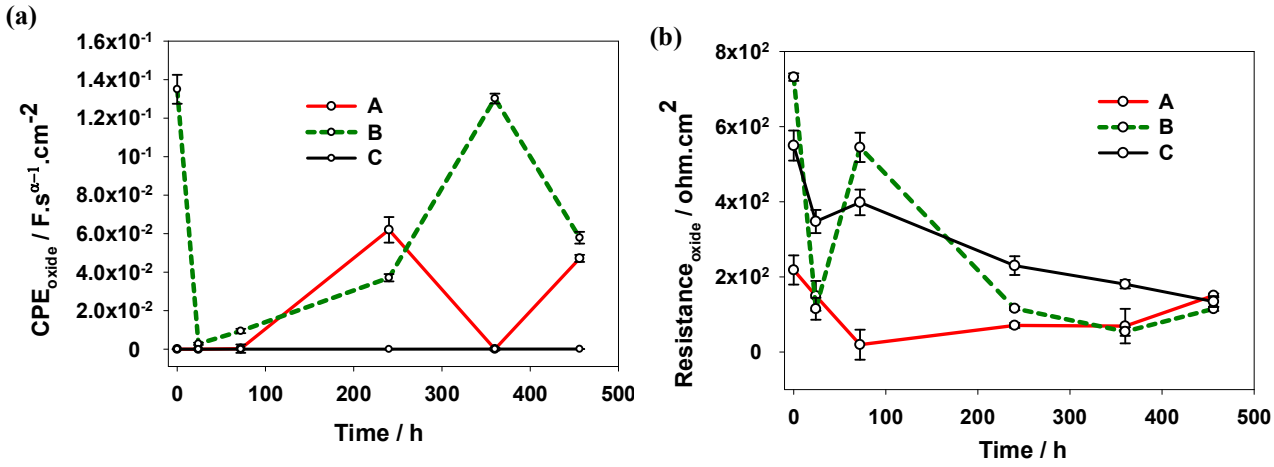

Figure 8.8. Evolution of the metal oxide layer capacitance (a) and resistance (b) during immersion in a 3.5% NaCl solution. Values were obtained by numerical fitting using the equivalent circuit depicted in figure 8.6.

In the case of silane coating (C), the capacitance (Figure 8.8a) reveals relatively stable values during immersion that correspond well with the thickness of the film. In contrast, the low-frequency resistance of the films (Figure 8.8b) showed a small drop during the first hours of immersion, and a recovery after 72 h of immersion. As the immersion time elapsed, there was a gradual decrease in resistance.

The silane coatings (A) and (B) showed some fluctuations in both the CPE values and the low-frequency resistance. For silane coating (B), the initial CPE values were on the order of 0.135 Fcm^{-2}, and, during the first day of immersion, the CPE values decreased by around

two orders of magnitude and stabilized at around 0.0579 Fcm^{-2}. This drop also occurred for silane coating (A), from 1.28×10^{-5} to 8.80×10^{-6} Fcm^{-2}, and it stabilized at around 0.0472 Fcm^{-2}. These values agree with the evolution of the low-frequency resistance of the film, which showed a rapid drop during the first hours of immersion, from 731.6 to 115 $\Omega\ cm^2$ in silane coating (B), and then a recovery after 72 h of immersion, followed by a gradual decrease and stabilization around 114.9 $\Omega\ cm^2$. For silane coating (A), the low-frequency resistance of the films revealed a gradual decrease during the 72 h of immersion, followed by an increase in the resistance and stabilization at around 150.5 $\Omega\ cm^2$.

In some cases, the evolution of the low-frequency resistance showed an increase after a few hours, accompanied by a decrease in the CPE. Since the corrosion activity occurred in localized areas, it is likely that the precipitation of the insoluble and passive corrosion products occurred at these locations, thereby decreasing the corrosion activity at the interface [9]. In fact, the most pronounced changes were observed for the silane coating doped with the highest amount of ceria nanoparticles (coating A), which presented the poorest barrier properties and was therefore most prone to early corrosion attack, as also observed by Schem et al. [31], who reported that an increase in nanoparticle loading hinders the barrier properties, resulting in a decrease in the low-frequency resistance of the silane film.

Potentiodynamic polarization scans of specimens, which were recorded after 1 h of immersion in the electrolyte, are presented in figure 8.9. The corrosion current density (i_{corr}) and corrosion potential (E_{corr}) were determined using Tafel extrapolation [20, 34]. The relevant parameters (Table 8.2) indicate the different effects of the ceria nanoparticle concentration on i_{corr} and E_{corr} of the silane coatings.

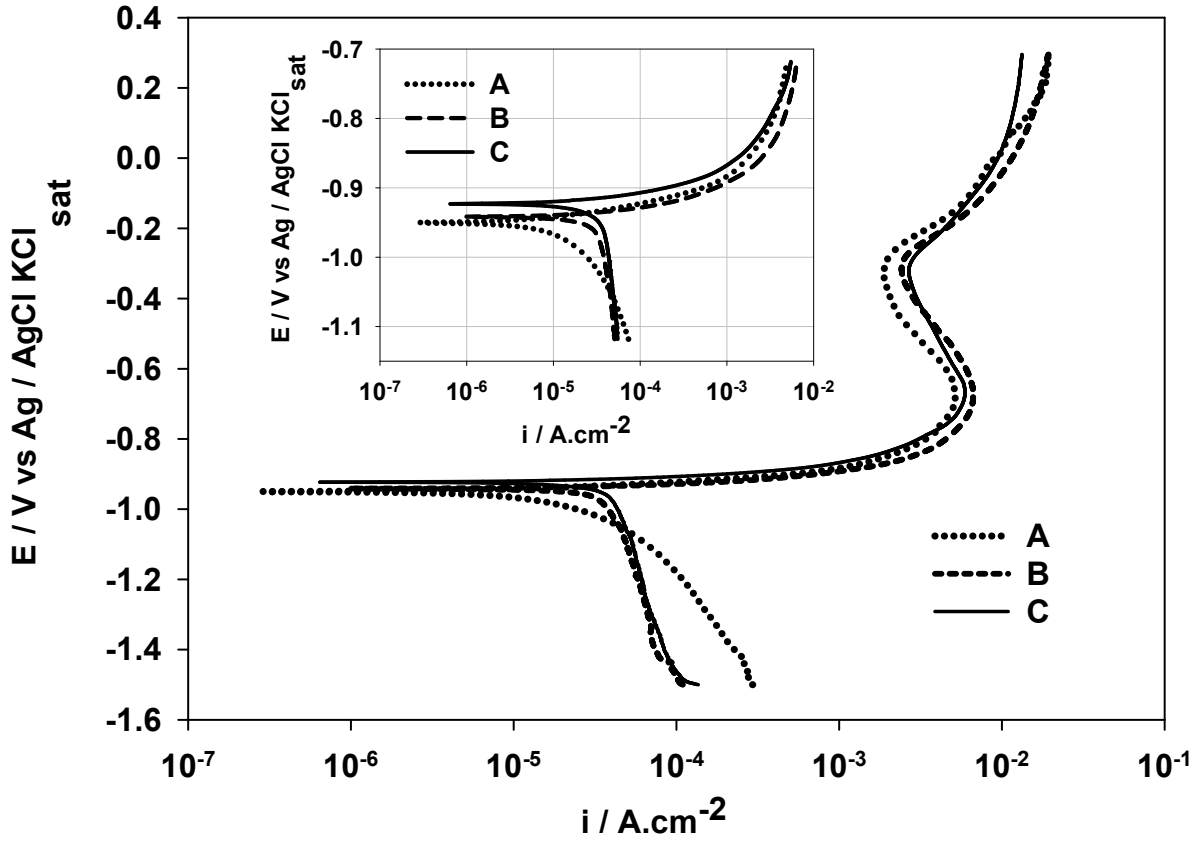

Figure 8.9. Potentiodynamic polarization curves for electro-galvanized steel samples coated with silane coatings A, B, and C, obtained after 1 h of immersion in a 3.5% NaCl solution. For comparison, the inset shows the potential depicted as the difference between the imposed potential and the corrosion potential. This approach allows increased separation of the anodic and cathodic polarization effects.

Figure 8.9 shows that cathodic polarization curves were shifted to lower current densities, whereas anodic polarization curves shifted to lower current densities by decreasing the ceria nanoparticle concentration. This suggests enhanced protection at both the cathodic and the anodic sites is offered by coating (C), which contains the lowest content of ceria nanoparticles. The corrosion potentials show a considerable shift in the noble direction for coating (C) (i.e., –0.923 V) compared with coating (A) (–0.950 V) and coating (B) (–0.942

V). The results summarized here are consistent with the crack-free surface morphology obtained for coating (C) before the corrosion test (Figure 8.3e).

The poor performance displayed by coatings (A) and (B) may be due to permeability of the coating associated with cracks or porosity, which allowed the aggressive electrolyte to come into contact with the metal surface, thus initiating corrosion [24]. These results are consistent with the SEM micrographs, which show porous microstructure for coatings (A) and (B) (Figures 8.3a and b, respectively).

Table 8.2. Summary of electrochemical parameters obtained from polarization, measured in a 3.5% NaCl solution.

Sample	E_{corr} (V)	i_{corr} (A cm^{-2})	b_c (V/dec)	b_a (V/dec)	Passive area (V)
A	–0.950	2.488×10^{-6}	0.013	0.026	–0.705 to –0.288
B	–0.942	8.704×10^{-6}	0.011	0.024	–0.715 to –0.282
C	–0.923	5.454×10^{-6}	0.010	0.016	–0.677 to –0.307

8.4. Conclusion

Cerium-silane hybrid coatings were synthesized from organic/inorganic precursors, with different concentrations of incorporated cerium-activated ceria nanoparticles, and fabricated on treated electro-galvanized steel surfaces. The coatings had relatively uniform thicknesses and distributions of nanoparticles. No cracking or delamination of the coatings was evident. Microscopic observations explain the longer durability of the silane coating doped with the lowest content of activated ceria nanoparticles after short-term corrosion tests (456 h). This coating resisted exposure in a neutral salt spray test for 288 h without general

corrosion, and showed reduced corrosion at an artificial scratch in the material compared with the silane coatings doped with higher contents of ceria nanoparticles.

The EIS results suggest that the concentration of nanoparticles has an important impact on the barrier properties of the silane films, as lower nanoparticle content results in better barrier properties. Enhanced protection at both the cathodic and the anodic sites was offered by the coating that contained the lowest content of ceria nanoparticles. During polarization in a 3.5% NaCl solution, the corrosion potentials showed a considerable shift in the noble direction for this coating, compared with the other coatings that contained higher contents of nanoparticles.

References

1. M. Hosseini, H. Ashassi-Sorkhabi, H.A.Y. Ghiasvand, Corrosion protection of electro-galvanized steel by green conversion coatings, Journal of Rare Earths, 25, 2007, pp. 537-543.
2. S. Dalbin, G. Maurin, R.P. Nogueira, J. Persello, N. Pommier, Silica-based coating for corrosion protection of electrogalvanized steel, Surface and Coatings Technology, 194, 2005, pp. 363-371.
3. D.E.J. Talbot, J.D.R. Talbot, Corrosion Science and Technology , CRC Press, Taylor and Francis Group, Abington, UK, 1997.
4. M.F. Montemor, W. Trabelsi, S.V. Lamaka, K.A. Yasakau, M.L. Zheludkevich, A.C. Bastos, M.G.S. Ferreira, The synergistic combination of bis-silane and CeO_2–ZrO_2 nanoparticles on the electrochemical behaviour of galvanised steel in NaCl solutions, Electrochimica Acta, 53, 2008, pp. 5913-5922.
5. W. Trabelsi, P. Cecílio, M.G.S. Ferreira, K. Yasakau, M.L. Zheludkevich, M.F. Montemor, Surface evaluation and electrochemical behaviour of doped silane pre-

treatments on galvanised steel substrates, Progress in Organic Coatings, 59, 2007, pp. 214-223.

6. W. Trabelsi, P. Cecilio, M.G.S. Ferreira, M.F. Montemor, Electrochemical assessment of the self-healing properties of Ce-doped silane solutions for the pre-treatment of galvanised steel substrates, Progress in Organic Coatings, 54, 2005, pp. 276-284.
7. M.L. Zheludkevich, R. Serra, M.F. Montemor, K.A. Yasakau, I.M.M. Salvado, M.G.S. Ferreira, Nanostructured sol–gel coatings doped with cerium nitrate as pre-treatments for AA2024-T3: corrosion protection performance, Electrochimica Acta, 51, 2005, pp. 208-217.
8. M.F. Montemor, M.G.S. Ferreira, Cerium salt activated nanoparticles as fillers for silane films: evaluation of the corrosion inhibition performance on galvanised steel substrates, Electrochimica Acta, 52, 2007, pp. 6976-6987.
9. M.F. Montemor, R. Pinto, M.G.S. Ferreira, Chemical composition and corrosion protection of silane films modified with CeO_2 nanoparticles, Electrochimica Acta, 54, 2009, pp. 5179-5189.
10. M.F. Montemor, W. Trabelsi, M. Zheludevich, M.G.S. Ferreira, Modification of bis-silane solutions with rare-earth cations for improved corrosion protection of galvanized steel substrates, Progress in Organic Coatings, 57, 2006, pp. 67-77.
11. K. Aramaki, Self-healing mechanism of a protective film prepared on a $Ce(NO_3)_3$-pretreated zinc electrode by modification with $Zn(NO_3)_2$ and Na_3PO_4, Corrosion Science, 45, 2003, pp. 1085-1101.
12. K. Aramaki, The inhibition effects of cation inhibitors on corrosion of zinc in aerated 0.5 M NaCl, Corrosion Science, 43, 2001, pp. 1573-1588.

13. K. Aramaki, Preparation of self-healing protective films on a zinc electrode treated in a cerium(III) nitrate solution and modified with sodium phosphate and cerium(III) nitrate, Corrosion Science, 46, 2004, pp. 1565-1579.
14. R.Z. Zand, K. Verbeken, A. Adriaens, Influence of the cerium concentration on the corrosion performance of Ce-doped silica hybrid coatings on hot dip galvanized steel substrates, International Journal of Electrochemical Science, 8, 2013, pp. 548-563.
15. R.Z. Zand, K. Verbeken, A. Adriaens, Evaluation of the corrosion inhibition performance of silane coatings filled with cerium salt-activated nanoparticles on hot-dip galvanized steel substrates, International Journal of Electrochemical Science, 8, 2013, pp. 4924-4940.
16. A.M. Cabral, W. Trabelsi, R. Serra, M.F. Montemor, M.L. Zheludkevich, M.G.S. Ferreira, The corrosion resistance of hot dip galvanised steel and AA2024-T3 pre-treated with bis-[triethoxysilylpropyl] tetrasulfide solutions doped with $Ce(NO_3)_3$, Corrosion Science, 48, 2006, pp. 3740-3758.
17. V. Palanivel, D. Zhu, W.J. van Ooij, Nanoparticle-filled silane films as chromate replacements for aluminum alloys, Progress in Organic Coatings, 47, 2003, pp. 384-392.
18. M.F. Montemor, M.G.S. Ferreira, Analytical characterization of silane films modified with cerium activated nanoparticles and its relation with the corrosion protection of galvanised steel substrates, Progress in Organic Coatings, 63, 2008, pp. 330-337.
19. M. Garcia-Heras, A. Jimenez-Morales, B. Casal, J.C. Galvan, S. Radzki, M.A. Villegas, Preparation and electrochemical study of cerium–silica sol–gel thin films, Journal of Alloys and Compounds, 380, 2004, pp. 219-224.
20. X. Zhong, Q. Li, J. Hu, X. Yang, F. Luo, Y. Dai, Effect of cerium concentration on microstructure, morphology and corrosion resistance of cerium–silica hybrid coatings on magnesium alloy AZ91D, Progress in Organic Coatings, 69, 2010, pp. 52-56.

21. R.Z. Zand, Investigation of corrosion, abrasion and weathering resistance in hybrid nanocomposite coatings based on epoxy-silica, Thesis, Azad University-Tehran North Branch, 2005.
22. R.Z. Zand, K. Verbeken, A. Adriaens, Corrosion resistance performance of cerium doped silica sol–gel coatings on 304L stainless steel, Progress in Organic Coatings, 75, 2012, pp. 463-473.
23. R.Z. Zand, K. Verbeken, A. Adriaens, The corrosion resistance of 316L stainless steel coated with a silane hybrid nanocomposite coating, Progress in Organic Coatings, 72, 2011, pp. 709-715.
24. A. Phanasgaonkar, V.S. Raja, Influence of curing temperature, silica nanoparticles- and cerium on surface morphology and corrosion behaviour of hybrid silane coatings on mild steel, Surface and Coatings Technology, 203, 2009, pp. 2260-2271.
25. M.F. Montemor, A.M. Cabral, M.L. Zheludkevich, M.G.S. Ferreira, The corrosion resistance of hot dip galvanized steel pretreated with Bis-functional silanes modified with microsilica, Surface and Coatings Technology, 200, 2006, pp. 2875-2885.
26. W. Trabelsi, E. Triki, L. Dhouibi, M.G.S. Ferreira, M.L. Zheludkevich, M.F. Montemor, The use of pre-treatments based on doped silane solutions for improved corrosion resistance of galvanised steel substrates, Surface and Coatings Technology, 200, 2006, pp. 4240-4250.
27. L.M. Palomino, P.H. Suegama, I.V. Aoki, M.F. Montemor, H.G. De Melo, Electrochemical study of modified cerium–silane bi-layer on Al alloy 2024-T3, Corrosion Science, 51, 2009, pp. 1238-1250.
28. S.M.A. Shibli, F. Chacko, CeO_2–TiO_2 mixed oxide incorporated high performance hot dip zinc coating, Surface and Coatings Technology, 205, 2011, pp. 2931-2937.

29. A. Pepe, M. Aparicio, A. Duran, S. Cere, Cerium hybrid silica coatings on stainless steel AISI 304 substrate, Journal of Sol-Gel Science and Technology, 39, 2006, pp. 131-138.
30. M.L. Zheludkevich, K.A. Yasakau, A.C. Bastos, O.V. Karavai, M.G.S. Ferreira, On the application of electrochemical impedance spectroscopy to study the self-healing properties of protective coatings, Electrochemistry Communications, 9, 2007, pp. 2622-2628.
31. M. Schem, T. Schmidt, J. Gerwann, M. Wittmar, M. Veith, G.E. Thompson, I.S. Molchan, T. Hashimoto, P. Skeldon, A.R. Phani, S. Santucci, M.L. Zheludkevich, CeO_2-filled sol–gel coatings for corrosion protection of AA2024-T3 aluminium alloy, Corrosion Science, 51, 2009, pp. 2304-2315.
32. P.H. Suegama, V.H.V. Sarmento, M.F. Montemor, A.V. Benedetti, H.G. de Melo, I.V. Aoki, C.V. Santilli, Effect of cerium (IV) ions on the anticorrosion properties of siloxane-poly(methyl methacrylate) based film applied on tin coated steel, Electrochimica Acta, 55, 2010, pp. 5100-5109.
33. H. Shi, F. Liu, E. Han, Corrosion behaviour of sol–gel coatings doped with cerium salts on 2024-T3 aluminum alloy, Materials Chemistry and Physics, 124, 2010, pp. 291-297.
34. ASTM G3–89; Standard practice for conventions applicable to electrochemical measurements in corrosion testing, Annual Book of ASTM Standards, 03.02, ASTM International, PA, USA, 2004.

9

Effect of activated ceria and zirconia nanoparticles on the protective behavior of silane coatings in chloride solutions [1]

9.1. Introduction

Hybrid silane sol-gel coatings as an environmentally friendly materials for corrosion protection of metals attracted considerable interest, as they provide the formation of a thin organic coating that confers surface functionalization [1]. These coatings create a dense, oxygen-rich coating that generates a protective physical barrier [2]. However, these coatings are inert, and do not provide any active protection if aggressive species reach the metallic surface and initiate corrosion [1, 3]. Indeed, silane coatings present small pores, pinholes or

[1] Published as full paper in International Journal Electrochemical Science, Volume 10, Roohangiz Zandi Zand, Victoria Flexer, Michel De Keersmaecker, Kim Verbeken, Annemie Adriaens, Effects of activated Ceria and Zirconia nanoparticles on the protective behaviour of silane coatings in chloride solutions, 997-1014, (2015).

micro cracks that facilitate electrolyte diffusion and the accumulation of aggressive species at the coating/substrate interface [4]. Therefore, the challenge is to modify the bulk properties of silane coatings by adding "active" protective species that further improve the corrosion resistance of the layer, or introduce self-healing capabilities [5].

A successful approach to improve the corrosion protection of silane coatings is based on the addition of oxide nanoparticles. These provide improved oxidation, corrosion, erosion and wear resistance. Extensive research has been carried out to enhance the corrosion resistance of metallic substrates by using ZrO_2 [1, 6-8], CeO_2 [9-12], SiO_2 [5, 9, 13-16], Al_2O_3 [17], TiO_2 [18, 19], and other mixed oxides. The amount of cracks and pores in sol-gel films can be decreased by incorporation of oxide nanoparticles into the hybrid matrix [6]. CeO_2 and ZrO_2, are particularly interesting due to their high corrosion, mechanical abrasion and wear resistance [1]. Montemor *et al.* [5] and Zheludkevich *et al.* [6] reported the modification of silane-based hybrid films with CeO_2, ZrO_2 or CeO_2-ZrO_2 nanoparticles. Results demonstrated that CeO_2 nanoparticles are very effective fillers, leading to both improved barrier and corrosion protection properties of the silane coatings. ZrO_2 nanoparticles produce an important enhancement of the barrier properties, and could act as a reservoir for corrosion inhibitors, but are otherwise inert.[1] Unfortunately, these films can no longer offer adequate protection if the coating is damaged due to the lack of self-healing capabilities.

Conversely, incorporation of corrosion inhibitors into sol-gel films can enhance the protective ability of the coatings, suppressing the corrosion process in the defects or where the coating has been damaged [6]. Among the most effective protective species, rare-earth salts offer good corrosion inhibition properties in addition to environmental friendliness [20]. Cerium nitrate has been successfully tested for corrosion protection of galvanized steel substrates, either as a conversion film [21-23] or as a corrosion inhibitor through addition to

the silane formulation [20, 24-26]. However, corrosion inhibitors that are directly introduced into the silane formulation have difficulties to provide long-term protection of metals. In order to heal corrosion spots, a slow release of inhibitor would be desirable [27, 28]. This shortcoming calls for the development of nano-reservoirs to isolate inhibitors and prevent its direct interaction with the sol-gel matrix. Moreover, nanoparticle activation with cerium ions could reduce nanoparticle agglomeration due to stabilization of the surface charge [5]. In this way, the nanoparticles fix the cerium ions on their surface, distributing the inhibitor molecules homogenously in the bulk of the film and producing a slow release when required [6, 7].

Despite extensive work on the study of the unique properties of either CeO_2 or ZrO_2 nanoparticles, very little has been reported using a combination of both in the field of protective pre-treatments. Montemor *et al.* [1] investigated the electrochemical behaviour of modified silane-based hybrid films with CeO_2-ZrO_2 nanoparticles on galvanized steel substrate in diluted NaCl solution (0.005 M). Results demonstrated that CeO_2-ZrO_2 nanoparticles play an active role in the corrosion protection performance when they are added as fillers to hybrid silane coatings. The work did not study the possibility of adding an active corrosion inhibitor such as cerium ions to enhance even further the protective protection. Additionally, a long term evaluation of corrosion inhibition of silane films modified with rare earth salts-oxide nanoparticles in aggressive media, including mechanisms to stress the coating or artificial damage to evaluate the self-healing properties, would fill an important gap in the field.

The objective of this work was to investigate the effect of ceria and zirconia nanoparticles on protective behaviour of uninhibited and cerium inhibited silane hybrid coatings in aggressive media (3.5% and 5% NaCl, as opposed to 0.005M NaCl for the uninhibited CeO_2-ZrO_2 coatings mentioned above [1]).

9.2. Sample preparation

Ceria and zirconia nanoparticles (10 wt% in water, particle size < 25 nm and < 100 nm respectively, Sigma Aldrich) were activated by ultrasonic dispersion in an aqueous solution of $Ce(NO_3)_3$ (Fluka). Four sets of aqueous solutions were prepared. Set D contained CeO_2 and ZrO_2 nanoparticles, and $Ce(NO_3)_3$, while sets A, B and C where prepared with only two of the components (see Table 9.1).

The silane solution was prepared by adding 4.084 mL of 3–glycidoxypropyl-trimethoxy silane (GPTMS, Merck) to 0.5 mL aqueous HCl (pH = 2), and stirred in a sealed beaker at room temperature for 20 min at 240 RPM to hydrolyze and condense the silane precursors. Next, the aqueous dispersion of nanoparticles was added and stirred for 10 min. For all samples the total Ce+Zr/Si mole ratio was 0.05. In the next step, 2.111 g of bisphenol A (BPA, Merck) was added to the solution as a cross-linking agent. The BPA was dissolved by mixing the solution for 80 minutes. To accelerate the condensation reaction, 0.0152 mL of 1–methylimidazol (MI, Merck) was added to the solution and stirred for 5 min. A clear, colourless, homogenous solution resulted [29, 30].

Electro-galvanized steel samples (Arcelor Mittal, Gent, Belgium) consisted of coupons (1.13 cm^2 area and 0.1 cm thickness, for the AFM and electrochemical tests), and plates (7 × 15 × 0.1 cm, and, for the salt spray tests). The zinc coating had a weight of 112 g/m^2, and a thickness of 8 μm. The galvanized steel specimens were degreased using an alkaline cleaner, washed with distilled water, dried in air, and immersed in the silane solution for 60 s. The coated specimens were dried at room temperature for 24 h, and subsequently submitted to a 25–130°C curing process with a heating rate of 7.5 °C/min for 90 minutes, to initiate extensive cross-linking in the hybrid films [30].

Table 9.1. Composition and thickness of the coatings.

Set	Molar ratio (mol %)			Coating thickness
	CeO_2 /Si	ZrO_2 /Si	Ce $(NO_3)_3$ /Si	(μm)
A (SHC- ZrO_2 + $Ce(NO_3)_3$)	-	0.0125	0.0375	61 ± 10
B (SHC- CeO_2 + $Ce(NO_3)_3$)	0.0125	-	0.0375	62 ± 12
C (SHC- ZrO_2 - CeO_2)	0.0250	0.0250	-	67 ± 15
D (SHC- ZrO_2- CeO_2+ $Ce(NO_3)_3$)	0.0125	0.0125	0.0250	75 ± 13

9.3. Results

The coating thickness values are shown in Table 9.1. All films showed similar thickness values. The mean thickness values show a slight increase in going from coating A to D. However, the error in thickness measurements is in the same order as the thickness variation between different films (15-22%). Therefore, it is dubious to ascribe differences in protective behaviour to this variable.

The general surface morphology and the nanoparticle distribution in the different modified silane films can be observed in figure 9.1. For coatings B and D, the surface morphology was very uniform with absence of defects or cracks. In coating D, the nanoparticles are about 20 – 50 nm in diameter and uniformly distributed in the matrix when compared with the other samples (A, B, and C). Very few brighter spots (100-200 nm in diameter) are visible, which could either be ZrO_2 nanoparticles in the upper size limit (the manufacturer only informs the upper size limit, but no size distribution); or agglomerates of smaller nanoparticles on the surface [19, 30]. The size difference between the known dimensions of the added nanoparticles and the values measured by AFM can be explained by the presence of a silane layer on top of the nanoparticles. Thus, AFM measures the convexity of the surface caused by the underlying nanoparticles [6, 19]

For coating B, the AFM images show the presence of both agglomerates and small nanoparticles. The individual nanoparticles also appear to be 20 - 50 nm in diameter. In this case, the larger spots (100-300 nm) are readily classified as agglomerates, since this sample does not contain the larger ZrO_2 nanoparticles.

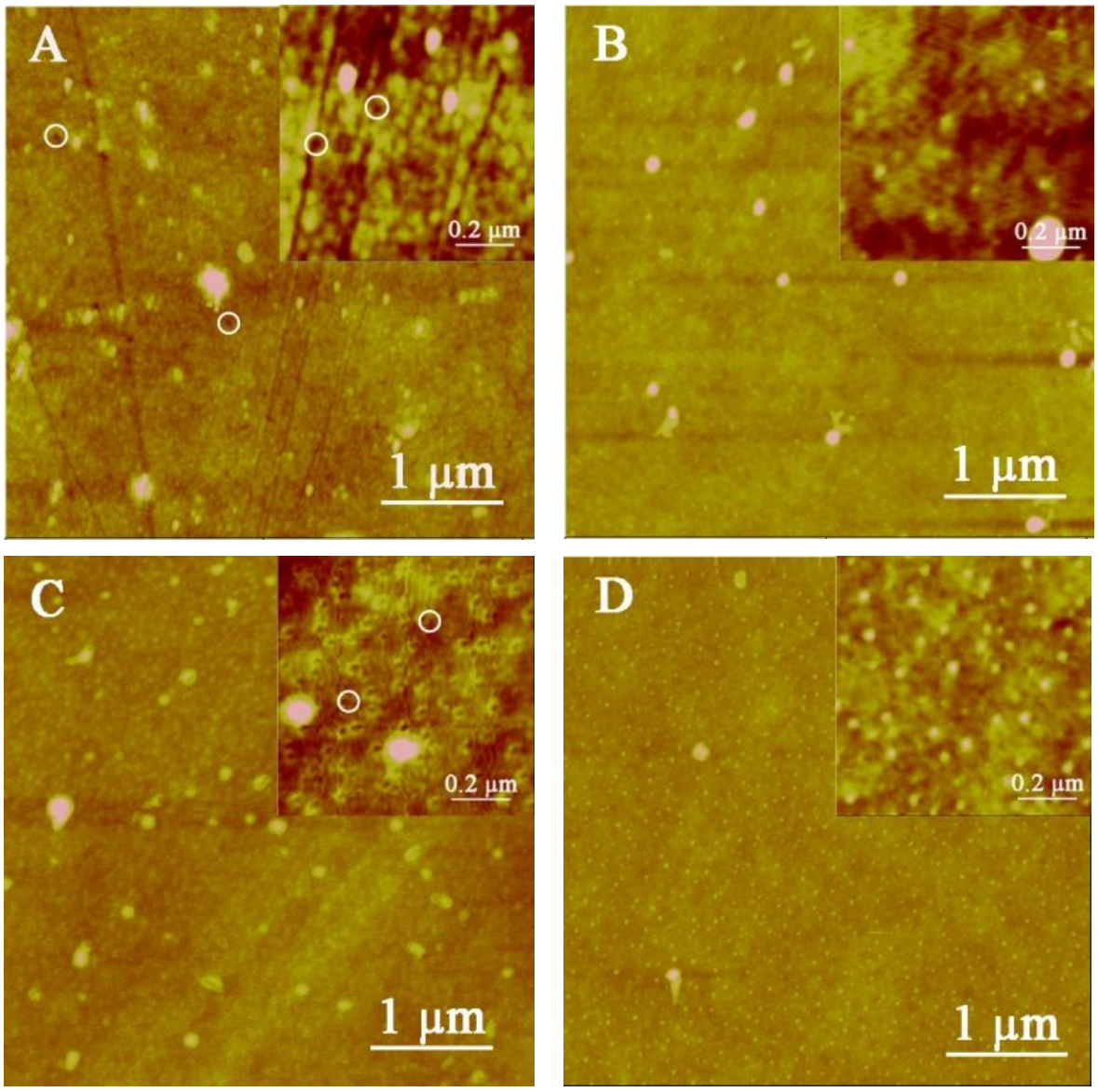

Figure 9.1. AFM top-view images of hybrid silane films modified with CeO_2 and ZrO_2 nanoparticles: (A) $Ce(NO_3)_3$ + ZrO_2; (B) $Ce(NO_3)_3$ + CeO_2; (C) CeO_2-ZrO_2; (D) $Ce(NO_3)_3$ + CeO_2-ZrO_2. Pin holes in coatings A and C marked by white circles. Inset is a zoom image over the same scan area.

Coatings A and C show numerous nanoparticles aggregates. Moreover, these images reveal the presence of some nano-sized holes in the coatings, particularly for coating C. Two examples of these holes are highlighted in figure 9.1C. The occurrence of coating defects is undesirable, since they may serve as initiators for pit corrosion through reduced coating thickness and/or as the initiation sites of fatigue cracks [31].

RMS surface roughness values of 0.722 nm, 0.955 nm, 0.855 nm, and 0.485 nm were measured for coatings A, B, C and D respectively. Differences in surface roughness arise from the presence of nanoparticles aggregates. Coating D distinctly shows the lowest surface roughness. Thus, AFM surface morphology demonstrates that the silane formulation D is the best for providing uniform morphology with low roughness, monodispersed nanoparticles, and absence of coating defects.

Figure 9.2a and b present results of the salt spray exposure tests after 168 h and 264 h. An uncoated substrate was tested as control. An artificial scratch was made to all coated samples to evaluate the protective efficiency of both the intact and damaged coatings.

After 168 h of exposure (Figure 9.2a), the uncoated substrate (Figure 9.2a,E) is heavily corroded with discoloration and pit formation. Samples A and C showed few spots of limited localized corrosion in the intact (non-damaged) coating, marked with black arrows in the images, which could be due to the presence of some pinholes in the coating layers as shown in AFM images (Figure 9.1 A and C). In contrast, for coatings B and D no sign of corrosion was detected in the intact coating after 168 h.

The protective performance around the artificial scratch reveals the capacity of the coating to overcome coating damage. Sample (C) is heavily corroded in and around the edges of the scribe area (and particularly in the cross point), and shows a number of blisters together

with white rust due to zinc coating degradation and formation of corrosion products such as zinc oxide and zinc hydroxide.

(a)

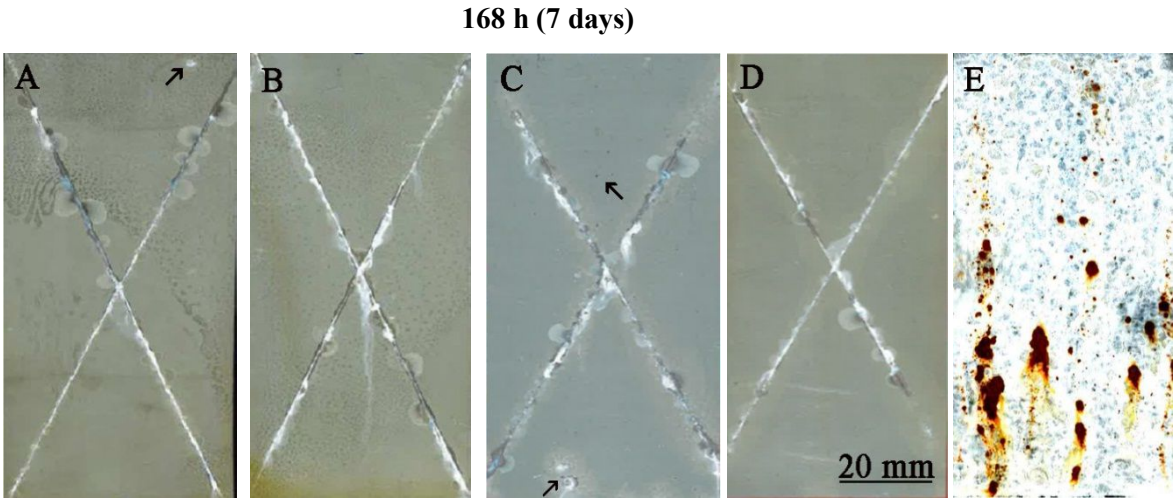

(b)

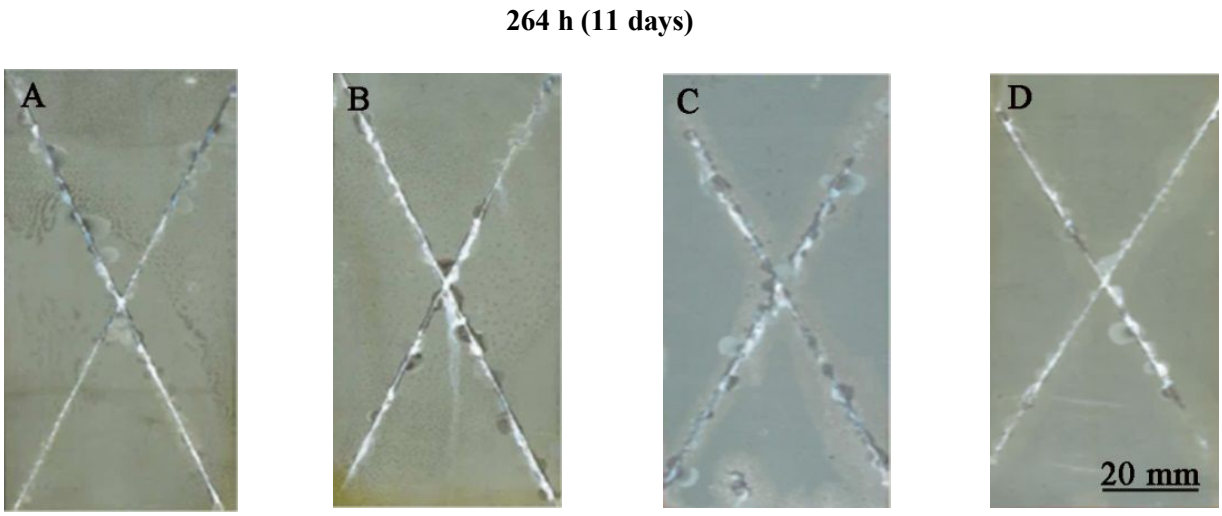

Figure 9.2. Photographs of uncoated and coated electro-galvanized steel samples with silane coatings A, B, C and D after 168 h (a) and 264 h (b) of salt spray exposure.

The samples containing cerium nitrate (A, B and D) show lower delamination and corrosion products along the scribe area, as compared with sample C. The limited

delamination in the presence of cerium nitrate suggests the availability of a corrosion inhibiting species.

After 264 h of exposure (Figure 9.2b), no considerable changes were detected in the intact area in none of the coated samples, pointing towards the good barrier properties of the intact coatings. The few spots observed in samples A and C at 168h remained the same size and aspect, suggesting self-healing capabilities to some extent for these coatings in the case of minor coating damage. In contrast, around the scribe area, the breakdown of the coating layers in samples B and C progressed and this was followed by formation of red rust around the blisters, suggesting the presence of iron oxides, *i.e.* the bulk steel has already been corroded. The best performance was observed for samples A and D, *i.e.* the samples containing activated ZrO_2. A few blisters are observed, but blister growth rate seems to be considerably lower when compared with samples B and C. Samples A and D do not show formation of red rust in and around the scribed area. These coatings seem to be the most capable of overcoming the effects of coating damage.

Potentiodynamic polarization scans of coated and uncoated samples recorded after 1 h of immersion in 3.5% NaCl are presented in figure 9.3. Both cathodic and anodic polarization curves were significantly shifted to lower current densities for all coated samples as compared to the uncoated sample. Moreover, the corrosion potentials showed a considerable shift in the noble direction. Because linearity is not achieved for a sufficiently large voltage interval, a quantitative Tafel analysis was not possible for any of the coated samples. The polarization curves still show qualitatively the good barrier properties of all four coatings, with anodic currents at least one order of magnitude lower than the blank. All four coatings considerable decrease the available surface area for the corrosion reactions (oxygen reduction and metal dissolution), slowing down the corrosion activity, and hence the corrosion current density.

These effects were more pronounced for coating D. Surprisingly; the initial slopes for the anodic branches of the coated samples are quite sharp, followed by a complete flattening of the current. This behaviour suggests that although the coatings are acting as a good barrier protecting most of the galvanized steel surface, the corrosion process is indeed very active in the few spots available for corrosion.

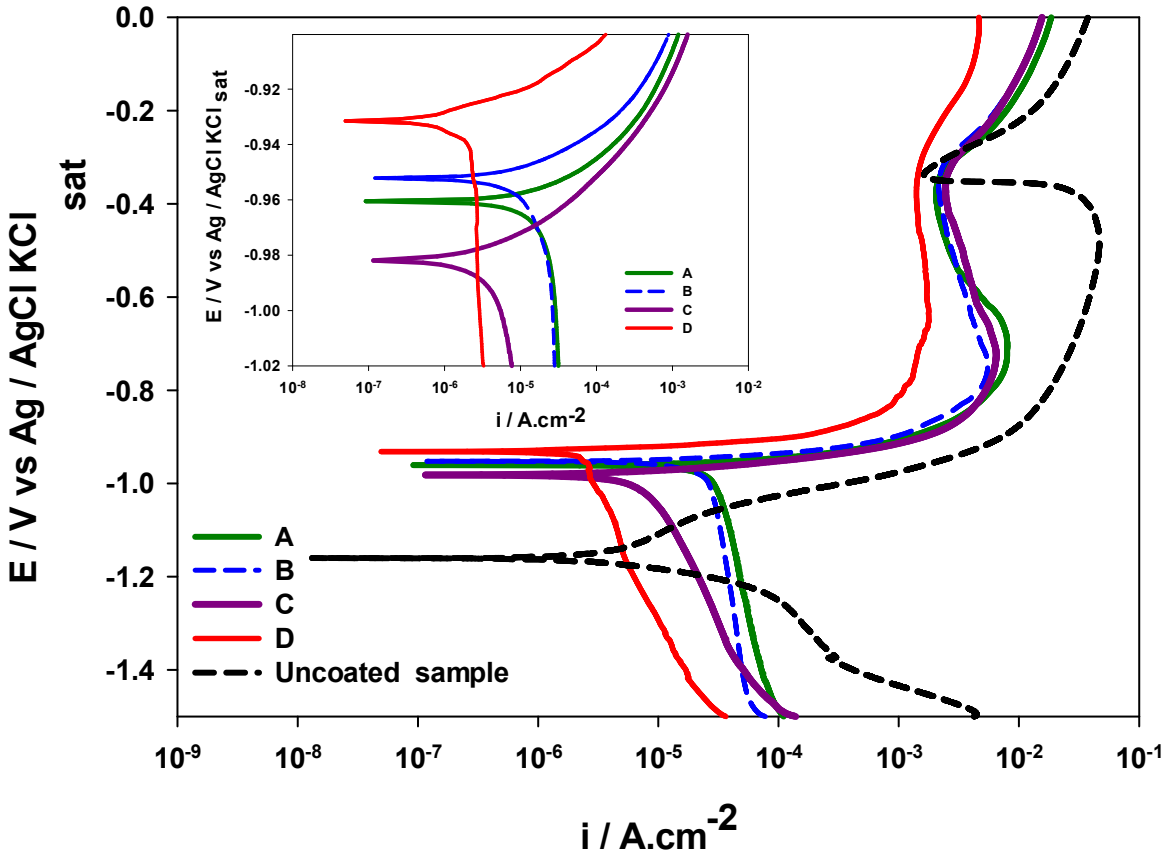

Figure 9.3. Potentiodynamic polarization curves for the uncoated and coated electro-galvanized steel samples with silane coatings A, B, C and D, obtained after 1 h of immersion in a 3.5% NaCl solution. The inset shows a zoom around the corrosion potential of the coated samples.

These results suggest that the enhanced corrosion protection of coating D is due to controllable release of cerium nitrate by nanoparticles (as reservoirs) in corroded spots, forming complexes with zinc charged species and reinforcing their protective role. These

more stable corrosion products decrease even more the active area available for corrosion reactions.

The Bode plots obtained for the substrates pre-treated with different modified silane films during 244 h immersion in 3.5% NaCl solution are depicted in figure 9.4. The Bode plots show that the impedance spectra are dependent on the nature of the dopant. Sample D showed impedance magnitude values that are almost three times higher than for the other samples at the initial stage of immersion (Figure 9.4g). After 48 h of immersion, the impedance of this sample decreases, which is most probably associated with water uptake. Water uptake could occur either around the few nanoparticle agglomerations, through nanopores of sizes below AFM resolution, or through pores formed at a later stage because of electrolyte exposure [32]. With further increase of immersion time, the impedance magnitude of sample D shows a considerable recovery, the EIS spectrum after 96 h shows very similar values to the original spectrum at the beginning of the immersion experiment. This recovery is attributed to the self-healing effect of cerium ions around the corrosion spots [4]. A new drop in impedance magnitude at 168 h is again followed by mild recovery at 244 h. Most important, after 244 h immersion, sample D still shows the highest impedance magnitude values at low frequencies of all four coatings. Such high impedance magnitude values confer higher corrosion protection of the silane films doped with $Ce(NO_3)_3$ and CeO_2-ZrO_2 nanoparticles.

Conversely, the impedance magnitude values for the other coatings (A, B and C) continuously decreased with time, except a small recovery for sample B after 168 h immersion (Figures 9.4 a, c and e). Sample C shows the lowest impedance magnitude values.

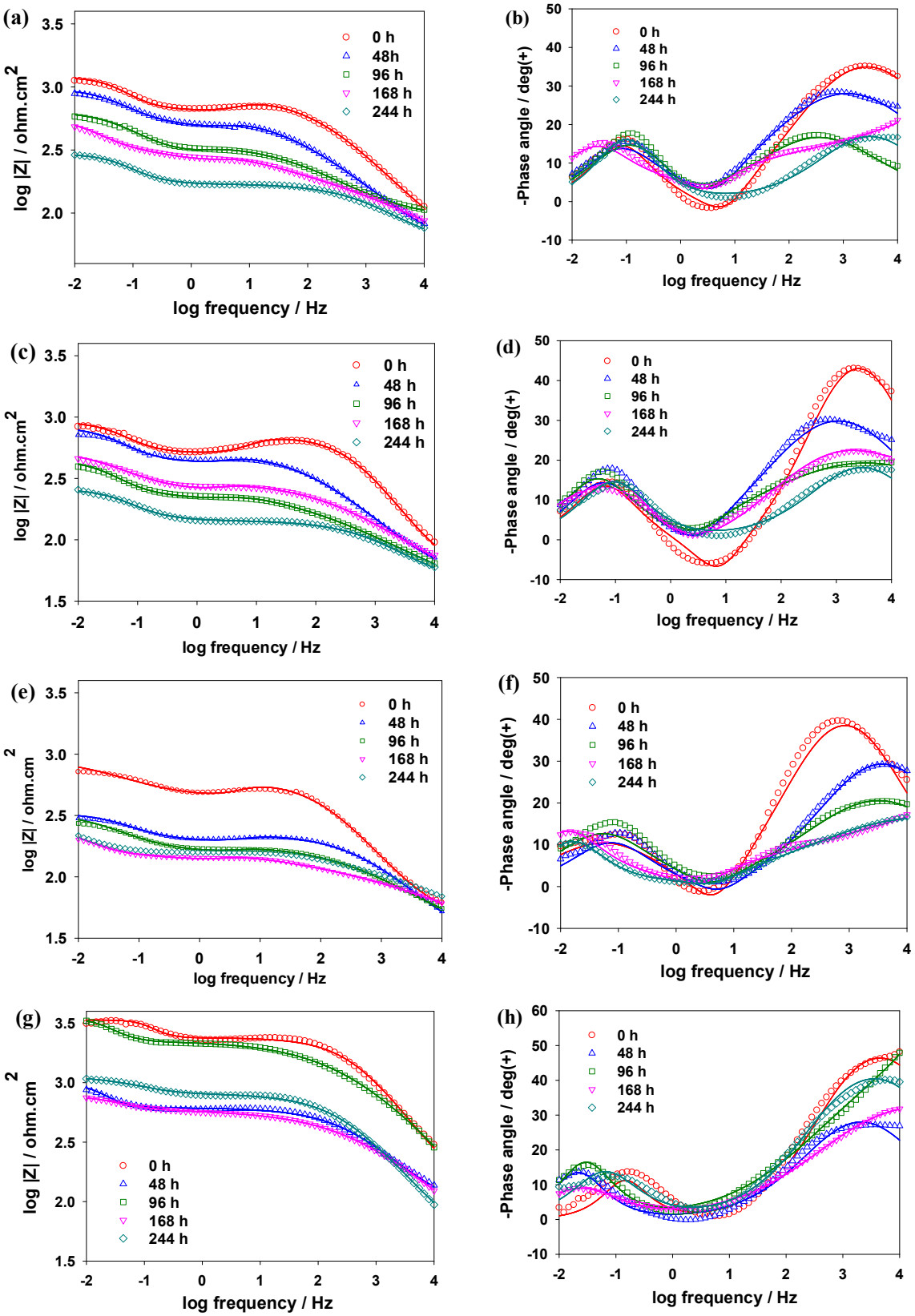

Figure 9.4. EIS Bode modulus (a, c, e, g) and phase angle (b, d, f, h) plots obtained for electro-galvanized steel samples pre-treated with silane coatings A (a, b), B (c, d), C (e, f), and D (g, h) during immersion in a 3.5% NaCl solution. Solid lines show the fitted results to the equivalent circuits in figure 5.

The shape of the phase angle plots, at the beginning of the immersion (0 h), indicated the presence of three time constants for coatings A, B and C (Figure 9.4b, d, f), consisting of a large capacitive loop at high frequencies (around 10^4 rad s^{-1}), which can be attributed to the capacitive behaviour of the silane film [33, 34]; an pseudo-inductive loop at medium frequencies (around 3.16 rad s^{-1}), which suggests may be related to the breakdown of the former protective surface film and corrosion activity due to adsorption of ions from the electrolyte solution (Cl^- and Na^+) through the pores of the coating [35-40]; and followed by the second capacitive loop at low frequencies (around 10^{-1} rad s^{-1}), which reveals corrosion activity and build-up of corrosion products [33, 34]. After a few hours of immersion, the EIS response starts to change and the phase angle plots evolved to two time constants consisting of two large capacitive loops at high (around 10^4 rad s^{-1}) and low (around 10^{-1} rad s^{-1}) frequencies. This change suggests that the coatings developed electrolyte conductive pathways through the pinholes and around the agglomerations (as shown in AFM images (Fig. 9.1 A-C)), whereby the electrolyte could reach the substrate. The inductive loop has disappeared once the substrate has been fully adsorbed with ions. These ions will then start the corrosion process. For sample D, during immersion, the shape of the phase angle plots also indicated two capacitive loops at high and low frequencies. Interestingly, we do not observe the inductive loop here. This is probably too small because the pinholes are much smaller and there are almost no nanoparticles aggregates, which means less electrolyte penetrates, and the absorption of ions is much slower and hence not apparent in the phase plot.

A more detailed interpretation of the EIS results can be made by numerical fitting of the experimental data to the equivalent circuits depicted in figure 9.5. Because the phase angle plots revealed two or three time constants at different immersion times, two different equivalent circuits were used to fit the data. The equivalent circuit shown in figure 9.5a was

used to model the EIS results of samples A, B and C at the beginning of immersion (0h). The equivalent circuit shown in figure 9.5b was used to model the EIS results of sample D during 244 h immersion, as well as samples A, B and C during 48 h to 244 h of immersion. The numerical simulations are plotted as full lines in figure 9.4a to h. These fittings are in very good agreement with the experimental data for all the 4 samples.

Thus, for the equivalent circuits shown in figure 9.5, R_s is interpreted as the resistance of the electrolyte; CPE_{Coat} ($0.63 < n_{coat} < 0.78$) and R_{Coat} represent the capacitance and resistance of the hybrid coatings, respectively; L and R_L represent the inductance and inductance resistance due to the adsorption reaction, respectively; CPE_{oxide} ($0.70 < n_{coat} < 0.87$) and R_{oxide} represent the capacitance and resistance of the metal oxide layer over the metal surface , respectively. In these equivalent circuits, constant phase elements (CPE) were used instead of pure capacitors, because of the non-ideal character of the corresponding response. This is due to presence of nanoparticles which give rise to a certain surface roughness and inhomogeneity's. The true capacitances can be calculated from the respective CPE parameters, as described elsewhere [29]. The inductor which arises from adsorption effects could be defined as $L=R_L\tau$, where τ is the relaxation time for adsorption on the electrode surface [38]. The variation of the fitted parameters (resistances and capacitances) with immersion time using the equivalent circuits of figure 9.5 is shown in figure 9.6. Values are shown with the errors from the numerical fitting ($10^{-4} <$ Chi-squared $< 10^{-3}$).

The change of the silane hybrid film's capacitance (CPE_{coat}) during immersion is presented in figure 9.6a. Generally the capacitance of dielectric films depends on the amount of absorbed water [6], thus increases in capacitance values are associated to water uptake [5]. Sample D has the lowest coating capacitance of the four systems examined over the whole immersion time. In addition, during immersion, the capacitance yields relatively constant

values, with only a small increase after 168 h of immersion. This suggests a lesser amount of water uptake, because of the smaller nanopores (below AFM resolution), or nanopores only formed later, or the almost absence of nanoparticle agglomerations (as mentioned above). Sample B is also relatively stable; showing a small capacitance increase after around 96 h.

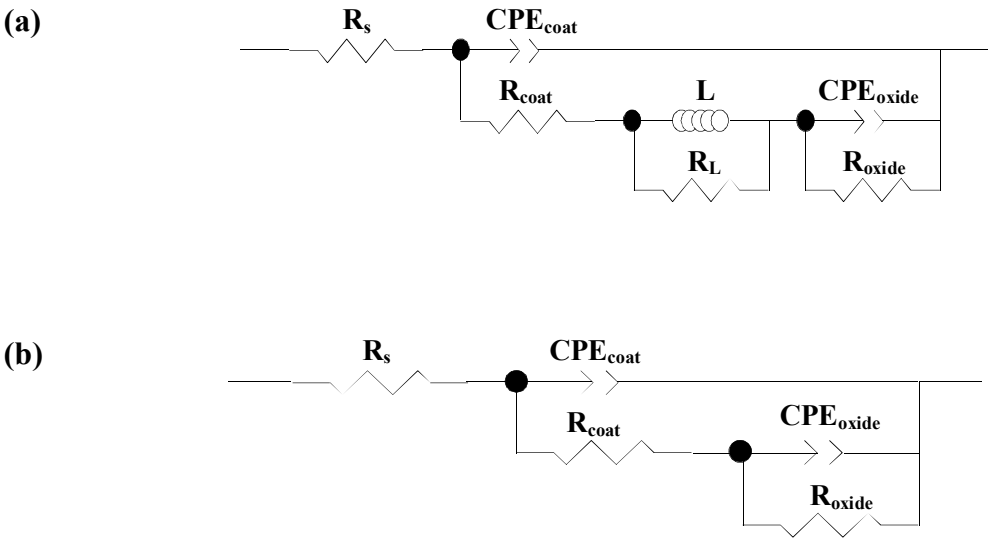

Figure 9.5. Equivalent circuits used for the numerical fitting of the EIS data during immersion in a 3.5% NaCl solution.

The capacitance of samples A and C exhibit significantly faster growth during 168 h of immersion, as a result of more water uptake through the pores/defects present in the films [10]. The access of aggressive species induces localised corrosion activity. This is followed by precipitation of either insoluble corrosion products or the inhibition activity of the film, which block the pores/defects at the coating/substrate interface leading to a partial recovery of the coating barrier properties. This precipitation is translated in a decrease in coating capacitance after the increase due to water uptake. Decreasing coating capacitance is more pronounced for samples A and B, in comparison to sample C, probably because of the

presence of cerium nitrate. These results suggest that the activation of nanoparticles with cerium ions had a beneficial impact on the coating capacitance and thus the protective behaviour.

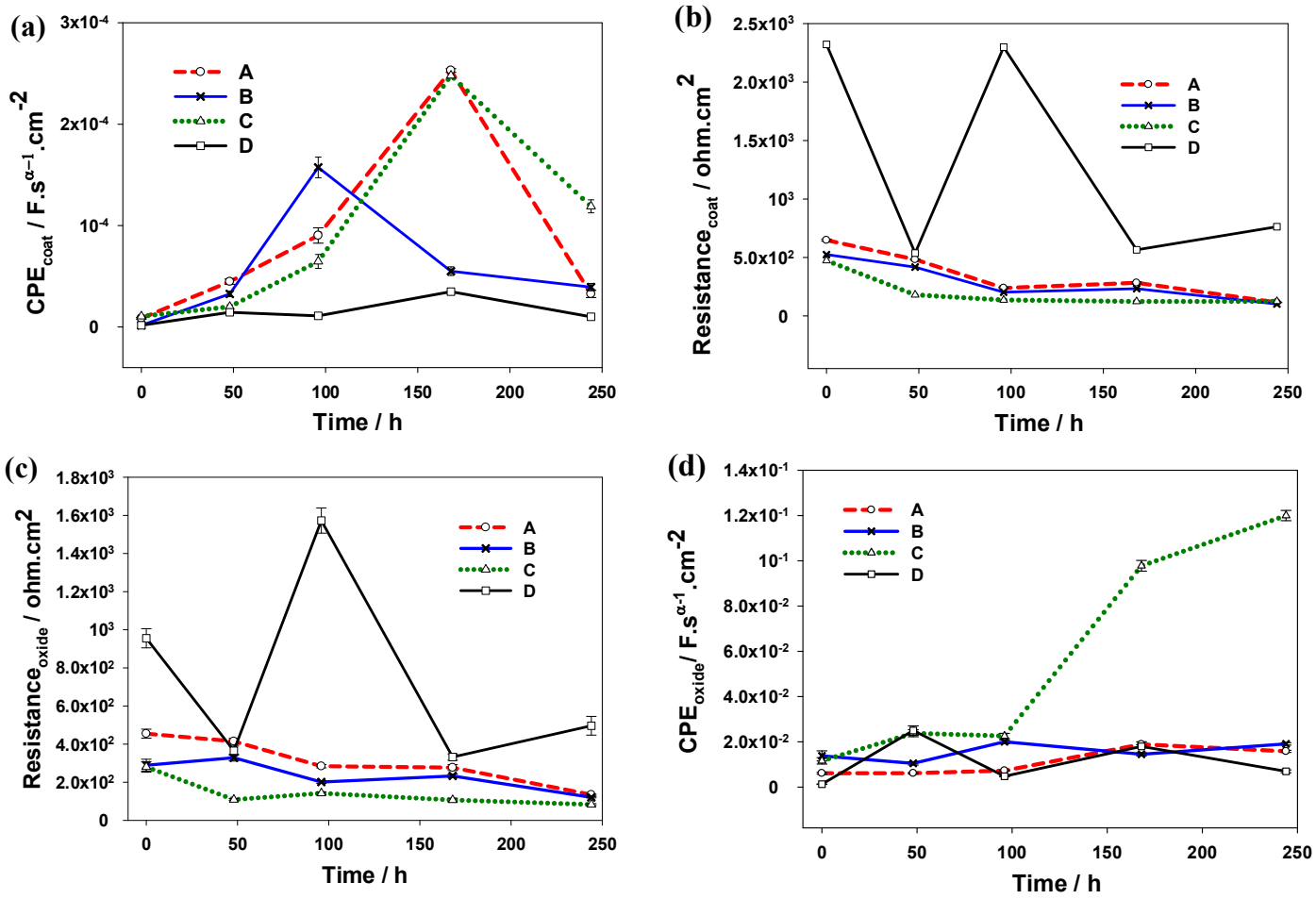

Figure 9.6. Evolution of the coating capacitance (a); coating resistance (b); metal oxide layer resistance (c); and metal oxide layer capacitance (d) during immersion in a 3.5 % NaCl solution.

The evolution of the coating resistance (R_{coat}) of the sol–gel layers, is shown in figure 9.6b. Sample D has the highest coating resistance during the 244 h immersion period; however the resistance decreases both at 48 h and 168 h suggesting the formation of some

pores or the enlargement of smaller pores in the sol–gel layer [32]. In both cases, the coating resistance recovers, which is attributed to the self-healing properties of this coating. The coating resistance of samples A, B and C is lower in comparison to coating D, particularly in the case of the coating C. The coating resistance values of these films show a gradual decrease during immersion because of their porous structures. Because these pores are larger than in the case of coating D, the self-healing capabilities are not enough and cannot compensate the damage. The coating resistance of sample D was always, even after 244 h exposure, at least twice as high as the other samples.

Figure 9.6c and d show the evolution of the metal oxide layer resistance (R_{oxide}) and capacitance (CPE_{oxide}) values during immersion that are associated with the development of a time constant in the low-frequency range of the EIS spectra. For samples A, B and C, the low frequency resistance (R_{oxide}) reveals lower values than for coating D and a small decrease during immersion (Figure 9.6c). In contrast, sample D shows some fluctuations, with a rapid drop and later recovery attributed to the self-healing properties. After 244 h of immersion, this coating shows a metal oxide resistance, which is about three times higher than the other sol-gel films.

The CPE associated with the corrosion process between metal oxide layer and electrolyte (CPE_{oxide}), remains almost constant for samples A and B over immersion for 244 h, reflecting the stability and the good barrier properties of the coating. In contrast, the CPE_{oxide} values for sample C are higher and showed a pronounced increase because of the enlargement of the pores, appearance of cracks or even peeling of the coating. Indeed some coating peeling was evident to the naked eye for coating C at the end of the immersion period. For sample D, the low-frequency capacitance passes through small maxima after 48h and 168 h immersion, and then starts to decrease. These values agree with the evolution of the low-

frequency resistance of the film. The evolution of the low-frequency resistance shows an increase after 96 h immersion, accompanied by a decrease in the CPE, i.e. as expected, the CPE_{oxide} changes in the opposite direction as R_{oxide}. Since the corrosion activity occurred in localised areas because of water uptake, it is likely that the precipitation of the insoluble and passive self-healing products occurred at these locations, thereby decreasing the corrosion activity at the interface [10].

9.4. Discussion

The electrochemical results are in good agreement with the AFM images and the salt-spray tests. There is a clear correlation between protective performance and surface morphology. Sample C, containing non-activated CeO_2-ZrO_2 nanoparticles, shows both a large number of nanoparticles aggregates as well as several cracks or pores. This sample was the least performing in all corrosion tests: faster corrosion, red rust formation and even some localised corrosion in the undamaged coating in the salt spray test; the lowest E_{corr}; and the impedance fitting parameters that showed the highest permeability to water, and hence aggressive species. Montemor *et al.* analysed this specific coating (CeO_2-ZrO_2 nanoparticles without cerium inhibitor) and found it was efficient and stable when exposed to diluted NaCl concentrations (0.005M) [1]. However, our results show that under more aggressive conditions, the nanoparticle reinforcing capabilities on the silane coating are not sufficient to protect the substrate.

While none of the analysed coatings remained unchanged under the extreme aggressive conditions applied, all experimental evidence shows that the combination of CeO_2 and ZrO_2 nanoparticles and cerium ions (coating D) outperforms the other coatings. The better performance in the corrosion tests strongly suggests that the addition of cerium ions to the CeO_2-ZrO_2 nanoparticles dispersion creates an important synergy, reinforcing the

protection of the silane films [5]. The combination of two types of nanoparticles and the cerium ions doping produces the more homogeneous coating. The almost absence of nanoparticle aggregates could be due to less attraction between different nanoparticles (ZrO_2 and CeO_2), the repulsive effects of charged particles (in the presence of $Ce(NO_3)_3$), and the stabilization of the surface charge, as previously reported [6]. These effects are also present in coatings A and B, but not C. Indeed, a plausible explanation for the higher degree of nanoparticle aggregation and probably related extended nanoporosity of coating C could be the non-activation of the nanoparticles. Thus, besides the already reported corrosion inhibition and healing capabilities of $Ce(NO_3)_3$ [6, 7, 20-23, 26], our experimental evidence suggests that in combination with ZrO_2 and/or CeO_2 nanoparticles, it contributes to the reinforcement of the coating, by diminishing its porosity.

EIS responses indicate changes in the coating long time before any visible damage occurs (as observed for example by salt spray test). Thus, while the salt spray is an excellent indicator of healing capabilities around coating damaged areas, EIS evaluates apparent intact coatings. Even though no pores or cracks were observed for coatings B and D by AFM, EIS showed that when subject to stressing conditions, water uptake does occur, and hence some corrosion activity starts to develop (though invisible to the naked eye at this point). The reported self-healing properties of cerium ions are most evident in the rather sharp changes in both coating and metal oxide resistance values for coating D. These changes are associated with recovery after an initial aggression.

Finally, performances shown by coatings A and B are quite similar. Coating A showed one spot of localised corrosion in an undamaged area and coating B did not. On the other hand, coating B showed some red rust around the damaged area after 264 h in salt spray, whereas coating A did not. Most probably the small spot of localised corrosion in A is

associated with the small pores observed by AFM (not observed for B). Conversely, the absence of red rust for this same coating, suggests that the ZrO_2 nanoparticles are more effective as nano-structured Ce-ion reservoirs and can provide longer release of the inhibitor ions [10], than the CeO_2 nanoparticles.

Previous work has outlined possible mechanisms to explain the corrosion inhibition effect silane films, rare earth salts and oxide nanoparticles. Water uptake through the pre-existent pinholes in the coating causes development of anodic and cathodic activity. Under the conditions tested in the present work, the main cathodic reaction is oxygen reduction with production of hydroxyl ions. The Zn^{2+} ions produced at the anodic areas migrate to the cathodic spots where they combine with OH^- to form zinc corrosion products, which in the presence of chloride ions also lead to the formation of simonkolleite and/or other zinc chloride charged ions as reported in the literature [1, 5]. Simultaneously to these processes, and under an increased pH, the Si-O-Si network starts to decompose into a hydrated and expanded gel [5, 10, 15]. In a first step there is formation of silicates, which may provide some protection in small defects or pores. It has been reported that a passive film composed of $Zn(OH)_2$, $ZnSi_2O_5$ may form on the active areas and that preferential precipitation of zinc silicate occurred on the defects of the passive film, delaying the corrosion activity [10].

As the pH becomes more alkaline, the deterioration of the silica network starts to release the CeO_2 and/or ZrO_2 nanoparticles, which are, in contrast, very stable under alkaline pH [5, 10]. The CeO_2 nanoparticles have a very high affinity for oxygen and for charged ions, like Zn^{2+}, compensating defects in the oxygen sub–lattice. CeO_2 can co-precipitate together with the zinc corrosion products, leading to a more stable and protective surface layer, which polarizes the anodic reactions and inhibits the corrosion activity [5, 10, 15].

Additionally, cerium ions released from the nanoparticles may form highly insoluble $Ce(OH)_3$ which can be formed in the spots where the cathodic reaction occurs [41]. The oxidation of Ce^{3+} to Ce^{4+} by peroxide species produce precipitation of $Ce(OH)_4$. ZrO_2 nanoparticles have been reported to act as a reservoirs for corrosion inhibitors, but are otherwise inert [1].

Finally, as briefly explained, because of the relatively large error in the thickness measurements, it is dubious to make assertions about the effect of a possible minor increase in coating thickness on going from coating A to D. After having analysed all the experimental evidence, we believe that the observed differences in performance are most probably not explained by the possible differences in coating thickness. Indeed, while coating D could be up to 20% thicker than its counterparts, it shows low frequency impedance values more than three times higher than the other coatings. Moreover, while coating C shows the putatively second largest thickness value, it is clearly the least performing coating.

9.5. Conclusion

Hybrid silane coatings doped with four different combinations of CeO_2 and ZrO_2 nanoparticles and $Ce(NO_3)_3$ ions were synthetized and tested as protective protection for electro-galvanized steel substrates. All coatings showed very high protection as compared to an uncoated sample.

Morphology and corrosion studies reveal that the presence of cerium ions reduces the corrosion rate of the metal substrate. These results show that cerium ions in combination with CeO_2 and ZrO_2 nanoparticles, produce a better sealed coating, with almost no nanopores or cracks. Incorporation of activated CeO_2-ZrO_2 nanoparticles reduces the cathodic and anodic current density to lower values and shifts the voltage to more positive potentials.

EIS results revealed self-healing properties of the Ce ions that were most evident in the rather sharp changes in both coating and metal oxide resistance values for the coating containing activated CeO_2-ZrO_2 nanoparticles. The highest impedance magnitude value of this coating suggested that the CeO_2-ZrO_2 nanoparticles are more effective as nanostructured cerium ion reservoirs and can provide prolonged release of the inhibitor ions. The prolonged release of cerium ions from oxide nano-reservoirs confers longer protection of the metallic substrate. This coating can be a prospective candidate for the development of new environmentally friendly protective pre-treatments.

References

1. M.F. Montemor, W. Trabelsi, S.V. Lamaka, K.A. Yasakau, M.L. Zheludkevich, A.C. Bastos, M.G.S. Ferreira, The synergistic combination of bis-silane and $CeO_2 \cdot ZrO_2$ nanoparticles on the electrochemical behaviour of galvanised steel in NaCl solutions, Electrochimica Acta, 53, 2008, pp. 5913-5922.
2. M. Wang, D. He, H. Xie, L. Fu, Y. Yu, Q. Zhang, Characterization of bis-[triethoxysilylpropyl] tetrasulfide layers on aluminum based on water-based silanization solution, Thin Solid Films, 520, 2012, pp. 5610-5615.
3. C. Motte, M. Poelman, A. Roobroeck, M. Fedel, F. Deflorian, M.G. Olivier, Improvement of corrosion protection offered to galvanized steel by incorporation of lanthanide modified nanoclays in silane layer, Progress in Organic Coatings, 74, 2012, pp. 326-333.
4. W. Trabelsi, P. Cecílio, M.G.S. Ferreira, K. Yasakau, M.L. Zheludkevich, M.F. Montemor, Surface evaluation and electrochemical behaviour of doped silane pre-treatments on galvanised steel substrates, Progress in Organic Coatings, 59, 2007, pp. 214-223.

5. M.F. Montemor, M.G.S. Ferreira, Cerium salt activated nanoparticles as fillers for silane films: evaluation of the corrosion inhibition performance on galvanised steel substrates, Electrochimica Acta, 52, 2007, pp. 6976-6987.
6. M.L. Zheludkevich, R. Serra, M.F. Montemor, K.A. Yasakau, I.M.M. Salvado, M.G.S. Ferreira, Nanostructured sol–gel coatings doped with cerium nitrate as pre-treatments for AA2024-T3: Corrosion protection performance, Electrochimica Acta, 51, 2005, pp. 208-217.
7. M.L. Zheludkevich, R. Serra, M.F. Montemor, M.G.S. Ferreira, Oxide nanoparticle reservoirs for storage and prolonged release of the corrosion inhibitors, Electrochemistry Communications, 7, 2005, pp. 836-840.
8. A.R. Phani, Gammel, F. J., Hack, T. and Haefke, H, Enhanced corrosioon resistance by sol-gel-based ZrO_2-CeO_2 coatings on magnesium alloys, Materials and Corrosion, 56, 2005, pp. 77–82.
9. F. Deflorian, M. Fedel, S. Rossi, P. Kamarchik, Evaluation of mechanically treated cerium (IV) oxides as corrosion inhibitors for galvanized steel, Electrochimica Acta, 56, 2011, pp. 7833-7844.
10. M.F. Montemor, R. Pinto, M.G.S. Ferreira, Chemical composition and corrosion protection of silane films modified with CeO_2 nanoparticles, Electrochimica Acta, 54, 2009, pp. 5179-5189.
11. F. Brusciotti, A. Batan, I. De Graeve, M. Wenkin, M. Biessemans, R. Willem, F. Reniers, J.J. Pireaux, M. Piens, J.Vereecken, H. Terryn, Characterization of thin water-based silane pre-treatments on aluminium with the incorporation of nano-dispersed CeO_2 particles, Surface and Coatings Technology, 205, 2010, pp. 603-613.
12. M. Schem, T. Schmidt, J. Gerwann, M. Wittmar, M. Veith, G.E. Thompson, I.S. Molchan, T. Hashimoto, P. Skeldon, A.R. Phani, S. Santucci, M.L. Zheludkevich, CeO_2-

filled sol–gel coatings for corrosion protection of AA2024-T3 aluminium alloy, Corrosion Science, 51, 2009, pp. 2304-2315.

13. B.P. Mosher, C. Wu, T. Sun, T. Zeng, Particle-reinforced water-based organic–inorganic nanocomposite coatings for tailored applications, Journal of Non-Crystalline Solids, 352, 2006, pp. 3295-3301.
14. A. Phanasgaonkar, V.S. Raja, Influence of curing temperature, silica nanoparticles- and cerium on surface morphology and corrosion behaviour of hybrid silane coatings on mild steel, Surface and Coatings Technology, 203, 2009, pp. 2260-2271.
15. M.F. Montemor, M.G.S. Ferreira, Analytical characterization of silane films modified with cerium activated nanoparticles and its relation with the corrosion protection of galvanised steel substrates, Progress in Organic Coatings, 63, 2008, pp. 330-337.
16. N.C. Rosero-Navarro, S.A. Pellice, A. Durán, M. Aparicio, Effects of Ce-containing sol–gel coatings reinforced with SiO_2 nanoparticles on the protection of AA2024, Corrosion Science, 50, 2008, pp. 1283-1291.
17. H.M. Hawthorne, A. Neville, T. Troczynski, X. Hu, M. Thammachart, Y. Xie, J. Fu, Q. Yang, Characterization of chemically bonded composite sol–gel based alumina coatings on steel substrates, Surface and Coatings Technology, 176, 2004, pp. 243-252.
18. S.V. Lamaka, M.L. Zheludkevich, K.A. Yasakau, R. Serra, S.K. Poznyak, M.G.S. Ferreira, Nanoporous titania interlayer as reservoir of corrosion inhibitors for coatings with self-healing ability, Progress in Organic Coatings, 58, 2007, pp. 127-135.
19. Q.W. Suning Li, Tao Chen, Zhihua Zhou, Ying Wang and Jiajun Fu, Study on cerium-doped nano-TiO_2 coatings for corrosion protection of 316 L stainless steel, Nanoscale Research Letters, 7, 2012, 7:227, pp. 227.

20. M.F. Montemor, W. Trabelsi, M. Zheludevich, M.G.S. Ferreira, Modification of bis-silane solutions with rare-earth cations for improved corrosion protection of galvanized steel substrates, Progress in Organic Coatings, 57, 2006, pp. 67-77.
21. K. Aramaki, Self-healing mechanism of a protective film prepared on a $Ce(NO_3)_3$-pretreated zinc electrode by modification with $Zn(NO_3)_2$ and Na_3PO_4, Corrosion Science, 45, 2003, pp. 1085-1101.
22. K. Aramaki, The inhibition effects of cation inhibitors on corrosion of zinc in aerated 0.5 M NaCl, Corrosion Science, 43, 2001, pp. 1573-1588.
23. K. Aramaki, Preparation of self-healing protective films on a zinc electrode treated in a cerium(III) nitrate solution and modified with sodium phosphate and cerium(III) nitrate, Corrosion Science, 46, 2004, pp. 1565-1579.
24. R.Z. Zand, K. Verbeken, A. Adriaens, Influence of the cerium concentration on the corrosion performance of Ce-doped silica hybrid coatings on hot dip galvanized steel substrates, International Journal of Electrochemical Science, 8, 2013, pp. 548-563.
25. R.Z. Zand, K. Verbeken, A. Adriaens, Evaluation of the corrosion inhibition performance of silane coatings filled with cerium salt-activated nanoparticles on hot-dip galvanized steel substrates, International Journal of Electrochemical Science, 8, 2013, pp. 4924-4940.
26. A.M. Cabral, W. Trabelsi, R. Serra, M.F. Montemor, M.L. Zheludkevich, M.G.S. Ferreira, The corrosion resistance of hot dip galvanised steel and AA2024-T3 pre-treated with bis-[triethoxysilylpropyl] tetrasulfide solutions doped with $Ce(NO_3)_3$, Corrosion Science, 48, 2006, pp. 3740-3758.
27. S. Zheng, J. Li, Inorganic–organic sol gel hybrid coatings for corrosion protection of metals, Journal of Sol-Gel Science and Technology, 54, 2010, pp. 174-187.

28. A.N. Khramov, N.N. Voevodin, V.N. Balbyshev, M.S. Donley, Hybrid organo-ceramic corrosion protection coatings with encapsulated organic corrosion inhibitors, Thin Solid Films, 447–448, 2004, pp. 549-557.
29. R.Z. Zand, K. Verbeken, A. Adriaens, Corrosion resistance performance of cerium doped silica sol–gel coatings on 304L stainless steel, Progress in Organic Coatings, 75, 2012, pp. 463-473.
30. R.Z. Zand, K. Verbeken, A. Adriaens, The corrosion resistance of 316L stainless steel coated with a silane hybrid nanocomposite coating, Progress in Organic Coatings, 72, 2011, pp. 709-715.
31. N.N. Voevodin, V.N. Balbyshev, M.S. Donley, Investigation of corrosion protection performance of sol–gel coatings on AA2024-T3, Progress in Organic Coatings, 52, 2005, pp. 28-33.
32. A. Pepe, M. Aparicio, A. Duran, S. Cere, Cerium hybrid silica coatings on stainless steel AISI 304 substrate, Journal of Sol-Gel Science and Technology, 39, 2006, pp. 131-138.
33. W. Trabelsi, P. Cecilio, M.G.S. Ferreira, M.F. Montemor, Electrochemical assessment of the self-healing properties of Ce-doped silane solutions for the pre-treatment of galvanised steel substrates, Progress in Organic Coatings, 54, 2005, pp. 276-284.
34. W. Trabelsi, E. Triki, L. Dhouibi, M.G.S. Ferreira, M.L. Zheludkevich, M.F. Montemor, The use of pre-treatments based on doped silane solutions for improved corrosion resistance of galvanised steel substrates, Surface and Coatings Technology, 200, 2006, pp. 4240-4250.
35. P.D. Deck, M. Moon, R.J. Sujdak, Investigation of fluoacid based conversion coatings on aluminum, Progress in Organic Coatings, 34, 1997, pp. 39-48.
36. A. Neville, C. Wang, Erosion–corrosion mitigation by corrosion inhibitors—An assessment of mechanisms, Wear, 267, 2009, pp. 195-203.

37. M.E.Orazem, B.Tribollet, Electrochemical impedance spectroscopy, John Wiley and Sons INC., Hoboken, NJ, USA, 2008.
38. S.A. Umoren, Y. Li, F.H. Wang, Effect of polyacrylic acid on the corrosion behaviour of aluminium in sulphuric acid solution, Journal of Solid State Electrochemistry, 14, 2010, pp. 2293-2305.
39. A. Zomorodian, F. Brusciotti, A. Fernandes, M.J. Carmezim, T. Moura e Silva, J.C.S. Fernandes, M.F. Montemor, Anti-corrosion performance of a new silane coating for corrosion protection of AZ31 magnesium alloy in Hank's solution, Surface and Coatings Technology, 206, 2012, pp. 4368-4375.
40. Z.Y. X. Liu, T. Romeo, J. Weber, T. Scheuermann, S. Moulton, G. Wallace, Biofunctionalized anti-corrosive silane coatings for magnesium alloys, Acta Biomaterialia, 9, 2013, pp. 8671-8677.
41. K.A. Yasakau, M.L. Zheludkevich, O.V. Karavai, M.G.S. Ferreira, Influence of inhibitor addition on the corrosion protection performance of sol–gel coatings on AA2024, Progress in Organic Coatings, 63, 2008, pp. 352-361.

10

CONCLUSIONS

Cerium-doped silane hybrid coatings employing 3-glycidoxypropyltrimethoxysilane (GPTMS) and bisphenol A (BPA), as a cross-linking agent, were synthesized via a sol–gel method and fabricated on treated steel surfaces (either austenitic 316L and 304L stainless steels or hot-dip and electro galvanized steels). The use of these substrates allowed investigating the effects of various parameters that influence the microstructure, morphology, and protective properties of the coatings. The use of the various substrates also allowed us to obtain a better view on the corrosion inhibition performance of the cerium doped silane hybrid coating and in some cases decreased the experimental time. An example of this is the duration of the salt spray test of the silane hybrid coatings modified with cerium nitrate and CeO_2 nanoparticles on 304L SS and HDG substrates which was reduced from 2000 h to 144 h respectively (Chapters 5 and 7). These parameters include the coatings drying condition, the

concentration of the cerium ions and CeO_2 nanoparticles, and additives such as bisphenol A, cerium nitrate, CeO_2 nanoparticles and ZrO_2 nanoparticles.

The results show that pre-treatments involving the thermal curing of the silane hybrid coatings led to improved corrosion resistance for the 316L SS substrates. Furthermore, the methodology proposed in this work is straightforward to apply and is compatible with actual environmental concerns.

FTIR spectroscopy and SEM confirmed the formation of crack-free cerium-doped silane hybrid coatings with Si–O−Si structural backbones and $–CH_2$ groups incorporated into the silica network. The resulting films were transparent and homogenous. The BPA cross-linking agent significantly affected the morphology and corrosion resistance of the cerium-doped silica coating. The lack of cross-linking agent (BPA) in the linear cross-linked cerium-doped silane hybrid coating caused it to show cracks, be very brittle, thereby promoting diffusion of the aggressive electrolyte toward the substrate and decreasing the corrosion resistance of the coating.

The results also show that the silane coatings modified with Ce nitrate hexahydrate provide good barrier properties and improve the corrosion protection in comparison with non-modified silane coatings when applied to 304L SS substrates. The Ce-inhibited system showed a slower electrochemical evolution than did the non-inhibited one, because the inhibition effect of the cerium ions reduced the corrosion kinetics.

Comparatively smooth nano-structured surfaces with low heterogeneity of coating thickness were observed in the silane coatings modified with cerium nitrate rather than CeO_2 nanoparticles. The use of CeO_2 nanoparticles led to a high heterogeneity of the coating thickness.

Corrosion testing indicated that the CeO_2 nanoparticles gave good corrosion inhibition properties to scratched surfaces because of their ability to complex with other species, therefore contributing to the stabilization of the passive film via an anodic inhibition mechanism. Modification of the silane solution with cerium nitrate led to improvements in the barrier properties, corrosion inhibition, and the self-repair of defects. The cerium ions can change the silane solution chemistry, promoting the formation of reactive silanol groups and more condensed species.

Electrochemical studies indicated general improvements due to the incorporation of cerium nitrate, although the performance of the coated substrate depended on the doping level. Too low or too high cerium concentrations led to reduced corrosion inhibition in the sol–gel matrix. EIS and polarization results confirmed that the optimal corrosion resistance was obtained at a cerium concentration of 0.05 M.

Modifying the silane coatings with cerium salt-activated CeO_2 nanoparticles led to formation of a comparatively smooth, nanostructured surface with a constant or near-constant coating thickness. Microscopic observations also confirmed that the integral surface morphology of the silane coating filled with activated CeO_2 nanoparticles was maintained after short-term corrosion testing for 144 h. Electrochemical tests showed that the presence of the nanoparticles reinforced the barrier properties of the silane films, and a synergy seemed to be created between the activated nanoparticles and the cerium ions, reducing the corrosion activity. The incorporation of activated CeO_2 nanoparticles reduced the cathodic current density by two orders of magnitude and shifted the voltage to more positive values (compared with the blank silane-coated substrate) during polarization in 3.5% NaCl solution.

The EIS results suggested that the concentration of the nanoparticles has an important impact on the barrier properties of the silane films, as lower nanoparticle content results in

better barrier properties. Enhanced protection at both the cathodic and the anodic sites was offered by the coating that contained the lowest content of ceria nanoparticles compared with the other coatings that contained higher contents of nanoparticles. Thicker and more protective silane films formed when the CeO_2 nanoparticles and cerium ions were used at proportions of 25% and 75%, respectively. Microscopic observations also confirmed that the integral surface morphology of the silane film was maintained after 456 h of immersion in a 3.5% NaCl solution.

Investigation the effect of ceria and zirconia nanoparticles on the anticorrosion behaviour of un–inhibited and cerium inhibited silane hybrid coatings, revealed the best performance for the coating that combines both CeO_2 and ZrO_2 nanoparticles activated by $Ce(NO_3)_3$ ions. EIS results suggested that the CeO_2-ZrO_2 nanoparticles are more effective as nanostructured cerium ion reservoirs and can provide prolonged release of the inhibitor ions. The prolonged release of cerium ions from oxide nano-reservoirs confers longer protection of the metallic substrate. This coating can be a prospective candidate for the development of new environmentally friendly anticorrosion pre-treatments.

The results of this work on electrochemical behavior of cerium modified silica hybrid coatings showed that despite the high corrosion protection performance of these coatings in high salinity solution (3.5% NaCl), but when dealing with longer immersion times of the coated object in NaCl, a fast deterioration of the barrier properties of the coating could also be observed. Therefore, we have concluded that it is very difficult to obtain both functionalities - barrier properties and active protection in a mono-layer sol–gel system. One possible way to further improve these coatings is to use systems composed of different layers. In these systems the bottom layer intends to provide corrosion protection and adherence to the metallic substrate, whereas the top layers complement the anticorrosive protection and, in addition,

must provide binding for potential future organic coatings. For example, a non-functional bis-silane, can be employed as the first layer, which is then topped with a functional silane layer, even though functional silanes have already been also employed as bottom layer.

Therefore, this work can be continue by study the corrosion protection behavior of electro-galvanized steel substrate coated with a cerium-doped silane bi-layer. Two types of silane layers will be prepared, non-inhibited and inhibited silane layer. The non-inhibited layer only provides a physical barrier against the environment, while the inhibited layer should provide an active corrosion protection.

LIST OF PUBLICATIONS

I) Book chapters

1. R. Zandi Zand, K. Verbeken, A. Adriaens, Synthesis and characterization of self-healing coatings for the corrosion protection of steel. In: Intelligent Coatings for Corrosion Control, A. Tiwari, L. Hihara, J. Rawlins (editors), Elsevier, Amsterdam, 2014, p. 135-194.

2. Papers in International Journals

1. Roohangiz Zandi Zand, Victoria Flexer, Michel De Keersmaecker, Kim Verbeken, Annemie Adriaens, Self-healing silane coatings of cerium salt activated nanoparticles, In preparation.

2. Roohangiz Zandi Zand, Victoria Flexer, Michel De Keersmaecker, Kim Verbeken, Annemie Adriaens, Effects of activated Ceria and Zirconia nanoparticles on the protective behaviour of silane coatings in chloride solutions, International Journal of Electrochemical Science 10(2015) 997-1014.

3. Roohangiz Zandi Zand, Kim Verbeken, Victoria Flexer, Annemie Adriaens, Effects of ceria nanoparticle concentrations on the morphology and corrosion resistance of cerium-silane hybrid coatings on electro-galvanized steel substrates, Materials Chemistry and Physics 145 (2014) 450-460.

4. Roohangiz Zandi Zand, Kim Verbeken, Annemie Adriaens, Evaluation of the corrosion inhibition performance of silane coatings filled with cerium salt-activated nanoparticles on hot-dip galvanized steel substrates, International Journal of Electrochemical Science 8 (2013) 4924-4940.

5. Roohangiz Zandi Zand, Kim Verbeken, Annemie Adriaens, Influence of the cerium concentration on the corrosion performance of Ce-doped silica hybrid coatings on hot dip galvanized steel substrates, International Journal of Electrochemical Science 8 (2013) 548-563.
6. Roohangiz Zandi Zand, Kim Verbeken, Annemie Adriaens, Electrochemical assessment of the self-healing properties of cerium doped sol-gel coatings on 304L stainless steel substrates, International Journal of Electrochemical Science 7 (2012) 9592-9608.
7. Roohangiz Zandi Zand, Kim Verbeken, Annemie Adriaens, Corrosion resistance performance of cerium doped silica sol–gel coatings on 304L stainless steel, Progress in Organic Coatings 75 (2012) 463-473.
8. Roohangiz Zandi Zand, Kim Verbeken, Annemie Adriaens, The corrosion resistance of 316L stainless steel coated with a silane hybrid nanocomposite coating, Progress in Organic Coatings 72 (2011) 709-715.

III) Conference abstracts

1. Roohangiz Zandi Zand, Kim Verbeken, Victoria Flexer, Annemie Adriaens, Self-healing silane coatings of cerium salt activated nanoparticles, ChemCYS 2014, Blankenberge, Belgium, 27-28 February 2014, oral presentation.
2. Roohangiz Zandi Zand, Kim Verbeken, Annemie Adriaens, Synthesis and characterization of cerium-silane films activated with nanoparticles for the corrosion protection of hot dip galvanized steel, European Corrosion Congress 2013, Estoril-Portugal, 1-5 September 1-5 2013, poster presentation.
3. Roohangiz Zandi Zand, Kim Verbeken, Annemie Adriaens, Effect of cerium concentration on corrosion performance of cerium modified silane films on hot dip

galvanized steel, 53rd Corrosion Science Symposium, Teddington-UK, 6-7 September 2012, poster presentation.

4. Roohangiz Zandi Zand, Kim Verbeken, Annemie Adriaens, Corrosion protection of silene films modified with CeO_2 nanoparticles, 53rd Corrosion Science Symposium, Teddington-UK, 6-7 September 2012, poster presentation.